NORTHWESTERN UNIVERSITY

Pathways for Metastable Carbonate Synthesis

A DISSERTATION

SUBMITTED TO THE GRADUATE SCHOOL
IN PARTIAL FULFULLMENT OF THE REQUIREMENTS

for the degree

DOCTOR OF PHILOSOPHY

Field of Materials Science and Engineering

By
Michael L Whittaker

EVANSTON, IL

September 2017

ABSTRACT

Pathways for Metastable Carbonate Synthesis

Michael L Whittaker

Carbonate minerals are integral to life on earth, as reservoirs for CO_2 in the earth's natural carbon cycle and as the skeletal elements of abundant organisms like corals and plankton. Because of its relevance, availability, and low toxicity, calcium carbonate is also an important model system for phase transformations in aqueous solutions. However, it often does not conform to classical theories of nucleation, prompting a critical reevaluation of both the pathways of carbonate mineralization and the theories that describe them. Most importantly, it has been shown that amorphous calcium carbonate (ACC) is frequently a precursor to crystalline calcium carbonate during precipitation, in both biological and inorganic systems. Amorphous precursors influence phase transformations in several ways, including decoupling densification of ions in solution from their arrangement on a crystalline lattice, altering solution thermodynamics, creating new interfaces, and changing kinetic barriers. To exert control over these processes *in vivo*, organisms generally confine precipitation reactions to small volumes, often within lipid membrane vesicles. Herein, I describe *in vitro* model systems designed to elucidate and replicate biological mineralization pathways. Giant unilamellar vesicles are shown to slow the rate of crystallization of ACC by excluding nucleation accelerants, and by preserving the high kinetic barriers to lower energy phases that result. Phosphatidylcholine, one of the most abun-

dant natural lipids, does not interact strongly with ACC, but the interfacial chemistry can be tuned by changing the lipid charge or reducing steric shielding. Microfluidically produced water-in-oil emulsions were used as liposome analogs to study crystallization kinetics. In ensembles of hundreds of emulsion drops, we show that vaterite forms from ACC via a classical, two-step nucleation process. We also extend the classical theory of nucleation to highly confined aqueous systems, where the formation of a nucleus changes the system composition. In systems chemically similar to ACC, amorphous strontium carbonate (ASC) is also observed in liposomes, but crystallizes rapidly, while amorphous barium carbonate (ABC) is not. We show that ACC can be made with over 50% barium, forming ACBC, but crystallizes at a dramatically faster rate with increasing barium. I demonstrate that this process dramatically departs from the classical description applied to ACC crystallization. It can be explained by the increasing short- and mid-range order in ACBC with increasing barium, which resembles that of crystalline $Ca_{1-x}Ba_xCO_3$ and selectively lowers the barrier to its formation relative to lower-energy structures. This $Ca_{1-x}Ba_xCO_3$ phase has been misidentified as calcite in the literature, but we solve the structure, assign the new spacegroup $R\bar{3}m$, and call it balcite. Balcite is only thermodynamically stable above 525°C, and is over 30% harder than calcite. In the absence of calcium, I show that ABC is a highly transient precursor to a previously uncharacterized $BaCO_3 \cdot H_2O$ phase. This phase forms as very thin (10 nm) and extremely anisotropic platelets, which themselves recrystallize rapidly into witherite ($BaCO_3$). These examples demonstrate the power of amorphous precursors to enable metastable crystalline materials through thermodynamically downhill transformations, and the ability of confined volumes to reduce the rate of these transformations and enable their quantification.

ACKNOWLEDGEMENTS

Being able to remain a student until nearly 30 does not happen by accident, but it has been an outstanding privilege enabled by many fantastic people. While supporting me during grad school was not always Meagan's ideal life trajectory, she did it with a smile on her face and I am much better off for it. I am excited to start the next chapter of my life with you, Ms. Norris. I would never have been in the position to think about higher education without the unconditional love and confidence of my parents, Lynn and Mary Beth Whittaker. I strive daily to match their sagacity and patience. While my path was always fairly easy to follow, my sister Laura Whittaker deserves high praise for her bravery in pursuing a less-traveled route, and succeeding through her own creativity.

Derk Joester taught me that an exceptional scientific mind matches skepticism with confidence, embracing uncertainty while striving for perfection. Much of what I learned from Derk can't be easily summarized in an anecdote, but was absorbed slowly through diffusion. This includes how to write a paper he's satisfied with in less than 10 drafts, where the tick marks are in the right place. Chantel Tester was an excellent mentor who paved the way so well that I continue to learn things from her years after her departure. Lyle Gordon was an inspiration and a tremendous resource. The Joester group, including Irene Chang, Emmie Campbell, Karen DeRocher, Robert Free, and Allessandra DiCorato have made a long and sometimes arduous experience immensely more bearable and a lot more fun. Special thanks to Jack Cavanaugh for buying into my ideas and then making them his own.

Beamline scientists Steven Weigand, Denis Keane, and Qing Ma deserve a lot of credit for helping execute my fanciful experiments, sometimes under considerable pressure and often after midnight (once on Denis' birthday). I am still amazed at the fact that they let me take control of a high powdered X-ray beam at a particle accelerator many times each year. And that good science has occasionally resulted. Seth Fraden and Achini Opthalage at Brandeis University were instrumental for enabling the microfluidics work.

Finally, the funding sources deserve a lot of credit for enabling the work presented here. Moreover, they've decided that investing in my education is in the nation's best interest, which is slightly unnerving but also incredibly humbling. The International Institute for Nanotechnology, NSF (DMR-1508399), and ARO (W911NF-16-1-0262) have all contributed to my success.

PREFACE

Chapter 1. A version of chapter 1 has been published as M. L. Whittaker, P. M. Dove, and D. Joester. Nucleation on Surfaces and in Confinement. *MRS. Bull.* **41**(05), 388-392 (2016). It was written by me and revised and edited by Patricia Dove and Derk Joester.

Chapter 2. This chapter presents the derivation of results presented in chapter 1. It was conceived by me and written and revised by both me and Derk.

Chapter 5. A version of chapter 5 has been published as C. C. Tester, M. L. Whittaker, and D. Joester. Controlling Nucleation in Giant Liposomes. *Chem. Comm.* **50**(42) 5619-22 (2014). Chantel Tester collected the data and wrote the manuscript. I assisted in data collection and interpretation of results.

Chapter 7. A version of chapter 7 has been submitted as J. Cavanaugh, M. L. Whittaker and D. Joester. Crystallization kinetics of ACC in Confinement. *Chem. Comm.* Jack Cavanaugh collected the data and wrote the manuscript as an undergraduate and Master's student under my supervision. I assisted with experimental design, data interpretation, and writing the manuscript.

Chapter 8. This chapter is an extension of the method described in chapter 7 to systems that include biomineralization proteins. I fabricated the devices and conducted all experiments. Keith Alveres extracted, purified, and characterized the proteins.

Chapter 9. A version of chapter 9 has been submitted as M. L. Whittaker, W. Sun, K. A. DeRocher, S. Jayaraman, G. Ceder, D. Joester. Structural Basis for Metastability in Amorphous Calcium Barium Carbonate (ACBC). *Chem. Mater*. I collected experimental data and wrote the manuscript. Karen DeRocher helped with Ca-K edge EXAFS. Simulations were run and analyzed by Wenhao Sun, using structures generated by Sai Jayaraman. Gerbrand Ceder edited the manuscript and it was revised and edited by and Derk Joester.

Chapter 10. This chapter is a manuscript draft in preparation. It will be submitted as M. L. Whittaker, E. Pri-Gal, A. Schmidt, D. Joester. Solution processing of high-temperature carbonates via amorphous precursors.

Chapter 11. A version of chapter 10 has been published as M. L. Whittaker and D. Joester. ACBC to Balcite: Synthesis of a Highly Substituted High-Temperature Phase from an Amorphous Precursor. *Adv. Mater.* **6**, 1606730-5 (2017). I collected the data and wrote the manuscript. It was revised and edited by and Derk Joester.

Chapter 12. A version of chapter 12 has been submitted as M.L. Whittaker, P. Smeets, H. Asayesh-Ardakani, R. Shahbazian-Yassar D. Joester. Aqueous synthesis of quasi-two-dimensional barium carbonate hydrate via a highly transient amorphous precursor. *J. Am. Chem. Soc.* I acquired the data, helped Paul Smeets collect EELS spectra, helped Hasti Asayesh-Ardakani acquire hr-TEM images, and wrote the manuscript. Reza Shahbazian-Yassar edited the manuscript and Derk Joester revised and edited the manuscript.

Table of Contents

List of Tables

List of Figures

1. Nucleation on surfaces and in confinement

1.1 Abstract

A review of current literature supports the notion that organisms may achieve nanoscale control over the hierarchical assembly of organic-inorganic materials by compartmentalizing reactions into small volumes containing specifically functionalized macromolecules. Confinement may introduce a degree of determinism to the stochastic process of nucleation by greatly reducing the number of nucleation events, allowing an organism to control nucleation using ‘soft’ organic substrates. In this way the polymorph, orientation, shape, and size of a crystalline building block can be selected, and its assembly into a larger structure orchestrated by the organic matrix.

1.2 Introduction

Mineralized tissues support locomotion, predation and defense; are used for sensing acceleration, gravity, light, and magnetic fields; and often double as nutrient/waste storage.[1] Many of their remarkable properties emerge from the hierarchical organization of organic and inorganic building blocks (Figure 1.1). Despite new experimental techniques[1-5] and continuous improvement of computational approaches,[6,7] we are still far from understanding how the organism directs mineral nucleation and subsequent processes that lead to assembly.[8-10] This review focuses on our current understanding of two critical aspects of biomineralization — how self-assembled surfaces direct location, orientation, and timing by heterogeneous nucleation, and the role of confinement within small volumes on the rate of phase transformations.

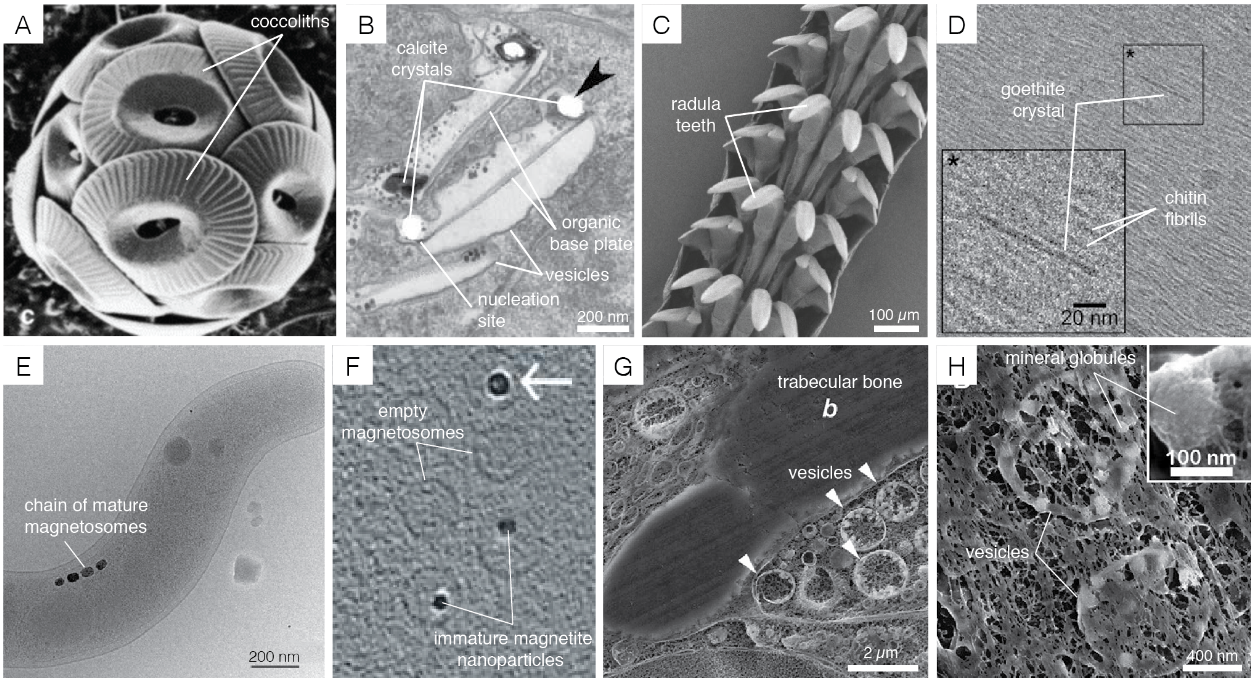

Figure 1.1. Heterogeneous nucleation and confinement in biomineralization. A. Coccoliths are elements of the extracellular coccosphere in the coccolithophores, a class of unicellular marine algae. Heterococcoliths are comprised of a ring of elaborately shaped calcite single crystals attached to an organic base plate. B. Coccolith synthesis is confined within vesicles inside the cell, and involves heterogeneous, oriented nucleation in specific locations in the periphery of the baseplate.[11,12] C. Limpets are intertidal mollusks that graze on rocks using exceptionally hard, iron oxide-based radula teeth. During mineralization, goethite crystals nucleate on a preformed matrix of chitin fibers.[13] E. In magnetotactic bacteria, magnetite nanoparticles are confined within magnetosome vesicles, allowing for alignment and navigation in magnetic fields.[14,15] G,H. Calcium phosphate mineral precipitates in intracellular vesicles observed in neonatal mouse calvaria, a model for human bone mineralization.[16]

1.3 A brief review of nucleation in biomineralization

Biomineralization typically starts with precipitation from a supersaturated aqueous solution.[9,17] The driving force for the formation of a new phase with the chemical formula $\left[(\mathrm{A}_1)_{k_1}(\mathrm{A}_2)_{k_2} \ldots (\mathrm{A}_i)_{k_i}\right]$ can be expressed in terms of the supersaturation

$$\sigma = ln\left[\frac{\prod_i [A_i]^{k_i}}{K_{\mathrm{sp}}}\right] \tag{1.1}$$

where K_{sp} is the solubility product of the new phase. Clusters of the new phase arise from concentration fluctuations. According to classical nucleation theory (CNT), a cluster that is exactly of critical size, the nucleus, is in unstable equilibrium, meaning that both loss and gain of additional building blocks will reduce its free energy. Smaller clusters will on average shrink, larger ones grow. The reversible work of nucleation W^* is the free energy cost (barrier) associated with the formation of a spherical, incompressible nucleus

$$W^* = \frac{16\pi}{3}\left(\frac{V_m}{RT}\right)^2 \frac{\gamma^3}{\sigma^2} \tag{1.2}$$

where γ is the (average) surface free energy of the newly-formed interface and V_m is the molar volume of the new phase.[18] As discussed in the article by Sear,[19] the intrinsic nucleation rate J_V, i.e. the number of nuclei formed per unit time and unit volume, then takes the form[20]

$$J_V \propto e^{-\frac{W^*}{kT}} \tag{1.3}$$

In the presence of heterogeneous nucleators, the height of the barrier is reduced by a structure factor, *S*, that depends upon the specific geometry of nucleus and interface.[21] Alternatively, the impact of heterogeneous nucleators can be expressed by assigning a net effective surface free energy γ_{net}.[22,23]

$$J_V^{\mathrm{het}} \propto e^{-\frac{W^*}{kT}S} = e^{-f\left(\frac{V_m}{RT}\right)^2 \frac{\gamma_{\mathrm{net}}^3}{\sigma^2}} \tag{1.4}$$

The nucleation rate is extremely sensitive to the presence of heterogeneous nucleators, about which little is known in bulk experiments. As a consequence, determination of γ from nucleation rate data is very difficult and a wide spread of the values are reported, for instance for calcite (64-1480 mJ/m²).[24-26] Similar to other crystalline solids, nucleation at moderate supersaturation is expected to proceed extremely slowly when heterogeneous nucleators are absent.[24,25] Metastable amorphous calcium carbonate (ACC), however, forms readily under the same conditions. While ACC is frequently observed in vivo and in vitro, the mechanism of its formation and subsequent transformation into one of crystalline polymorphs remains the topic of much debate.[6,27]

1.4 Nucleation on surfaces

Irrespective of whether a metastable phase such as ACC precedes the formation of a biomineral, the onset of mineralization likely involves heterogeneous nucleators. In biomineralization, this includes fibers and membranes constructed from (macro)molecules of the organic matrix, phospholipid bilayers with associated macromolecules that delimit the mineralization site, and the surface of any precursors present.[28,29] A particularly impressive example is the nucleation of a ring of calcite crystals with alternating orientations on the organic baseplate of the coccolith; there are many more (Figure 1.1).[11-16,30,31]

The impact of the interface on nucleation density, polymorph, and crystallographic orientation is apparent in studies of self-assembled monolayers (SAMs).[32,33] Early reports attribute rapid nucleation of calcite on carboxylate-terminated alkanethiol-based SAMs to a close match in lattice parameters, but ignore the effect of strain at coherent interfaces.[34] More recently, it has become clear that during oriented nucleation, both sides of the interface cooperatively reorganize.[35] A fundamental limitation of the early experiments is that conclusions were necessarily based on observations made fairly far into the growth stage. Much detail regarding relative rates of nucleation and subsequent growth rates of nuclei, for instance in different orientations, is therefore lost, and unambiguous interpretation challenging.

Microfluidic devices can generate supersaturated solutions and maintain a constant flow parallel to a functionalized interface, while allowing in situ observation.[24] Heterogeneous nucleation rates of calcite on SAMs were found to be consistent with the predictions of CNT,[22,23,36] and provide estimates of γ_{net} in the range of ~70-100 mJ/m^2 for polysaccharide- and alkanethiol-functionalized surfaces. Furthermore, there is a direct relationship between γ_{net} and the free energy of binding between calcite and a series of functional groups, consistent with the conventional wisdom that "good binders are good nucleators".[23]

Functional patterning of substrates is thought to be integral to controlling the location of nucleation events, and by extension, hierarchical assembly in biomineralization.[37,38] Looking ahead, such patterning will be essential to improving our understanding of cooperative effects such the synergy gained from the presence of both carboxylate and amine-terminated SAMs in the formation of amorphous silica.[40]

1.5 Nucleation in confinement

We refer to systems as confined if (a) the phase transformation occurs from one or more small volumes of a supersaturated solution and (b) transport of at least one building block of the new phase is prevented between the volumes. After division of a bulk system into a large number of small volumes, only a subset of them will contain suspended nucleators,[39] and phase transformation cannot 'spread' from one volume to the next. In the ideal case, the boundary is a poor heterogeneous nucleator and the rate converges to that of homogenous nucleation.[39-41]

Phase transformation in confinement will appear to slow down unless very large numbers of droplets are observed. This is because in any system consisting of N identical volumes V_d, with a uniform steady-state intrinsic nucleation rate J_V, the fraction of droplets in which nucleation has occurred is[42]

$$f = 1 - e^{-J_V N V_\mathrm{d} t} \tag{1.5}$$

The time until nucleation has occurred in 50% of the droplets ($\tau_{1/2}$) is inversely proportional to the number and the volume of the droplets (Figure 1.2a, b). In other words, even if the barrier is unchanged, the extrinsic nucleation rate, $J = J_V N V_\mathrm{d}$, decreases with the size of the system.

When confinement approaches the nanoscale, the assumption that nucleation does not affect the composition of the aqueous phase breaks down. For example, if nucleation of an AB solid at some initial σ_i consumes an amount of A and B such that their activities each drop to one half, supersaturation is reduced by $\Delta\sigma = \sigma_\mathrm{i} - \sigma_\mathrm{f} \cong 1.4$, where σ_f is the final value. As a consequence, the particle that just formed is subcritical in size and cannot be the nucleus. This effect is more pronounced in smaller confining volumes, for less soluble precipitates, and at lower initial supersaturation (Figure 1.2c).

One can show that at a given σ_i in a confined system of radius R_c, only a particle with radius $r \ll R_\mathrm{c}$ that meets the following equality is in equilibrium after formation:

$$e^{\frac{\gamma V_{\mathrm{m}}}{kN_aT}\cdot\frac{1}{r}} + \frac{r^3}{V_m\sqrt{K_{\mathrm{sp}}}{R_{\mathrm{c}}}^3} - e^{\frac{\sigma_{\mathrm{i}}}{2}} = 0 \tag{1.6}$$

where N_a is Avagadro's number (derivation in chapter 2). Below a critical initial supersaturation σ_i^*, this equation does not have a solution and nucleation cannot occur. Above σ_i^*, the smaller of two solutions corresponds the nucleus, the larger to the particle in final, stable equilibrium, i.e. the end point of the phase transformation (Figure 1.2d,e).

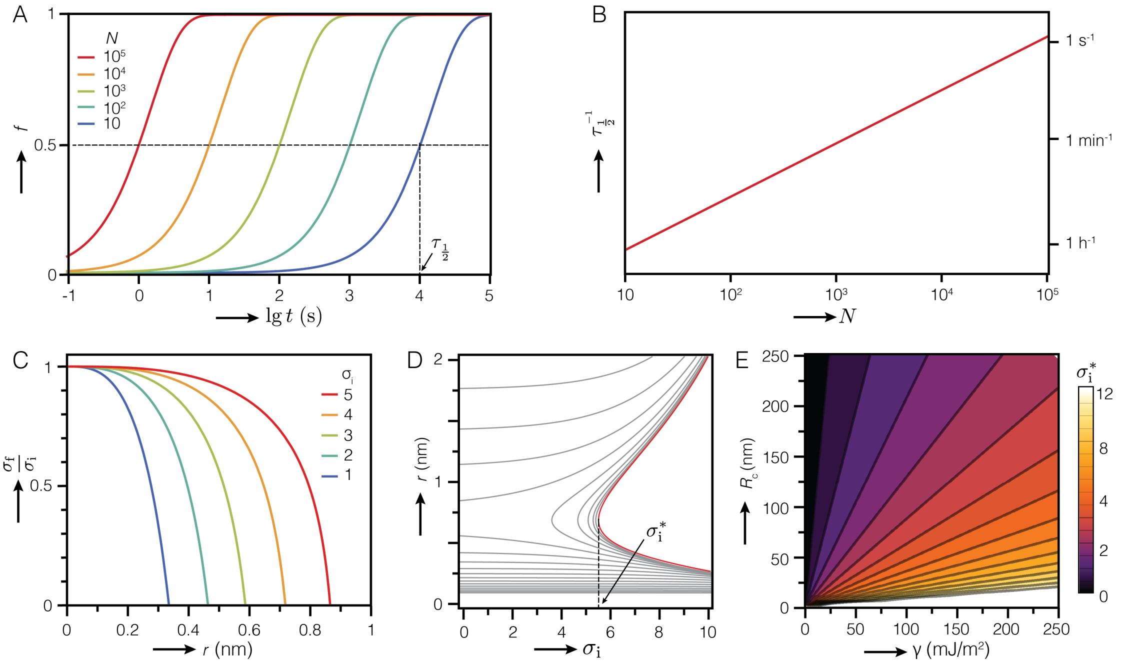

Figure 1.2. The effect of confinement on nucleation. (A) Plot of the fraction f of N volumes in which nucleation has occurred against log time ($J_V=10^8\ \mathrm{m}^{-3}\mathrm{s}^{-1}$; $V_d = 65$ pL). (B) Log-log plot of $\tau_{1/2}^{-1}$ vs. N showing the increase in conversion rate with system size. (C-E) Effect of confinement in spherical containers with $R_c=30$ nm on supersaturation for calcite particles ($K_{sp}=10^{-8.48}\ \mathrm{M}^2$, $V_m=36.9\ \mathrm{cm}^3/\mathrm{mol}$, $\gamma=0.1\ \mathrm{J/m}^2$). (C) Fractional drop in supersaturation as a function of particle radius r. (D) Contour plot of the left hand side of Equation (1.6) as a function of the initial supersaturation and the particle radius. The solution of Equation (1.6) is indicated by the red contour line. (E) Contour plot of the critical supersaturation σ_i^* for nucleation of calcite as a function of the surface free energy and the confining radius.

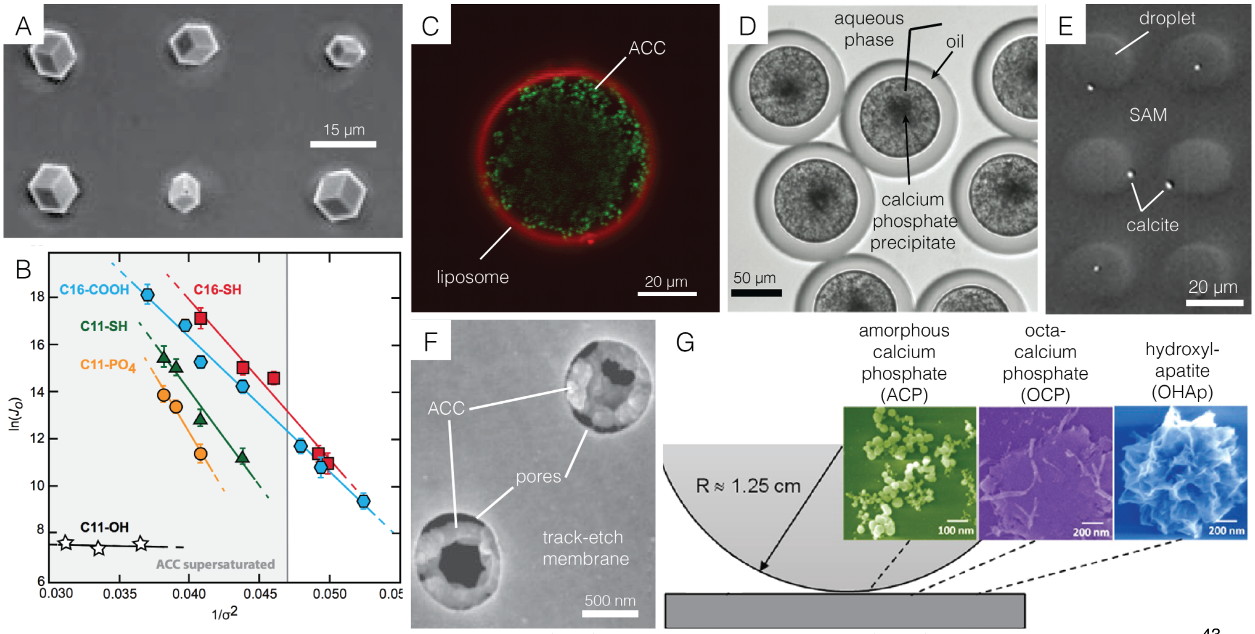

Figure 1.3. A. Calcite crystals nucleated on the (001) plane on a SAM of $HS(CH_2)_{11}SO_3^-$ supported on Pd.[43] B. Nucleation rate as a function of supersaturation for calcite nucleated on SAMs with a range of functional head groups follows predictions of CNT, with constant slope proportional to the interfacial energy, γ.[23] C. ACC rather than calcite precipitates in confinement in giant liposomes, and is stable for long periods of time.[44] D. Calcium phosphate precipitates formed in double emulsion droplets eventually transform into hydroxylapatite.[45] E. Calcium carbonate precipitation in aqueous droplets trapped on a patterned SAM results in extended stability of ACC, but eventually calcite forms; this is likely due to heterogeneous nucleation at the triple line or on the SAM.[46] F. ACC formed in semi-confining pores (d = 800 nm) in a track-etched membrane.[47] G. Partial confinement between a cylinder and a flat substrate resulted in differential stabilization of several metastable intermediates that are typically observed sequentially in hydroxylapatite synthesis.[49]

Closely resembling ideal confinement, individual acoustically levitated drops have been used to identify amorphous precipitates of MCO_3 (M = Ca, Sr, Ba, Mn, Cd, Pb) that remained transiently stable for hundreds of seconds.[48] Larger quantities of precipitate produced in a conceptually similar way can be achieved by spray-drying drops with ultrasonic air flow.[49] However, these techniques rely on reaction quenching due to the rapid evaporation of water, making quantification difficult. Liposomes establish a confined volume within an aqueous phase more closely resembling those found biology, and have been used to study phase transformations of iron oxides, calcium phosphates, and earth alkaline carbonates (Figure 1.3a).[50,51] When $CaCO_3$ is precipitated in liposomes between 50 nm and 50 μm in diameter (~130 aL to 130 nL), ACC forms rapidly and the supersaturation with respect to calcite is reset to $\sigma = \ln\left[K_{\mathrm{sp}}^{\mathrm{ACC}}/K_{\mathrm{sp}}^{\mathrm{calcite}}\right] \approx 4.8$. This increases the nucleation barrier. In sufficiently small liposomes, the supersaturation may even fall below σ_i^*, such that calcite formation becomes impossible. Where nucleation is possible, the time until it is observed in 50 out of 100 liposomes further increases by a factor of 10^4 for the largest, and a factor of 10^{13} for the smallest liposomes when compared to a bulk reaction in 130 mL, because of the effect of small volumes on the extrinsic nucleation rate. Taken together, confinement effects dramatically delay the formation of calcite and increase the life time of ACC.[44]

Surfactant-stabilized micro-emulsions of aqueous droplets in oil offer low polydispersity and improved efficiency of encapsulation (Figure 1.3b).[45,52] In the $CaCO_3$ system, confinement in droplets trapped on a patterned SAM (V_{d} ~ 1 pL, Figure 1.3d) resulted in a rapid ACC formation but delayed nucleation of crystalline polymorphs, despite the presence of a relatively powerful nucleating surface.[53] Confinement further allowed investigating the impact of reagent concentrations on $CaCO_3$ polymorph selectivity, and of solubility and nucleation of KNO_3.[54]

A range of effects consistent with confinement has been observed in systems where unlike in liposomes or droplets, transport of building blocks is possible in at least one direction in space. For example, it has been inferred that the nucleation rate of calcite decreases more rapidly than that of ACC as the diameter of pores in track-etch membranes is reduced from 3 μm to 200 nm (Figure 1.3f).[47,55] Similar observations were made in the calcium phosphate system.[56] The wedge between a solid half-cylinder resting on a flat substrate constitutes a yet more complex system (Figure 1.3d), where the degree of confinement can be thought of as rapidly increasing with decreasing distance to the contact line.[46,57] Consequently, metastable precursors of crystalline calcium carbonates, sulfates, and phosphates persist for much longer times closer to the contact line. As a result, the "Ostwald" sequence of increasingly stable phases observed over time in the bulk system is instead patterned in space. While quantitative treatment of these partially confined systems is more difficult because much depends on geometrical parameters, diffusivities, and mixing, they can be used to rapidly screen for metastable precursors that are very challenging to observe in bulk reactions.

1.6 **Conclusions**

Heterogeneous nucleation and confinement are integral factors to biological control over location, timing, and polymorph selection in biomineralization, but remain challenging to probe quantitatively. This review highlights recent in vitro experiments that show that the influence of heterogeneous nucleators can be understood in the context of CNT without needing to invoke "non-classical" effects. Based on recent experiments and simple thermodynamic considerations, we suggest that there are three ways in which confinement reduces nucleation rates of crystalline biominerals. Amorphous intermediates appear to be less affected. As a result, the lifetime of amorphous precursors can be dramatically longer, even in the absence of any stabilizing additives. This effect may open a window for the organism to manipulate the amorphous material with a low risk of spurious nucleation. Controlled transformation into a crystalline polymorph could then occur by introducing a heterogeneous nucleator into the confined volume, before, or after the amorphous intermediate has formed.

2. Nucleation theory in confinement

2.1 Confinement

It likely comes as no surprise that squeezing material into small spaces can cause it to behave differently than in the large systems our intuition is accustomed to. Indeed, the first effect of confinement described in chapter 1 (equation 1.5 and Figure 1.2A and B) is simply one of perception. If we rapidly mixed concentrated solutions of $CaCl_2$ and Na_2CO_3 and were instructed to determine the moment precipitation took place in a 1 L bottle, and then compare to a 0.1 L beaker and a 0.01 mL conical tube, we would likely see immediate precipitation in all three cases. This may lead us to conclude that the size of the container does not impact the precipitation rate. Unfortunately, our intuitive experience would fail as the container shrunk to, for example, 10^{-9} L. This is not simply a limitation of the speed of our visual processing or resolution. Instead, in our macroscopic viewpoint we are biased towards things that happen, at the expense of what is *not* happening!

When we determine the moment that we perceive crystallization to occur, we are looking for signs of a precipitate: cloudiness, opacity, a change in color. These are relatively easy to distinguish from transparent aqueous solutions. But what we fail to recognize is that at the moment we detect the first signs of precipitation, in most of the solution there is still nothing happening! Since it is much more difficult to determine where crystallization is *not* occurring than where it is, we assert that crystallization has happened *somewhere*. But as we shrink the size of our container, the probability that we are looking at a region in which "nothing" is happening grows faster than the probability that we are looking at something, because on average, most of the solution does not contain precipitates.

Even though the processes in large and small containers occur at the same rate (the same supersaturation, etc.), it takes longer, on average, in smaller volumes. This is the principal effect of confinement. Therefore, if we look at small enough volumes, we should begin to see a clear distinction between nothing (supersaturated solution) at the earliest times and something happening (precipitation) over time. This concept has been utilized by atmospheric scientists interested in understanding the nucleation of ice crystals at the supercooled conditions of the troposphere[58-60] in experiments like those described in section 1.5.

2.2 Impurities

Despite the increasing utilization of confined systems, crystallization rates measured in large numbers of small volumes still rarely agree qualitatively with classical nucleation theory. Part of the problem has been known since Fahrenheit in 1794, but proven difficult to solve even now: As sure as death and taxes, aqueous solutions contain impurities. An ‘impurity’ is a catch-all description for an entity that that differs in composition or phase from the newly forming precipitate or the parent phase from which it forms. These impurities may be benign and have no influence on nucleation, but they may also present geometries and/or interfaces that are more favorable for nucleation than the surrounding bulk solution.[19]

A second advantage of miniaturization is that while not all impurities can be eliminated, they are, by definition, trace components and in a finely divided system are relegated to a small fraction of the total. Turnbull was the first to quantify this effect, noting that the crystallization rate of liquid metal drops decreased as the size of the drops shrank, until a lower limit was reached.[39] This rate may be due to the onset of homogeneous nucleation[40] or heterogeneous nucleation on the interface.[41]

2.3 Precursors

A final consideration needed to understand phase transformations in confinement is the formation of metastable phases that precede the final, equilibrium structure. It has been observed in many systems that metastable materials generally have lower interfacial energies than more stable materials with the same composition.[17] Because the nucleation barrier is so strongly dependent on the interfacial energy (Equation 1.2) even slightly lower values of γ can lead to a dramatic acceleration of the nucleation rate.

Reduction in the barrier height for metastable precursors is a consequence of lower metastability (lower free energy) at the length scale typical of a nucleus. This can be seen schematically in Figure 2.1, where the barrier between free ions in the supersaturated solution and ACC is lower than that to vaterite and calcite. In fact, the barrier to ACC may be negligible if it forms through spinodal decomposition as some have suggested. [6,61,62] It has recently been suggested that thermodynamic stability may in fact be a *requirement* for metastable materials to form.[63]

With increasingly reliable simulations and materials databases, hypothetical structures can be ranked based on stability and compared to known phases. There appear to be predicted phases that energetically reside between two known materials, but have not been realized experimentally. This seems to conflict with the Ostwald-Lussac rule of stages, which implies a direct cascade of transformations from lower to higher stability. It may be the case that the Ostwald-Lussac rule is only a heuristic that does not apply to all transformations. Another possibility is that intermediate phases do form, but are too small and too transient to observe. Alternatively, it may be that the thermodynamic stability *of the critical nucleus,* not the bulk phase, that determines the sequence of transformations, and that the inclusion of both interfacial and bulk energies changes the order of stability relative to bulk free energies alone. This last case may be difficult to investigate experimentally. However, in highly confined aqueous systems, it may be possible to reduce the number of nuclei to one. This paradigm may offer clues about how to investigate the process of nucleation and the energy balance of a critical nucleus, but also requires a reevaluation of classical nucleation theory.

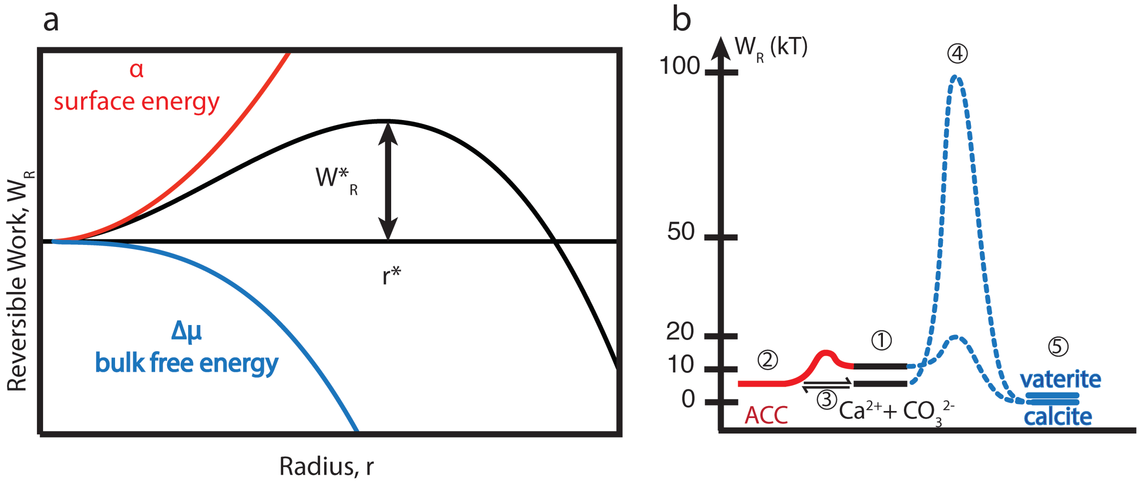

Figure 2.1. Barriers to classical nucleation. The tradeoff between favorable bulk free energy (Δμ) and unfavorable surface energy (α), lead to an activation barrier given by W^*_R at a critical radius r^* (a). In the $CaCO_3$ system, nucleation from supersaturated conditions (1) leads to the formation of ACC (2) more rapidly than crystalline polymorphs due to its smaller (hypothesized) activation barrier. Once ACC equilibrates with the solution (3) the activity of ions in solution is reduced and the expected barrier to calcite nucleation reaches 100 kT, a nearly insurmountable barrier.

2.4 Classical nucleation theory

Equation 1.6 and Figure 1.2 show that the formation of a critical nucleus in confinement changes the system composition in a non-negligible way, violating one of the fundamental assumptions of classical nucleation theory. In condensed (non-aqueous) systems, such small system sizes would likely depart from a continuum description and require special atomistic treatment. However, aqueous systems are typically around 50 M water and less than 1 M ions, meaning that ~98% of the volume is not directly participating in the transformation, such that these systems can be described by continuum theory and still be sensitive to very small changes in the system composition. A derivation of Equation (1.6) in Chapter 1 was omitted for space, but will be presented in full here.

In solution, individual ions form clusters through concentration fluctuations. In undersaturated solutions ($\sigma < 0$) these clusters inevitably dissolve back into individual ions because the energy penalty of creating a new interface between the solution and the cluster, γ, is greater than the energy gained by bringing ions together. In supersaturated solutions ($\sigma > 0$) a cluster may form that reaches unstable equilibrium with the surrounding solution. This cluster is the critical nucleus. Because it is in equilibrium, it has a well-defined pressure difference across its interface, given by the Laplace-Young equation

$$P^{\beta} - P^{\alpha} = (C_1 + C_2)\gamma \qquad (2.1)$$

where C_1 and C_2 are the principle curvatures. For a spherical nucleus

$$P^{\beta} - P^{\alpha} = \frac{2\gamma}{r^{*}} \qquad (2.2)$$

The case of very small nuclei may represent the limit of applicability for the continuum description of mechanical stability in Equation 2.2,[64] and may be a source of departure between the theory and experiments. Nucleus size depends on the solution composition and conditions, so the possible violation of this assumption must be evaluated on a system-by-system basis.

From Equation 2.1 nucleation is not a constant pressure process. Therefore, the Gibbs free energy cannot be used to determine the energy barrier to nucleation. In fact, the Gibbs free energy change for nucleation can be shown to be zero.[65] If the conditions for equilibrium during nucleation are constant chemical potential, μ, temperature, T, and volume, V, the Landau potential, Ω, describes the change in free energy. The Landau potential before nucleation is

$$\Omega_{initial} = V\Omega_V^{\alpha}(a_i, P^{\alpha}) \tag{2.3}$$

where Ω_V^L is the Landau potential per unit volume in the aqueous phase. After nucleation, the Landau potential is

$$\Omega_{final} = (V - V^*)\Omega_V^{\alpha}(a_i, P^{\alpha}) + V^*\Omega_V^{\beta}\left(a_i, P^{\beta}\right) + A^*\gamma \tag{2.4}$$

where Ω_V^{β} is the Landau potential per unit volume in the solid phase and A^* is the interfacial area of the critical nucleus. The change in Landau potential upon nucleation is therefore

$$\Omega_{final} - \Omega_{initial} = W_R^* = V^*(P^{\beta} - P^{\alpha}) + A^*\gamma \tag{2.5}$$

Where W_R^* is the reversible work of nucleation. We assume the nucleus is spherical, giving

$$W_R^* = \frac{4\pi {r^*}^3}{3}(P^{\beta} - P^{\alpha}) + 4\pi {r^*}^2\gamma \tag{2.6}$$

And using Equation 2.2 for the difference in pressure between solution and nucleus, W_R^* can be written as

$$W_R^* = \frac{16\pi\gamma^3}{3(P^{\beta} - P^{\alpha})^2} \tag{2.7}$$

An arbitrarily shaped nucleus will have a different shape factor, but the same dependence on γ and $(P^{\beta} - P^{\alpha})$. For an incompressible nucleus, the dependence of the chemical potential on pressure is simply given by

$$\mu_i^{\alpha}(P^{\alpha}) - \mu_i^{\beta}\left(P^{\beta}\right) = V_{m,i}(P^{\alpha} - P^{\beta}) \tag{2.8}$$

where $V_{m,i}$ is the partial molar volume of component i. In a two-component system, the difference in pressure is then fixed by the conditions for (unstable) equilibrium, $\Delta\mu$, between β and α for each component A (i.e., Ca^{2+}) and B (i.e., CO_3^{2-})

$$\mu_A^{\alpha}(a_B^{\alpha}, P^{\alpha}) = \mu_A^{*}(a_B^{*}, P^{*}) + V_{m,A}^{*}\left(P^{\beta} - P^{\alpha}\right) \tag{2.9}$$

$$\mu_B^{\alpha}(a_B^{\alpha}, P^{\alpha}) = \mu_B^{*}(a_B^{*}, P^{*}) + V_{m,B}^{*}\left(P^{\beta} - P^{\alpha}\right) \tag{2.10}$$

Solving Equations 2.9 and 2.10, $\Delta P = (P^{\beta} - P^{\alpha})$ is given by

$$\Delta P = -\frac{\Delta G_m^{\alpha\rightarrow\alpha+\beta}}{V_m^{\beta}} \tag{2.11}$$

where V_m^{β} is the molar volume of the solid and $\Delta G_m^{\alpha\rightarrow\alpha+\beta}$ is the molar free energy change upon the formation of a nucleus of β in α.

2.5 Nucleation in aqueous solution

We are interested in the pseudobinary system $CaCO_3$-H_2O, in which a solid $CaCO_3$ particle (β) nucleates within an aqueous solution (α) containing Ca^{2+} and CO_3^{2-} ions. The thermodynamic condition for nucleation is that the solution is supersaturated, as defined in Equation 1.1. Supersaturation is set by the activity product, *AP*, of the ions in solution

$$AP \equiv \prod_i a_i \tag{2.12}$$

The solubility product, K_{sp}, defined as the product of the activities, a_i, of the components in equilibrium with the solid given by

$$K_{sp} \equiv \prod_i a_i^e \tag{2.13}$$

When activities are low, like a_i^e for insoluble solids, they are often approximated by concentrations, as given in Equation 1.1.

An AP larger than K_{sp} provides the thermodynamic driving force to overcome the pressure difference across the critical nucleus in Equation 2.11. It is customary[20] to approximate $\Delta G_m^{\alpha\rightarrow\alpha+\beta}$ in Equation 2.11 as

$$\Delta G_m^{\alpha\rightarrow\alpha+\beta} = RT ln \frac{AP}{K_{sp}} = RT\sigma \tag{2.14}$$

We can then rewrite equations (2.2) and (2.7) as

$$r^* = \frac{2V_m^\beta}{RT}\frac{\gamma}{\sigma} \tag{2.15}$$

$$W_R^* = \frac{16\pi}{3}\left(\frac{2V_m^\beta}{RT}\right)^2\frac{\gamma^3}{\sigma^2} \tag{2.16}$$

This is the critical radius and activation barrier for classical homogeneous nucleation. These quantities determine the rate at which phases form in the absence of heterogeneous nucleators, represented schematically in Figure 1.1a. Using literature values for K_{sp} and γ of calcium carbonate phases ACC, vaterite, and calcite, the barrier heights for homogeneous nucleation relative barrier to the free ions in solution are given in Figure 1.1b.[44] Details are given in chapter 5.

2.6 Effects of confinement

Assume that nucleation occurs in a small container with impermeable walls and a constant volume of supersaturated solution V_{conf}. The supersaturation prior to nucleation shall be σ_{pre}. Solving Equation 1.1 for the *AP*, we can determine the activity product in the container prior to nucleation with respect to the equilibrium solubility product of *β*,

$$AP_{pre} = K_{sp}e^{\sigma_{pre}} \tag{2.17}$$

If we continue to assume an AB type solid (A = Ca^{2+}, B = CO_3^{2-}) and equal amounts of A and B in the liquid phase, the activity of either A or B is given by

$$a_i = \sqrt{AP} = \sqrt{K_{sp}e^{\sigma}} = \sqrt{K_{sp}}e^{\frac{\sigma}{2}} \tag{2.18}$$

The formation of a cluster with volume V_{nuc} requires the following amount of A and B

$$n_{A,B} = \frac{\rho_\beta}{M_\beta}V_{nuc} = \frac{V_{nuc}}{V_m^\beta} \tag{2.19}$$

where ρ_β is the density of the β phase and M_β is the molecular weight. The activity of A and B in the confined volume therefore drops by

$$\Delta a_{A,B} = \frac{\rho_\beta}{M_\beta}\frac{V_{nuc}}{V_{conf}} = \frac{V_{nuc}}{V_m^\beta V_{conf}} \tag{2.20}$$

If the volume fraction of the nucleus in the confined volume, *f*, is

$$f = \frac{V_{nuc}}{V_{conf}} \tag{2.21}$$

then we can write the activity of A and B in the confining volume after nucleation, a_{post}, as

$$a_{post} = a_{pre} - \Delta a_{A,B} = \sqrt{K_{sp}} e^{\frac{\sigma_{pre}}{2}} - \frac{f}{V_m^s} \tag{2.22}$$

With this, we can write

$$AP_{post} = \left(\sqrt{K_{sp}} e^{\frac{\sigma_{pre}}{2}} - \frac{f}{V_m^\beta} \right)^2 \tag{2.23}$$

$$\sigma_{post}^{\infty} = ln \left[\frac{\sqrt{K_{sp}} e^{\frac{\sigma_{pre}}{2}} - \frac{f}{V_m^\beta}}{K_{sp}} \right] = 2ln \left[e^{\frac{\sigma_{pre}}{2}} - \frac{f}{\sqrt{K_{sp}} V_m^\beta} \right] \tag{2.24}$$

Note that σ_{post}^{∞} is the supersaturation with respect to a particle of β with a flat interface (infinite radius), after the formation of one nucleus with a critical radius given by Equation 2.15.

Nucleation removes monomers from α, lowering their activity. The supersaturation therefore changes. CNT assumes that these changes are very small. However, in a confined volume, this may not be the case. If we require that α remain supersaturated throughout the entire process of critical cluster formation,

$$a_{post} \geq \sqrt{K_{sp}} \tag{2.25}$$

Then, we can substitute Equation 2.22

$$\sqrt{K_{sp}} e^{\frac{\sigma_{pre}}{2}} - \frac{f}{V_m} \geq \sqrt{K_{sp}} \tag{2.26}$$

and solve for the volume of the cluster

$$f \leq V_m^\beta \sqrt{K_{sp}} \left(e^{\frac{\sigma_{pre}}{2}} - \sigma_{pre} \right) \tag{2.27}$$

The maximum volume fraction of the nucleus is therefore

$$f_{max} = V_m^{\beta}\sqrt{K_{sp}}\left(e^{\frac{\sigma_{pre}}{2}} - 1\right) \tag{2.28}$$

Equation 2.28 is valid for both homogenous and heterogeneous nucleation (i.e., nuclei of any shape). If we assume that the shape of the nucleus is that of a spherical cap with contact angle θ, we can write

$$V_{nuc}(\theta) = \frac{\pi}{3}r_{crit}^3(2 - 3cos\theta + cos^3\theta) \tag{2.29}$$

If we further assume that the confining container is spherical with radius R_{conf}, we can rewrite

$$f = \frac{1}{4}(2 - 3cos\theta + cos^3\theta)\left(\frac{r_{crit}}{R_{conf}}\right)^3 \tag{2.30}$$

$$f = \frac{1}{4}(2 - 3cos\theta + cos^3\theta)\left(\frac{2\gamma V_m^{\beta}}{RT\sigma_{pre}R_{conf}}\right)^3 \tag{2.31}$$

$$\sigma_{post}^{\infty} = 2ln\left[e^{\frac{\sigma_{pre}}{2}} - \frac{(2-3cos\theta+cos^3\theta)}{4\sqrt{K_{sp}}V_m^{\beta}}\left(\frac{2\gamma V_m^{\beta}}{RT\sigma_{pre}R_{conf}}\right)^3\right] \tag{2.32}$$

This is the supersaturation after the cluster has formed. The condition nucleation in confinement is therefore $\sigma_{post}^{\infty} > 0$. To find the radius of the container such that α remains supersaturated after nucleation for a given initial supersaturation σ_{pre},

$$0 \leq \sigma_{post}^{\infty} \tag{2.33}$$

$$1 \leq e^{\frac{\sigma_{pre}}{2}} - \frac{(2-3cos\theta+cos^3\theta)}{4\sqrt{K_{sp}}V_m^{\beta}}\left(\frac{2\gamma V_m^{\beta}}{RT\sigma_{pre}R_{conf}}\right)^3 \tag{2.34}$$

$$R_{conf} \geq \left(e^{\frac{\sigma_{pre}}{2}} - \frac{(2-3cos\theta+cos^3\theta)}{4\sqrt{K_{sp}}V_m^{\beta}}\right)^{1/3}\left(\frac{2\gamma V_m^{\beta}}{RT\sigma_{pre}}\right) \tag{2.35}$$

A different approach is to ask what is the radius, r, of a β phase precipitate that is in equilibrium with α after it has formed. This is equivalent to the radius at σ_{post}, so by rearranging Equation 2.15

$$\sigma_{post} = \frac{1}{r_{crit}} \frac{2\gamma V_m^s}{RT} \tag{2.36}$$

Again, assuming a spherical particle and container, we can substitute Equation 2.18 into Equation 2.22 and arrive at

$$\sqrt{K_{sp}} e^{\frac{\sigma_{post}}{2}} = \sqrt{K_{sp}} e^{\frac{\sigma_{pre}}{2}} - \frac{f}{V_m^s} \tag{2.37}$$

which states that the activity of ions in solution after the critical cluster has formed is equal to that prior to cluster formation minus the ions removed to form the cluster. Substituting Equation 2.31 for f, and Equation 2.36 for σ_{post}, we arrive at Equation 1.6

$$e^{\frac{\gamma V_{\mathrm{m}}}{k N_a T} \cdot \frac{1}{r}} + \frac{r^3}{V_m \sqrt{K_{\mathrm{sp}}} {R_{\mathrm{c}}}^3} - e^{\frac{\sigma_{\mathrm{i}}}{2}} = 0 \tag{2.38}$$

3. Outline

3.1 Motivation

As Henry Ford said, “Nothing is particularly hard if you divide it into small jobs”. Biomineralization *is* particularly hard to study because of the small length scales at which processes of interest occur, the existence of hard/soft and buried materials interfaces, and the interconnectivity between the biomineral and the rest of the organism that creates and sustains it. My motivation in this dissertation is to divide commonly observed biomineralization strategies into simple, independent, *in vitro* analogs and explore their consequences in isolation. Specifically, I chose confinement in small volumes, the precipitation of metastable precursors, and the use of biomineralization proteins to affect crystallization.

3.2 Overview

My investigation of the role of confinement begins in chapter 5. Synthetic giant unilamellar vesicles (GUVs) are a model system employed by my predecessor, Chantel Tester, to extend her work on 100 nm – 1 μm liposomes to visible length scales. After Chantel established that ACC persisted in GUVs up to 100 μm in diameter, I explored the generality of this effect in other carbonate systems. Specifically, I replicated her experiments with $CaCO_3$ using $SrCO_3$ and $BaCO_3$. In chapter 6 I extend Chantel’s investigation of the effects of lipid chemistry on ACC precipitation in small liposomes to GUVs.

Vesicles were important to establish fundamental concepts of confinement, but proved to be too unstable to withstand high salt concentrations for long periods of time. This motivated the implementation of an emulsion based system, in which a fluorinated oil containing an amphiphilic surfactant stabilized aqueous drops against coalescence for weeks. I learned droplet synthesis microfluidic techniques through a 2-week visit to the Fraden lab at Brandies University, and brought them back to investigate ACC crystallization. Mineral precipitation destabilized the droplets, however, requiring the design of a storage chip in which to store the drops separately while precipitation was initiated. Jack Cavanaugh undertook the task of designing and fabricating the device and running the experiments, which are summarized in chapter 7. An ongoing investigation into the effects of biomineralization proteins extracted from sea urchins using Jack's device is presented in chapter 8.

I change gears in chapter 9, moving away from confinement and instead focusing on bulk samples. Through synchrotron based X-ray characterization and other bulk techniques, the effects of barium on ACC structure at the nanoscale are presented. Chapter 10 contains a detailed description of the crystallization of ACBC to a previously unrecognized phase we call balcite. Balcite is metastable but is highly persistent, and exhibits enhanced mechanical properties, described in chapter 11. Finally, a synthesis of the first known $BaCO_3{\cdot}H_2O$ phase we call gortotowskite is described in chapter 12. These results are summarized in chapter 13, and a few of the most promising extensions of this work are proposed.

4. Summary of experimental techniques

This chapter will provide an overview of the experimental techniques used to characterize the structure and transformation of metastable carbonates. Of primary importance is the ability to quickly distinguish amorphous materials from crystalline ones, for example using the absence of birefringence under crossed polarizers in optical microscopy, or diffraction of electrons or X-rays. Techniques specifically suited for the direct characterization of amorphous materials, like X-ray absorption spectroscopy (XAS) and X-ray total scattering for atomic pair distance distribution function (PDF) analysis, provide greater detail on the structural motifs exhibited by these materials.

While these measurements reveal many static aspects of persistent materials like ACBC, other metastable carbonates like ABC and gortotowskite transform rapidly. These materials must be characterized *in situ* or quickly after formation. Synchrotron X-ray scattering at small- (SAXS), medium- (MAXS) and wide angles (WAXS) in conjunction with stopped-flow mixing enabled millisecond time resolution to capture very rapid transformations *in situ*. Snapshots of these reactions, literally frozen in time, were obtained by cryo-scanning transmission electron microscopy (cryo-STEM) of aqueous samples vitrified by plunge-freezing at various times during precipitation.

Complimentary vibrational spectroscopy techniques of Fourier transform infrared spectroscopy (FTIR) and Raman provided information about carbonate anions and water, which interact with X-rays and electrons much less than heavier atoms like calcium and barium. High-temperature methods like thermogravimetric analysis (TGA) and differential scanning calorimetry (DSC) were used to determine the amount of residual water associated with precipitates formed in aqueous solution, and to accelerate transformations that were slow at ambient temperature. Together, these techniques help elucidate the structure of metastable carbonates, both amorphous and crystalline, from the perspective of all the atoms in a material.

4.1 Polarized light microscopy

Optical imaging using polarized light is an experimentally straightforward method for establishing the presence or absence of macroscopic crystals. This is critical for determining whether the amorphous precipitate within an emulsion drop has crystallized, for example in chapters 7, 8, and 10. In an experiment, unpolarized light is sent through a linearly polarized filter (polarizer) before passing through the sample. The light emerging from the sample is passed through a second linearly polarized filter (analyzer) with an orientation that is rotated 90° with respect to the polarizer. All light that does not change polarization due to its interaction with the sample is attenuated by the analyzer, causing the field of view to appear dark. Samples that alter the polarization of the incident light allow at least some fraction to be transmitted through the analyzer and onto a detector. Light that passes between medium 1 (e.g., air) and medium 2 (e.g., sample) changes speed and direction according to Snell's law

$$\frac{sin\theta_1}{sin\theta_2} = \frac{n_2}{n_1} \tag{4.1}$$

where θ is the angle of light propagation relative to the surface normal, and n is the refractive index. In isotropic materials, like amorphous solids, n is independent of the direction of propagation and light polarized in any direction will propagate with the same speed. The result is that θ will be unchanged after interacting with the sample. However, for crystalline materials, n differs along different crystallographic directions in any of the anisotropic symmetry groups, which includes all crystalline polymorphs of $CaCO_3$. For example, in calcite the c-axis index is 1.658 while the a-axes index is 1.486. In this case, light changes polarization due to interaction with the crystalline solid, and the analyzer attenuates only part of the total intensity. Crystalline regions therefore appear bright against a dark background. A striking example of birefringence is also observed in the Maltese cross pattern of balcite spherulites, reflecting the radial orientation of many small crystallites that alternate between complete extinction and transmission every 45° (chapter 11).

4.2 Vibrational spectroscopy

Ions in carbonate minerals vibrate with characteristic frequencies that are dependent on structural symmetry and sensitive to composition. These vibrational frequencies (or modes) have energies corresponding to the visible and infrared portion of the electromagnetic spectrum, where FTIR and Raman spectroscopies are ideally suited. These complimentary techniques rely on the absorption (FTIR) or inelastic scattering (Raman) of light. Whether a vibrational mode will absorb or scatter is dependent on its symmetry.

Modes for which there is a net dynamic dipole are IR active, while those with a net polarizability are Raman active.

Carbonate anions are roughly trigonal planar in all carbonates, but additional constraints imposed by neighboring ions, whether in a crystalline lattice or amorphous aggregate, alter their vibrational mode symmetry and frequency. This allows structures with different carbonate environments to be distinguished by modes that are Raman and/or IR active, and by the frequency of vibration. For example, the symmetric stretching mode (υ_1) can be used to distinguish calcite, with a Raman shift of 1086 cm^{-1}, from vaterite, which exhibits three Raman active υ_1 modes at 1074, 1080, and 1090 cm^{-1}. Amorphous carbonates contain a distribution of carbonate configurations and therefore the peaks are much broader (υ_1 full width at half maximum, FWHM = 23.5 cm^{-1} in ACC) than in crystalline compounds (calcite υ_1 FWHM = 2.0 cm^{-1}). In addition to carbonate vibrational modes (also called internal modes or optical phonons), collective vibrations of both anions and cations (lattice modes or acoustic phonons) are also observed in vibrational spectroscopy. In a crystalline solid these appear as relatively sharp, low-frequency peaks, while in an amorphous solid a broad continuum of modes is generally observed.

Raman and FTIR spectroscopy were used to characterize the impact of barium on ACC (chapter 9), and to investigate the effects of barium on calcite and balcite (chapters 10 and 11). Structural water in gortotowskite was confirmed by FTIR (chapter 12). Because water is only weakly Raman active, this technique was uniquely suited to interrogate the structure and composition of precipitates in liposomes (chapters 5 and 6) and emulsion drops (chapters 7, 8, and 10) *in situ*.

Raman spectra were obtained on a Horiba LabRam confocal Raman microscope with a laser of wavelength λ = 532 nm, operating at a power of 49 mW, and using a diffraction grating with 1800 gr/mm, resulting in a final spectral resolution of 0.39 cm^{-1}. For dried powders, approximately 5 mg was pressed onto a glass slide for Raman analysis. Microfluidic storage devices were inverted so that only a thin cover glass separated the drop from the microscope objective. All spectra were recorded from individual precipitate particles using 50x or 100x objective lens in air (0.9 NA, minimum resolution ~361 nm). Mode centers, relative intensities, and full peak width at half maximal intensity (FWHM) were determined by fitting one or more Gaussians to the spectral region of interest. Fitting was performed manually using in-house code written in Mathematica.

Bulk FTIR spectra from KBr pellets containing ~5.0 wt% ACBC powder were acquired in the range from 400-4000 cm^{-1} on a Thermo Nicolet Nexuz 870 FT-IR in transmission geometry, with a spectral resolution of 1-4 cm^{-1}. To prepare samples, ~8 mg of the dry powder was mixed with ~160 mg KBr in a mortar and pestle. Approximately 25 mg of the mixture was then pressed into a partially transparent window at 7 MPa.

4.3 (High resolution) powder X-ray diffraction

For over a century, the ability of crystals to diffract X-rays has been indispensable for elucidating the structures of solids. Bragg's law defines the condition for constructive interference. Monochromatic electromagnetic radiation with a wavelength, λ, will diffract from lattice planes separated by a distance, d, when

$$n\lambda = 2dsin\theta \tag{4.2}$$

where n is an integer and θ is the angle of incident radiation. In an XRD experiment the intensity of an X-ray beam is measured over a wide range of angles, θ. High intensity peaks are recorded when the Bragg condition is satisfied. In powder samples with randomly oriented particles, like those investigated throughout this work, diffraction is isotropic, and one dimensional profiles capture all necessary structural information.

When the Bragg angle is rewritten as the magnitude of the scattering vector, q, defined as

$$q = \frac{4\pi sin\theta}{\lambda} \tag{4.3}$$

diffraction profiles from different X-ray sources (e.g., laboratory vs. synchrotron) with different radiation wavelengths are normalized to equivalent scales. Experimental patterns can then be compared to reference profiles for phase identification by qualitatively matching the location and relative intensity of peaks. This is the case for crystalline precipitates found during ACBC synthesis (chapters 9 and 11). For sufficiently high quality data like that obtained from synchrotron sources, structure-based models like Rietveld refinement can help determine the crystallographic symmetry, lattice parameters, and crystallite size (chapters 10 and 11).

Because the constructive interference of X-rays makes diffracted signal orders of magnitude more intense than the diffuse scattering between Bragg peaks, the absence of diffraction is a strong indication that a material is amorphous. The absence of diffraction was used to confirm that ACC and ACBC precipitates were indeed amorphous (chapters 9, 10, and 11). Emergence of subtle Bragg peaks with increasing barium content established the composition at which ACBC could no longer be synthesized by our method.

Lab source X-ray diffraction patterns were acquired on a Rigaku Ultima diffractometer using copper Kα radiation (λ = 1.504 Å), 2θ = 0.05° step size, and sample-to-detector distance of 285 mm. Synchrotron powder XRD was performed at sector 5-BM-D and sector 11-BM of the Advanced Photon Source at Argonne National Laboratory. At 5-BM-D the wavelength, λ, was set to 0.2748 Å (50.00 keV) and collected on a MAR345 two-dimensional plate detector. Data were calibrated with polycrystalline silicon and integrated with Datasqueeze. At 11-BM a wavelength of λ = 0.414529 Å (29.9097 keV) was set with a Si(111) double crystal (bounce up geometry) and focused with a sagittally bent Si(111) crystal in the horizontal and a 1 meter Si/Pt mirror in the vertical, enabling a resolution of 2θ = 0.001°.[66] Where necessary, patterns were indexed with JADE2010 software.

4.4 X-ray total scattering for pair distance distribution function analysis

When XRD is carried out to very high angles (i.e., $\theta \rightarrow 90°$ or $q \rightarrow 30$ Å^{-1}) information can be gleaned not only from the Bragg peaks but also the diffuse scattering in between and underneath. A wider range q (generally written as an upper case 'Q' by this rebellious community) is needed in order to capture the total scattering from diffuse features that are not sharply peaked at a very narrow range of Q. Real-space information about defects and local order that are often obscured by the reciprocal space (Q-space) representation can be obtained. This technique is also particularly important for characterizing the structure of amorphous materials, which do not diffract and only exhibit diffuse scattering.

X-ray total scattering intensity, $I(Q)$, is collected over a wide range of q for a sample with known composition. Then, the contribution to scattering from individual ions with a concentration c_i and X-ray form factor $f_i(Q)$ is subtracted from $I(Q)$ and normalized by the sample averaged scattering intensity to give the structure function, S(Q)

$$S(Q) = \frac{I(Q) - \sum_i c_i |f_i(Q)|^2}{\sum_i |c_i f_i(Q)|^2} + 1 \tag{4.4}$$

This quantity describes the distribution of ions within the sample in reciprocal space. The real space atomic pair distance distribution function (PDF), $G(r)$, is then obtained by taking the Fourier transform of the reduced structure factor, $Q[S(Q) - 1]$,

$$G(r) = \frac{2}{\pi} \int_{Q_{min}}^{Q_{max}} Q[S(Q) - 1] \, sin(Qr) \, dQ \tag{4.5}$$

where $Q_{\max}$ and $Q_{\min}$ are the limits of experimental data collection. Fourier termination artifacts arise if $Q_{\max}$ - $Q_{\min}$ is too small, highlighting the importance of collecting data over a large range of Q.

The PDF is the probability that ion pairs are found at a given distance. As expected, broad features that rapidly decay in amorphous materials starkly contrast to the sharp pair correlations that reflect the long range crystalline order of, e.g., calcite. PDF analysis was used to compare ACBC to ACC and calcite (chapters 10 and 11). This real space representation of the structure in PDF quantifies what was hypothesized from the absence of Bragg peaks in XRD: order in ACC and ACBC extends over at most ~1 nm. Similarities in the PDFs of ACBC and balcite were used to compare local order in these materials and support a mechanistic description of the transformation between the two (chapter 10 and 11). PDFs were also calculated from simulated ACBC structures and closely matched those determined experimentally. Simulations provided deconvoluted radial distribution functions (RDF) for each pair of ions, something that is not possible without an atomistic structural model.

X-ray total scattering was performed at the Dow-Northwestern-Dupont collaborative access team (DND-CAT), Sector 5-BM-D of the Advanced Photon Source at Argonne National Laboratory. The X-ray energy (20.000 keV, λ = 0.6195 Å) was selected with a Si(111) monochromator, and calibrated with a Mo foil at the Mo K-edge. Data was collected in Bragg-Brentano geometry with a Huber D8219 diffractometer (2θ = 4-169°). The step size was 0.5° and the dwell time was 10 s. Four Si-drift solid state detectors with multichannel analyzers (MCA, ~250 eV resolution at 20 keV) were used to simultaneously measure elastic scattering, Ca K-edge, and Ba L-edge fluorescence. Total fluorescence signal was used to normalize the q-dependence of the elastic scattering. Spectra were also normalized for incident beam intensity measured with an ion chamber (pN_2 = 550 Torr and pAr = 16 Torr). Scattering from the sample holder and Compton scattering were subtracted, and an absorption correction applied based on sample composition using GetPDFx2 package.[67]

4.5 Small-, medium-, and wide angle X-ray scattering

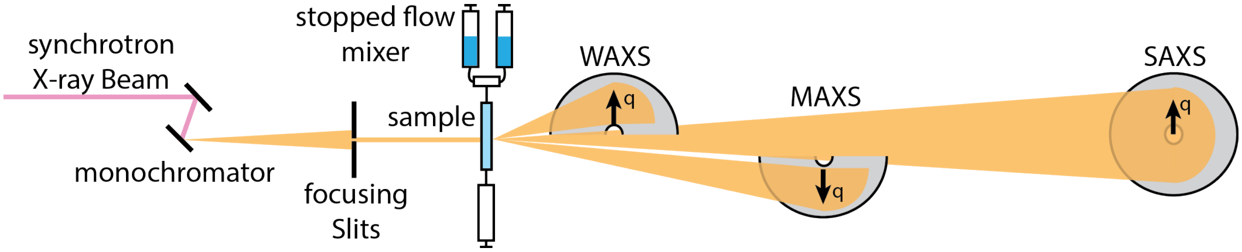

Figure 4.1. Schematic of time-resolved X-ray scattering configuration. A stopped-flow mixer allowed for rapid and repeatable precipitation in solution. The aqueous precipitate was passed through a thin walled (100 µm) glass capillary, where scattering was acquired over a continuous range of scattering vectors q = 0.002 – 5 Å^{1} with three separate detectors.

If instead of measuring X-ray scattering at large q (returning to the more commonly used lower case convention), interest is focused on the region $q < 1$ Å^{-1}, information about the shape, size, and arrangement of particles themselves can be obtained. Scattering at small q has the same physical basis as diffraction or diffuse scattering at higher q, namely, variations in electron density. However, because these variations are much larger than the X-ray wavelength, the resulting patterns are interpreted with a separate theoretical framework. Synchrotron sources enable X-ray intensities sufficient to penetrate thin (< ~1 cm) samples and rapidly collect data over a large range of q using two dimensional detectors. Combining these sources with a stopped-flow mixing device, precipitation in aqueous samples can be observed with millisecond time resolution.

Wide angle X-ray scattering (WAXS) is conceptually identical to XRD. Instead of sequentially measuring intensity at discrete increments of q, an entire 2D pattern is obtained simultaneously, and azimuthally integrated to reveal Bragg peaks (from crystalline samples) or diffuse scattering (from amorphous materials or aqueous solutions) over the range $1 < q < 10$ Å^{-1}. Medium angle X-ray scattering (MAXS) bridges an intermediate range ($0.1 < q < 1$ Å^{-1}) between WAXS and small angle scattering (SAXS). Bragg diffraction from features with periodicity on the nanometer scale that are outside the range of conventional WAXS can observed in MAXS. In addition, MAXS records the high-q tail of scattering from the SAXS region, where the typically large range of intensities ($> 10^5$ in many samples) results in significant noise in this region when collected on a SAXS detector alone. Scattering from larger objects, like ABC particles or gortotowskite platelets, is measured $q < 0.1$ Å^{-1} in SAXS.

In analogy to diffraction by atoms, particles may have a regular arrangement or periodicity which gives rise to coherent scattering. However, particles precipitating from solution, like ABC and gortotowskite in chapter 12, are assumed to have no such spatial or orientational correlation over the short time intervals (< 5 s) of the experiments. Therefore, they can be treated as dilute, non-interacting particles that only scatter incoherently. In this case, the scattering amplitude $A(q)$ for a single particle of volume v is

$$A(q) = \int_v \rho(r) e^{-iqr} dr \tag{4.6}$$

where $\rho(r)$ is the electron scattering length distribution relative to the surrounding medium and r is the particle radius. The intensity is given by

$$I(q) = A^*(q)A(q) = \left|\int_v \rho(r)e^{-iqr}dr\right|^2 \tag{4.7}$$

where $A^*(q)$ is the complex conjugate of $A(q)$. This general expression can be solved explicitly if the particle shape (hence, $\rho(r)$) is known. However, significant information can be obtained without exact knowledge about the scattering objects. For example, the invariant, Q_v, is a measure of the total scattering intensity from the sample and is directly proportional to the precipitate volume

$$Q_v = \frac{1}{2\pi}\int_0^\infty q^2 I(q)dq \tag{4.8}$$

The invariant is completely independent of how the atoms in a system are arranged, and is applicable across all q. Morphological characteristics can also be deduced from scattering data. For instance, by defining the radius of gyration, R_g, of an arbitrarily shaped particle as

$$R_g^2 = \frac{\int r^2\rho(r)dr}{\int \rho(r)dr} \tag{4.9}$$

scattering from any shape or size particle can be analyzed the limiting regimes of $q << 1$ $Å^{-1}$ and $q \to 1$ $Å^{-1}$.

At $q << 1$ $Å^{-1}$, the scattering amplitude can be expressed as a truncated power series of equation 4.7, and the intensity given by

$$I(q) = \rho_o^2 v^2 e^{-\frac{q^2R_g^2}{3}} \tag{4.10}$$

commonly known as Guinier's law, where ρ_o is the (assumed) constant scattering length density within a particle. Particle dimensions can be calculated from the R_g extracted from a plot of $logI(q)$ vs. q^2. For example, the thickness, T, of flat platelets like gortotowskite is given by

$$T = \sqrt{2}R_g \tag{4.11}$$

Guinier's law fails in the limit of $q \to 1$ Å^{-1}. In this region Porod's law dominates, and is expressed as

$$I(q) = \frac{2\pi\rho_o^2 S}{q^4} \tag{4.12}$$

where S is the total surface area of a particle. For 3D particles, it follows that $I(q) \propto q^{-4}$. However, if any of the particle dimensions, d_m, become small such that $\frac{1}{d_m} \to q \to 1$ Å^{-1}, scattering from the surface can no longer be ignored and S will have a q dependence. In such a case, $I(q) \propto q^{-P}$, where P is the Porod slope. For a thin disk or platelet, P = 2. This is the behavior exhibited by gortotowskite at small q. Non-integer values of P intermediate to 2D disks or 3D spheres, like those from gortotowskite at $q \to 1$ Å^{-1} can be described as fractals.

These two limiting regimes can be unified with minimal loss of detail, where the scattering intensity from low and high q can be considered independent and additive,[68] giving a total scattering intensity

$$I_i(q) = \sum_i G_i e^{-\frac{(qR_g)^2}{3}} + e^{-\frac{(qR_{g,CO})^2}{3}} B_i \left[\frac{erf\,(\frac{qR_g}{\sqrt{6}})^3}{q}\right]^{P_i} \tag{4.13}$$

where i is the number of scattering levels (e.g. 2 for discs, one each for the thickness and diameter), $G = \rho_o^2 v^2$, and $B = 2\pi\rho_o^2 S$. $R_{g,CO}$ is the cutoff radius from a smaller level, effectively limiting the contribution of smaller particles on the scattering from larger ones and allowing multiple regimes to be treated independently.

Simultaneous SAXS/MAXS/WAXS was conducted at beamline 5-ID-D at the Advanced Photon Source (APS). A wavelength of 0.7293 Å (17.000 keV) was selected with a silicon (111) monochromator and calibrated with lanthanum hexaboride (WAXS) silver behenate (MAXS) or glassy carbon (SAXS). Two-dimensional images were collected simultaneously on Rayonix LX170HS (WAXS and MAXS) and MX170HS (small-angle) CCD area detectors at distances of 199.83, 1012.68 and 8503.3 mm. Pixels (0.08860 mm) were binned 2x2 for high q resolution and 6x6 for high time resolution (chapter 12). Transmitted beam intensity was monitored using a $CdWO_4$ crystal-coupled diode which was used to correct for any incident beam and sample transmission variation. Standard corrections for flat field response and spatial distortion were applied in the vendor software. Isotropic scattering patterns were corrected for varying incident beam intensity and sample transmission using a $CdWO_4$ crystal-coupled diode in the beam stop. The data was then normalized to an absolute scale using the measured transmission, sample thickness, and a scale factor calibrated from water. Two-dimensional images were radially integrated and corrected for polarization and detector geometry with GSAS-II[39], a vendor applied offset was then subtracted and the scattering intensity corrected based on the measured transmitted beam intensity using beamline software Data fitting was performed in the Irena package[69] for Igor Pro. The ‘Unified Fit’ model[68] was applied to all data.

Using a syringe pump, 500 μL of each solution were mixed in a stopped flow mixing device (Biologic SFM400) controlled with Bio-kine software. Mixed solutions were passed through a thin walled fused quartz capillary (100 µm). Data collection was software triggered to begin simultaneously with solution flow. A minimum time resolution of 50 ms, following an initial 10 ms dead time resulting from the device geometry, was achieved.

4.6 **X-ray absorption spectroscopy**

The preceding discussion of X-ray diffraction and scattering relied on the elastic scattering of X-rays by electrons. However, X-rays are also absorbed by ions in a solid through the photoelectric effect that won Einstein his Nobel Prize in 1921. This is an inelastic interaction that is necessarily associated with a transfer of energy. Energy lost by the X-ray photon is absorbed by an electron, which is promoted to an excited state. Using X-rays in the 1-100 keV energy range, core electronic levels can be excited with chemical specificity. For example, the binding energy of core electrons in calcium is 4.038 keV while that for barium is 37.441 keV. By using X-ray energies near 4 keV, the absorption from calcium changes dramatically more than barium, and the resulting information will be chemically specific. X-ray absorption spectroscopy (XAS) is the broad term that describes the investigation of this absorption process. In addition to chemical specificity, XAS probes only the local environment around a given ion and therefore is agnostic to long-range order, making it a common but powerful technique for characterizing amorphous materials.

Beer's law describes the intensity of light, I, absorbed by a material with a thickness t, and an absorption coefficient μ

$$I = I_o(1 - e^{-\mu t}) \tag{4.14}$$

At most X-ray energies μ is a smooth function of energy, E, that decays as E^{-3}

$$\mu(E) = \frac{1}{V_m}\frac{Z^4}{E^3} \tag{4.15}$$

where Z is the atomic number of the material and V_m is the molar volume. This origin of this absorption is the excitation of valence electrons, which generally occupy finely spaced energy levels near the continuum level. However, when the X-ray energy approaches that of the binding energy of a core electron, there is a discontinuous jump in $\mu(E)$ due to absorption, called the absorption edge. X-ray absorption near-edge structure (XANES) describes the features occurring within ~30 eV to either side of the edge energy. These include pre-edge features from transitions to energy states that lie below the continuum, like the 1s → 3d or 1s → 4p transitions at the calcium K-edge, a shift in the edge energy based on oxidation state, coordination number, or coordination geometry, and the 'white line', the most intense feature above the absorption edge.

While XANES is commonly used for qualitative comparisons, the theory of X-ray absorption is not well developed for energies very close to the absorption edge. More quantitative information can be obtained by analyzing the so-called fine structure in the

$\mu(E)$ > 30 eV above the absorption edge. This can be expressed as χ, the the X-ray absorption fine structure (XAFS),

$$\chi(E) = \frac{\mu(E) - \mu_o(E)}{\Delta\mu_o(E)} \tag{4.16}$$

where $\mu_o(E)$ is the absorption from an isolated atom in the absence of fine structure, and $\Delta\mu_o(E)$ is the difference in absorption below and above the absorption edge.

The photoelectron promoted by the absorbed X-ray can be scattered back to the absorber, which modulates its local electronic density of states. Scattering of the photoelectron is more easily understood when it is treated as a wave, with a wavevector k equal to

$$k = \sqrt{\frac{2m(E - E_o)}{\hbar^2}} \tag{4.17}$$

where E_o is the absorption edge energy and m is the electron mass. If a significant portion of the fine structure is measured (~ 1 keV above the absorption edge), the extended X-ray absorption fine structure (EXAFS) is given by

$$\chi(k) = \sum_i \frac{S_o^2 N_i f_i(k)}{kR_i^2} e^{-2k^2\sigma_i^2} e^{-\frac{2R_i}{\lambda(k)}} sin\left[2kR_j + \delta_i(k)\right] \tag{4.18}$$

S_o^2: amplitude reduction factor due to the core-hole in the absorber

N_i: number of atoms of type i (scatterers) around the absorber

R_i: distance of atom of type i from the absorber

σ_i^2: root mean squared displacement from the equilibrium position, R_i, of atom of type i

$f_i(k)$: atomic scattering amplitude of atom of type i, which varies with k

$\delta_i(k)$: scattering phase shift of atom of type i

$\lambda(k)$: inelastic mean free path

Values for S_o^2, N_i, R_i, and σ_i^2 can be obtained by fitting experimental data to equation 4.18, provided the $f_i(k)$ and $\delta_i(k)$ are known. The average coordination number around both barium and calcium in ACBC and balcite were determined this way and compared to crystalline reference compounds (chapters 9, 10, and 11).

Measurements were performed at the Dow-Northwestern-Dupont collaborative access team (DND-CAT), Sector 5-BM-D of the Advanced Photon Source at Argonne National Laboratory. Samples were spread on 8 μm Kapton tape and kept dry under a stream of He gas. Calibration at the Ca K-edge was performed with a geological Iceland spar (calcite) standard, for which the edge energy was set at 4038 eV. ACBC samples were measured relative to this value. Data was analyzed using the Demeter package.[70,71] Normalization and background subtraction were carried out in Athena using Autobk. χ-data were weighted by k , k^2, and k^3 between 1.6 < k < 11.5 Å^{-1} for the Ca K-edge and between 2 < k < 14 Å^{-1} for the Ba K-edge.

4.7 **X-ray fluorescence**

Filling of the the core hole created by the promotion of a photoelectron places a limit on the lifetime of this excited state, and thus the magnitude of the EXAFS. However, this process also releases an amount of energy that is equivalent to that originally absorbed by the photoelectron, and is, like EXAFS, element specific. If a material is illuminated with monochromatic high-energy X-rays, all atoms with absorption edges below the X-ray energy will undergo excitation, and the filling of these core holes (also called fluorescence) will result in the emission of X-rays of lower energy than the incident beam that are characteristic of the elements in the material. Therefore, this process can be useful for chemical identification.

X-ray fluorescence (XRF) occurs in all elements, but is particularly well suited for heavier elements like calcium and barium, and was therefore used to measure the concentrations of these elements in bulk samples of ACBC and balcite. Intensities of XRF peaks are directly proportional to the atomic concentrations, after correcting for absorption and Compton scattering.

The barium mole fraction, x, of single-phase balcite was determined on a custom-built X-ray fluorimeter with an Ag-anode operating at 15 mA and 40 kV. Detector calibration was performed using the Fe and Mo K_{α} lines of a stainless steel ingot of known composition. Background scattering was subtracted from the raw spectra, and corrections for matrix absorption and Compton scattering were applied using XRF-FP v5.2.7 software from CrossRoads Scientific. Integrated barium $L_{\alpha,1}$ and Ca K_{α} fluorescence intensity was obtained by fitting Gaussian peak profiles to all calcium and barium fluorescence peaks. From the barium $L_{\alpha,1}$ and calcium K_{α} fluorescence intensities, x was determined.

4.8 Electron microscopy

Electron microscopy is unrivaled in its ability to image nanoscale objects in real space. Surface features, including the overall particle size and shape, can be investigated with scanning electron microscopy (SEM). A 1-20 keV electron beam is focused to a sub-nanometer probe with electromagnetic lenses and rastered across the sample. Most of the incident electrons penetrate the sample and are absorbed. The inelastically scattered electrons that manage to escape from the sample surface have greatly reduced energy from (< 100 eV). These low energy electrons are strongly impacted by the distance that they travel in the sample, providing topographical contrast. Some of the incident electrons are scattered elastically, a process which is highly sensitive to the atomic number of the illuminated region in the sample and provides compositional contrast. SEM was used to image ACBC and balcite particles in chapters 9, 10, and 11.

SEM was performed on approximately 5 mg of dry powder was deposited on carbon tape, attached to a piece of single-crystal silicon mounted on an aluminum holder and coated with ~8 nm osmium with an SPI OPC-60A Osmium Plasma Coater. Imaging was performed in a Hitachi S4800 FE-SEM or Hitachi S8030 operating at 10-20 keV at a working distance of ~10 mm.

Scanning transmission electron microscopy (STEM) is conceptually similar to SEM. Like in SEM, an electron beam is rastered over the sample, but in STEM the samples are thin (< 1 μm) and accelerating voltages are higher (100-200 kV) to reduce the fraction of the incident beam that is absorbed. Imaging of secondary electrons is also possible in STEM. In addition, high angle annular dark field (HAADF) images can be obtained from the electrons scattered elastically away from the axis of the primary beam. Heavier elements, like barium, have larger elastic scattering cross sections and therefore produce brighter contrast in HAADF.

Using a sample holder maintained at cryogenic temperatures, frozen samples can be imaged in STEM. For example, aqueous suspensions of particles can be deposited on a conventional TEM grid and plunge frozen in liquid ethane. This process cools the sample at a rate of > 100,000 K/s, vitrifying water before ice crystals can form and preserving the state of the system in a nearly undisturbed state. This technique was used to image gortotowskite particles in chapter 12.

Conventional transmission electron microscopy (TEM) uses similar samples and accelerating voltages to STEM. One significant advantage of TEM is that the focused, rastered beam is replaced with a broad beam that illuminates the sample simultaneously. This allows for the collection selected area electron diffraction (SAED) from specific sample regions. SAED is conceptually similar to X-ray diffraction. The electron wavelength (λ = 0.037 Å at 100 keV) is smaller than the interplanar spacing of a crystal lattice and constructively interferes when the Bragg condition (equation 4.2) is satisfied. Similar to WAXS, SAED enables simultaneous measurement of diffraction over a large range of q with a two dimensional CCD detector. Because electron beams can be focused to relatively small sizes with electromagnetic lenses, diffraction from sample volumes only a few hundred nanometers across can be achieved. Using this technique, ACBC was found to be amorphous on the >100 nm length scale from the absence of strong diffraction and the presence of diffuse, isotropic rings (chapters 9 and 11). SAED was also used to investigate the structure of thin gortotowskite platelets (chapter 12).

4.9 **Electron energy loss spectroscopy**

Electron energy loss spectroscopy is performed in the STEM. The same type of inelastic scattering of the incident beam that produces secondary electrons in SEM is also responsible for the deceleration transmitted electrons in STEM. In fact, the transfer of energy from incident electrons to electronic states in the sample is analogous to absorption of X-rays in XAS. If an incident electron, with an energy (100 keV) much greater than the binding energy of a core electron (4.038 keV at the calcium K-edge) excites the core electron into the continuum, the incident electron will have lost an amount of energy equal to the binding energy (4.038 keV). Instead of increasing the electron beam energy to pass over an absorption edge, as was done with the X-ray beam in XAS, all of the inelastically scattered electrons are collected simultaneously and focused into an EELS spectrometer. These inelastically scattered electrons are separated by their energy relative to the transmitted beam with a strong magnetic field. The result is an EELS spectrum which exhibits absorption edges directly analogous to those measured in XAS. In addition, the intensity of the transmitted beam (zero-loss peak) can be used to determine the thickness of samples with known composition. The presence of barium in gortotowskite platelets, and thicknesses of approximately 10nm, were confirmed by EELS.

4.10 Energy dispersive spectroscopy

Many of the X-ray techniques descried above have analogs in electron microscopy, like WAXS and SAED, XAS and EELS. Energy dispersive spectroscopy (EDS) is the electron analog to XRF. Instead of exiting a core electron with X-rays, the inelastic scattering responsible for EELS, as described in section 4.9, also results in core holes generated by excited electrons that produce characteristic X-rays as the core holes are filled. While the details of the excitation process differ between X-rays and electrons, the fluorescence process is identical in both cases.

EDS was collected using AZtec software (Oxford Instruments) using an Oxford AZtec X-max 80 SDD EDS detector. Spectra were collected from rectangular areas approximately 5 µm x 5 µm within five separate particles and averaged. Data were fit with a Gaussian peak profiles and converted to atomic percent using calibrated standards MgO (Mg K-edge 1.0 – 1.4 keV), $CaCO_3$ (Ca K-edge 3.5 – 3.9 keV), and $BaTiO_3$ (Ba L-edges 4.3 – 5.7 keV). The cation mole fraction for barium (or magnesium) was normalized by the total cation mole fraction to give $x = \frac{[\mathrm{Ba}]}{[\mathrm{Ca}]+[\mathrm{Ba}]}$, or $x = \frac{[\mathrm{Mg}]}{[\mathrm{Ca}]+[\mathrm{Mg}]}$ to give the overall composition $Ca_{1-x}Ba_xCO_3$ or $Ca_{1-x}Mg_xCO_3$. Line scans across balcite and calcite particle cross sections were collected at 30 keV for a minimum of 600 seconds total collection time, with 100 µs dwell time at 50 nm intervals. Data was smoothed with a mean filter distance of five, and normalized to the overall composition measured on a 5 µm x 5 µm rectangular area.

4.11 Thermal analysis

Vibrational spectroscopy revealed the presence of water in ACC, ACBC, balcite, and gortotowskite but could not be used to quantify the exact amount. For that, samples were heated at a constant and well controlled rate on a sensitive microbalance in order to remove structural water. The weight lost upon the removal of water could then be compared to the initial mass of the sample to determine the molar concentration water. This process, called thermogravimetric analysis (TGA), is commonly used to quantify the amount of volatile components in otherwise stable materials. Simultaneously acquired differential thermal analysis (DTA) was used to determine whether weight loss was exothermic or endothermic by comparing the actual sample temperature with that set by the constant heating rate. Differential scanning calorimetry (DSC) is complimentary to DTA, and can be more precise because it relies on measuring the power delivered to the sample necessary to keep it at the set temperature and equal to that of a reference sample that does not undergo any thermal transitions.

TGA and DTA was performed simultaneously using a Mettler Toledo SDTA851. Analysis was performed on ACBC powders dried in vacuum for exactly 24 hours after synthesis. Approximately 5 mg of the dry powder was held at 30 °C for 10 minutes to stabilize the sample environment, then heated to 1000 °C at a rate of 10 °C/min under dry N_2 flowing at a rate of 20 mL/min.

Weight change was tracked by the variable α, defined as

$$\alpha = \frac{w_o - w_i}{w_o} = \frac{\Delta w}{w_o} \tag{4.19}$$

where w_0 is the initial weight and w_i is the instantaneous weight. The total fractional weight change, α_T, is the value of α at the final weight, $w_i = w_f$. Total fractional weight loss, $\Delta\ \alpha_T$, is defined as $1-\alpha_T$. Fractional weight loss upon crystallization, $\Delta\ \alpha_c$, is defined as $\alpha_{c1}-\alpha_{c2}$, where α_{c1} and α_{c2} are the values of α at temperatures corresponding to either side of the crystallization exotherm peak in differential scanning calorimetry, determined using the StarE v8.1 software package (Mettler Toledo). When multiple crystallization peaks were present, α_{c2} was chosen as the end of the final crystallization event. The molar water content, n, of the powders was calculated from

$$n = \frac{M_{H_2O}/\alpha_T}{(1-x_{Ba})M_{Ca}+x_{Ba}M_{Ba}+M_C+3M_O} \tag{4.20}$$

where M is the molecular mass of the subscripted species, the numerator is the molar fraction of water, the denominator is the molar fraction of $Ca_{1-x}Ba_xCO_3$, and x is the stoichiometric coefficient determined by XRF.

Differential scanning calorimetry and TGA were conducted in parallel on separate powder samples drawn from the same batch. Heat flow data in DSC was corroborated by simultaneous DTA (SDTA) performed during TGA runs and was in good qualitative agreement. Differential scanning calorimetry was performed on a Mettler Toledo DSC822e using the same approximate sample mass and N_2 flow rate as TGA, with the same heating schedule up to the instrument maximum of 500 °C. The crystallization temperature T_c was calculated from the onset of the crystallization exotherm in DSC curves determined with the StarE v8.1 software package.

4.12 Inductively coupled plasma – optical emission spectrometry

While the composition of ACBC and balcite can be determined by XRF or EDS, these techniques tend to be accurate only to within ± 1%. Inductively coupled plasma–optical emission spectroscopy (ICP-OES) has a sensitivity in the parts-per-million, and is therefore the gold standard for stoichiometry determination. It is also inherently easier to examine aqueous samples, like the starting solutions used to make ACBC and balcite in chapters 9, 10, and 11.

The barium mole fraction of solutions of the starting materials (x^{feed}) was determined by ICP-OES, using a Thermo iCAP 7600 instrument. Solutions were diluted 100x in water and then 200x in 3% by volume aqueous nitric acid. Intensities for the four strongest emission lines of barium (λ = 230.424, 233.527, 455.403, and 493.409 nm) and Ca (λ =315.887, 393.366, 396.847, and 422.673 nm) were recorded in both axial and radial geometries. Intensities were converted to absolute concentrations using a calibration curve recorded for a series of eight standard solutions ranging from 10 μg/mL to 4 ng/mL that were prepared by serial dilution. An average concentration and standard deviation for barium and calcium was determined from 8 individual values (4 different emission lines in two geometries each). Finally, x^{feed} was calculated according to $x^{\text{feed}} = \frac{[\text{Ca}]}{[\text{Ca}]+[\text{Ba}]}$, using the limits of uncertainty for individual measurements as bounds for the reported error.

ICP-OES was also used confirm the composition of some ACBC samples. An aliquot of the dry powder (~1 mg) was dissolved in 3% nitric acid (10 mL), and then diluted by 100x in 3% aqueous nitric acid. This solution was then measured in the same way described above.

4.13 Nanoindentation

Nanoindentation is a commonly used technique to interrogate the mechanical properties, including indentation modulus, E_I and hardness, H, of small samples.[72] A shallow triangular pyramid (Berkovich) diamond indenter, with pyramid face normal at 65.27° from the indentation axis, is pressed into a flat sample at a constant loading rate until either a fixed load or displacement is reached. The load, P, and displacement, h, are recorded during indentation. Normally both plastic and elastic deformation occur during the formation of an indent, which makes the loading curve difficult to interpret. However, it is assumed that only elastic recovery occurs upon unloading, so that the unloading curve contains much of the useful information in a nanoindentation experiment.

The stiffness, S, is simply given by

$$S = \frac{dP}{dh} \tag{4.21}$$

This is taken as the initial slope of the unloading curve, as van der Waals and other adhesion forces begin to dominate at lower loads. The elastic contribution to the indent, or sink-in h_s, is calculated from

$$h_s = \epsilon \frac{P_{max}}{S} \tag{4.22}$$

where $P_{\max}$ is the maximum load (or the load at maximum displacement). The contact height, h_c, is then given by

$$h_c = h_{max} - h_s \tag{4.23}$$

The contact area of the indenter is calibrated on a sample of known harness and stiffness to correct for deviations from ideality. Typically fused silica, which exhibits minimal pile-up and has a low E/H, is indented to an h_c comparable to that in the sample of interest. The (known) hardness is simply given by

$$H = \frac{P_{max}}{A} \tag{4.24}$$

and so the area can be fit with an empirical function

$$A = \sum_{n=0}^{8} C_n h_c^{n-2} \tag{4.25}$$

Updated methods for area calibration have also been described.[72] Samples can be indented with a calibrated tip and the hardness found straightforwardly from Equation 4.24. From the same curve, E_I can be extracted from

$$E_I = \frac{\sqrt{\pi}S}{2\beta\sqrt{A}} \tag{4.26}$$

where $\beta \cong 1$.

Balcite powders were mounted in EpoTek epoxy resin, with a 4:1 ratio of base to curing agent, cured for at least 24 hours at room temperature. Flat surfaces were obtained via argon ion milling in a Leica TIC3X equipped with a cryo-stage, operating at 8 kV and 3 mA, $5 \cdot 10^{-6}$ mbar, and a stage temperature set point of -25°C. Milling was followed by air plasma treatment at $6 \cdot 10^{-1}$ Torr for 2 min for a final surface cleaning. Nanoindentation was performed in a Hysitron TI 950 TriboIndenter using a Berkovich diamond indenter geometry to a peak load of 1000 μN. Tip shape and piezo control were calibrated with a fused quartz standard prior to testing each sample. Particle surfaces were imaged with the same in diamond tip before and after indentation. Porosity in the center of the spherulite particles, measured from the root-mean-squared height profile from images obtained with the indenter tip, required indents to be taken from ~5-10 μm thick shells on the outside of the particles that were fully dense and had roughness less than 1 nm rms. After elastic relaxation, indents were approximately 50 nm deep and 1.5 μm across. At least 10 measurements across at least 3 particles each were collected for as-synthesized balcite, balcite heated to 600°C, spherulitic magnesian calcite, and single crystalline calcite.

5. Controlling nucleation in giant liposomes

5.1 Abstract

We introduce giant liposomes to investigate phase transformations in picoliter volumes. Precipitation of calcium carbonate in the confinement of DPPC liposomes leads to dramatic stabilization of amorphous calcium carbonate (ACC). In contrast, amorphous strontium carbonate (ASC) is a transient species, and $BaCO_3$ precipitation leads directly to the formation of crystalline witherite.

5.2 Results and discussion

The use of metastable amorphous minerals is a widespread strategy in biological crystal growth.[73] Prominent examples are the synthesis of single crystalline spicules using an ACC precursor,[74-76] vesicle-borne amorphous calcium phosphate in bone mineralization,[77] and use of amorphous iron oxides.[78] It is conceptually related to sol-gel processing of ceramics,[17] may involve a fluid/fluid transition similar to those observed in protein crystallization,[6,79] and has generated a lot of interest as a possible model system for non-classical nucleation. [41,80]

At this time, there is a fascinating disconnect between experimental observations, theoretical considerations, and simulations regarding the stability of ACC in confinement. Several groups have reported an increased lifetime for ACC when confined in pores,[47] between crossed cylinders,[46] in picoliter droplets,[53] within a silica coating,[81] or in liposomes.[82,83] In bulk solution, crystallization of ACC particles larger than 70-100 nm was reported. [84,85] Navrotsky argued that there is a threshold size, below which amorphous nanoparticles are thermodynamically more stable.[17] However, others have pointed out, and simulations have confirmed, that for $CaCO_3$ this crossover should occur at a radius of 1-2 nm. [41,53,86]

Noting that synthetic ACC contains up to one formula unit of water, has a long lifetime while dry, and appears to dehydrate over time even in solution, it has been suggested that biological stabilization may rely on preventing release of or contact with water. [53,81,87,88] While this may be true in certain *in vitro* systems, biomineralization generally occurs in compartments delimited by phospholipid bilayer membranes that have high permeability for water.[78] In fact, ACC nanoparticles up to 200 nm in diameter can be synthesized in phospholipid vesicles (liposomes) where they remain stable against crystallization in direct contact with water. [82,83] Therefore, liposome reactors are ideally suited to study the dual roles of confinement and the membrane itself in biological crystallization.

Herein, we study $CaCO_3$ phase transformations in giant liposomes (d = 20-50 μm). We demonstrate confinement in giant liposomes results in ACC particles that are exceptionally stable despite a much increased size and exposure to water. We attribute the extended stability to the exclusion of heterogeneous nucleators and qualitatively compare the kinetics of phase transformations observed for Ca, Sr, and Ba carbonates.

Giant liposomes were synthesized using the method of Horger and coworkers.[89] Briefly, a dry film of phosphatidylcholine (PC) supported on agarose was gently hydrated with 1 M aqueous $CaCl_2$. The resulting liposomes are 20-50 μm in diameter (Figure 5.1A), with varying number of lamellae. Ca^{2+} remaining in solution outside the liposomes was exchanged against an isosmotic solution of NaCl. Precipitation of $CaCO_3$ in the lumen, i.e. the aqueous interior of the liposome, was initiated by addition of aqueous $(NH_4)_2CO_3$.[82,83] Within 4-5 min, a large number of precipitates appear all at once throughout the lumen (Figure 5.1B), consistent with homogenous nucleation, nucleation on suspended nucleators, or spinodal decomposition, but not heterogeneous nucleation on the membrane.[6,61]

Particles rapidly aggregate and sink to the bottom of the liposome (Figure 5.1C/D). Over the course of 24 h, further aggregation and coarsening leads to formation of a roughly textured mass that has a diameter of 10-40 μm. Precipitates are not birefringent and remain so for up to 8 days. Confocal Raman spectra recorded *in situ* show the typical features of bulk synthetic ACC (Figure 5.2 and SI).[73] SEM reveals that aggregates consist

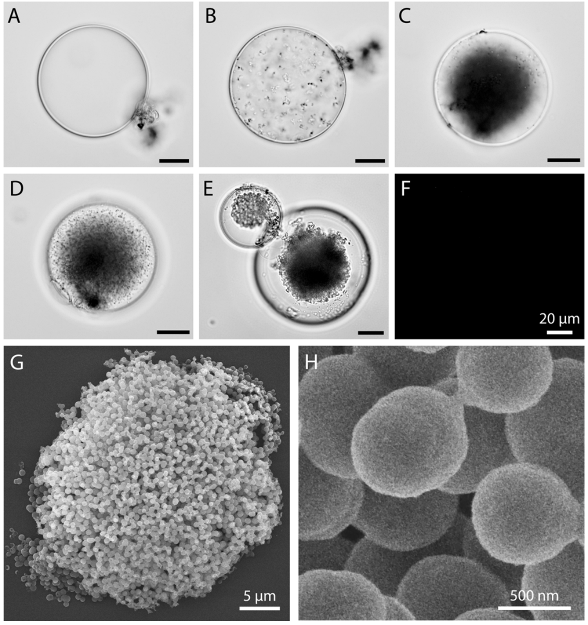

Figure 5.1. (A-F) Light microscopy images of Ca-loaded giant PC liposomes (A) before the addition of $(NH_4)_2CO_3$; (B) within 5 min after addition, a great number of particles precipitate; (C-D) within 2 h, particles aggregate and sink to the bottom (two different focal planes shown); (E-F) within 24 h, the aggregate condenses and exhibits a rough surface, but under polarized light is not birefringent (F); (G-H) SEM images of an isolated ACC aggregate (G), consisting of ACC nanoparticles 650 ± 5 nm in diameter (H)

of spherical particles ~ 650 nm in diameter (Figure 5.1G/H). In combination, this is strong evidence that liposome-encapsulated ACC is identical to hydrated ACC precipitated in bulk.

For bulk ACC, however, moisture in the ambient air is sufficient to cause crystallization.[90] Confocal fluorescence microscopy reveals that ACC does not form on or coat the membrane, suggesting that the interaction is weak (SI). As Langmuir monolayers of PC do not prevent nucleation of vaterite and calcite,[91] we can rule out that the membrane itself stabilizes ACC. To further confirm that ACC precipitates are stabilized exclusively by confinement, liposomes were lysed with detergent (Figure 5.3). As soon as liposomes break open, we observe rapid precipitation of calcite, and concurrent dissolution of ACC. Calcite crystals preferentially form on the glass substrate in the vicinity of the dissolving precipitate. While we cannot exclude that some calcite crystals nucleate on the surface of ACC particles, it is clear that this does not occur in the liposome before lysis.

We estimate that the total volume of the ACC aggregate in a giant liposome with *d* = 50 μm to be of 2-3x10^3 μm^3. This aggregate consists of ACC nanoparticles that are each ~1,000 times larger in volume than current estimates for the threshold of stability, and they are in direct contact with water. It is thus unlikely that a) there is a threshold size for the stability of the particles, and b) that limiting the ability to release water, or limiting the contact with water stabilizes ACC in this system. However, ACC could be kinetically stable in the absence of suitable heterogeneous nucleators for one of the crystalline polymorphs This is analogous to the classical observation that small liquid metal droplets display large supercooling on account of a low number of heterogeneous nucleators.[39] For liposomes, it is well documented, if poorly understood, that large molecules and particles are encapsulated at rather low efficiency.[92] Thus, it is conceivable that the number of heterogeneous nucleators in the liposome is lower than in bulk.

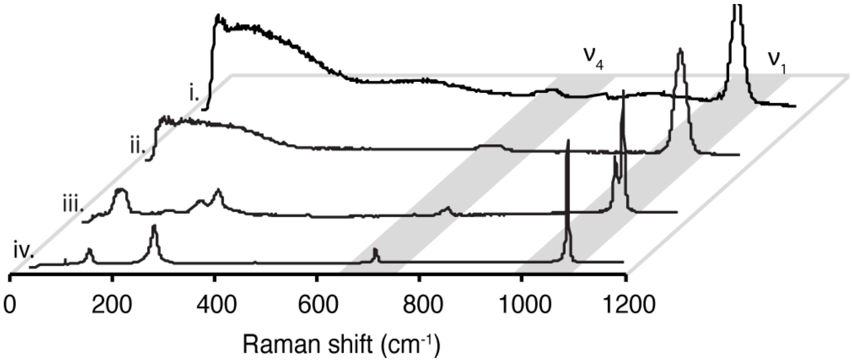

Figure 5.2. Raman spectra of (i) a liposome-encapsulated ACC aggregate recorded *in situ*, and of bulk synthetic (ii) ACC, (iii) vaterite, and (iv) calcite powders.

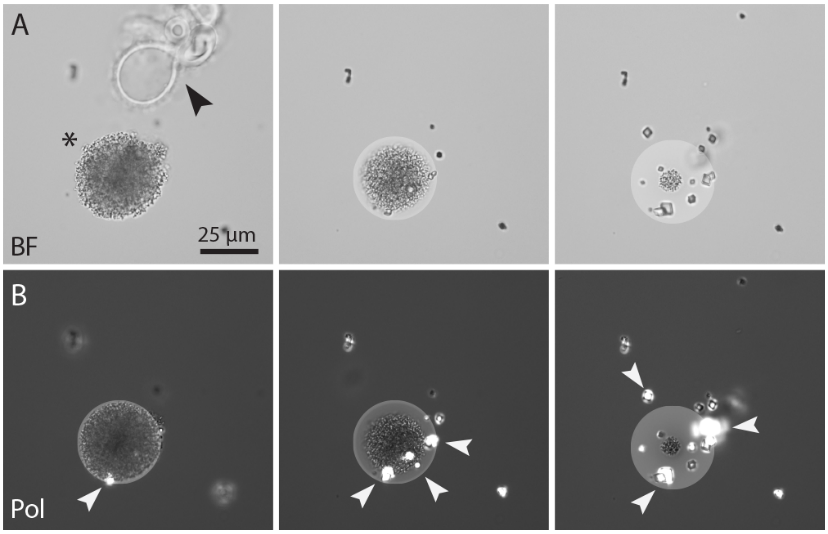

Figure 5.3. Lysis of liposomes (black arrowhead) with 3% Triton-X results in dissolution of encapsulated ACC (asterisk), and re-precipitation of calcite in the immediate vicinity (white arrowheads). (A) Bright field (BF) images taken over ~ 5 min, and (B) polarized light (Pol) images taken immediately after images in A. The white circle indicates the size of the original ACC precipitate.

To establish how general this phenomenon is, we investigated the precipitation of $SrCO_3$ and $BaCO_3$ at approximately equal initial supersaturation ($\sigma \approx 12$, see SI). Precipitation of $SrCO_3$ is similar to $CaCO_3$, with many small precipitates formed within the first 3-4 minutes. that do not exhibit birefringence (Figure 5.4). However, within 5-10 min, one birefringent particle appears that grows rapidly while the first-formed precipitates dissolve. In the case of $BaCO_3$, there was no intermediate precipitate and one or more spherulitic sheaves were observed as early as one minute into the precipitation. Birefringent precipitates were identified as strontianite ($SrCO_3$) and witherite ($BaCO_3$) by *in situ* Raman microscopy (SI). While we were unable to record spectra for the transient $SrCO_3$ precipitate, we interpret the absence of birefringence and the rapid dissolution-reprecipitation as evidence that it is metastable ASC. We find no indication for the formation of amorphous barium carbonate (ABC). Tremel and Gower previously reported evidence for transient ASC and ABC.[48,93]

Within the time resolution of our experiments, there is no difference in the rate by which ACC and ASC are formed. However, the lifetime of the amorphous metal carbonate decreases dramatically, from at least $7 \cdot 10^5$ s for ACC to $2\text{-}3 \cdot 10^2$ s for ASC to infinitesimal, for (hypothetical) ABC. This is to be expected if the lifetime of the amorphous carbonate is determined by the relative height of the barrier to nucleation of the amorphous vs. the crystalline carbonate (Scheme 5.1). While the barrier to ACC formation (W_1^*) is low (and may be absent entirely in case of spinodal decomposition[6,61]), the absence of a heterogeneous nucleator for one of the crystalline polymorphs results in a very high barrier W_2^*.[22,25] Thus, ACC forms rapidly, decreasing the supersaturation σ for the crystalline polymorphs because the activities of Ca^{2+} and CO_3^{2-} are now set by the solubility of ACC. As $W^* \propto \sigma^{-2}$, the resulting increase in barrier height – by a factor of up to ~5 in our system – kinetically traps metastable ACC (W_3^*). In the case of $SrCO_3$, the barrier to nucleation of ASC is likely similar in magnitude to that of ACC. The barrier for strontianite formation, however, is significantly reduced. Even though ASC precipitates first, lowering supersaturation, the resulting delay is brief. As soon as strontianite nucleates and grows, the resulting drop in ion activities leads to rapid dissolution of ASC. Finally, the barrier to witherite nucleation appears to be close to or below that of ABC.

The acceleration of the rate of crystallization from calcite to witherite could be a consequence of a lower barrier to homogeneous nucleation (SI). As heterogeneous nucleation in most systems remains far more likely, relative rates are likely also affected by the interfacial energy between nuclei of the crystalline polymorphs and the liposome membrane, the amorphous precursor, or random impurities.

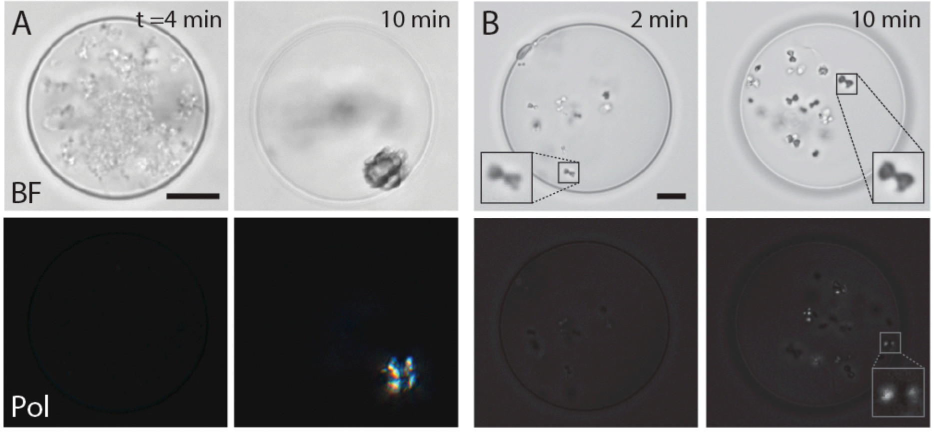

Figure 5.4. Precipitation of $SrCO_3$ (A) and $BaCO_3$ (B) in giant PC liposomes. Absence of birefringence in (A) at 4 min indicates formation of ASC. Birefringence in A at 10 min, and in B at 4 min and 10 min indicates rapid nucleation and growth of crystalline strontianite and witherite, respectively. Scale bar represents 10 µm.

Obviously, organisms that choose confinement to control biomineralization must carefully engineer the surface properties of the confining structure and of any surfaces within.

5.3 Conclusions

From these experiments, we draw two important conclusions with implications for biological and bio-inspired crystal growth in confinement: I) nucleation kinetics of the crystalline Ca/Sr/Ba-carbonate can control the lifetime of the amorphous carbonates; II) exclusion of heterogeneous nucleators for ACC present in bulk may be an intrinsic feature of mineralization in intracellular compartments. Given the diverse chemistry of lipids, it may be possible to tune liposome composition to prevent, or control nucleation of specific polymorphs. We envisage that giant liposomes will emerge as a powerful platform to study the role of confinement also of proteins and pharmaceuticals. Clearly, however, $CaCO_3$ is special in that ACC can be stabilized with minimal effort. Whether this is fortuitous, or a consequence of evolutionary optimization of lipid structure or biomineral use, is another fascinating topic.

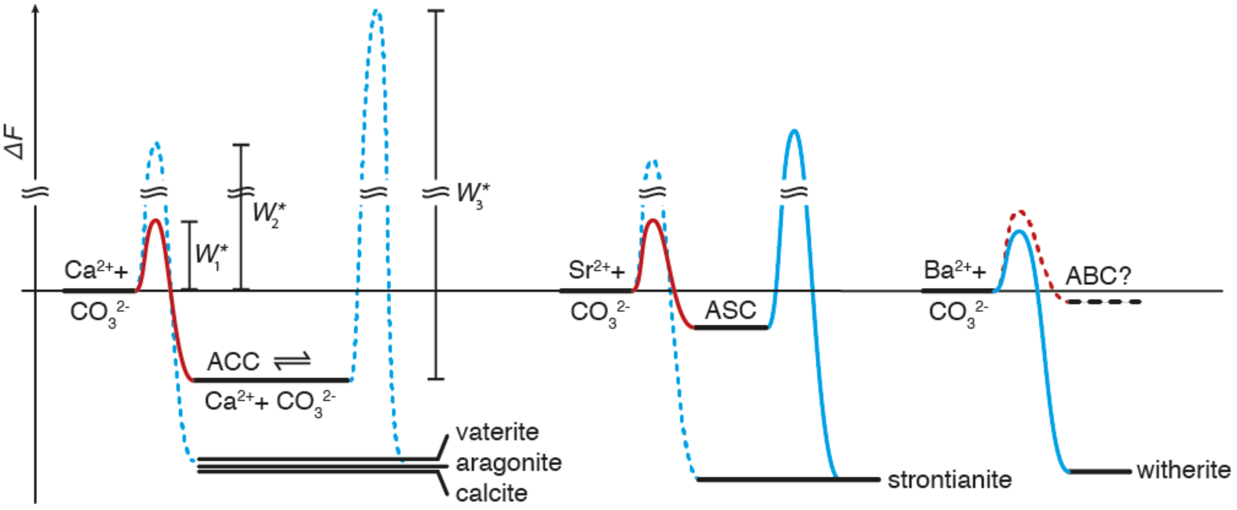

Scheme 5.1. Suggested free energy diagram for phase transformations in supersaturated solutions of calcium, strontium, and barium carbonate. Formation of the amorphous phase is controlled by the relative height of barriers W_1^* and W_2^*, its lifetime by W_3^*. Solid lines correspond to processes observed in giant liposomes, dashed lines to those not observed.

5.4 Materials and methods

5.4.1 *Materials*

Agarose II (Amresco, Solon, OH). 1,2-dioleoyl-*sn*-glycero-3-phosphocholine (DOPC), 1,2-dipalmitoyl-*sn*-glycero-3-phosphoethanolamine-N-(lissamine rhodamine B sulfonyl) (Rhodamine-PE) (PC, Avanti Polar Lipids, Alabaster, AL). Calcium chloride dihydrate (BDH Chemicals, Westchester, PA). Strontium chloride hexahydrate (Alfa Aesar, Ward Hill, MA). Barium chloride dehydrate (EMD Millipore, Billerica, MA). Ammonium carbonate, Sodium chloride, Dichloromethane (Mallinckrodt Baker, Phillipsburg, NJ). Calcein (TCI America, Portland, OR). Molecular Porous Membrane Tubing (MWCO: 3500, Spectrum Laboratories, Rancho Dominguez, CA). Unless otherwise noted, all solutions where prepared in ultra-pure water (ρ = 18.2 MΩ cm) prepared with a Barnstead NanoDiamond UF + UV purification unit.

5.4.2 *Liposome preparation*

The procedure for the preparation of giant liposomes was adapted from Horger and coworkers.[89] Agarose films were deposited on a glass coverslip by dip coating one side of the glass onto the surface of a melted 1 wt% agarose solution. The agarose films were then dried at 40°C overnight in a convection oven. The lipid films were deposited by pipetting 50 µL of 5 mg/mL lipids in dichloromethane onto the agarose-coated coverslip. Dichloromethane was removed by placing the films under vacuum for at least 20 min. To form liposomes the lipid+agarose films were rehydrated by submerging the coverslips in 1 mL of aqueous $CaCl_2$, $SrCl_2$ or $BaCl_2$ for 1 h. The concentrations of the $CaCl_2$, $SrCl_2$ or $BaCl_2$ solutions were 1.0, 0.17, and 0.77 M, respectively (see below for a discussion of the supersaturation). To remove unencapsulated cations the resulting liposome suspension was dialyzed against 500 mL of isosmotic aqueous NaCl. The dialysis bath was replaced 4 times over 24 h.

5.4.3 *Precipitation inside liposomes*

Precipitation of calcium, strontium, and barium carbonate inside the giant liposomes was initiated by gentle mixing of 800 μL of liposome suspension with 200 μL of 1.5 M $(NH_4)_2CO_3$ for a final concentration of 300 mM $(NH_4)_2CO_3$. Liposome suspensions were imaged in a Leica DMI6000B microscope equipped with polarized light optics. Due to the small size and rapid movement of initial precipitates of witherite ($BaCO_3$), their birefringence is difficult to capture, but is obvious when observed by eye.

5.4.4 *Supersaturation inside liposomes*

Assuming that equilibration outside the liposome, transport CO_2 and NH_3 across the membrane, and equilibration inside the liposome are fast compared to the timescale of phase transformation, and neglecting activity coefficients and pH effects, the maximum possible supersaturation for the crystalline polymorphs calcite, strontianite, and witherite inside the liposomes is $\sigma = \ln([M^{2+}][CO_3^{2-}]/K_{sp}) \sim 18$ for all three cations. Accounting for speciation and activity using Visual MINTEQ, we expect upper limits for the supersaturation $\sigma_{calcite} \leq 10.8$, $\sigma_{strontianite} \leq 12$, and $\sigma_{witherite} \leq 11.5$. Note that there will be a time interval during which the supersaturation increases rapidly, and that the final value may not be reached if an amorphous carbonate precipitates early in the process. Given that precursor growth is fast compared to trans-membrane transport,83 the supersaturation inside liposomes after formation of the precursor will remain approximately constant and close to σ = ln(Ksp, amorphous/Ksp, crystalline). For ACC and calcite, we calculate σ = 4.8 based on pKsp, ACC = 6.4 (ref94 or σ = 5.6 based on pKsp, ACC = 6.04 (ref95).

While the overall development of the supersaturation over time for SrCl2 and BaCl2-loaded liposomes is likely similar, in the absence of solubility data for the amorphous carbonates, equivalent supersaturation values cannot be calculated.

5.4.5 *Lysis of liposomes*

Lysis of phospholipid membrane was performed 4 h from the addition of ammonium carbonate, by addition of 100 μL of 30 wt% Triton-X to 900 μL of liposome suspension.

6. Influence of lipid chemistry on ACC precipitation in liposomes

6.1 Introduction

Exclusion of heterogeneous nucleators, prevention of Ca^{2+} transport between liposomes, and the resulting large barriers to crystalline $CaCO_3$ at the solubility limit of ACC were cited as likely explanations for the extended lifetime of ACC in liposomes. In this chapter, we confirm that phosphatidylcholine (PC) lipid membranes do not interact strongly with newly forming mineral. We show that decreasing the screening of the positively charged primary amine in PC by replacing methyl groups with hydrogen increases the degree of membrane-mineral interaction. In addition, charged lipids like phosphatidic acid (PA) and phosphatidylserine (PS) also promote mineral formation on or within the membrane, while neutral lipids like phosphatidylgylcerol (PG) behave like PC. We show that many of the liposomes are multilamellar using small angle X-ray scattering, and that salt concentration, $(NH_4)_2CO_3$ diffusion, and mineralization affect the interlamellar spacing.

6.2 The role of phosphatidylcholine and agarose in stabilizing ACC

The inner leaflet of the membrane provides a surface that may play a role in the formation and/or stabilization of ACC. In addition, some agarose present during liposome formation may be encapsulated in the liposomes. We therefore used confocal microscopy to investigate where ACC forms and whether it interacts with the lipid membrane or agarose. Precipitation experiments were performed in liposomes containing 0.5 wt% rhodamine-labeled PE that were a) loaded with both Ca^{2+} and the fluorescent dye calcein (Figure 6.1); or b) prepared on fluorescein-labeled agarose films (Figure 6.2). After addition of a solution of $(NH_4)_2CO_3$ to Ca^{2+} and calcein loaded liposomes, highly fluorescent, calcein-labeled ACC nanoparticles form throughout the lumen, confirming results from bright field microscopy (Figure 5.1). It is thus clear that ACC does not preferentially form at the membrane. Optical sections through the liposome volume at 4 h (Figure 6.1) show that ACC nanoparticles have loosely aggregated at the bottom of the liposome ra-

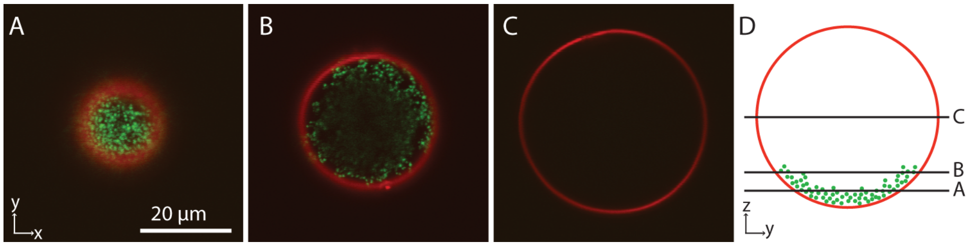

Figure 6.1. (A, B, C) Optical sections of a giant PC liposome (red) with encapsulated ACC nanoparticles (green) at 4h. (D) Approximate location of the sections A-C. Precipitation experiments were performed in liposomes containing 0.5wt% rhodamine-labeled PE and loaded with both Ca^{2+} and calcein.

ther than coating the entire membrane surface. This suggests that that interaction between ACC and the PC membrane is weak. In liposomes prepared from fluorescein-labeled agarose films, fluorescein is confined to the phospholipid membrane (Figure 6.2), and is absent from the lumen of the liposome. This suggests that while a small amount of agarose is incorporated into the lamellae of giant liposomes, it is excluded from the precipitate and does not play role in the nucleation and stabilization of ACC.

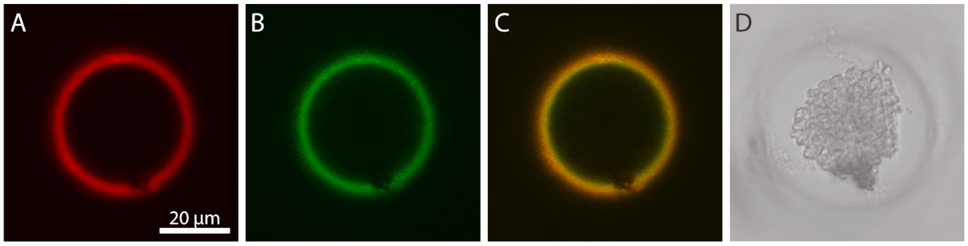

Figure 6.2. Confocal microscopy images of (A) the phospholipid membrane with 0.5% rhodamine-PE (red), (B) agarose labeled with FITC (green), and (C) composite of the two images in which agarose colocalized with membrane appears yellow. The optical sections were recorded from the bottom half of the liposome. The location of the ACC precipitate is visible in the bright field image (D) recorded from the same focal plane.

6.3 Comparison of lipid headgroup charge screening

Common biological lipid headgroups PC and PE are shown in Figure 6.3a, along with mono- and di-methyl PE, which form a series of increasing amine methylation. The net charge of all these zwitterionic lipids is zero due to the compensation between negatively charge phosphate and positively charged amine. However, with fewer methyl groups screening the positive charge on the amine, the degree of mineral interaction with the membrane increases (Figure 6.3b-g). 25 mol% dm-PE, mm-PE, and PE were added to PC to make liposomes as described in chapter 5. Precipitation was initiated identically in each case, the precipitation rate was comparable, and precipitates remained amorphous. In both small liposomes (Figure 6.3b-d) and GUVs (Figure 6.3e-g), the mineral became increasingly conformal with the membrane, and less was found throughout the volume of the lumen. In GUVs precipitation distorted the membrane in the mm-PE and PE samples (Figure 6.3f, g), evidence that appreciable forces were generated through the interaction between the membrane and the growing mineral.

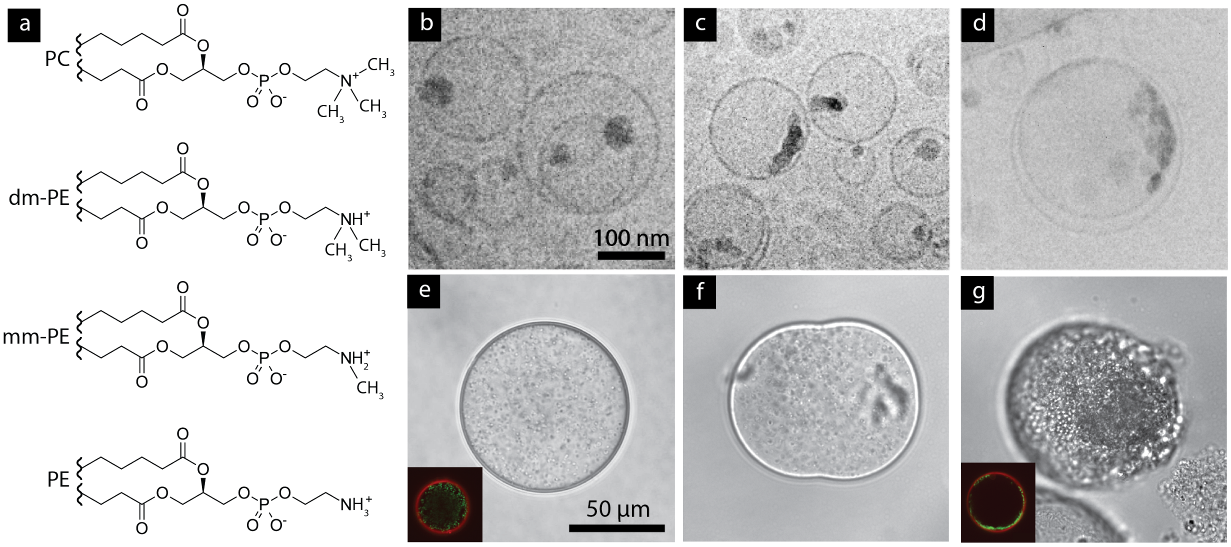

Figure 6.3. (a) Common biological lipids phosphatidylcholine (PC) and phosphatidylethanolamine (PE), and mono- and di-methyl PE. These lipids form a series with increasing methylation of the amine going from PE to PC. (b-g) When 25 mol% mm-PE the interaction between the lipid and mineral changes dramatically. (b, e) PC does not appear to interact strongly with the mineral, which is roughly isotropic in cryo-TEM (b) and distributed throughout the lumen volume in optical microscopy (e). Similar behavior is observed for dm-PE (not shown). (c, f) mm-PE alters the ACC particle morphology to become more conformal with the liposome (c) and can distort the lumen during precipitation (f). PE (d, g) is highly conformal with the lipid membrane in cryo-TEM (d) optical microscopy (g) and confocal laser scanning microscopy (inset).

6.4 *In situ* X-ray scattering

Time-resolved WAXS/MAXS/SAXS was used to follow precipitation within giant liposomes *in situ*. Liposomes were made as described in chapter 5, and concentrated in quartz X-ray capillaries with gentle centrifugation. A controlled volume of ammonium carbonate was dosed to the capillary using a syringe pump, and data acquisition was software triggered to begin simultaneously. Scans were collected every second for 60 seconds. WAXS confirmed that the particles were amorphous over the course of the experiments (up to 1 hour) from the absence of Bragg diffraction, and SAXS confirmed that large (<200 nm) particles formed in all cases. SAXS and MAXS were similar in all samples, and representative experiments are presented in Figure 6.4.

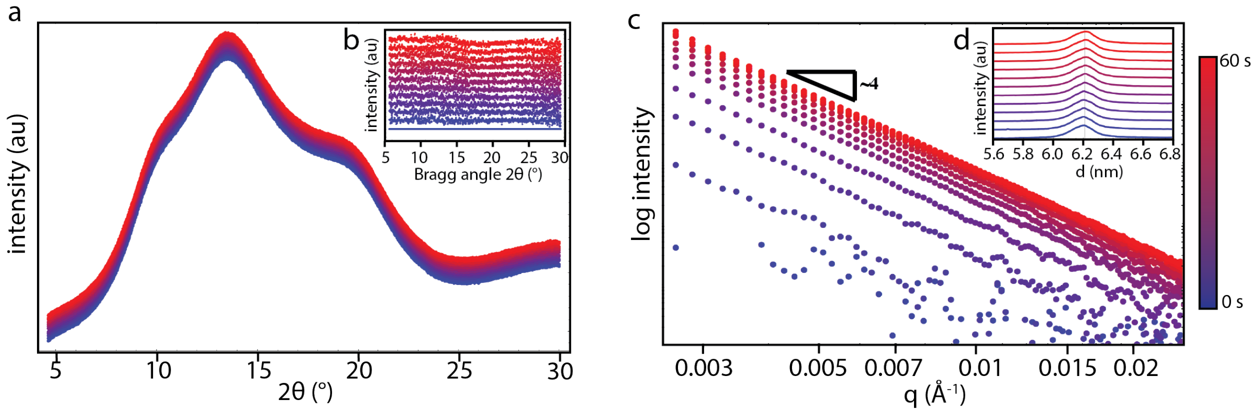

Figure 6.4. (a, b) Representative WAXS, (c) SAXS and (d) MAXS curves for the precipitation of ACC in PC liposomes. (a) Absence of Bragg peaks over the course of the experiment confirms that no crystalline precipitates formed. (b) Subtraction of the initial scan (background) reveals subtle increase in intensity around 12 and 24 °, consistent with amorphous mineral. (c) SAXS intensity increases within 5 seconds of ammonium carbonate addition, confirming that transport is rapid through the membrane. Even at the earliest times, no SAXS features are observed and a slope of -4 indicates the presence of large, 3D particles. (d) MAXS confirms that the liposomes are multilamellar from the diffraction peak at 6.2 nm, which is expected from DOPC.

Unlike WAXS and SAXS, MAXS revealed different behavior depending on the membrane chemistry. Diffraction peaks from multilamellar GUVs appeared at a *d*-spacing of approximately 6 nm, as expected for lipids with dioleoyl (DO) tails. This distance corresponds to the thickness of a bilayer of lipids, and the water and counterions on either side that separate individual bilayers. Despite having identical tails, headgroup methylation changed the initial spacing between bilayers, even before the reaction (Figure 6.5). PC started at 6.21 nm, mm-PE at 6.11 nm and PE at 6.15 nm. Over the course of precipitation the inter-bilayer spacing of PC did not change appreciably, while mm-PE expanded from 6.11 to 6.15 nm and PE established new, larger thickness at 6.23 nm after approximately 40 s. Clearly, increasing exposure of the amine from the reduction of methylation increased the magnitude of the response to precipitation. This response must be related to the increasing affinity of the mineral for the membrane. We suggest that the formation of a salt bridge between carbonate ions from solution and the amine can explain these observations. An ionic interaction between negatively charged carbonate and positively charged amine exists in all cases, but with decreasing methylation of the amine, the ability to simultaneously form hydrogen bonds between carbonate oxygens and hydrogens on the amine in-

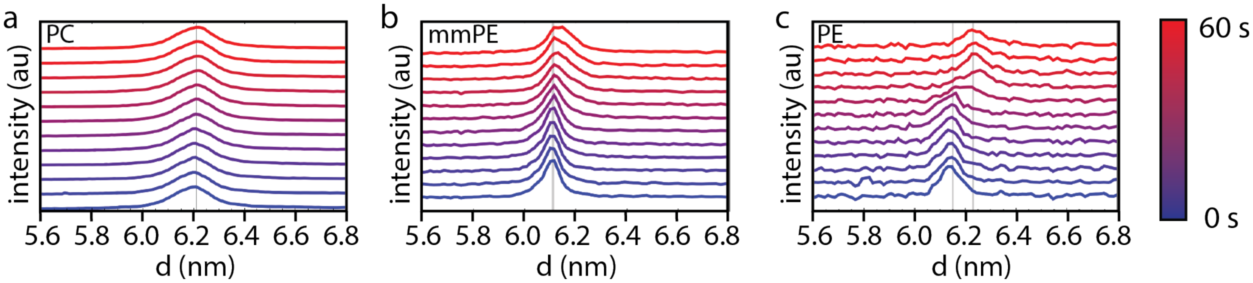

Figure 6.5. MAXS of diffraction from lipid membranes during precipitation of ACC over the first 60 seconds. (a) PC, (b) mm-PE, and (c) PE. PC spacing didn't change appreciably from its 6.21 nm spacing, while mm-PE expanded from 6.11 to 6.15 nm and PE established new, larger spacing at 6.23 nm after approximately 40 s.

creases the strength of the bond. With carbonate more tightly bound to the membrane, precipitation of ACC becomes much more likely to occur near the solution/membrane interface.

6.5 **Lipid membrane charge**

Charge interaction at the lipid headgroup can clearly have an impact on the precipitation of ACC. Given how dramatic this effect was for zwitterionic lipids, we explored charged and neutral lipids to expand our understanding of the role of membrane chemistry on mineralization. Neutral phosphatidylglycerol (PG) was compared to negatively charged phosphatidic acid (PA) at the same concentration of 25 mol% in PC (Figure 6.6). Consistent with expectations, PA exhibited strong membrane-mineral interactions, while PG was nearly indistinguishable from PC.

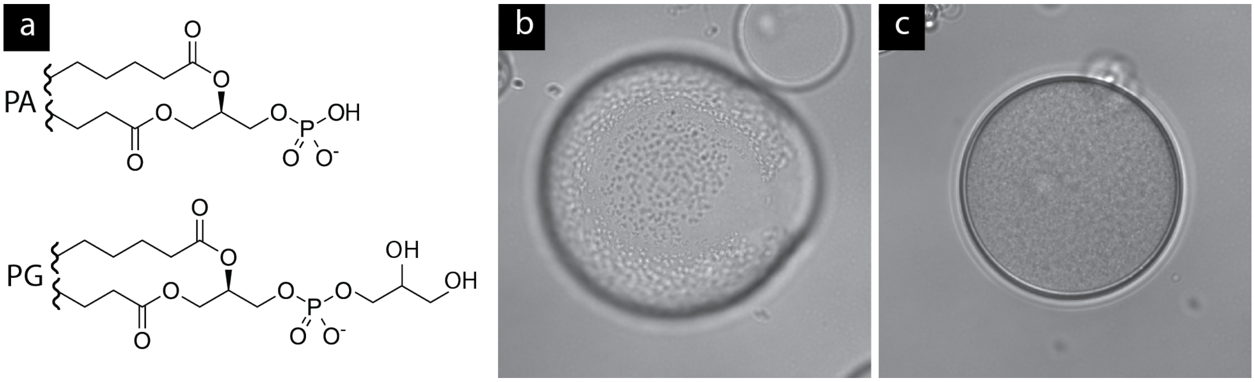

Figure 6.6. Effect of lipid membrane charge in GUVs. (a) Negatively charged PA and neutral PG. (b) PA had a strong membrane-mineral interaction, precipitating on the membrane wall while (c) PG appeared to have little interaction.

6.6 **Summary**

The assumption that the lipid chemistry of PC is not responsible for stabilizing ACC put forth in chapter 5 appears to be well grounded. Strong lipid mineral interaction in PE is easily distinguished from precipitation throughout the lumen of the liposome. The hypothesis that charge interaction at the inner membrane interface mediates the degree to which precipitation occurs on the membrane is supported by evidence of similar behavior in negatively charged PA and the apparent absence of such an interaction in neutral PG. Stearic hindrance around the quaternary amine in PC headgroups reduces the amount of charge interaction with ions in solution, and replacing methyl groups with hydrogens increases the degree of membrane mineral interaction.

7. Droplet based microfluidic platform enables quantification of amorphous calcium carbonate crystallization kinetics

7.1 Abstract

In situ characterization of hundreds of emulsion droplets within a microfluidic reaction chamber enables the quantification of the crystallization rate of vaterite from ACC. This process occurs through dissolution-reprecipitation and follows classical nucleation kinetics with a rate of 1.7 cm^{-3} s^{-1}.

7.2 Results and discussion

Biomineralization often proceeds through metastable precursors,[73] which may enable compositions and structures not accessible through classical crystal formation mechanisms.[9] Perhaps the most widely characterized is amorphous calcium carbonate (ACC), a precursor to all three crystalline polymorphs of $CaCO_3$ both in vivo and in vitro.[31,96] Despite its prevalence, many questions remain about the crystallization of ACC under ambient conditions.[74-76,88,97] Direct observation and quantification of the kinetics of ACC crystallization will contribute greatly to our understanding of this process, and lay the groundwork for investigating conditions replicating those found in nature.

Synthetic ACC is typically a transient intermediate in bulk solution, crystallizing within minutes.[98] It is much more persistent in confinement, even in the absence of stabilizing additives.[46,53,82,83] Small volumes decrease the impact of the presence of heterogeneous nucleators that cause spurious nucleation.[39] Once ACC has formed, high barriers to nucleation of a crystal kinetically trap it in a metastable state.[44,99]

In bulk solution, crystallization kinetics of ACC to calcite via vaterite have been characterized,[98,100] but the effects of nucleation are difficult to separate from those of growth. *In situ* TEM observations of crystallization from individual ACC particles indicate that many crystallization pathways may exist.[4] However, these measurements are sensitive to imaging conditions and cannot establish the relative rates at which these processes might occur. Droplet based microfluidics is ideally situated to probe individual crystallization events in real time for quantitative kinetic information. Nucleation rates of ice, pharmaceuticals, proteins, and potassium nitrate have been investigated this way using ensembles of monodisperse aqueous droplets.[19,54]

We used a hydrodynamic flow-focusing microfluidic device made of polydimethylsiloxane (PDMS) to produce aqueous droplets in fluorocarbon oil (HFE7500) containing 2% (w/w) triblock copolymer surfactant (RAN Biotechnologies).[101] The surfactant consists of two perfluoropolyether (PFPE) tails separated by a polyethyleneglycol (PEG) head group. Droplets of concentrated aqueous calcium chloride (1 M) had low polydispersity and were stable for >7 days. However, colloidal stability was lost upon precipitation of $CaCO_3$ (not shown). We therefore developed a 'droplet orchard' storage device (Figure 7.1) in which droplets could be separated prior to the initiation of precipitation and observed over extended periods of time.

The flow rate at which droplets are produced in the flow focusing device (~300 μL/hour) was far too fast for loading the droplet orchard (~5 μL/hour), so the two were

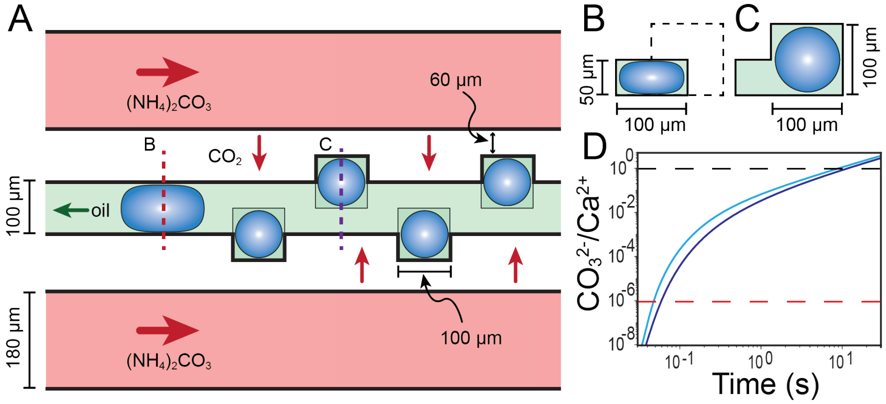

Figure 7.1. Schematic representation of the storage device with aqueous droplets parked in wells along the oil channel, flanked by parallel channels which deliver aqueous $(NH_4)_2CO_3$. Droplets are compressed in the channel (B) and relax to a spherical shape in wells (C). (D) Simulated ratio of delivered carbon dioxide to the amount of encapsulated calcium (CO_2/Ca^{2+}) versus time in droplets in conditions of perfect oil mixing (light blue) and no oil mixing (dark blue). Dashed lines indicate the ACC solubility product (red) and where $CO_2/Ca^{2+} = 1$.

decoupled. Droplets produced in the flow-focusing device were captured in Teflon™ tubing, detached, and reattached to the droplet orchard (Figure 7.1). It consists of cubic wells (edge length 100 µm) connected to a channel with rectangular cross section (100 µm width, 50 µm height). Droplets with 100 µm diameter are compressed channel (Figure 7.1**b**), and can reduce their interfacial energy by entering a well (Figure 7.1c). In combination with buoyant forces resulting from the lower density of the aqueous solution (ρ= 1.09 g cm^{-3}) compared to that of the oil (ρ= 1.6 g cm^{-3}), droplets become trapped in the wells.

Precipitation was induced via flowing aqueous ammonium carbonate in two channels (180 µm width, 50 µm height) flanking the central storage channel (Figure 7.1a). Ammonium carbonate (1.5 M) is a source of gaseous carbon dioxide and ammonia, which diffuse through PDMS and the oil and into the droplets, where they re-establish aqueous equilibria. Chemical kinetics of carbon dioxide equilibration to HCO_3^- and CO_3^{2-} are rapid, on the order of seconds or less.[102]

Gas diffusion across the device was modelled by finite-element analysis (Figure 7.1D). Upper and lower bounds for the gas transport rate were approximated by the limiting cases of either perfect mixing or no mixing (purely diffusive transport), in the oil phase. Simulations predict that in the case of slowest (completely diffusive) transport, the ratio of delivered carbon dioxide to the amount of encapsulated calcium reaches an amount sufficient to supersaturate the solution with respect to ACC within 50 milliseconds, and reaches unity within 10 s (Figure 7.1D). This confirms that gas transport in the device is comparable to the timescale of chemical equilibrium.

Many particles appeared simultaneously throughout the volume of each droplet within five minutes of the initiation of $(NH_4)_2CO_3$ flow (Figure 7.2A). Particles grew over the course of ~30 minutes and sank to the bottom of droplets (Figure 7.2B). This was confirmed by confocal fluorescence microscopy in the presence of calcein, which is occluded

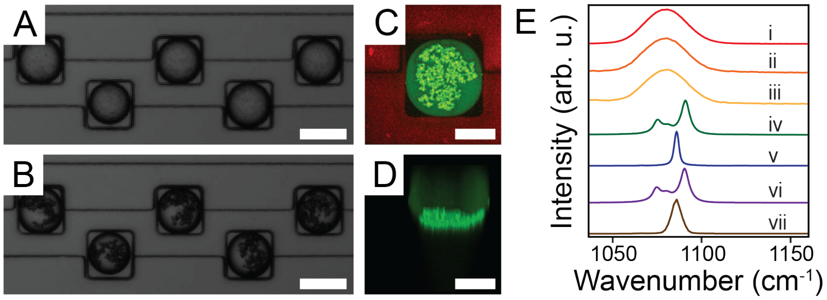

Figure 7.2. Droplet-confined precipitates. (A-B) Polarized light microscopy of parked droplets loaded with 1 M $CaCl_2$ (A) 5 minutes and (B) 25 minutes after starting flow of 1.5 M $(NH_4)_2CO_3$. Scale bar represents 100 µm. (C) Top-view and (D) side-view of a 3D reconstruction from confocal fluorescence microscopy showing aggregated particles at the bottom of a droplet after approximately 30 minutes in the presence of 30 µM calcein, and 40 µM rhodamine B. Scale bar represents 50 µm. (E) Confocal Raman spectroscopy of (i) bulk

synthetic ACC, (ii) ACC in a liposome, (iii) mineral in a droplet after 30 minutes, (iv) polycrystalline mineral (v) single-crystalline mineral, bulk (vi) vaterite and (vii) calcite powders.

in the mineral,[34] and rhodamine B, which segregates to the PDMS (Figure 7.2C,D).

We confirmed that precipitates were ACC using confocal Raman microspectroscopy (Figure 7.2E). Specifically, the center of the most intense carbonate ν_1 mode appeared at 1080 cm^{-1} with a full width at half maximum of 19 cm^{-1} and was indistinguishable from bulk ACC powder and ACC stabilized in liposomes.[44]

Growth of ACC particles slowed after ~30 minutes. This suggests that supersaturation with respect to ACC was reduced to nearly zero. Under these conditions, particles may still increase in size through coarsening, but the total volume of ACC remains constant. ACC is then in metastable equilibrium with the encapsulated solution, and the supersaturation with respect to the more stable polymorphs of calcium carbonate, vaterite, aragonite, and calcite is fixed by ACC solubility.

We followed the transformation of ACC to crystalline calcium carbonate by time-lapse polarized light microscopy. Non-birefringent ACC is easily distinguished from the birefringent crystalline polymorphs of $CaCO_3$. Onset of crystallization was detected by a strong increase in brightness, consistent with the formation of birefringent material (Figure 7.3). Birefringent particles grew over the course of up to an hour through the re-precipitation of dissolving ACC. Most were aggregates of 10-20 μm spherical particles, while a small percentage (~14%) exhibited sharp, crystalline facets reminiscent of calcite. Raman spectra of the former were consistent with vaterite, while those recorded on the latter were confirmed to be calcite. Vaterite particles were polycrystalline, confirmed from the rotation of drops caused by minor pressure fluctuations in the oil channel, while calcite particles extinguished birefringence upon rotation, indicating that they were single crystals.

Crystals were typically 5 – 10 μm wide at first detection (Figure 7.3B), and were thus detected at some time after nucleation. An analysis of the size of birefringent particles in subsequent frames revealed that the radius initially increased approximately as the square root of time. Extrapolating to radii on the order of one nanometer, we estimate that the time between nucleation and growth to a detectable size is below one minute. Uncertainty in determining the time of nucleation is therefore on the order of the frame rate (0.2 min^{-1}).

In a system of identically supersaturated droplets, the cumulative probability, $P_o(t)$ that nucleation in a volume V has not occurred at a time t is given by:[59]

$$P_0(t) = e^{-J\cdot V\cdot t} \cong N_0/N \tag{7.1}$$

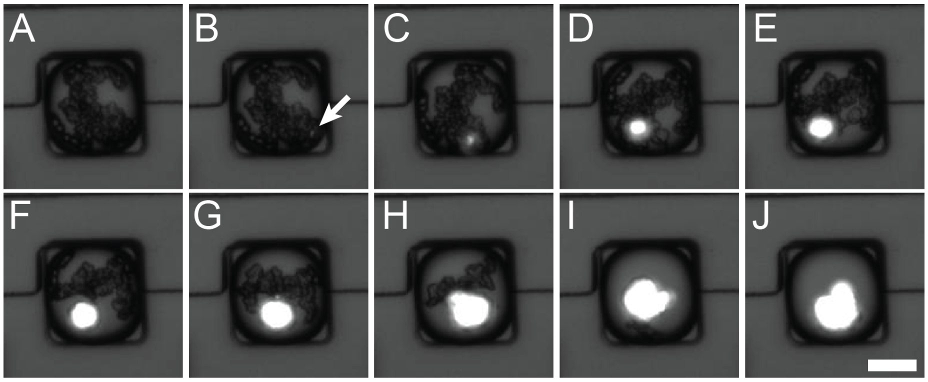

Figure 7.3. Polarized light microscopy of a parked droplet containing ACC at (A) t = 14 hours and 20 minutes after starting flow of 1.5 M $(NH_4)_2CO_3$ and (B-J) at 5 minute increments until growth of a birefringent crystal consumes all ACC in the droplet. An arrow points to the crystal at first detection in the image captured at t = 14 hours and 25 minutes. Scale bar represents 50 μm.

where N_0 is the number of droplets which do not contain crystals and N is the total number of droplets. From Equation 1, the natural log of N_0/N plotted against time is equal to -$J \cdot V$. The droplet volume is known and constant, so J can be calculated directly.

Nucleation events were relatively rare, with an average of 14% of droplets showing birefringence after 52h. Extracting the time at which nucleation events occurred in four independent experiments with 99, 97, 95, and 53 (average 86) droplets, we determined the fraction of droplets without nucleation events, N_0/N over time. Significant variability between individual experiments is evident (Figure 7.4A), but under the assumption that the conditions were identical in each experiment, all four trails can be combined and analyzed in aggregate.[26] Linear regression with a high coefficient of determination (R^2 = 0.985) indicates that the nucleation rate is J = 1.67 cm^{-3} s^{-1} and is constant over the first 52 hours (Figure 7.4B).

Monte Carlo simulations were performed to investigate the expected variation between the four individual experiments simply from the inherent randomness in finite sample sizes. Crystallization in each droplet was treated as a random process, with a probability that crystallization did not occur at each time step Δt equal to $P_0(\Delta t)$. For each droplet that did not contain a crystal, a pseudorandom number n; $0 < n < 1$ was generated to determine whether a crystal did ($n > P_0(\Delta t)$) or did not ($n \le P_0(\Delta t)$) nucleate.

Droplets were removed from consideration after crystallization had occurred. Each simulation was carried out over 52 hours in time steps of 5 minutes, and this was repeated 10^6 times.

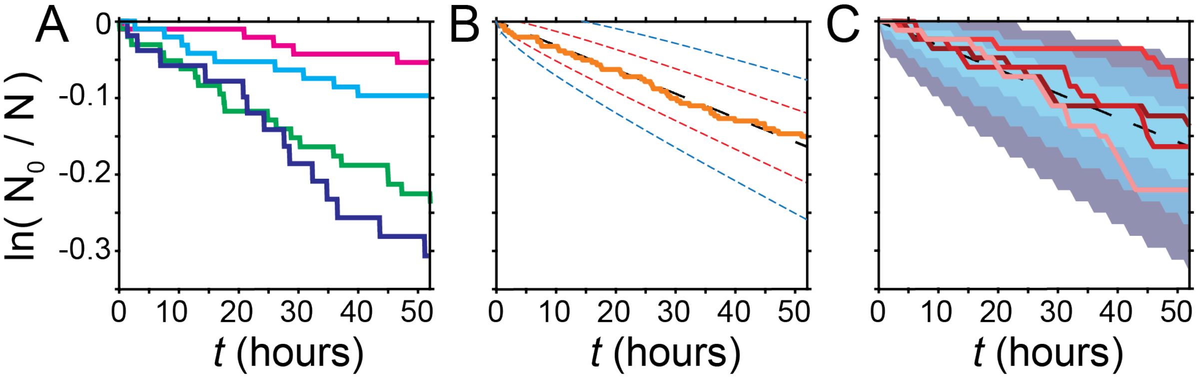

Figure 7.4. Plot of the natural log of N_0/N versus t. (A) Four independent droplet experiments. (B) Sum of all 344 droplets from (A) (orange), linear fit to the data (black, dashed) 2σ confidence interval (~95% of experiments) from the mean of a binomial distribution centered around the regression for 86 trials (blue, dashed) and 344 trials (red, dashed). (C) Four Monte Carlo simulations of 86-droplet nucleation experiments (shades of red). In (C), blue regions denote N_0/N for 68, 95, and 99.7% of 10^6 86-droplet Monte Carlo simulations with time step $\Delta t = 1$ hour and $P_0(\Delta t) = 0.9969$.

Simulations show that the variability observed between experiments fits within the bounds of the 3σ (99.7%) confidence interval of a large number of 86-droplet Monte Carlo trials (Figure 7.4C). This confirms that small samples can deviate considerably from the actual rate, and highlights the importance of using large ensembles of droplets. The 99.7% confidence interval for N_0/N at 52 hours is $3\sigma = 0.06$.

While experimental effects, like differences in impurities across experiments, may also contribute to the variability between the four experiments, replication of the observed scatter in simulated trials indicates that the dominant effect is the randomness inherent in nucleation. It should be noted that the exact location of nucleation could not be determined; it could occur homogeneously in solution, or heterogeneously on or within

ACC or at the interface between ACC and the surfactant. Our results do not distinguish between these possibilities. However, they do clearly indicate that ACC is *not* a good nucleator for crystalline $CaCO_3$.

This is somewhat counterintuitive, as ACC is often observed to transform to vaterite within minutes.[98] In droplets, eliminating diffusion of at least one building block (Ca^{2+} in this case) ensures that each nucleation event is independent and that each drop *must* contain at least one nucleation event for crystallization to occur. Because at most one nucleation event is observed per drop, dissolution of ACC and growth of vaterite must be much more rapid than nucleation. In contrast to the bulk solutions in which this process is often examined, division of the total precipitate into many droplets therefore reduces the amount of material that transforms through growth.

ACC crystallization is consistent with a classical mechanism, in which a single, constant barrier lies between amorphous and crystalline states. According to classical nucleation theory, the critical work necessary to form a nucleus, W^*, sets the nucleation rate via the expression

$$J = Ae^{-\frac{W^*}{k_B T}} \tag{7.2}$$

where A depends on the geometry and physical properties (e.g., density) of the system and k_B is the Boltzmann constant. Using a typical value for A,[103] the barrier height for the crystallization of ACC to vaterite is $W^* = 78\ k_B T$ (203 kJ/mol). This is a considerable barrier, greater than those presented by self-assembled monolayers or polysaccharide surfaces.[22,23,36] This may shed light on the role of ACC in, e.g., the endoskeletal spicule of the sea urchin embryo, which forms via a single nucleation event but grows through the addition of ACC. Low nucleation rates from ACC may also help explain why ACC is commonly observed *in vitro*, while amorphous strontium carbonate crystallizes within minutes, and amorphous barium carbonate crystallizes within seconds, even in confinement (chapter 12).

The nucleation barrier is a function of the supersaturation, σ, and the net interfacial energy, γ_{net}, according to

$$W^* = \frac{F V_m^2 \gamma_{net}^3}{k_b T \sigma^2} \tag{7.3}$$

where F reflects the shape of the nucleus and V_m. Given that the supersaturation in solution is fixed at the solubility limit of ACC, Equation 7.3 can be used to calculate γ_{net}. This approach has been used to determine the interfacial energy of many insoluble solids precipitated in aqueous solution.

Because ACC is a poor nucleator for vaterite, we expect the contact angle between a vaterite nucleus and the ACC surface to be large, and we approximate the nucleus shape as a sphere. While the solubility of ACC in the droplets is not known, for ACC solubilities reported in the literature, we estimate γ_{net} = 42, 47, 100, or 115 mJ/m^2.[80,94,95] If the nucleus were instead a hemispherical cap with a contact angle of 90°, these values would increase by 26%. Calcite was only observed in a small fraction of the total drops, and given that it has not been observed to form directly from ACC[4] likely forms via vaterite. However, using the solubility limit of calcite instead of vaterite yields γ_{net} = 75-140 mJ/m^2. This range of (hypothetical) ACC-calcite interfacial energies is conspicuously similar to previous estimates for the interfacial energy of calcite in aqueous solution (64-109 mJ/m^2),[25,104] The formation of a 'gel', now widely understood to be ACC, and vaterite precursors are reported to precede calcite in the experiments that calculate these values.[103] The exact value for γ_{net} in this study is difficult to determine exactly due to its dependence on the unknown nucleus shape and solubility limit of ACC in droplets. However, interfacial energies for calcite are an order of magnitude higher in experiments and simulations not sensitive to the formation of precursors,[25,104] suggesting that the true interfacial energy of calcite is much higher than 109 mJ/m^2.

Droplet microfluidics presents a powerful approach for quantifying the nucleation of crystalline $CaCO_3$. Controlled delivery of ammonium carbonate to hundreds of separated droplets permits parallel execution of many crystallization experiments. Confinement to ~500 pL in volume delays nucleation of crystalline $CaCO_3$ compared to precipitation in bulk due to the larger volume of material that must transform via nucleation instead of growth. The resulting high kinetic barriers to calcite and vaterite prolongs the lifetime of ACC such that the transformation from amorphous precursor to crystalline mineral is well-defined and occurs on a perceivable timescale. While the location of the crystal at nucleation was below the limit of resolution in this study, the nucleation rate fits a model grounded in classical nucleation theory. With facile methods for detecting crystals and identifying polymorphs, the device presented in this study holds promise for quantifying the impact of additives relevant to biomineralization, including proteins and Mg^{2+} ions, on the crystallization of $CaCO_3$ from solution containing ACC.

8. Effects of biomineralization proteins on ACC crystallization

8.1 Introduction

Biominerals are composites that exhibit enhanced properties due to the hierarchical interplay between organic and inorganic components.[105] Despite our best efforts to replicate such structures, even the state of the art in current materials processing bears only nominal resemblance to biominerals.[106] Our inability to replicate the nanoscale control orchestrated by biomineralization proteins is the most significant shortcoming. Even relatively simple organisms, like sea urchins, have hundreds of proteins that are associated with biominerals, and these may differ by location, even for parts made from the same mineral.[107,108] The function of very few of them are known.[109] Some may be active participants in the mineralization process while others may be kinetically incorporated during growth while performing other functions.

In vitro crystallization assays are popular investigative tools to study the influence of individual proteins on the process of crystallization. [110-113] These studies enable the effect of a single protein on crystal polymorph, shape, and texture to be investigated, often with dramatic results.[114] However, the inability to distinguish between effects on nucleation and those on growth from bulk *in vitro* studies make comparisons to *in vivo* mineralization challenging. Typically, qualitative differences in crystal shape, size, or quantity are reported. In addition, these studies often require relatively large volumes of protein, which can be cost prohibitive. We believe that the microfluidic system described in chapter 7 is ideally suited to address these shortcomings.

8.2 Proteins as nucleation accelerants

Proteins occluded within the Aristotle's lantern of two species of sea urchin, *Litechinus pictus* and *Strongelocentrotus purpuratus*, were investigated for their effects on the crystallization rate of ACC. The lantern is, like all other skeletal elements of the sea urchin, made of $CaCO_3$ and is located inside the test. It is the structural support for the teeth as part of the chewing organ. The lantern was chosen because it is large enough to provide ample quantities of proteins, and because it is the only skeletal element of *S. purpuratus* on which a proteomic analysis has not been performed. Over the course of the investigation we intend to analyze the proteome of the lantern and isolate proteins from the raw extract that appear to have the most significant effect on mineralization. Experimental details of the protein extraction will be reported in a future manuscript.

Protein extracts with 1 mg/mL concentrations in either Tris buffer (pH 7.4) or water (pH 5.5) were combined with 2 M calcium chloride (pH 6.5) in the flow-focusing emulsion droplet synthesis devices described in chapter 7 for a final protein concentration of 0.5 mg/mL and calcium concentration of 1 M. A control solution of bovine serum albumin (BSA), a 66.5 kDa protein that remains soluble in solutions with elevated levels of calcium, was prepared at the same concentration 1 mg/mL. Droplets were loaded into storage devices and precipitation was initiated with flowing 1.5 M ammonium carbonate in the flanking channels. Preparation and characterization were carried out following the same procedure as those in chapter 7. Each condition was repeated at least three times to ensure replicability.

ACC precipitated in each drop, and was indistinguishable from ACC formed in the absence of additives in polarized light microscopy and Raman spectra (not shown). A plot comparing N_0/N for the crystallization of ACC in the presence of BSA, *L. pictus* extract, or *S. purpuratus* extract confirm that proteins dramatically accelerate crystallization compared to ACC without additives (Figure 8.1a). ACC in the presence of *S. purpuratus* extract crystallized within one hour. With *L. pictus* extract, crystallization took nearly twice as long, but was complete in less than two hours. Surprisingly, BSA also accelerated crystallization, with over half of the drops containing crystals by 10 hours. For comparison, less than 4% of all ACC without additives had crystallized by this time.

Droplets containing sea urchin protein extract crystallized so rapidly that the same theoretical treatment applied to droplets without additives in chapter 7 could not be used here. Specifically, the supersaturation in the drops takes approximately 30 minutes to stabilize at the solubility limit of ACC once its growth slows (chapter 7). Crystallization before ACC was had finished growing would likely originate from conditions where the supersaturation was not constant, and would probably be higher than that in equilibrium with ACC. This is consistent with the dramatic increase in the crystallization rate. Nonetheless, it is clear that proteins from both species have an incredible effect on the nucleation rate.

Applying Equation 7.1 to the BSA curve yields a crystallization rate of 48.0 cm^{-3} s^{-1} (R^2 = 0.986). BSA therefore accelerates crystallization by over 28x the rate without additives. While this is a dramatic effect, the exponential dependence of nucleation rate on the cube of the interfacial energy (Equation 1.3) means that all else being equal, this increase may be the result of <2% decrease in γ. From these results, we cannot determine exactly what the mechanism of this acceleration is. It may become occluded within the ACC and change the thermodynamic stability, simultaneously altering the ion concentrations in solution. However, proteins *must* be in contact with the interface between ACC and solution, and given that the interfacial energy is the dominant parameter controlling the nucleation rate, future investigations should begin by exploring interfacial effects further.

Interestingly, the Tris buffer initially used to dissolve the proteins was found to have a similar accelerating effect on the crystallization of ACC to that of BSA, even when no proteins were present. Figure 8.1b shows that Tris and BSA reached nearly the same value of N_0/N after 10 hours. This is a surprising but important discovery. Buffer conditions are generally not considered to have an active role in *in vitro* crystallization assays, and vary widely from study to study. [110-113] Despite the active role of the buffer, if the protein has a much more dramatic effect, as it does in the case of *L. pictus* (Figure 8.1b), buffer conditions do not significantly impact the resulting crystallization rate. The sensitivity of these measurements to such subtle effects and ability to quantify the resulting rates will greatly enhance our ability to determine the effects of various proteins *in vitro*.

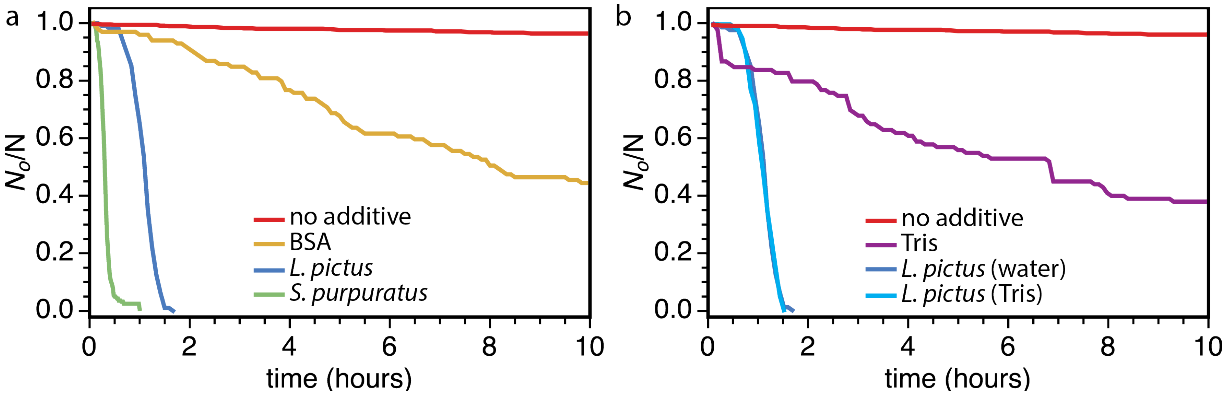

Figure 8.1. Plot of N_o/N for the crystallization of ACC in the presence of (a) three protein solutions, compared to the control with no additives, and (b) the effect of the Tris buffer solution.

8.3 **Outlook**

Surprisingly, the crystallization products in each case were overwhelmingly vaterite, as confirmed by Raman spectroscopy (not shown). Given that the proteins were extracted from calcite biominerals, we expected that at least some enhancement in the fraction of calcite would be observed. That this was not the case reinforces the need to develop a better understanding of the composition of the protein extract and the role of individual proteins, both *in vitro* and *in vivo*. For example, conventional wisdom asserts that acidic proteins are largely responsible chelating calcium and directing crystallization.[115] However, the most abundant acidic proteins in sea urchin biominerals (SM30 family) can be reduced to extremely low levels with no change in phenotype, while abundant basic proteins (SM50 family) appear to play an integral role. [116]

The sensitivity of our microfluidic devices to crystallization rate and polymorph make them a promising platform to explore the role of biomineralization proteins further. Future work will focus on fractioning the raw extract from the lantern by molecular weight and charge, to determine if there are any obvious differences between fractions. Proteomic analysis will be used to identify all proteins in any fraction with dramatic effects on crystallization. To conclude, we will investigate the effects of purified SM30 and SM50 proteins individually.

9. Structural basis for metastability in amorphous calcium barium carbonate (ACBC)

9.1 Abstract

Metastable amorphous precursors are emerging as valuable intermediates for the synthesis of materials with compositions and structures far from equilibrium. Recently, we found that bio-inspired amorphous calcium-barium carbonate (ACBC) enables the synthesis of highly barium-substituted 'balcite', a metastable high temperature modification of calcite with exceptional hardness. Herein, we present a systematic analysis ACBC ($Ca_{1-x}Ba_xCO_3 \cdot 1.2H_2O$) over a wide range of compositions, using a combination of experiments and MD/DFT simulations. There appears to be only a minor energetic penalty associated with the incorporation of barium, likely because barium ions prove to be much more flexible in their coordination than calcium ions. Furthermore, the water content is not correlated with the level of barium substitution. However, ACBC local order continuously evolves towards that of balcite with increasing barium content, and mid-range order similar to balcite begins to emerge at a composition that approaches the limit of ACBC stability ($x > 0.5$). We further find that ACBC transforms into balcite much more readily at high barium content in an aqueous environment. Taken together, this provides support for the hypothesis that it is the increasing structural complementarity between ACBC and balcite that selectively lowers the barrier to balcite nucleation.

9.2 Introduction

Carbonate mineralization is at the heart of many natural processes, including biomineralization and geological inorganic carbon cycling.[104] Crystalline carbonates are often preceded by amorphous precursors[73] that can have a strong influence on phase transformations and the structure and properties of the resulting crystals.[10] For example, it has been suggested that ACC occurs in several polyamorphs, which transform preferentially into the crystalline polymorph with the closest similarity in short range order.[117-120] Similarly, balcite, a metastable, barium-substituted analog of high-temperature calcite with very high hardness, seems to be accessible only through an amorphous calcium-barium carbonate (ACBC) precursor with similar short range order.[121] Local order 'imprinted' in the precursor is implicated in polymorph selectivity of subsequent phase transformations in these systems. Analogously, the local order of amorphous copper zinc carbonates is imprinted in Cu-Zn-oxide catalysts synthesized from them, which greatly enhances catalytic activity and lifetime compared to crystalline precursors.[122] Thus, local order established in diverse amorphous carbonate precursor phases may be utilized to access compositions and structures that are difficult to synthesize directly.[123] As polyamorphism is a common phenomenon in, for example, glasses of silica, ice, and metals, a deeper understanding of the interdependence of composition, structure, energetics, and crystallization pathways in (poly)amorphous structures is clearly needed.[124-126]

A significant factor affecting the lifetime of amorphous carbonates appears to be the ionic radius of the cation. While those with cations smaller than Ca^{2+}, including Mg^{2+},

Fe^{2+}, and Mn^{2+}, have been synthesized as bulk powders,[24,122,127-130] those of larger cations, such as Sr^{2+} and Ba^{2+}, have not been observed in the absence of stabilizing additives[93,131,132] or in confinement[48] (with the notable exception of amorphous $RaCO_3$)[133]. Structural water is thought to play an important role in controlling life time and phase transformation rates of amorphous carbonates.[88,134,135] However, the impact of chemical composition or water content on amorphous carbonate structure remains poorly understood. To move towards a predictive theory of crystallization that accounts for metastable intermediates, it is therefore critical to elucidate the structural characteristics with the strongest influence over transformation rates in amorphous materials.[63]

In this work, we describe the synthesis and structure of metastable but long-lived ACBC ($Ca_{1-x}Ba_xCO_3{\cdot}nH_2O$). Using experimental techniques that interrogate the structure from the perspective of the cations (X-ray absorption spectroscopy at both calcium and barium K-edges), the anions (Raman and IR spectroscopy), and all atoms (electron diffraction, X-ray scattering, and pair distribution function analysis), we thoroughly characterize the short- (<5 Å) and mid-range (<15 Å) structure of ACBC. A combined molecular dynamics/density functional theory (MD/DFT) approach was utilized to connect structural motifs to thermodynamic properties. These analyses establish the importance of coordination geometry and carbonate orientation on the thermodynamics of amorphous carbonates, and help elucidate transformation pathways between metastable phases in the relatively unexplored Ca-Ba-CO_3-(H_2O) system.

9.3 **Experimental**

9.3.1 *Consumables*

Unless otherwise noted, all aqueous solutions were prepared using ultra-pure water (ρ = 18.2 MOhm·cm) prepared with a Barnstead NanoDiamond UF + UV purification unit. Reagent grade (>99%) $BaCl_2{\cdot}2H_2O$, $CaCl_2{\cdot}2H_2O$, $Na_2CO_3{\cdot}2H_2O$, $CaCO_3$, $BaCO_3$, (Sigma-Aldrich), $(NH_4)_2CO_3$ (Fischer Scientific) were used without further purification. Iceland spar calcite was obtained from Dave's Down to Earth Rock Shop in Evanston, IL, USA. Geological reference materials witherite (cat #M21424) and barytocalcite (cat #M2145) were provided by the Field Museum of Natural History in Chicago, IL USA.

9.3.2 *ACBC synthesis*

Amorphous calcium barium carbonate (ACBC) was synthesized by rapid mixing of a cold aqueous solution of the alkaline earth chlorides ($[Ca^{2+}]+[Ba^{2+}]$ = 1 M, pH 5.6-5.7, solution A) with a cold aqueous solution of Na_2CO_3 (1 M, pH 11.7, solution B). The mole fraction of Ba, x^{feed}, was varied between 0 and 1. For instance, to prepare solution A with x^{feed} = 0.50, 3.053 g $BaCl_2{\cdot}2H_2O$ (12.5 mmol) and 1.838 g $CaCl_2{\cdot}2H_2O$ (12.5 mmol) were dissolved in water to a final volume of 25 mL. For solution B, 3.100 g Na_2CO_3 (250 mmol) were dissolved in water to a final volume of 25 mL. Both solutions were then stored on ice for 2 h. Ice cold solution B was rapidly added to solution A, and the resulting solution mixed rapidly and thoroughly by vigorous shaking for 30 s. The resulting white precipitate was immediately collected by vacuum filtration through a 100 mm diameter Whatman no. 4 cellulose filter paper, washed 3 times with 5 mL cool water (T = 10°C), and dried under vacuum (R.T., $p \approx 10$ Pa = 10^{-1} Torr, 24h). Unless otherwise noted, characterization was performed immediately thereafter.

9.3.3 *Thermogravimetric analysis*

Thermogravimetric analysis (TGA) and differential thermal analysis (DTA) was performed simultaneously using a Mettler Toledo SDTA851. Analysis was performed on ACBC powders dried in vacuum for exactly 24 hours after synthesis. Approximately 5 mg of the dry powder was held at 30 °C for 10 minutes to stabilize the sample environment, then heated to 1000 °C at a rate of 10 °C/min under dry N_2 flowing at a rate of 20 mL/min. Weight change was tracked by the variable α, defined as

$$\alpha = \frac{w_o - w_i}{w_o} = \frac{\Delta w}{w_o} \tag{9.1}$$

where w_o is the initial weight and w_i is the instantaneous weight. The total fractional weight change, α_T, is the value of α at the final weight, $w_i = w_f$. Total fractional weight loss, Δa_T, is defined as $1\text{-}a_T$. Fractional weight loss upon crystallization, Δa_c, is defined as α_{c1}- α_{c2}, where α_{c1} and α_{c2} are the values of α at temperatures corresponding to either side of the crystallization exotherm peak in differential scanning calorimetry, determined using the StarE v8.1 software package (Mettler Toledo). When multiple crystallization peaks were present, α_{c2} was chosen as the end of the final exothermic event. The molar water content, n, of the powders was calculated from

$$n = \frac{M_{H_2O}/\alpha_T}{(1-x_{Ba})M_{Ca}+x_{Ba}M_{Ba}+M_C+3M_O} \quad (9.2)$$

where M is the molecular mass of the subscripted species, the numerator is the molar fraction of water, the denominator is the molar fraction of $Ca_{1-x}Ba_xCO_3$, and x is the stoichiometric coefficient determined by XRF.

9.3.4 *Differential scanning calorimetry*

Differential scanning calorimetry and TGA were conducted in parallel on separate powder samples drawn from the same batch. Heat flow data in DSC was corroborated by simultaneous DTA (SDTA) performed during TGA runs (Figure 15.1, 9.8) and was in good qualitative agreement. Differential scanning calorimetry was performed on a Mettler Toledo DSC822e using the same approximate sample mass and N_2 flow rate as TGA, with the same heating schedule up to the instrument maximum of 500 °C. The crystallization temperature T_c was calculated from the onset of the crystallization exotherm in DSC curves determined with the StarE v8.1 software package.

9.3.5 *X-ray absorption spectroscopy*

Samples for X-ray absorption spectroscopy were synthesized in the same way as above, with drying times of at least 4 hours under vacuum. Measurements were performed at the Dow-Northwestern-Dupont collaborative access team (DND-CAT), Sector 5-BM-D of the Advanced Photon Source at Argonne National Laboratory. Samples for calcium K-edge measurements were spread on 8 μm Kapton tape and kept dry under a stream of He gas. For measurements performed at the barium K-edge, powders were loaded in quartz capillaries (0.5-1.5 mm outer diameter with 100 μm wall thickness). Larger diameter capillaries (1.5 mm) were used for samples synthesized at lower x (e.g., x = 0.01), while smaller capillaries (0.5 mm) were used at higher x (e.g. x = 0.50). Calibration at the calcium K-edge was performed with a geological Iceland spar (calcite) standard, for which the edge energy was set at 4038 eV. ACBC samples were measured relative to this value. Molybdenum foil (K-edge at 20.000 eV) was used to calibrate the barium K-edge to an absolute scale.

Data was analyzed using the Demeter package.[70] Normalization and background subtraction were carried out in Athena using Autobk. χ-data were weighted by k , k^2, and k^3 between $1.6 < k < 11.5$ Å^{-1} for the calcium K-edge and between $2 < k < 14$ Å^{-1} for the barium K-edge. Fitting of the data to the crystal structures was performed using Artemis. The theoretical photoelectron scatting amplitudes and phase shifts were calculated using FEFF1. To generate the feff.inp file, which contains a list of the atomic coordinates centered at the absorbing atom, Atoms[71] was used to calculate the atomic coordinates centered at calcium. The total theoretical $\chi(k)$ for each model was then constructed from the most important scattering paths and fit in R-space (calcium K-edge) or k-space (barium K-edge). Multiple scattering was not considered in amorphous materials. While maintaining sufficient number of degrees of freedom, as defined by the Nyquist criterion, the coordination number, bond distance, Debye-Waller factor, amplitude reduction factor, S_o^2, and shift in energy origin, ΔE_o were allowed to float. S_o^2 and ΔE_o were determined by simultaneously fitting all ACBC samples at either the calcium or barium K-edges. A total R-factor of 0.007 was obtained for simultaneous fitting of all six data sets for ACBC, with a reduced χ^2 of 558. Satisfactory fits were not obtained using S_o^2 from the crystalline reference samples, which for calcite and witherite were >1. Coordination numbers and Debye-Waller factors are highly correlated and were fit separately, but in each case with all other parameters floating. The validity of the fits was determined by the *R*-factor, which was minimized to ≤0.01. Complete fitting parameters are reported in the Supporting Information.

9.3.6 *X-ray total scattering*

X-ray total scattering was performed at the Dow-Northwestern-Dupont collaborative access team (DND-CAT), Sector 5-BM-D of the Advanced Photon Source at Argonne National Laboratory. The X-ray energy (20.000 keV, λ = 0.6195 Å) was selected with a Si(111) monochromator, and calibrated with a molybdenum foil at the K-edge. Data was collected in Bragg-Brentano geometry with a Huber D8219 diffractometer (2θ = 4-169°). The step size was 0.5° and the dwell time was 10 s. Four Si-drift solid state detectors with multichannel analyzers (MCA, ~250 eV resolution at 20 keV) were used to simultaneously measure elastic scattering, calcium K-edge, and barium L-edge fluorescence. Total fluorescence signal was used for normalization of the elastic scattering. Spectra were also normalized for incident beam intensity measured with an ion chamber ($p\mathrm{N}_2$ = 550 Torr and pAr = 16 Torr). Scattering from the sample holder and Compton scattering were subtracted, and an absorption correction applied based on sample composition using GetPDFx2 software.[67]

9.3.7 *Raman microscopy*

Approximately 5 mg of the dry powder was pressed onto a glass slide for Raman analysis. Raman spectra were obtained on a Horiba LabRam confocal Raman microscope with a laser of wavelength λ = 532 nm, operating at a power of 49 mW, and using a diffraction grating with 1800 gr/mm, resulting in a final spectral resolution of 0.39 cm^{-1}. All spectra were recorded from individual precipitate particles using a 100x objective lens in air (0.9 NA, minimum resolution ~361 nm). Mode centers, relative intensities, and full peak width at half maximal intensity (FWHM) were determined by fitting one or more Gaussians to the spectral region of interest. Fitting was performed manually using in-house code written in Mathematica.

9.3.8 *Fourier transform infrared spectroscopy (FT-IR)*

Immediately following Raman microscopy, ~8 mg of the dry powder was mixed with ~160 mg KBr in a mortar and pestle. Approximately 25 mg of the mixture was then pressed into a pellet at 7 MPa. Bulk FTIR spectra from KBr pellets containing ~5.0 wt% ACBC powder were acquired in the range from 400-4000 cm^{-1} on a Thermo Nicolet Nexuz 870 FT-IR in transmission geometry, with a spectral resolution of 4 cm^{-1}.

9.3.9 *MD/DFT*

Amorphous $CaCO_3$-$BaCO_3$ solid-solution calculations were prepared from supercells of the rhombohedral and orthorhombic carbonate structures. The rhombohedral supercell was constructed from a 2x2x2 primitive Calcite unit cell (16 formula units), the orthorhombic unit cell from a 2x2x1 conventional Aragonite unit cell (16 formula units). The amorphous structure was prepared by annealing the pristine calcium carbonate structures in LAMMPS[136] under NPT conditions at 10,000K, using an empirically-fitted $CaCO_3$ potential.[137] Snapshots of the melt were then quenched and equilibrated at 298 K. Finally, the amorphous unit cell was relaxed in DFT at T = 0 K with full ionic and unit-cell relaxations.

DFT calculations were performed using the Vienna Ab-Initio Software Package (VASP),[138] using the projector augmented wave (PAW)[139] method with the Perdew-Burke-Erzhenhoff (PBE)[140] generalized-gradient approximation. Plane-wave basis cutoff energies were set at 520 eV for all calculations. Brillouin Zones were sampled using Gaussian smearing, with at least 1000 *k*-points per reciprocal atom. Atoms were initially relaxed until energy differences between ionic steps were 1 meV/atom. All structure preparations were performed using the Python Materials Genomic (Pymatgen) package.[141]

These ACBC structural models are not truly amorphous, but are rather periodic approximants, with lattices that satisfy periodic boundary conditions. Periodic approximants all have dimensions of at least 12Å×12Å×12Å, so the long-range interactions of the lattice are only minor contributions to the total energy of the structure, allowing our periodic approximants to be reasonable models for the energetics and local structure of the amorphous $Ca_{1-x}Ba_xCO_3$ phase.

Solid-solution supercells were initialized by substituting Ba^{2+} onto the Ca^{2+} sites, and rescaling the molar volume of the supercell by Vegard's law.[142] A modified Ewald summation was used to bias solid-solutions towards structures with maximized Ba^{2+}-Ba^{2+} interatomic distances under periodic boundary conditions. Total energies of the supercells were calculated in DFT, with full ionic and unit-cell relaxations. Coordination analyses were performed using a weighted Voronoi coordination method,[143] as found in the structure analyzer package of Pymatgen. We used a larger Voronoi cutoff radius for Ba (3.48 Å) than for Ca (3.0 Å). Molar volumes of ACBC were compared to an ideal aragonite-type solid solution, calculated by extrapolation between aragonite and witherite, also using Vegard's law.

Computed radial distribution functions were calculated using a kernel density estimate of the two-specie pair-correlations in the crystal structure under periodic boundary conditions. The radial distributions for each pair of species, $G_{ij}(r)$, were summed to form the pair-distribution function by the equation

$$G(r) = \sum_{i,j} w_{i,j} G_{i,j}(r) \tag{9.3}$$

where the weighting factor w_{ij} depends on the concentration and scattering power f(q) of the atomic species by

$$w_{i,j} = \frac{c_i c_j f_i(q) f_j(q)}{[\sum c_i f_i(q)]^2} \tag{9.4}$$

For this work, w_{ij} was evaluated for $q = 0$.

9.4 **Results**

9.4.1 *Synthesis and stability*

We synthesized ACBC ($Ca_{1-x}Ba_xCO_3 \cdot nH_2O$) over a range of compositions, as described previously.[121] Briefly, ice cold aqueous solutions of alkaline earth chloride(s) with a total cation concentration of 1M were rapidly mixed with equal volumes of ice cold aqueous 1M sodium carbonate. The resulting precipitate was filtered after 30s, washed with water at 10°C, and dried at reduced pressure (50 mbar) at ambient temperature for 24 hours. Approximately 86% of the barium in solution is incorporated into ACBC.[121]

Synchrotron based X-ray total scattering confirmed that the precipitates were amorphous up to $x = 0.55$ (Figure 9.1a). Thermal analysis was conducted immediately following synthesis to determine the amount of residual water and examine crystallization at elevated temperatures. Thermogravimetric analysis (TGA) indicated that ACBC contained, on average, $n = 1.2 \pm 0.2$ formula units of water (Figure 15.1). Similar amounts of water were found using ammonium carbonate instead of sodium carbonate, and at lower ion concentrations (Supporting Information). There was no correlation between the barium cation fraction, x, and total water content. Differential scanning calorimetry (DSC), acquired separately, in good agreement with simultaneous differential thermal analysis (DTA), was used to identify crystallization exotherms (Figure 15.2). The temperature at which a crystallization exotherm first appeared in DTA and DSC increased with increasing barium (Table 15.1). Crystallization of ACBC with x = 0.50 at elevated temperatures produced balcite (Figure 15.3).

9.4.2 *Vibrational spectroscopy*

Raman spectra of ACBC samples with $x \leq 0.55$ were qualitatively similar to those of ACC (Figure 9.1b, Figure 15.4,11, Table 15.2). There were, however, systematic changes in the peak position and full width half maximum (FWHM) of several modes with increasing barium content. Line shapes of the most intense feature in Raman spectra, the ν_1 mode (symmetric carbonate stretch), were broad and Gaussian, in contrast to the narrow Voigt profiles of calcite and witherite. The ν_1 mode shifted to lower wavenumber, i.e. towards its position in witherite, and the full width-half maximum (FWHM) decreased with increasing barium content (Figure 15.5). The much weaker ν_4 mode (in-plane bending,

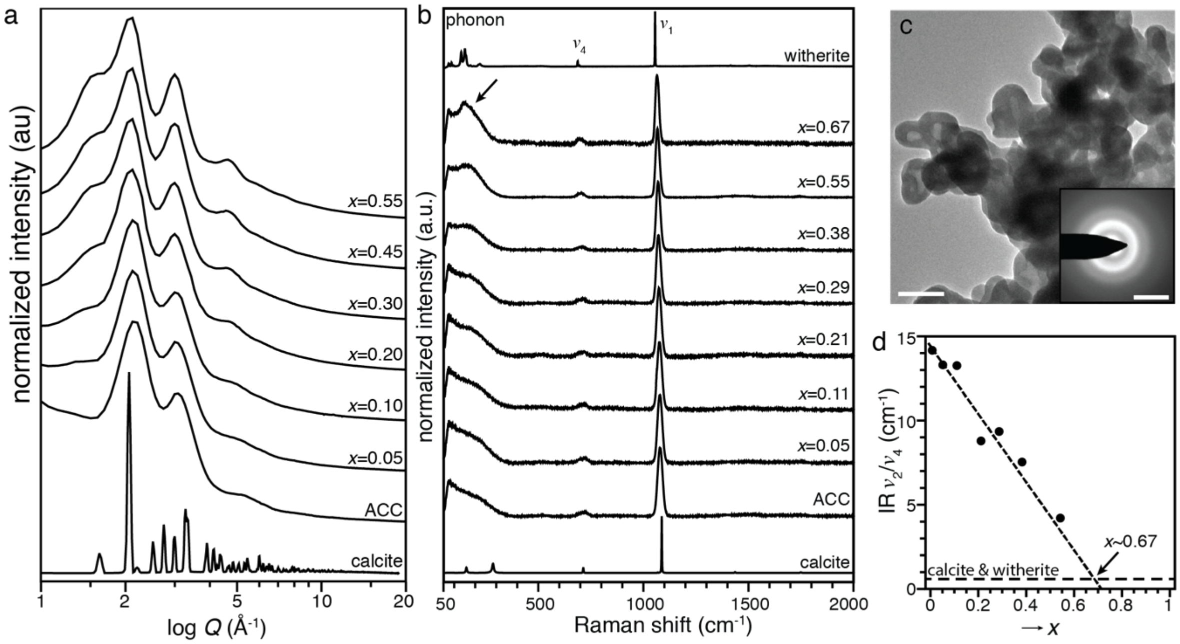

Figure 9.1. Characterization of ACBC precipitates. (a) Synchrotron X-ray total scattering of ACBC compared to ACC and calcite. (b) Raman spectra of ACC, ACBC and reference compounds calcite and witherite, showing the ν_1, ν_4, and lattice phonon regions (arrow). For additional detail see Supporting Figures 4-6. (c) TEM image of ACBC with x = 0.51, with SAED (inset, scale bar 5 nm^{-1}). Scale bar represents 100 nm. (d) Plot of the ratio of intensities of the ν_2 and ν_4 modes in IR spectra vs. the barium cation mole fraction, x.

Figure 15.5) was split in two, and was also considerably broadened compared to crystalline reference materials. Structural water and/or OH groups in both ACC and ACBC were confirmed by a characteristic broad band in the range ~2800-3700 cm^{-1} (O-H stretch) and a very weak, broad band in the range of 1600-1700 cm^{-1} (H-O-H bending, Figure 15.4-9.12). IR spectra contain complementary information, and are discussed in detail the Supporting Information. When ACBC with x = 0.41 was dried under vacuum at elevated temperature (6.67×10^3 Pa, 50°C, 8 hours), the intensity of the O-H band between ~2800-3700 decreased in intensity, and a subtle peak at 2940 cm^{-1} sharpened (Figure 15.5). This is consistent with the partial removal and reorganization of structural water.

A broad feature below 300 cm^{-1}, commonly observed in ACC,[73] was also present in Raman spectra of ACBC. It shifted to lower wavenumbers with increasing barium content, increased in intensity, and sharpened, forming a broad but discernable peak centered at 145 cm^{-1} at x = 0.67 (Figure 9.1b). This peak coincided with the strongest acoustic phonon modes in witherite. Other witherite modes, especially the most intense ν_1 at 1059 cm^{-1}, were absent. Drying ACBC with x = 0.41 at slightly elevated temperature and reduced pressure, as described above, in did not impact the intensity of shape of this feature. It is therefore unlikely to be connected to structural water.

In addition to the behavior of individual modes, ratios of the intensity of IR internal mode peaks provide information about ordering in both amorphous and crystalline calcium carbonates.[96,118,144] In ACBC, the ν_2/ν_4 ratio decreased with increasing barium cation fraction, from 13.9 in ACC at x = 0, to 4.4 at x = 0.55 (Figure 9.1d), but remained higher than that of calcite (1.2) and witherite (1.0).

9.4.3 *Modeling*

Structural models for the ACBC phases were prepared using a combined molecular dynamics (MD) and density functional theory (DFT) approach. Supercells of 2x2x2 standard unit cells of calcite or aragonite were annealed using molecular dynamics at 10,000 K under NVT conditions (conservation of the number of ions, volume and temperature), with an empirically-fitted $CaCO_3$ potential.[137] Snapshots of the melt were gradually equilibrated to 298 K using MD, then fully relaxed using DFT (Figure 9.2 and Figure 15.7). This process was repeated to generate six different ACC structures. We calculate the difference in enthalpies between the lowest-energy anhydrous ACC structures and calcite to be ΔH = 19-25 kJ/mol (Figure 9.2), in excellent agreement with experimental calorimetry measurements of ACC.[128,134] The aqueous solubility for the lowest enthalpy ACC (described in detail in the Supporting Information) estimated only from ΔH is $K_{\mathrm{sp,ACC}}=10^{-5.3}$ M^2. The difference between the calculated K_{sp} from the experimentally measured $K_{\mathrm{sp,ACC}}\sim 10^{-6.04} - 10^{-7.5}$ M^2 (refs[27,94,95]) allows us to estimate a standard entropy of formation of ACC of approximately 21-40 $J{\cdot}mol^{-1}{\cdot}K^{-1}$.

ACBC was created by substituting Ba^{2+} for Ca^{2+} into ACC prior to the DFT-relaxation, giving an overall composition of $Ca_xBa_{1-x}CO_3$ in increments of Δx = 0.0625.

Structurally, DFT relaxation coincided with a marked increase in carbonate ordering. Specifically, the vector normal to the plane containing the three carbonate oxygens was essentially randomly oriented in space in MD-generated structures, while those in DFT-relaxed ACBC were mostly within approximately 20 degrees of one another (Figure 15.9).

For all structures and across all compositions, the formation enthalpy Δ*H* was determined as the difference in enthalpy between ACBC and a phase-separated mixture of calcite ($CaCO_3$) and witherite ($BaCO_3$) at an equivalent overall composition. Solubility products for ACBC were determined in the same manner as those of ACC. The difference in molar volume, ΔV_m, between the V_m of the simulated structure and an ideal, aragonite/witherite-type $Ca_{1-x}Ba_xCO_3$ solid solution were calculated for each structure. Aragonite structure was chosen because it is the densest crystalline polymorph of $CaCO_3$, and

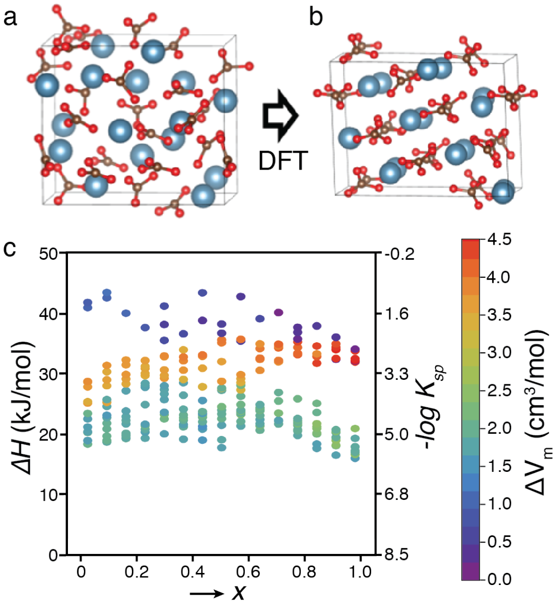

Figure 9.2. Example structures of (a) MD generated and (b) DFT-relaxed ACC. (b) Plot of ΔH (left axis) and negative logarithm of the predicted solubility product (right axis) of DFT-relaxed ACBC structures against

barium fraction x. Each marker corresponds to a fully relaxed structure; the marker color indicates the difference in molar volume (ΔV_m, cm^3/mol) between the amorphous structure and an ideal orthorhombic-type $Ca_{(1-x)}Ba_xCO_3$ solid solution of the same composition. Note that structures fall into three horizontal bands with similar molar volume change (color).

because calcite-type $BaCO_3$ has not been observed. In summary, ΔH tells us how much heat would be released by the transformation from ACBC to a mixture of pure calcite and witherite, and ΔV_m is the amount by which the molar volume decreases (density increases) if ACBC were to transform into a hypothetical aragonite structure with the same composition.

Inspection of a plot of ΔH and ΔV_m against the barium content (Figure 9.2c) revealed that the simulated ACBC structures fall into three distinct groups. While the lowest energy structures had an intermediate molar volume difference (ΔH = 19-25 $kJ\cdot mol^{-1}$, $1.0 < \Delta V_m < 3.0$ $cm^3\cdot mol^{-1}$), the highest energy structures had molar volume differences at the low end (ΔH = 40 kJ/mol, $\Delta V_m \cong 0.5$ cm^3/mol), and the intermediate energy structures had molar volume differences at the high end (ΔH = 30-35 $kJ\cdot mol^{-1}$, $\Delta V_m > 3.0$ $cm^3\cdot mol^{-1}$). Therefore, at any given composition the structures with the lowest energy do not have the highest density. This is also true for crystalline $CaCO_3$, emphasizing the importance of determining ΔH for benchmarking the simulations. In addition, the three groups could be distinguished by their average cation coordination number (Figure 15.10), calculated by a Voronoi polyhedron method.[143] Strikingly, the structures with intermediate ΔH had the lowest average coordination number at any given composition. The low energy and high energy groups had similar average CNs. In all groups, the average CN increased with increasing barium content.

Given the stratification observed in the simulated structures, it made sense to consider the structures with low ΔH, consistent with literature values, and intermediate ΔV_m as representative of the lowest energy polyamorph. This allowed us to take a closer look at the distribution of the coordination numbers (CNs) for calcium and barium at each composition (Figure 9.3). The calcium CN decreased from 7.7 ± 0.7 ($N = 64$) at $x = 0$ to 7.1 ± 0.7 ($N = 64$) at $x = 0.5$, and remained at this value for higher barium contents. Unlike in reverse Monte Carlo fitting of experimental PDF data from ACC, where CNs as low as 3 were predicted,[145] we found that calcium appeared at least 5-fold, but mostly 6-fold and higher coordinated. The barium CN also decreased, from 9.8 ± 0.7 ($N = 9$) to 9.1 ± 0.8 ($N = 64$), and outside the experimentally investigated range, declined further to 8.3 ± 0.4 at $x = 1$ (N = 80). Even though the CNs for both cations individually decreased, the average CNs increased, from 7.7 ± 0.7 ($N = 64$) at $x = 0$ to 8.1 ± 1.3 ($N = 128$) at $x = 0.5$ and 8.3 ± 0.4 ($N = 80$) at $x = 1$, as the barium content increased (not shown).

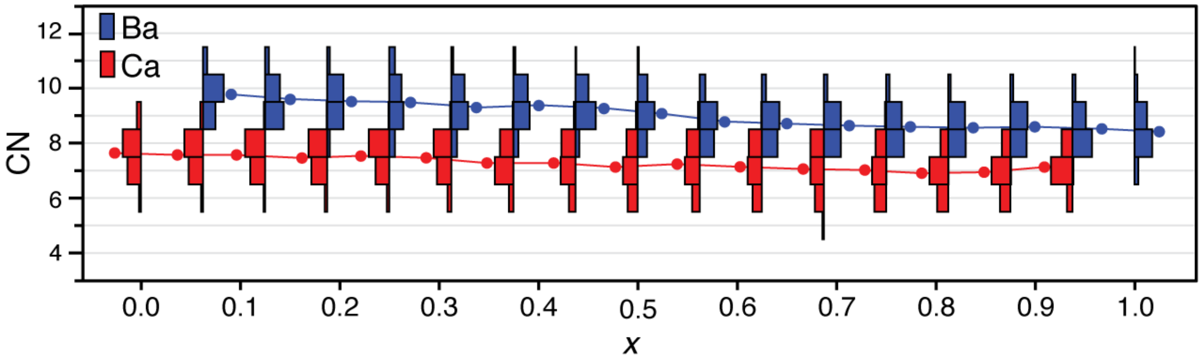

Figure 9.3. Histograms of the frequency at which coordination numbers for calcium ions (red bars) and barium ions (blue bars) occur in the lowest energy ACBC polyamorph (i.e., MD/DFT-simulated structures with

$\Delta H = 19\text{-}25\ \mathrm{kJ{\cdot}mol^{-1}}$ and $1.0 < \Delta V_m < 3.0\ \mathrm{cm^3{\cdot}mol^{-1}}$), as a function of barium content. The mean CN at each composition is indicated by a full circle and connected by lines as a guide to the eye.

9.4.4 *X-Ray absorption spectroscopy*

X-ray absorption spectra provide information about the symmetry in the first coordination shell of the probed cation, including average coordination number, lengths and average disorder of bonds, as well as order beyond the first coordination shell. X-ray absorption near-edge structure (XANES) spectra at the calcium K-edge exhibit a number of identifying features, including the sharp absorption edge, pre-edge peaks, white line peak above the edge, and post-edge oscillations (Figure 9.4). The position of the edge is sensitive to the coordination number, for example, exhibiting a shift of 0.7 ± 0.1 eV towards higher energy relative to the calcite edge for each additional oxygen beyond the sixth.[118,146] Consistent with this notion, the edge energy of reference materials calcite and barytocalcite ($Ba_{0.5}Ca_{0.5}CO_3$), both with 6-fold calcium coordination, was identical within the experimental error (Table 15.3). For ACBC with a barium fraction $x \leq 0.38$, the relative edge shift was nearly identical to that of ACC at 0.5 ± 0.1 eV, indicating an average coordination number of 6.8 ± 0.3 in the first shell. This is consistent with previous reports of ACC.[118,147] At $x = 0.55$, the edge shift was slightly smaller, and the apparent coordination number dropped to 6.4 ± 0.2.

Lowest in energy among the pre-edge features is the a very weak 1s→3d transition, approximately 10 eV below the edge, which appears split in calcite and barytocalcite.[147]

This feature is a singlet and is markedly more intense in ACC and ACBC (Figure 9.4b), indicating that the configuration of the first shell lacks an inversion center.[148] Two shoulders at slightly higher energy, around 4 eV below the edge result from 1s→4p transitions,[147] and are more pronounced in the crystalline reference compounds than in ACC and ACBC. While the position of the pre-edge features is largely independent of the barium content, the 1s→3d transition decreased in intensity and became broader at $x = 0.55$. At the same time, the relative intensity of 1s→4p transition at higher energy increased relative to that at lower energy. While the significance of this shift is unclear, the pre-edge region of ACBC ($x = 0.55$) qualitatively resembled that of barytocalcite and balcite (Figure 9.4a,b),[121] and may therefore be associated with the reduction in average coordination number towards six, and an associated increase in symmetry.

The post edge region of ACBC does not bear resemblance to either calcite nor barytocalcite, nor to that of aragonite, vaterite,[117] monohydrocalcite ($CaCO_3{\cdot}H_2O$), and ikaite ($CaCO_3{\cdot}6H_2O$),[149,150] but it has been shown to resemble that of balcite.[121] Because the balcite structure does not have well defined crystallographic positions for carbonate oxygens, a

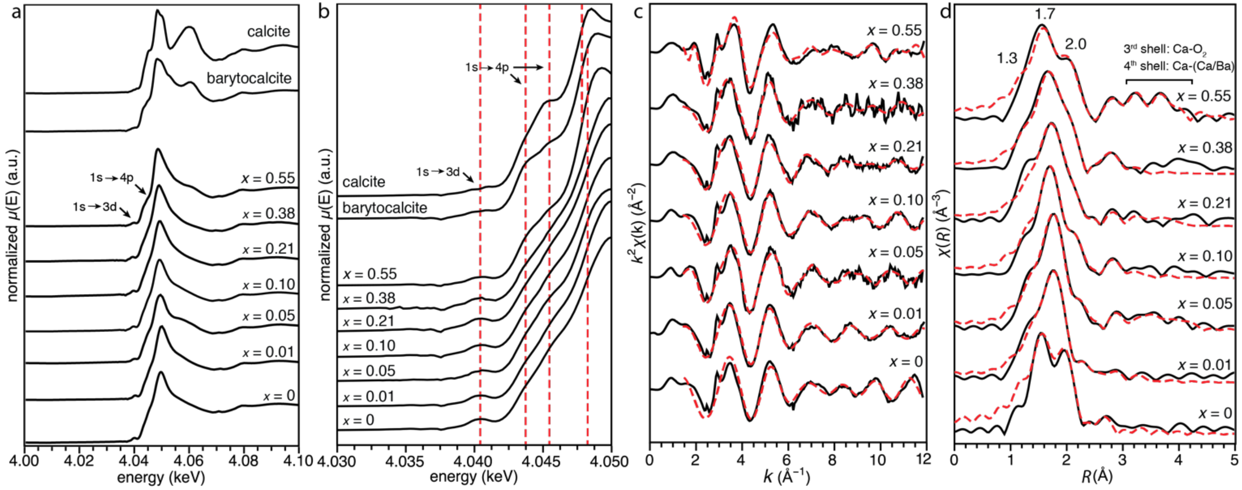

Figure 9.4. Calcium K-edge X-ray absorption spectroscopy of ACBC and reference compounds. (a) XANES of calcite and barytocalcite reference materials, compared to ACBC with x = 0 - 0.55. (b) Close up of the pre-edge features associated with a 1s→3d transition (~4.041 keV), a 1s→4p transition (~4.044 keV, 4.045 keV), and the absorption edge (~4048.5 keV). (b) k-space and (c) R-space EXAFS experimental data (black line) and fitted curves (dashed red line).

structural model based on calcite, but with the coordination number in the first shell ($Ca-O_1$) fixed to the value determined by analysis of XANES spectra, was used to fit the extended X-ray absorption fine structure (EXAFS) spectra (Figure 9.4c,d). Varying the coordination number within the limits of the error did not produce a significant change in the quality of the fits (R-factor < 0.02). However, two separate bond distances were required for the fits to converge, i.e., $Ca-O_1$ was split into $Ca-O_{1,1}$ and $Ca-O_{1,2}$. This is consistent with previously reported EXAFS spectra of ACC.[118]

Across all compositions, the distribution of oxygen between the Ca-O subshells evolved with increasing barium content (Table 15.3) and resulted in changes in the peak intensities in R-space spectra at approximately 1.4 Å, 1.7 Å, and 2.0 Å (Figure 9.4d). The most obvious effect of increasing barium content, however, was an increase in intensity of features associated with the third and fourth coordination shells ($Ca-O_2$ and Ca-(Ca/Ba)) at $x = 0.55$. Overlapping scattering contributions resulted in low sensitivity for differences between calcium and barium in the fourth shell, which had a roughly equal probability of occupancy at $x = 0.55$. However, it is clear that contributions from next-nearest neighbor cations in the fourth coordination shell emerged at this composition.

Near edge spectra at the barium K-edge were qualitatively much more similar to each other than those at the calcium K-edge (Figure 9.5a). There were only two pronounced peaks of approximately equal intensity, the white line just above the edge at ~37,450 eV, and another peak approximately 40 eV above the edge, but no pre-edge features. The lack of characteristic features in barium K-edge XANES spectra of crystalline carbonates, sulfates, and hydroxides has been attributed to relatively poor electron scattering compared to the absorber and low symmetry of the first few coordination shells.[151]

To the best of our knowledge, there has been no systematic survey of the barium K-edge energy as a function of the number of oxygen ligands in the first shell. We find that the edge energy of witherite and barytocalcite, both of which exhibit irregular 9-fold coordination around barium,[151] is identical within experimental error. The energy resolution near the barium K-edge was ~1 eV, compared to 0.2 eV at the calcium K-edge. XANES spectra of ACBC were similar to the reference compounds, differing only in the depth of the valley between the two peaks above the edge. The edge energy shift in ACBC across all compositions varied between -5 and 1 eV relative to the crystalline samples. The

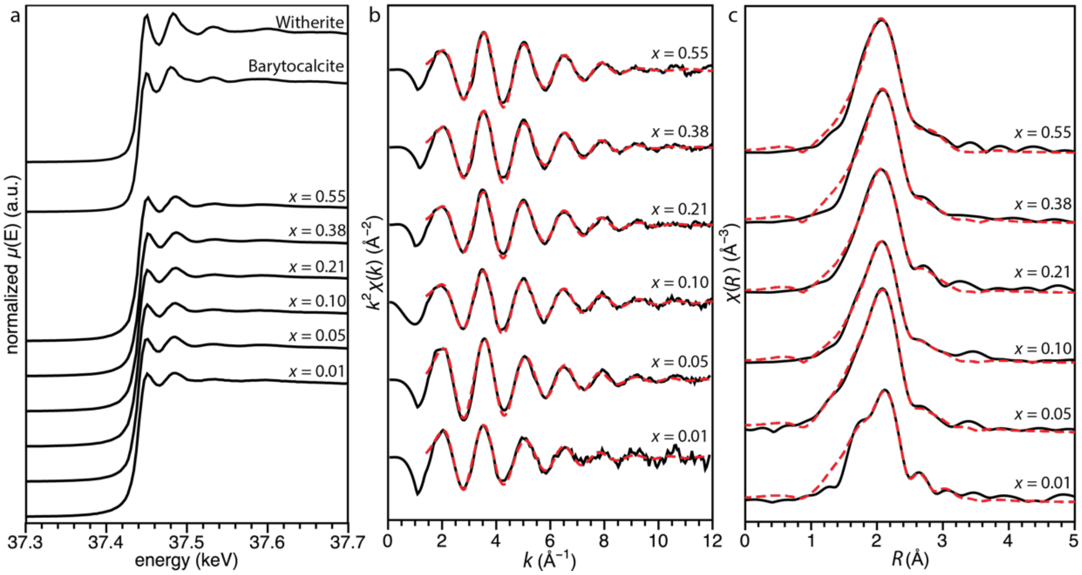

Figure 9.5. Barium K-edge X-ray absorption spectroscopy of ACBC and reference compounds. (a) XANES spectra of ACBC with x = 0.01 - 0.55 compared to crystalline barytocalcite and witherite. (b) EXAFS k-space and (c) R-space spectra (black lines) and fitted curves (red dashed lines).

magnitude of the shift was not correlated with barium content and could not be used to determine the coordination number of barium.

Barium K-edge EXAFS spectra of ACBC (Figure 9.5b) were fit with a structural model based on witherite (Table 9.1). The five inequivalent Ba-O distances in witherite were averaged to two to reduce the number of free parameters. Only the first (Ba-O) and second (Ba-C) shells were needed for accurate fitting (R-factor < 0.01). For all spectra, the coordination number was highly correlated with the Debye-Waller factor, and therefore the two were fit separately. Varying the coordination number within the calculated error did not change the fit quality appreciably. At all compositions, the coordination number of barium was significantly higher than that of calcium. At low barium content, the Ba coordination number was large (11-12), but its value decreased with increasing barium content. Note that the standard deviation associated with the coordination number is large (> 1.0 for most compositions, Table 9.1), an indication of a broad distribution of coordination environments.

Table 9.1 Structure of the first coordination shell of Ca and Ba in ACBC determined by EXAFS.

	Calcium K-edge								Barium K-edge						
x	CN[#]	R (Å)			σ^2 (10^{-3} Å^2)				CN[$]	R (Å)			σ^2 (10^{-3} Å^2)		
		Ca-O_1	Ca-O_2	St.Dev.	Ca-O_1	Ca-O_2	St.Dev.			Ba-O_1	Ba-O_2	St.Dev.	Ba-O_1	Ba-O_2	St.Dev.
0	6.8 ± 0.3	2.21	2.40	0.010	2	2	1		--	--	--	--	--	--	--
0.01	6.8± 0.3	2.32	2.48	0.01	22	5	2		11 ± 1.0	2.62	2.79	0.14	19	13	20
0.05	6.8± 0.3	2.31	2.50	0.007	7	5	1		12 ± 0.7	2.75	2.78	0.02	10	23	3
0.10	6.8± 0.3	2.29	2.47	0.006	2	2	1		9.5 ± 1.1	2.76	2.89	0.04	11	16	7
0.21	6.8± 0.3	2.30	2.47	0.003	3	3	1		9 ± 1.6	2.70	2.81	0.01	7	13	3
0.38	6.8± 0.3	2.28	2.45	0.003	2	2	1		8 ± 1.2	2.71	2.83	0.01	9	10	1
0.55	6.4± 0.2	2.19	2.39	0.003	1	4	1		8 ± 1.0	2.69	2.84	0.01	7	9	1

#. CN determined by edge energy shift from XANES

$. CN determined by *k*-space EXAFS fitting

9.4.5 *PDF analysis*

Pair distribution function analysis of X-ray total scattering data is a commonly used technique to study amorphous materials with no long-range order. Information about interatomic distances in real space can be obtained, and, with an appropriate structural model, can be assigned to specific atom-pair correlations.[145,152] We performed pair distribution function (PDF) analysis of total X-ray scattering (Figure 9.6a) on ACC and ACBC between x = 0.05 - 0.55. The reduced structure factor $f(Q)$ was determined from the total scattering intensity $I(Q)$. Real-space information was then obtained by Fourier transformation of $f(Q)$. The resulting pair distribution function, $G(r)$, is the probability of finding an arbitrary pair of atoms separated by the distance r, and provides real space information about the interatomic distances on the ~1-50 Å length scale. We further calculated the PDF for the simulated structures up to r = 8 Å (for an example at x = 0.5, see Figure 9.6b).

In calcite, sharp Bragg peaks are the dominant features in plots of the scattering intensity $I(Q)$ against the scattering vector Q (Figure 9.1a) Long range crystalline order responsible for these Bragg peaks gives rise to sharp pair distance correlations well beyond r = 50 Å (Figure 9.6a). In contrast, scattering of ACC is characterized by broad features at Q = 2.15 and 3.08 Å^{-1} (Figure 9.1a). Scattering from ACBC at low barium content strongly resembles that of ACC. With increasing x, a shoulder at Q ~ 1.5 Å^{-1} and a peak at 4.7 Å^{-1} increase in intensity and shift to lower Q, i.e., larger separation in real space.

Unlike the sharp pair correlations in calcite, the PDF of ACC is dominated by broad correlations at r = 2.1 Å, 4.3 Å and 6.3 Å and a much broader feature at 8.9 Å (Figure 9.6a), consistent with prior results.[145,147] Pair correlations in $G(r)$ of ACC break down after ~10 Å, as previously observed for both ACC and ACMC.[128,135,147] Pair distribution functions for ACBC strongly resemble that of ACC, with four maxima at ~2.5 Å, 4.1 Å, 6.3 Å and 8.9 Å. With increasing barium content, there was a systematic shift of these correlations to higher r. For example, the position of the maximum at 2.5 Å in ACC, which is primarily attributable to the Ca-O nearest-neighbor distance,[135,147] increases continuously with x up to a value of 2.8 Å in ACBC at x = 0.55. The height of the maximum at ~4.2 Å increases relative to that at 2.5 Å, and narrows subtly. A fifth, rather weak feature above 12.5 Å subtly becomes more pronounced with increasing barium content.

The experimental pair distribution function is the sum of all two-species radial distribution functions (RDFs), weighted by the associated atomic X-ray scattering factors. While RDFs cannot be determined directly from experimental data, it is straighforward to extract them from simulated structural models (Figure 9.6c). The first major correlation in simulated RDFs at 2.5-2.8 Å, contains contributions from O-O pairs on the same carbonate anion, and Ca-O/Ba-O distances (i.e., the first coordination shell). These RDFs are relatively featureless beyond ~4 Å and are similar between different simulated

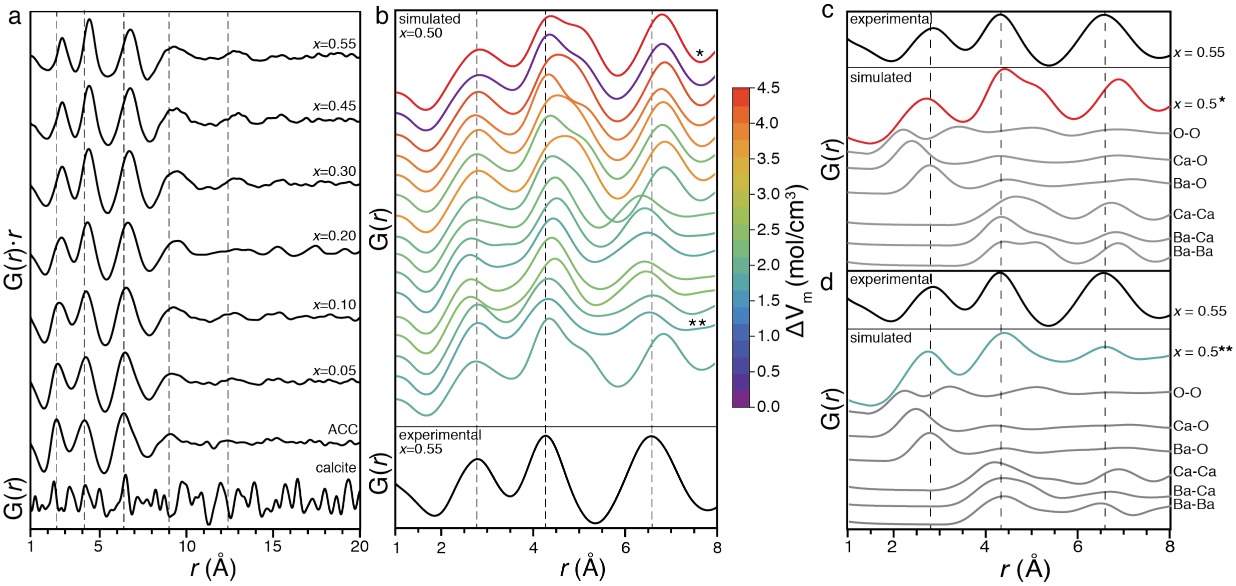

Figure 9.6. Analysis of experimental and simulated pair distribution functions (PDF). (a) Plot of the experimental PDF for calcite, and of the r-weighted PDF for ACC and ACBCs, against the pair distance r. PDFs were calculated from scattering data presented in Figure 1. (b) A comparison of the experimental PDF of ACBC at x = 0.55 (black line) with PDFs calculated from simulated structures at x = 0.50. Simulated PDFs are stacked in order of ΔH, with the least stable structure (highest ΔH) at the top and the most stable structure at the bottom. PDFs are colored by ΔV_m. (c) Plot of radial distribution functions for individual ion-ion pair correlation for two representative PDFs from (b), showing both high enthalpy (*) and low enthalpy (**) structures.

structures, and therefore do not contribute significantly to the PDFs beyond the first shell (Figure 9.6b). We find that correlations that extend beyond the first coordination shell, at 4.1-4.4 Å and 6.3-6.8 Å, are mostly associated with cation-cation (i.e., Ca-Ca, Ca-Ba, Ba-Ba) pairs.

Interestingly, we observe that the distance and magnitude of correlations are generally conserved between simulated polyamorphs from Figure 9.2. For example, at $x = 0.5$, higher energy structures with higher ΔV_m exhibit a split peak at 4.1-4.4 Å (Figure 9.6b), which the RDF indicates is due to two distinct Ba-Ba distances. The lower energy group of structures exhibits a single Ba-Ba distance. It should be noted that this relationship is not completely deterministic, as the lowest energy simulated structure at $x = 0.5$ more closely resembled the highest energy structure than the group most similar in ΔV_m. However, at all compositions the groups of structures with similar ΔV_m and ΔH could generally be distinguished also by their PDFs.

9.5 Discussion

9.5.1 *Synthesis and amorphous character*

We have previously shown that hydrated amorphous calcium barium carbonate (ACBC, $Ca_{1-x}Ba_xCO_3 \cdot n\ H_2O$) can be prepared by a variant of the low-temperature aqueous phase synthesis for amorphous calcium carbonate (ACC).[121,153] In our hands, phase-pure ACBC could be isolated up to $x = 0.55$, but required short reaction times, rapid filtration and washing at low temperature. ACBC incorporated a significant fraction of barium cations present in the feed solution, on average ~86 mol%. This is in sharp contrast to the ~1% solubility limit of barium in calcite[154] and aragonite[155], and of calcium in witherite.[156] Independent of the barium content, ACBC powders resembled ACC in that they were composed of partially aggregated, roughly spherical particles approximately 100 nm in diameter (Figure 9.1). ACBC did not exhibit birefringence, and appeared amorphous by electron and X-ray diffraction. We note that these features are consistent with both a highly disordered material and an extremely fine grained structure with crystallite dimensions below 1 nm.[157]

9.5.2 *Metastability*

ACBC is metastable and converts to metastable 'balcite' ($Ca_{1-x}Ba_xCO_3$ with $R\bar{3}m$ spacegroup) rather than stable calcite and witherite, both in the presence of water and when heated in air. Qualitatively, it appears that, in the mother liquor at ambient conditions, the rate of crystallization increases with the barium content, from approximately one hour below $x < 0.55$ to a matter of seconds with barium in excess of this amount.[121] This is likely the reason why we have been unable to prepare phase pure ACBC at $x > 0.55$. A quantitative analysis of the kinetics of phase transformations involving ACBC is in progress and will be detailed elsewhere. Similar to ACC, ACBC does not readily undergo phase transformation when kept dry, but crystallizes at elevated temperatures. Increasing barium content increased the temperature at which crystallization exotherms were first detected by DSC and DTA, from 290°C at $x = 0$ to 335 °C at $x = 0.43$ (Figure 15.2-9.9).

In summary, barium acts to accelerate the transformation of ACC in aqueous solution, but retards transformation at elevated temperature. This behavior is appears to be unique to barium, as large organic macromolecules have the opposite effect,[158] and magnesium,[128,158] phosphate,[159] and sulfate[158] ions inhibit both aqueous crystallization and crystallization at elevated temperature. In both cases, the formation of stable calcite and witherite is suppressed. A likely scenario is that the barrier to nucleation of balcite is lowered below those for calcite and witherite, and that higher barium content further lowers the barrier for balcite in the aqueous system. However, we cannot rule out that the barium content differentially influences the rate of crystal growth after nucleation, for example, at elevated temperatures, thereby affecting the overall rate of transformation.

In any case, it is clear that the composition of ACBC has a significant effect on its lifetime. We therefore set out to perform an in-depth analysis of ACBC structure as a function of the barium content. A comprehensive suite of techniques, including Raman and IR spectroscopy, X-ray absorption spectroscopy at both the calcium and barium K-edge, and pair distribution function analysis of X-ray total scattering data was employed. Atomic-scale simulations were used to determine thermodynamic properties of ACBC and relate them to atomic-scale structural motifs, and to extend the analysis to compositions that were not experimentally accessible. In order to do this, the role of structural water in ACBC was carefully considered.

9.5.3 *The role of water in ACBC*

Analysis of ACBC by TGA (x = 0 – 0.55, Figure 15.1) revealed that the water content remained relatively constant at n = 1.2 ± 0.2 across all compositions. In this respect ACBC behaves similarly to amorphous magnesium carbonate (AMC, n = 1.3), ACMC (n = 1.3-1.5),[128,160] and ACC (n ≅ 1.4).[88,128,135,160] The lack of a correlation between ionic radius of the cation and the water content is surprising, because the strength of dative water-metal bonds in the alkaline earth group decreases by a factor of two, and residence time of water decreases by over four orders of magnitude, going from Mg^{2+} to Ba^{2+}.[161-164] We would therefore expect to see a change in water content depending on the cation radius, for instance when comparing AMC and ACC. Further, we would expect the amount of water to depend on the mole fraction of magnesium in ACMC and of barium in ACBC. This is clearly not the case. As a consequence, there is no correlation between the water content of ACBC and the crystallization temperature, or its persistence at ambient temperature. Similarly, the crystallization enthalpy of synthetic ACC and ACMC does not correlate with water content.[128,160] This indicates that the role of barium in ACBC, and of magnesium in ACMC, can be decoupled from that of water.

Biogenic ACCs, which may contain Mg^{2+}, PO_4^{2-}, and acidic proteins, exhibit different water content and crystallization enthalpies, and there is evidence that a hydrated form has longer life time than a dehydrated form.[134] Decreasing water content appears to correlate with a decreasing ν_2/ν_4 ratio in IR, an indication of increasing order that also corresponds to lower enthalpy structures.[134] However, the thermodynamic driving force for water removal is the formation of a crystalline phase,[159] so it is unclear whether changing water content is the cause or effect of crystallization. Water is expected to have complex interactions with charged species in the solid state.[162] It appears to partially dissociate, and it may exhibit rapid dynamics in solid state NMR.[88,135,145,159,165] There is evidence that it may be kinetically trapped during formation,[6,7,162] that it may be occluded in nanoscale pores,[88,145] and that its distribution changes over the lifetime of amorphous precipitates.[88,159] Perhaps most importantly, water can be removed from ACC with minimal change to the overall structure, as assessed by XAS and PDF.[135,159]

Therefore, it is unclear how much water should be included *a priori* in a simulated structure. As a consequence, we decided to exclude water from simulations altogether. While this approach has obvious limitations, it does provide significant detail about a very similar, and much less uncertain, approximation of the structure. If water does not have a significant effect on the thermodynamics of bulk ACBC, a great deal can be gleaned from the water-free model. Any discrepancies between experiments and water-free simulations may therefore highlight the most significant impacts that water has on the structure. This should be seen as a first step of a much more comprehensive approach that does include the water that is known to exist. However, inclusion of water would require much larger systems, and consideration of a much greater number of variables, and is therefore beyond the scope of this paper.

9.5.4 *ACBC is a solid solution*

Inspection of diffraction patterns (Figure 9.1a) shows that none of the more stable crystalline phases, such as calcite, witherite, or balcite are present in ACBC. In addition, we do not find any indication for unmixing of ACBC into calcium and barium-rich amorphous phases. This is also clear from vibrational spectra, where the position of several internal modes of the carbonate ion (Raman: $\nu_1, \nu_{4,1}$; IR: ν_3, ν_4) systematically shifted to lower wavenumber with increasing barium content (Figure 9.1b, d, Figure 15.4-9.12, Table 15.1). In case of unmixing, we would expect the spectra to be linear combinations of the pure compounds, and exhibit split or asymmetric peaks. Further support for homogenous distribution of calcium and barium ions comes from the continuous shift in bond lengths and coordination numbers in the first shell extracted from XAS (Figure 9.3-9.5 and Table 15.1), which would be unaffected by the barium content if calcium and barium were not in molecular proximity. A micro-phase separation was postulated in the ACMC system, based on calorimetric data.[128] Consistent with this notion, the continuously changing ratios of fixed Ca-O and Mg-O bond distances were observed in PDF of ACMC. We did not observe an equivalent trend for ACBC within the resolution of our experiments (Figure 9.6, Figure 15.2). We therefore conclude that for $x \leq 0.55$, ACBC is indeed a solid solution, in which calcium and barium are homogeneously distributed.

9.5.5 *Simulation of anhydrous ACBC*

As discussed in the preceding sections, we propose that simulating ACBC as an anhydrous solid solution is a reasonable first approximation. To accomplish this, a number of model structures were generated at each composition, using a two-step procedure in which an ACC structure was generated by MD, and ACC and ACBC structures were created from these by substitution and relaxation using DFT. The enthalpy of formation (ΔH = 19-25 kJ/mol) for the lowest energy ACC structures generated in this way showed excellent agreement to calorimetric data,[128,134] providing confidence that the structures for which no thermochemical data is available are a reasonable approximation of the actual structure. Quite unexpectedly, we found that when MD-generated ACC and ACBC structures were relaxed using DFT, there was a distinct increase in the alignment of the carbonate ions (Figure 15.9), but no obvious increase in cation lattice order. Orientational ordering upon the removal of water in MD generated ACC has been suggested to produce vaterite-like local order.[166] An analysis of ΔH, estimated solubility product, difference in molar volume to a reference state (ΔV_m), and average coordination number revealed a stratification of the simulated structures consistent with the existence of three polyamorphs (Figure 9.2).

Overall, we find that simulations reproduce fairly well those structural features that we could probe experimentally. For example, the majority of PDFs of simulated structures grouped together as the lowest energy polyamorph closely resemble the experimental PDFs at similar composition (though this is not strictly true for *all* structures).

Compare for example the PDFs of the simulated structures at $x = 0.5$ with the experimental PDF at 0.55 (Figure 9.6). Lower energy structures had a single pair correlation at 4.1-4.4 Å, where higher energy structures exhibited a split peak due to multiple Ba-Ca correlations (apparent in the RDFs, Figure 9.6c). Lower energy structures also predicted the location of the pair correlation at 6.3-6.8 Å in the experimental PDF more accurately. Finally, the PDFs of simulated structures capture the systematic shifts with increasing barium content, which can be seen especially well for the pair correlation at 2.5-2.8 Å. The close match between the PDFs of the lowest energy simulated structures and the experimental data inspires confidence that we can use the radial distribution functions (RDFs) that contribute to the simulated PDFs to identify the contributions of specific pairs of atoms to the experimental PDFs.

We further find that the bond distances and coordination numbers extracted from the lowest energy simulated structures (Figure 9.3 and Figure 15.11), and their dependence on the barium content, agreed well with trends observed in X-ray absorption spectroscopy (Table 9.1). For example, both the calcium and barium coordination numbers decrease between $x = 0 - 0.5$, with barium decreasing to a much greater extent (Figure 9.3, Table 9.1). Taken together, we find that despite the absence of water from the simulations, there is a fairly good match between predictions from the models and experimental data. We therefore feel confident that analysis of the simulated structures may provide valuable insights, especially where experimental data reports average numbers, for instance coordination numbers, but simulations allow a more detailed analysis of coordination number distributions.

For amorphous carbonates synthesized previously that show extended life times when kept dry, Δ*H* decreases in magnitude with increasing cation radius.[24,122,127-130] Consistent with this general trend, we find that Δ*H* for the lowest energy simulated amorphous barium carbonate structure (ABC, or ACBC with $x = 1$) is the lowest of any reported value at 16 kJ/mol. However, the difference in Δ*H* between AMC and ACC (~19 kJ/mol) is much larger than that between ACC and ABC (~3 kJ/mol), even though the difference in ionic radii is similar in both cases[104]. In mixed cation systems, experimental thermochemical data is only available for ACMC, where Δ*H* varies by as much as 25 kJ/mol with magnesium content.[128] In contrast, our simulations predict that Δ*H* of the lowest energy ACBC differs by less than 5 kJ/mol over the entire compositional range (Figure 9.2). While thermochemical experiments analogous to those performed on ACMC would provide confirmation, barium substitution seems to carry a minimal energy penalty.

Somewhat counterintuitively, the more soluble amorphous carbonates with higher Δ*H* have appear to be more persistent.[44] This means that despite the nominally higher supersaturation for ground state crystalline phases, nucleation and/or growth occur more slowly. Many amorphous carbonates of cations smaller than Ca^{2+}, including Mg^{2+}, Fe^{2+}, and Mn^{2+} have been synthesized as bulk powders,[24,122,127-130] while those of larger cations such as Sr^{2+} and Ba^{2+} have not been observed in the absence of stabilizing additives[93,131,132] or confinement.[48] Consistent with this observation, ACBC at $x = 0.5$ is ~18 kJ/mol above the ground state, yet transforms rapidly. At higher barium content, predicted ΔH values become even lower, and experimentally crystallization accelerates to the point where ACBC cannot be isolated in pure form. The magnitude of the effect is clearly not in proportion to the change in the predicted ΔH. Previously, we proposed that the rapid transformation of highly substituted ACBC may be due to non-classical nucleation of balcite on or in ACBC, which is dependent on increasing structural similarity between ACBC and balcite.[121] We therefore performed a careful analysis of local and mid-range structure in ACBC as a function of barium content.

9.5.6 *Influence of barium content on cation coordination in the first shell*

We used XAS at the calcium and barium K-edge to investigate short range (< 5 Å) order around both cations, and specifically the symmetry and distribution of bond lengths in the first coordination shell of the cation. The presence of the single 1s→3d pre-edge feature at the calcium K-edge (Figure 9.4a,b) indicates that the first shell of calcium in ACBC, unlike that in calcite, is not centro-symmetric at any composition.[147] Consistent with this, both experiments (Figure 9.4, Table 9.1) and simulations (Figure 9.3) predict a significant fraction of calcium ions in 7-fold coordination, where centro-symmetry is impossible. At a CN of 8 and 6, centro-symmetry is in principle possible, but inspection of simulations indicates that the coordination geometry around most cations was irregular, with a range of bond distances (Figure 15.7, 9.17). Splitting of the first shell oxygen distance, required for convergence of EXAFS fitting, and large Debye-Waller factors with high uncertainty (Table 9.1) also support this notion. Taken together, simulations and EXAFS data both indicate that there is considerable disorder in the first coordination shell of calcium.

Based on the edge energy shift in XANES relative to calcite, calcium coordination in ACBC remains just below 7-fold up to x = 0.38, and drops to 6.4 at x = 0.55. While EXAFS is weighted towards shorter distances (smaller coordination number) due to inelastic photoelectron scattering and short core-hole lifetimes, the simulations have complete fidelity for more distant neighbors, and the coordination number for calcium determined from simulations (~8) was slightly higher than those determined experimentally. Structural water may contribute to this difference. However, trends in the coordination number extracted from the lowest-energy simulated structures are in good agreement with the experimental data. Specifically, the most frequent coordination number for calcium in simulated ACC is 8 (48 %, Figure 9.3), followed by 7 (36 %) and 9 (7 %), but with increasing barium content there is a reduction in the number of 8-coordinated calcium (to 30% at x = 0.50) and an increase in 6-coordinated calcium (27 %). Even though the of the Ba K-edge energy seems to be insensitive to the coordination number, fitting of EXAFS data revealed a pronounced shift, with a drop in average CN from 11-12 at low x to 8 at x = 0.55 (Table 9.1). Inspection of the simulated structures revealed the same trend towards lower CN with increasing barium content, and a significant increase of 8-fold coordinated barium for $x \geq 0.5$ (Figure 9.3). This prediction is surprising, because barium is very rarely found in 8-fold coordination in inorganic crystals, and we would therefore expect it would come with an energetic penalty. As discussed above, this does not seem to be the case.

In summary, barium coordination in ACBC is much more strongly impacted by barium content than that of calcium. While at low concentration barium ions compete only with neighboring calcium ions for carbonate ligands, with increasing concentration, they will eventually start compete with each other, and as a consequence have to accept lower average CN. It seems likely that this competition affects the chemical environment and bonding of carbonate ions in ACBC beyond the changes in bond length and stiffness that we expect when substituting barium for calcium.

9.5.7 *The carbonate environment in ACBC*

While the trigonal-planar geometry of carbonate anions distorts only subtly in response to changes in the local chemical environment,[165] vibrational modes are quite sensitive differences in symmetry. We therefore analyzed Raman and IR spectra of ACBC as a function of barium content. In IR spectra, the ν_2 (out-of-plane bending) mode frequency and intensity is relatively invariant, while a reduction in the ν_4 (in-plane bending) mode intensity is observed with increasing local disorder.[144] The ratio of the integrated intensity of the ν_2 to the ν_4 mode (ν_2/ν_4) is used as an indicator of the width of the distribution of the Ca-O bond distance.[144] An increase in carbonate alignment has also been predicted to result in a decrease of the IR ν_2/ν_4 ratio in calcite,[167] suggesting that the co-alignment of carbonates is correlated with the degree of local disorder. Significant reduction in ΔH

upon DFT relaxation as a result of increasing carbonate alignment in simulated ACBC supports this notion.

In simulations of ACC, the ratio of IR ν_2/ν_4 mode intensities ranges from 3 for calcite to 10 as the Ca-O bond length distribution increases.[144] These values agree qualitatively with measurements of calcite and ACC.[144] We observed a decrease in the ν_2/ν_4 ratio from 13.9 in ACC at x = 0 to 4.4 at x = 0.55, indicative of a narrowing of the number of different chemical environments from the perspective of the carbonate ions, equivalent to an increase in order. Further support for an increase in order at high barium content comes from the observation that while the Raman ν_1 (symmetric stretch) mode was much broader in ACBC than in calcite or witherite, and its full width at half maximum (FWHM) decreased as the barium content increased (Figure 15.5). With increasing barium content, the Raman ν_1 mode center shifted linearly from its position in ACC, close to that of calcite, towards lower wavenumbers near its position in witherite (Figure 15.4, 9.11). The split ν_4 mode showed a qualitatively similar trend. However, while the $\nu_{4,1}$ shift scaled with the barium content, the shift of the $\nu_{4,2}$ mode quickly reached a plateau at x = 0.21 (Figure 15.5). In addition, the $\nu_{4,2}$ mode increased in intensity relative to the $\nu_{4,1}$ mode. This shift increasingly resembled the ν_4 modes of aragonite-type carbonates (like witherite). In these materials three monodentate and three bidentate carbonates bind to each cation, with five separate oxygen distances, resulting in low-symmetry ν_4 modes the exhibit multiple peaks. Observations of changing oxygen distributions in the first coordination shell of both cations in EXAFS are consistent with decreasing bidentate binding relative to monodentate binding (Supporting Information).

9.5.8 *Influence of barium content on mid-range order*

There are several indicators of increasing mid-range order with increasing barium content. The strong reduction of the IR ν_2/ν_4 ratio discussed in the previous section is one. Emergence of broad features with higher intensity in the lattice phonon mode region of Raman spectra is another (Figure 9.1b, Figure 15.4). A number of sharp features corresponding to acoustic phonon modes below ~300 cm^{-1} are frequently used to identify crystalline carbonates.[168-170] Low frequency phonon modes require positional ordering over at least one cation-cation distance (~4-5 Å).[169] As scattering intensity scales with the fraction of ions oscillating in-phase, the increasing intensity of features below 300 cm^{-1}, and the emergence of even sharper peaks at ~150 cm^{-1} at x = 0.67 (Figure 9.1b, Figure 15.4-9.11, Table 15.2), are strong indications that there is increasing coherency in the collective vibrations of both cations and anions as the barium content increases to x = 0.5. Partial drying does not affect these features (Figure 1.1), indicating that structural water us unlikely to be responsible.

An increase in order with increasing barium content was also apparent in EXAFS and PDF. Due to the rapid decay of signal with growing distance from the absorber in EXAFS, barium content had a rather subtle effect. At x = 0.55, an increase in the calcium K-edge *R*-space signal corresponding to the fourth shell (Ca-Ca/Ba, Figure 9.4) is indicative of increased positional ordering of cations within approximately 5 Å. This is complemented by the decomposed RDFs, in which we observe an increase in the magnitude of correlations at 4.1-4.4 Å relative to that at 2.5-2.8 Å. An associated increasing frequency and narrower distribution of Ca-Ca, Ca-Ba, and Ba-Ba distances (Figure 9.6c) was observed in both experimental and simulated PDFs. Pair-correlations at 8.3 Å and 12.4 Å increased only subtly in experimental *G*(*r*), placing an upper limit on the length scale of this ordering (Figure 9.6a), and suggesting that next-nearest-neighbor cation ordering is the dominant feature of ACBC order. Together, these observations confirm that order at mid-range length scales (5-15 Å) increases with increasing barium content. In this respect, ACBC is distinct from ACMC, where order appears to be limited to the first coordination shell.[128,171] It is this mid-range order, on the length scale of critical nucleus sizes in carbonate systems,[22] that may contribute to structural similarity that promotes the formation of balcite.[121]

9.6 **Conclusions**

We find that substitution of up to 55 mol% of calcium with barium in ACC gives rise to ACBC that by all methods utilized appears amorphous. However, the transformation of ACBC to balcite in aqueous solution accelerates with increasing barium content. Simulations of anhydrous ACBC indicate that there exist as many as three polyamorphs of ACBC. Predictions based on structures associated with the lowest energy polyamorph matched experimental observations quite well, and suggest that the decrease in lifetime of ACBC with increasing barium content is not due an increase in solubility that would affect the supersaturation. Instead, ACBC short-range order evolved continuously, and mid-range order increased with increasing barium content. Specifically, cation-cation nearest neighbor ordering in ACBC emerged above a barium content of 50 mol%, and the ACBC local order becomes rather similar to that of balcite. This coincided with the composition at which the transformation to balcite becomes so rapid that it is no longer possible to prepare phase pure ACBC. Taken together, this provides support for the hypothesis that the presence of highly substituted ACBC lowers the barrier to balcite nucleation selectively. A likely scenario is that ACBC acts as a heterogeneous nucleator with decreasing interfacial energy as the barium content increases. These findings contribute significantly to an understanding of amorphous carbonate structures, their impact on thermodynamics, and a potential link to subsequent multistep transformation pathways that may appear to be 'non-classical' if the intermediate phase is too short-lived to be easily detected, for instance in the present system at very high barium content. Extending the structure-property relationships discovered for ACBC to other amorphous precursors will provide an appealing route to extend the design space of materials solid-solution compositions beyond thermodynamic solubility limits.

10. Solution processing of high-temperature carbonates under ambient conditions

10.1 Abstract

A high temperature phase of $Ca_{1-x}Ba_xCO_3$ ("balcite", $0.2 < x < 0.50$), thermodynamically stable only above 525-850°C depending on composition, was synthesized at room temperature via amorphous calcium barium carbonate (ACBC) precursors. Balcite formation was only observed under conditions where ACBC preceded crystallization. While the equilibrium solubility of barium in the calcite ($CaCO_3$) lattice is no more than ~1% due to the significant difference in ionic radii between Ba^{2+} and Ca^{2+}, balcite contained up to 50 times more barium. Static disorder of carbonate ions due to barium substitution is analogous to the dynamic in-plane rotation observed during upon heating calcite to high temperatures. Balcite remained stable after heating to 600°C, and could be recovered at ambient temperature without transformation into barytocalcite ($Ca_{0.5}Ba_{0.5}CO_3$), a balcite polymorph with greater stability, or phase separated calcite and witherite. *In situ* crystallization experiments confirmed the downhill nature of the transformation from supersaturated solution → ACBC → balcite → calcite + witherite. Evidence suggests balcite can form, and its composition can evolve, via dissolution-reprecipitation, but that its initial formation from ACBC follows kinetics that deviate from a classical description. These observations have important implications for modeling solid solubility and ion substitution in calcite and related carbonates, e.g., paleoproxies used for climate modeling.

10.2 **Introduction**

Calcium carbonate ($CaCO_3$) is an abundant mineral in natural environments, and has attracted significant interest for its roles in geological carbon cycling and biomineralization.[104] Although less abundant in the lithosphere, barium carbonate ($BaCO_3$) has recently received attention for the complex 'biomorphic' crystals that can be made in the absence of organic additives, prompting a critical evaluation of fossil record evidence for early life.[172-175] Mixed-cation phases in the $CaCO_3$-$BaCO_3$ system have been investigated as products of biologically induced mineralization,[176,177] for paelothermometry,[154,155] as components of the earth's mantle,[178] and carbon-14 conditioning matrices,[179] as well as precursors for ferroelectrics[180] and thermoionic emitters.[181]

It has recently been shown that metastable balcite[121] ($Ca_{0.5}Ba_{0.5}CO_3$) can be synthesized from amorphous calcium barium carbonate (ACBC, $Ca_{1-x}Ba_xCO_3{\cdot}1.2H_2O$) with x = 0.55 (chapter 9) Balcite is a metastable high temperature phase that is harder than geological calcite and equally as hard as biominerals containing occluded amino acids or proteins. This synthesis pathway via amorphous precursors highlights their role in enabling the formation of non-equilibrium materials with desirable properties. A better mechanistic understanding of such pathways may have important implications for the rational design of metastable materials.[63] Therefore, it is important to understand the transformation from ACBC to balcite, and to fully characterize its impact on the resulting balcite structure.

Herein, we describe the crystallization of amorphous calcium barium carbonate (ACBC) under ambient conditions. A continuum of structures, intermediate to calcite and balcite end members, are observed between $0 < x < 0.50$. We extend the 'balcite' label to materials with approximately $0.25 < x \leq 0.50$, characterized by the complete transition from the $R\bar{3}c$ spacegroup of calcite to $R\bar{3}m$ symmetry of balcite. Direct observation of the crystallization process in nanoliter water-in-oil emulsion drops indicates that crystallization of ACC is accelerated by barium. At low barium concentrations ACBC crystallizes through dissolution and reprecipitation, similar to ACC without barium. At higher concentrations, the ACBC to balcite transformation proceeds at a rate that is at least two orders of magnitude faster and dramatically departs from the classical kinetics that describe the crystallization of ACC. It appears that this transformation proceeds with limited long-range diffusion, and may be a solid state transformation.

10.3 **Results**

10.3.1 *Synthesis*

We recently described a synthetic route to prepare amorphous calcium barium carbonate (ACBC, $Ca_{1-x}Ba_xCO_3 \cdot nH_2O$ where n ≅ 1.2 and $0 < x < 0.55$, chapter 9) Approximately 85% of the barium in solution ($x^{feed} = [Ba^{2+}]/[Ca^{2+}][Ba^{2+}]$) partitions into ACBC under these conditions. At $x \cong 0.5$, ACBC transforms into a high temperature calcite-type carbonate with very high barium substitution on calcium lattice sites that we call 'balcite'.[121] In this work, crystallization across the entire range of ACBC compositions for which no crystalline precipitates were observed ($0 < x < 0.55$) was investigated. After aging ACBC for 24 hours in the mother liquor, a white precipitate settled out of solution, was filtered, washed with cold water, and dried at 110°C for 1 hour. Birefringent particles were observed in optical microscopy under crossed polarizers at all compositions (not shown). Samples prepared without barium had the distinctive rhombohedral faceting of single-crystalline calcite in scanning electron microscopy (SEM) (Figure 10.1a). In contrast, ACBC-derived precipitates evolved from roughened triradiate crystals (Figure 10.1b) to spherulitic polycrystals (Figure 10.1c-f) with increasing barium content. Barium content was measured on at least five individual precipitates at each composition listed in Figure 10.2 using EDS (Table 16.1). Herein x will refer to the barium concentration of these crystalline precipitates. The phase assemblage, composition, and structure of the precipitates depended on the solution composition, aging time, and stirring, discussed in further detail below.

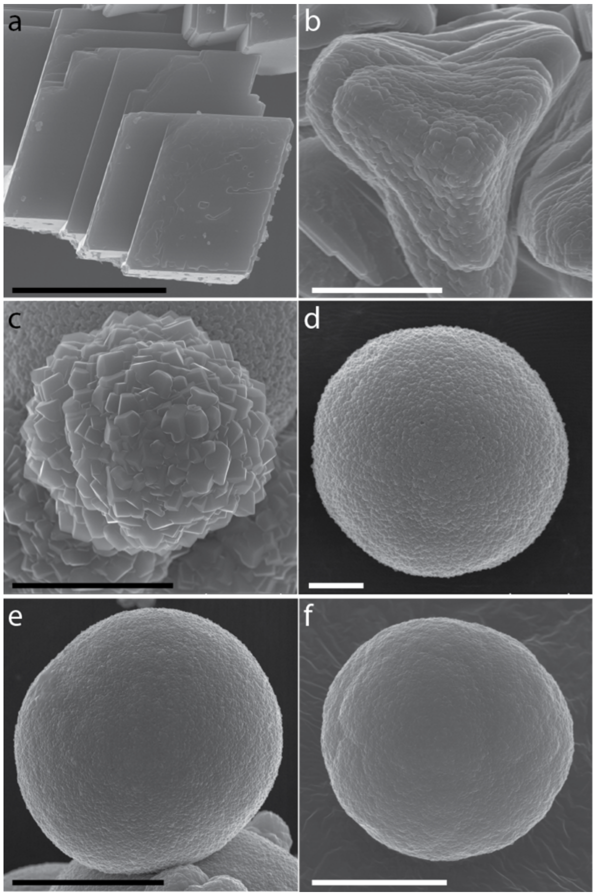

Figure 10.1.Crystallite habit of (a) calcite compared to (b) barium-substituted calcite and (c-f) balcite with x = 0.34-0.51. (b) Crystals adopted a stacked triradiate structure at x = 0.10. (c) Isotropic polycrystals were observed at x = 0.21. (d-f) At x > 0.21, polycrystalline spherical particles composed of ~100 nm crystallites were observed. Scale bars represent 10 μm, except (c) and (d) which are 2.5 μm.

10.3.2 *XRD and Rietveld refinement*

X-ray diffraction (XRD) of precipitates obtained from ACBC confirmed that they had crystallized after 24 hours in their mother liquor (Figure 10.2). A primary phase with Bragg peaks matching the most intense reflections of calcite (low x) or balcite (high x) were observed (Figure 10.2a). For $x \leq 0.34$, the calcite-type precipitates were enriched with barium and co-precipitated with vaterite. In agreement with previous reports,[23] these materials were prepared from solutions with a barium fraction, $x^{\text{feed}} \leq 0.25$ (Table 16.1). A gradual shift of the XRD peak positions of calcite to lower Bragg angles, towards those of balcite, was observed with increasing x. This is consistent with larger barium cations substituting on calcium lattice sites and expanding the calcite unit cell. With increasing barium concentration, the relative intensity of the (104) reflection decreased. In addition, the (113) calcite diffraction peak decreased in intensity relative to the (104), and became undetectable in precipitates with $x \geq 0.34$. Single phase materials by XRD ($0.34 \leq x \leq 0.51$) had compositions nearly identical to the ACBC precursors by EDS (Table 16.1). Above $x = 0.51$, broad peaks consistent with witherite as a secondary phase were consistently observed. To understand the transition from calcite to balcite structures, and the phase segregation observed outside the composition range $0.25 < x < 0.51$ a more detailed understanding of the balcite structure was sought.

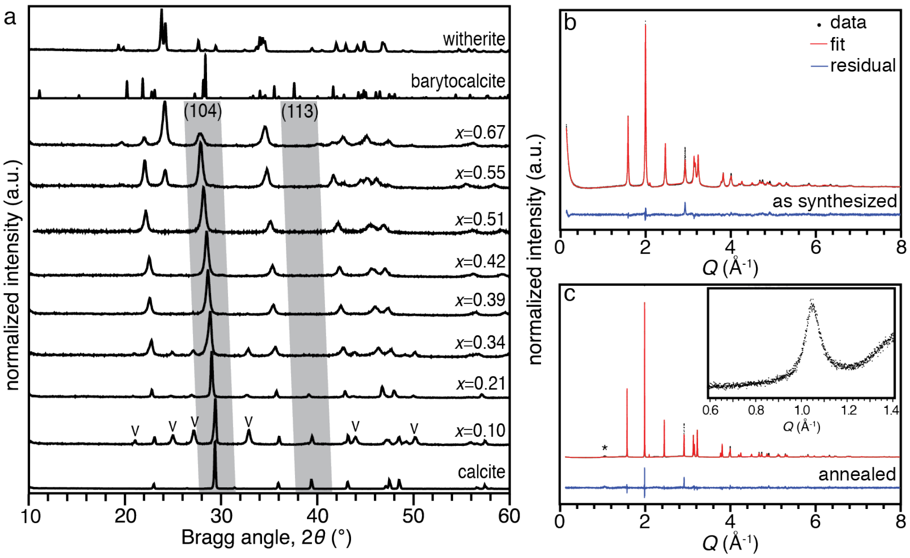

Figure 10.2. Evolution of the $Ca_{1-x}Ba_xCO_3$ crystal structure though X-ray diffraction. (a) XRD of $Ca_{1-x}Ba_xCO_3$ made from ACBC ranging from x = 0 - 0.67, normalized to the most intense reflection. (b) HR-pXRD of as

synthesized balcite and (c) balcite annealed at 600°C. Annealed balcite remained in the $R\bar{3}m$ spacegroup, but peak width decreased dramatically and the small-angle signal below Q = 0.20 $Å^{-1}$ disappeared. In addition, a small, broad peak emerged at Q = 1.05 $Å^{-1}$, consistent with a superlattice reflection along the c-axis.

Calculated profiles from Rietveld refinement confirm the overall $R\bar{3}m$ symmetry of balcite. Heating balcite with $x = 0.50$ to 600°C for 10 minutes at a rate of 10°C/minute, and cooling to 25°C at the same rate, did not significantly alter the Bragg peak positions and relative intensities found in the as-synthesized material in high resolution powder X-ray diffraction (hr-pXRD, Figure 10.2b, c). However, broad peaks in the as-synthesized material were considerably narrower after annealing (Figure 16.2). This is consistent with previous reports.[121] Application of the Scherrer equation to calculated profiles indicated that the average crystallite size in the as-synthesized material was 34 ± 4 nm, while in the annealed sample it was > 250 nm. Scattering intensity at scattering vectors $Q < 0.2$ $Å^{-1}$ in the as-synthesized sample disappeared from hr-pXRD after annealing. Simultaneous medium- and wide-angle X-ray scattering (MAXS/WAXS) collected *in situ* while heating showed that this scattering shifted to lower Q as the temperature increased (Figure 16.2), consistent with coarsening of small particles.

Close inspection of the annealed sample revealed a weak, broad feature at $Q = 1.05$ $Å^{-1}$ (Figure 10.2c), which emerges during heating (Figure 16.2). This appears to be a superlattice reflection of the balcite (003) at $Q = 2.10$ $Å^{-1}$, corresponding to the 5.98 Å spacing between three cation planes in the c-axis direction. Emergence of this reflection suggests that there is cation ordering that begins to occur at elevated temperatures, with barium and calcium segregating to alternating planes. Underestimation of the intensity of the (012) reflection at $Q = 2.0$ $Å^{-1}$ and the (021) at $Q = 2.9$ $Å^{-1}$ in the annealed materials reflects this ordering. Fourier difference maps between the calculated and observed diffraction patterns indicated there is residual electron density at the 3a Wykoff position (0, 0, 0), representing the ten cation sites.

10.3.3 *XANES/EXAFS*

Complimentary information about the cation coordination environments was determined by element specific XAS at both the calcium and barium K-edges (Figure 10.3). X-ray absorption near edge spectra (XANES) provides information about the coordination number (CN) of the cation and the ordering of the most closely coordinated carbonates. Near edge spectra of crystalline compounds at the calcium K-edge exhibit a number of identifying features (Figure 10.3). The position of the edge (defined as the maximum in the first derivative of the intensity) is very sensitive to the coordination number (CN), with a shift of 0.7 ± 0.1 eV towards higher energy (relative to the calcite edge) for each additional oxygen beyond the sixth.[146] In ACBC, there are two pre-edge features, one weak one ~10 eV below the edge, and one more pronounced ~4 eV below (Figure 10.3a). The former corresponds to a 1s→3d transition that is forbidden in centrosymmetric structures and appears split in calcite due to quadrupolar coupling.[147] The second, more intense pre-edge feature corresponds to the 1s→4p transition.

A comparison of Ca K-edge XANES of as-prepared ACBC and balcite with $x = 0.50$ to calcite (Figure 10.3a) shows that the local environment of balcite more closely resembles that of ACBC than calcite, as previously observed. The edge energy of ACBC and Ca_{1-}

${}_x$Ba$_x$CO$_3$ were both shifted 0.5 eV relative to calcite, an indication that the average CN in both materials was approximately 6.8 ± 0.2. A shoulder above the white line at 4.045 is keV was more apparent in balcite than ACBC and a peak at 4.06 keV was slightly more pronounced, but was not as prominent as that observed in calcite.

Data in the Ca K-edge EXAFS region were fit *R*-space with a structural model based on calcite (Figure 10.3b, c, Table 10.1). Two separate distances were needed for each Ca-O$_1$ (first shell), Ca-C$_1$ (second shell), and Ca-O$_2$ (third shell) for both ACBC and balcite. ACBC had shorter Ca-O$_1$ distances (2.19, 2.39 Å) than balcite (2.37, 2.55 Å). The CN-weighted average was 2.32 Å vs 2.42 Å, indicating that first-shell oxygens were more tightly bound in the amorphous structure. The Debye-Waller factors, σ^2, were appreciably higher in balcite (0.007, 0.006 Å^2) than ACBC (0.001, 0.004 Å^2). In addition, balcite required the inclusion of Ca-Ba (fourth shell) for the fit to converge.

Barium K edge XANES of ACBC and balcite were qualitatively very similar, and differed only slightly from witherite (Figure 10.3d). The edge energies of ACBC and balcite were both shifted -3.7 eV relative to witherite, an indication that the CN was similar in these two materials and less than nine. No correlation between oxygen CN and edge energy shift has been determined at the Ba K edge to our knowledge. In the EXAFS region, data were fit in *k*-space with a model based on witherite. In the witherite reference material, the five separate Ba-O distances were reduced to three to limit the number of free parameters given the resolution of the measurements (~ 0.02 Å). Two oxygen distances and a CN of eight produced the best fit for both ACBC and balcite. Ba-O distances were longer in ACBC (2.68, 2.83) than balcite (2.55, 2.73 Å), with the CN-weighted averages of 2.77 Å and 2.69 Å, respectively. Only a single Ba-C_1 (second shell) was needed for a convergent fit to ACBC, while balcite required two Ba-C_1 distances, two Ba-O_2 (third shell) distances, Ba-Ca (fourth shell), and a Ba-O_3 (fifth shell).

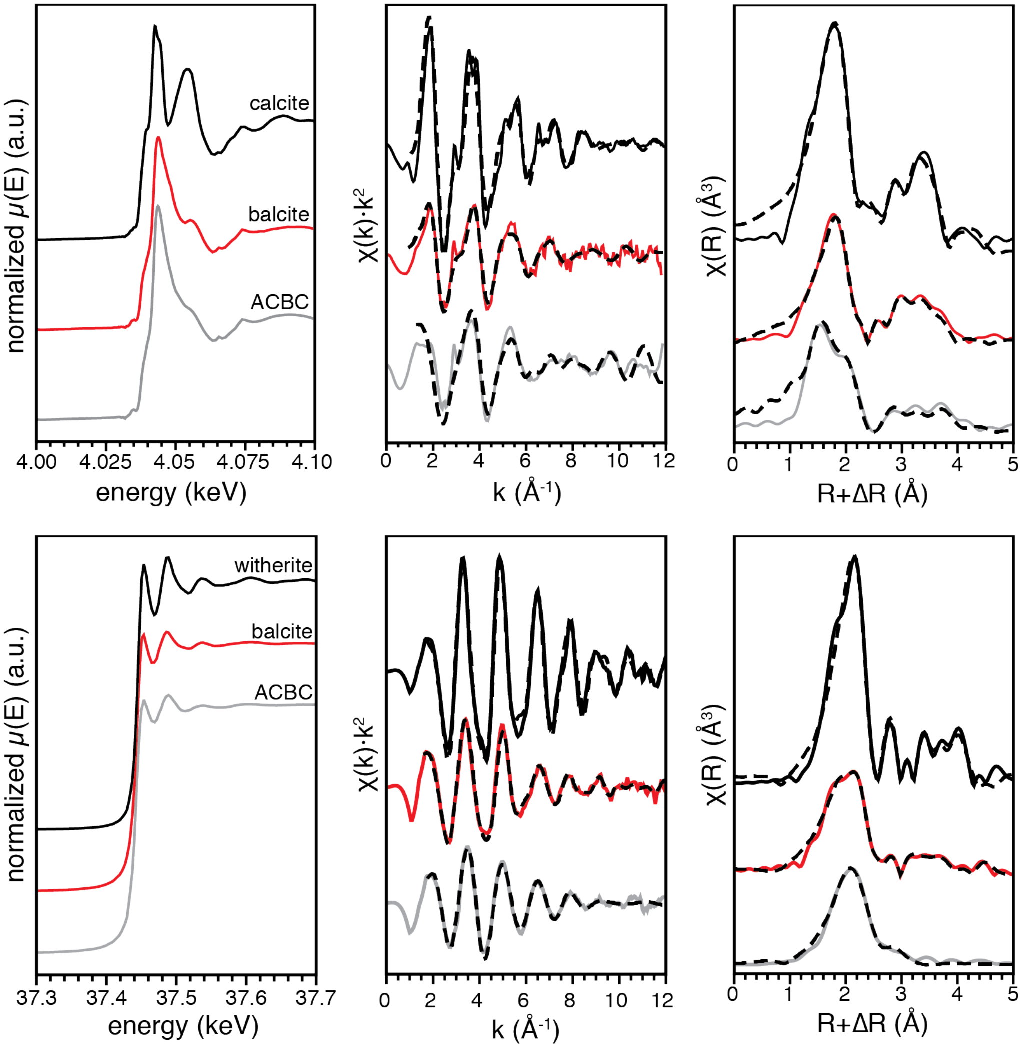

Figure 10.3. X-ray absorption spectroscopy at the Ca K-edge (a-c) and Ba K-edge (d-f).

Table 10.1. First Shell EXAFS fitting

	Ca K-edge				Ba K-edge		
	CN	$R\ Ca-O$ (Å)	σ^2 (Å^2)		CN	$R\ Ba-O$ (Å)	σ^2 (Å^2)
Calcite	6	2.39 (0.01)	0.010 (0.001)		--	--	--
ACBC	2.28, 4.22	2.19, 2.39 (0.01)	0.001, 0.004 (0.001)		3.17, 4.83	2.68, 2.83 (0.01)	0.005, 0.007 (0.002)
Balcite	4.07, 1.93	2.37, 2.55 (0.02)	0.007, 0.006 (0.004)		1.74, 6.26	2.55, 2.73 (0.01)	0.006, 0.007 (0.001)
Witherite	--	--	--		3, 4, 2	2.73, 2.85, 2.91 (0.02)	0.004, 0.008, 0.008 (0.004)

10.3.4 *Solid-State NMR*

Solid-state nuclear magnetic resonance (NMR) was used to probe the change in local order of carbonate ions upon crystallization of ACBC to balcite, and the effect of water on this transformation. Samples were prepared through the same procedure described previously, but with 20% of the Na_2CO_3 enriched with ^{13}C for NMR analysis. ACBC samples were filtered and washed with cold water immediately after precipitation, as described previously.[121] Balcite samples were allowed to age for 24 hours in their mother liquor. Direct excitation (DE) magic angle spinning (MAS) spectra provide information about the immediate molecular environment of either ^{13}C or ^{1}H. To determine the relationship between ^{1}H and ^{13}C containing species (i.e., water and carbonate), cross polarization (CP) MAS NMR was used to reveal only those hydrogen-bearing species seen in the ^{1}H spectra (or a subset of them) in close molecular proximity to carbon species.

ACBC samples were precipitated from solutions with nominal x^{feed} = 0.05, 0.15, 0.30, 0.50. Both the ^{13}C DE and CP MAS spectra (Figure 10.4a) of the four ACBC precipitates exhibit a single broad peak at 169.0 ± 0.2 ppm peak ($\delta\nu$ = 3.4 ppm full width at half maximum, FWHM), independent of barium content. As the hydrogen atoms of water molecules are the only source of the carbonate peak intensity in the CP spectra, the similarity of the CP and DE MAS spectra demonstrates the homogeneous dispersion of water molecules throughout this disordered ACBC phase. The ^{1}H DE MAS spectra of the four ACBC Ba ratios exhibit a single broad peak (δ = 4.9 ± 0.2 ppm; $\delta\nu$ ~ 3.0; Figure 10.4, bottom) similar to amorphous calcium carbonate phosphate (ACCP).[159]

Crystallized ACBC was also investigated by solid state NMR. Four balcite samples with overall compositions of x = 0.24, 0.31, 0.41, 0.51 ± 0.02 (measured by XRF) were prepared. While this range of compositions yielded single-phase materials using Na_2CO_3 with natural isotope abundance (Figure 10.4), the ^{13}C-enriched sample with x = 0.24 contained vaterite, and the x = 0.51 sample contained witherite as a secondary phase in XRD (Figure 16.5). This suggests that isotopic composition has an impact on the transformation of ACBC to balcite, which will be discussed further below. Nonetheless, each sample contained mostly balcite (Figure 16.5).

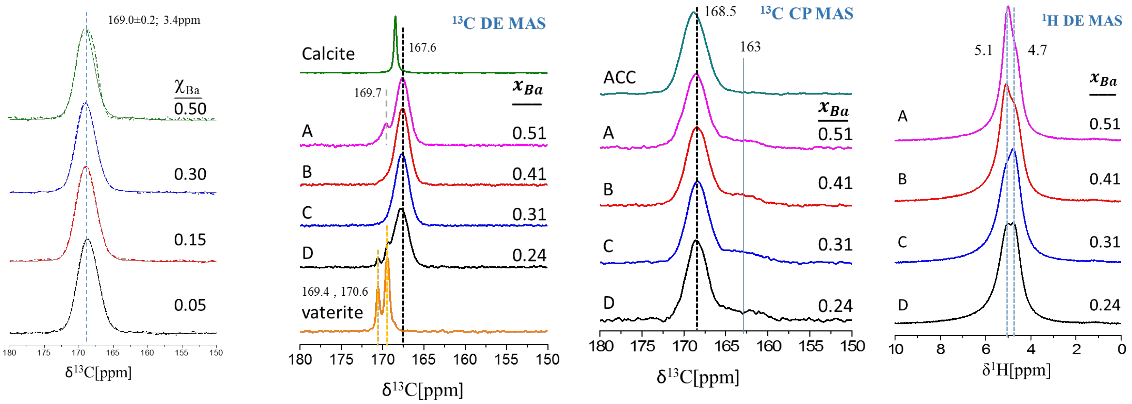

Figure 10.4: (a) : 75.4 MHz ^{13}C MAS NMR spectra, expansion of the carbonate region, of [20%-^{13}C] ACBC with x_{feed}, 0.05, 0.15, 0.30, 0.50. DE spectra (dashed) are overlaid on the CP spectra. Repetition delay of 1000s ensures full relaxation and makes the DE spectra quantitative. The carbonates in molecular proximity to the hydrogen-baring water molecules are exposed in the CP spectra. ACBC-50% is from Batch I. (b) Quantitative 125.8 MHz ^{13}C DE MAS spectra, expansion of the carbonate region, of the [^{13}C-20%]balcite samples with [^{13}C-15%]vaterite and [^{13}C-15%]calcite for a reference. Dashed lines are drawn as reference markers of balcite, witherite and vaterite (167.6, black; 169.7 ppm, gray; 169.4 and 170.6, orange). (c) 500.3 MHz ^{1}H DE MAS spectra of the [^{13}C-20%]balcite samples showing two water environments. (d) 125.8 MHz ^{13}C CP MAS spectra of the [^{13}C-20%]balcite samples with [^{13}C-15%]ACC for a reference.

^{13}C DE spectra of the four samples show one major peak centered at 167.6 ppm that is assigned to balcite (Figure 10.4). This chemical shift (isotropic) is clearly different from either those of calcite (168.4-168.8 ppm) and witherite (170.0 ppm)[165,182] and is independent of x. Broad balcite peaks ($\delta\nu$ = 2.0 ppm FWHM) resemble mixed lattices such as magnesium calcites.[183] This is in marked contrast to the peak widths of homogeneous carbonates like calcite (~0.15 ppm), aragonite (~0.20 ppm), vaterite (0.4-0.6 ppm), and witherite (0.20 ppm) whose narrow linewidths reflect the overall structural-chemical uniformity. In the $x = 0.24$ sample, two narrower peaks (169.4 and 170.6 ppm, $\delta\nu$ = 0.4 and 0.6 ppm FWHM) representing 10 ± 1 mol% vaterite component were observed. An additional peak in the $x = 0.51$ sample at 169.7 ppm (1.0 ppm linewidth) is attributed to the occurrence of 17 ± 1 mole% witherite, consistent with the XRD data.

Thermogravimetric analysis indicated that balcite lost 1-2% of its mass upon heating to 600°C (Figure 16.3). Most of the mass loss occurred gradually up to approximately 450°C, below the decomposition temperatures of calcite or witherite,[156] suggesting that this loss is due to the removal of water. The presence of water in balcite, suggested by weight loss in TGA, was confirmed by ^{1}H DE MAS NMR spectra (Figure 10.4b). All four balcite precipitates show two partially resolved spectral components whose deconvolution yields 5.1 ppm and 4.7 ppm contributions. This is a clear indication of the presence of two distinct structural water environments that are equivalent across all four compositions, but occur in different ratios. There is no evidence of hydroxyl groups, which appear near 1.5 ppm in amorphous calcium carbonate,[135,184] nor bicarbonate, which is generally observed above 13 ppm.[184]

To determine the relationship of this water to carbonate ions, cross polarization (CP) MAS NMR was used to reveal only those hydrogen-bearing species seen in the ^{1}H spectra (or a subset of them) in close molecular proximity to carbon species (Figure 10.4c). Notably, the CP MAS spectra select a different population of carbonates (168.6 ppm) than those of the bulk balcite carbonates depicted in the DE spectra (167.6 ppm), and of larger heterogeneity ($\delta\nu$ = 3 vs. 2 ppm). Similar to the DE MAS peak, the carbonate CP peak is independent of x. A broad composite peak is seen at ~163 ppm in the four CP MAS spectra (Figure 10.5) and is attributed to residual bicarbonates,[184] perhaps associated with trace amounts of sodium detected by EDS (not shown).

Both spectral features (168.5 and 163 ppm) seen in the CP MAS spectra represent hydrated disordered environments, whose occurrence is not resolved by the (quantitative) DE MAS spectra. This implies that carbonates in molecular proximity to water are a small fraction of the carbonate content. These fractions are estimated to be below 15% (see below). As an additional means to explore the interactions between carbonates and water, we performed ^{1}H-^{13}C 2D HETCOR (heteronuclear correlation) measurements, which show crosspeaks between carbons and hydrogens that are spatially correlated. A representative spectrum (Figure 10.5) of the x = 0.24 sample clearly resolves crosspeaks between the two hydrogen environments (as seen above) to the "168.5 ppm" carbonates. The 2D crosspeaks indicate that the "168.5 ppm" peak is in fact composed of (at least) two distinct carbonates at 168.2 and 169.2 which are not resolved in the 1D CP MAS spectra.

The two H-environments were detected in the 2D spectra of all compositions; the distinction between the two carbonates was possible in the x = 0.24 and x = 0.51 samples.

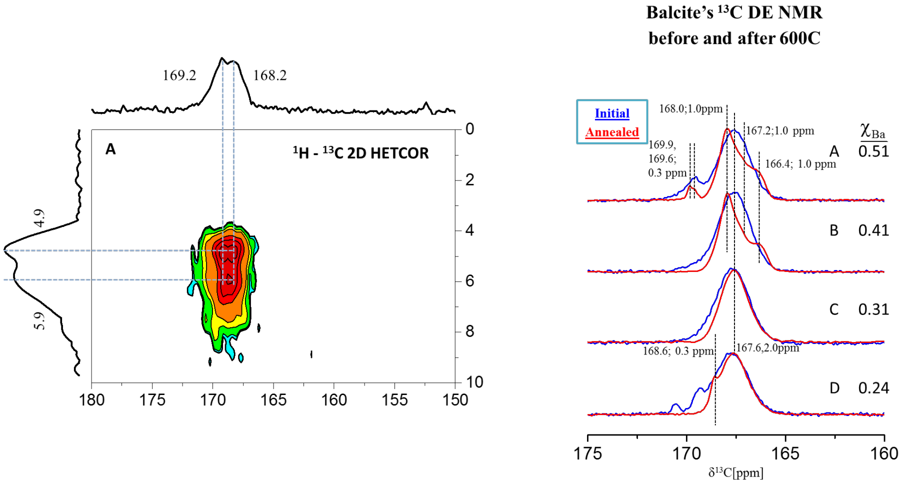

Figure 10.5: (a) 500/125 MHz $\{^1H\}^{13}C$ 2D-HETCOR spectrum focusing on the carbonate region, showing carbon-hydrogen spatial correlations. [pd = 2s, ct = 2ms, ν_R = 10 kHz]. (b) ^{13}C DE MAS spectra of heated balcite samples.

^{13}C DE spectra were also obtained on heated samples to better understand the influence of the removal of water on balcite structure. Samples were heated to 600°C at 10°C/minute and cooled back to 25°C at the same rate, reproducing the conditions used for the hrPXRD sample in Figure 10.2c. Heating removed all water from the structure, such that no ^{1}H signal was obtained. Vaterite present in the x = 0.24 sample crystallized to calcite, as evidenced by the replacement of the two peaks at 169.4 and 170.6 with a single peak at 168.3. The balcite peak at 167.6 ppm did not change appreciably. At x = 0.31 the 167.6 ppm balcite peak narrowed and shifted slightly to lower chemical shift. In the x =

0.41 sample the balcite peak split into at least three distinct components at 168.0, 167.2, and 166.4 ppm. These components were also observed in the $x = 0.51$ sample, in addition to the witherite peak, which shifted up to 169.9 ppm. This indicates that balcite at $x \leq 0.31$ behaves differently than balcite with $x \geq 0.41$ at high temperatures.

10.3.5 *Vibrational spectra*

Raman microscopy of balcite made from ACBC with x = 0.05 - 0.67 was compared with geological calcite and witherite reference materials (Figure 10.6). Vaterite that had co-precipitated with balcite between x = 0 – 0.34 was easily distinguished based on particle morphology and spectral characteristics (Figure 16.4). Witherite was absent in all but the x > 0.51 samples, where it was clearly discernable from the strong ν_1 (symmetric stretching) mode (Figure 10.6a,b) at 1059 cm^{-1}. The calcite ν_1 at 1086 cm^{-1}, ν_4 (in-plane bending) at 712 cm^{-1} and translational (T) and librational (L) phonon modes at 150 and 277 cm^{-1}, were also present in balcite. Weak ν_3 (asymmetric stretch at 1435 cm^{-1}) and $2\nu_2$ modes in calcite (out-of-plane bending overtone at 1747 cm^{-1}) were observed in balcite, as well as the ν_2 fundamental at 875 cm^{-1} that is not Raman active in calcite.

Most of these modes were split, shifted, and/or broadened with increasing x in balcite. The balcite ν_1 mode broadened and became asymmetric (Figure 10.6b). Two pseudo-Voigt functions provided the best fit, an indication of two populations of carbonate symmetric stretching frequencies. The peak at lower wavenumbers ($\nu_{1,2}$) shifted linearly towards the ν_1 mode of witherite, while the $\nu_{1,1}$ peak shifted only slightly to lower wavenumbers (Figure 10.6c). In the x = 0.67 sample that contained primarily witherite, the witherite ν_1 mode was broadened and shifted to higher wavenumbers, consistent with calcium substitution for barium in the witherite lattice. The single ν_4 mode of calcite at 712 cm^{-1} broadened and split into two distinct modes with increasing x (Figure 10.6d, e). The ratio of the intensities of these two peaks inverted with increasing barium, evolving towards that found in witherite. Witherite had three distinct ν_4 peaks, and the witherite-containing samples at x = 0.55 and x = 0.67 were better fit with a third pseudo-Voigt peak near 750 cm^{-1}. Deconvolution of contributions from balcite and witherite was not possible due to the high degree of overlap.

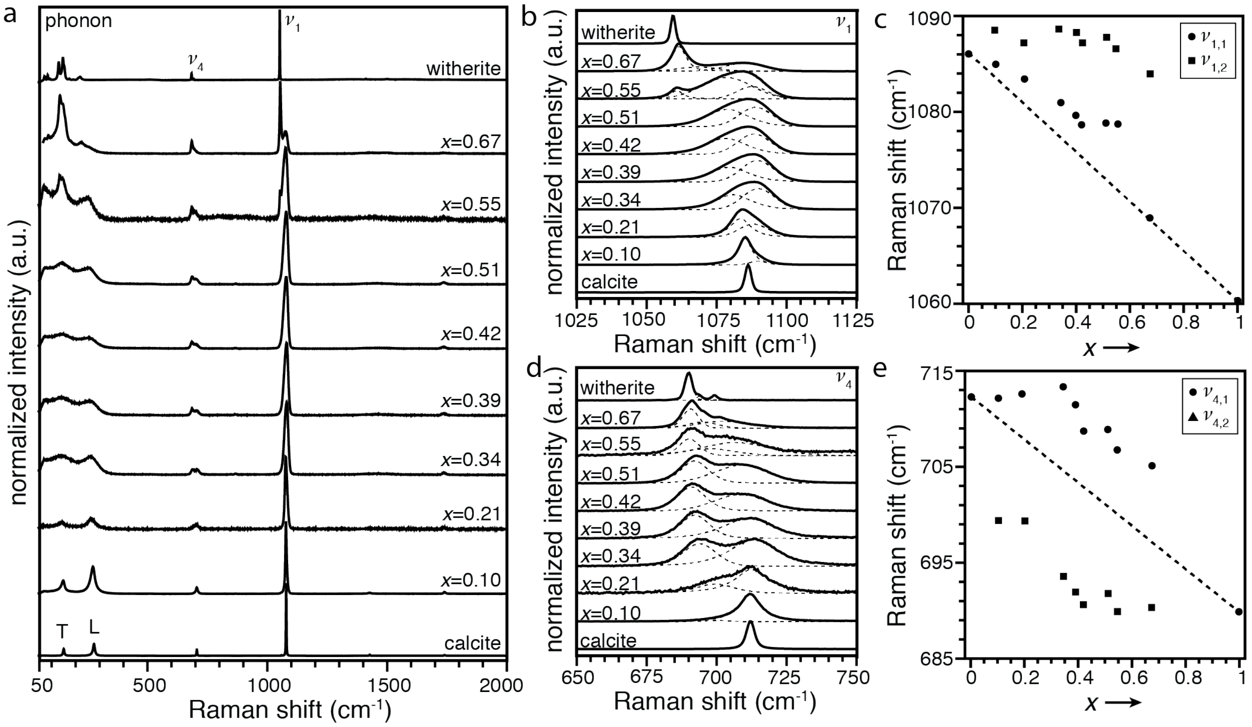

Figure 10.6. Raman spectroscopy of crystalline precipitates from ACBC precursors. (a) Full spectra of geological calcite (bottom) and witherite (top) and $Ca_{1-x}Ba_xCO_3$ materials with x = 0.05, 0.11, 0.21, 0.29, 0.38, 0.51, 0.55, and 0.67. The phonon modes (T and L in calcite) broaden and shift to lower wavenumbers, but are clearly present up to x = 0.51. (b, c) The $\nu_1$mode of calcite splits into two distinct modes ($\nu_{1,1}$, $\nu_{1,2}$) with increasing x, which shift linearly up to x = 0.50. (d, e) The ν_4 mode also splits into two ($\nu_{4,1}$, $\nu_{4,2}$).

10.4 **ACBC Transformation**

10.4.1 *Aqueous solution*

Stirring ACBC solutions during aging produced different products than aged solutions that were not stirred. ACBC was prepared as described above, but was placed in a separate beaker and stirred with a Teflon coated magnetic stir bar at 100 rpm for 24 hours. For the compositions at which vaterite was initially present with balcite by XRD in the aged material ($x \leq 0.34$, Figure 10.2**a**), more vaterite and less balcite was obtained by stirring. In the most extreme example, at $x = 0.10$, balcite completely dissolved and only vaterite remained after 24 hours of stirring (Figure 16.7). At initial compositions $x = 0.21$ and 0.34, the (102) peak shifted to lower Bragg angles after stirring, while diffraction from vaterite increased in relative intensity. This is an indication that balcite became enriched with barium as more vaterite formed. While balcite with $x = 0.39$ did not co-precipitate with vaterite, its peaks also shifted slightly to lower Bragg angles after stirring, consistent with a reduction in the calcium to barium ratio in the precipitate. Unlike precipitates with lower barium content, XRD of the material at $x = 0.42$ did not change appreciably over the course of 24 hours.

At $x = 0.48$, balcite diffraction was largely unchanged even after one month of constant stirring. Balcite with $x = 0.48$ was equilibrated with Nanopure water and samples were removed after one, three, seven, and 12 months, washed with water, dried, and pXRD was collected (see Materials and Methods). After one month there was no appreciable change in the diffraction pattern (Figure 16.6). After three months, balcite had partially dissociated into calcite and witherite. More witherite and calcite were observed after seven months. At this composition balcite appeared to be converted into similar structures with different stoichiometry, as evidenced by multiple Bragg peaks near the balcite (102) at $2\theta = 28.2°$. After 12 months mostly witherite and calcite remained, and the balcite (102) peak was replaced by two small Bragg peaks to either side of the original peak, at 27.8° and 28.5°. Clearly, the persistence of balcite is highly dependent on its composition. Therefore, it is of interest to understand differences in how balcite forms at from ACBC.

10.4.2 *Solid State NMR*

While the three lower Ba ratio solutions yielded ACBC that is temporally stable (>2 months), ACBC's precipitated from 50% solutions, spontaneously transformed to balcite and phase-separated witherite. Three ACBC preparations with 12, 8 and 6 hours water evacuation at the final step, completed the transformation within over a week and down one day. The two shorter evacuation periods (8 and 6 hours) resulted in the faster transformations, suggesting therefore that water excess enhance the transformation rate.

The transformation of the ACBC-50% precipitates is evidenced (Figure 10.4b) by the carbonate peak changing from the characteristic ACBC chemical shift of ~169 ppm, to the that of the "neat" balcite at ~ 167.6 ppm (DE), accompanied by the formation of phase separated witherite as seen by the 169.7 ppm partially resolved shoulder.

The water content in the spontaneously transforming ACBC was directly followed by ^{1}H DE MAS NMR (Figure 10.4b). As the transformation progresses, the broad structural water peak (δ ~ 4.7, δν ~ 3.0 ppm) significantly narrows and shifts to high field (δ ~ 4.4, δν

~ 0.15 ppm), representing extraction of these waters and their accumulation as mobile water molecules comprising clusters residing at/between crystallite edges. Noteworthy, the extraction of water from within the amorphous ACBC solid was detected in the ^{1}H spectra prior to the detection of crystalline balcite via ^{13}C DE MAS (Figure 10.4a, +15 hours spectra). ACBCs prepared with lower Ba ratios did not show any change of the ^{1}H spectrum with time, hence making the ^{1}H spectra a pre-transformation marker. Mild evacuation of the ACBC-50% precipitates after crystallization for10-70 minutes, gradually removed most of the mobile, non-structural waters, as manifested by disappearance of the narrow peak, keeping the structural waters of the residual hydrated ACBC form as evidenced by exposing only their broad structural water peak (Figure 10.4b, dashed trace).

The overlaid ^{13}C CP and DE MAS spectra vs. time (Figure 10.4a), clearly show the diminishing CP intensity, further attesting for the disappearance of the hydrated ACBC form as a result of its conversion to anhydrous crystalline balcite (accompanied by water extraction; Figure 10.4b) and phase separated witherite.

Considering the 50% starting conditions for ACBC and balcite precipitation, below 5% hydrated ACBC remains after the spontaneous transformation, yet 15-25% remain after standard balcite precipitation (24 hrs incubation in the mother liquor followed by oven drying at 110 °C, x = 0.24-0.51), therefore indicating that the spontaneous transformation reaches higher completeness and yields “purer” balcite phases (not shown). This difference in behavior is attributed to the difference in water content and its impact on the kinetics and/or thermodynamics. In one case, crystallization proceeds while soaked in the mother liquor - “water” excess, while in the second case, a “measured” removal of excess water is employed upon isolation of ACBC(-50%). Of interest is that instability that leads to ambient spontaneous transformation is found only for ACBC’s with the high Ba content, a point that calls for broader consideration.

Witherite content varied some between the preparations of the three ACBC-50% and of the five directly precipitated balcite samples, hence spanning the practical variability involved in sample preparations (not shown).

10.5 **Crystallization in confinement**

Recently, the crystallization mechanism of ACC and kinetics of its transformation to vaterite were quantified using a water-in-oil emulsion drop system (chapter 7) Here, we have extended this method to ACBC in order to observe the impact of barium on the crystallization of ACC. Briefly, aqueous droplets were produced in fluorocarbon oil (HFE7500) using a polydimethylsiloxane (PDMS) microfluidic device with a hydrodynamic flow-focusing geometry. To stabilize droplets against coalescence, the fluorocarbon phase contained 2% (w/w) block copolymer surfactant. Aqueous $BaCl_2/CaCl_2$ mixtures with 1 M total concentration were encapsulated in drops. The barium fraction in aqueous solutions (x^{feed}) was determined by inductively coupled plasma – optical emission spectrometry (ICP-OES) to be 0.144 ± 0.001, 0.167 ± 0.003, 0.255 ± 0.002, 0.345 ± 0.008, or 0.534 ± 0.005. Drops were collected at the outlet of the flow-focusing device and then loaded into a second device designed to store the drops in individual wells for imaging.

Precipitation was initiated via gas diffusion from aqueous ammonium carbonate channels separated from the drop storage wells by PDMS.

Images of between 75-100 drops were acquired every minute after the start of ammonium carbonate flow. Each experiment was repeated three times, for a total of 267-290 drops. Similar to ACC, ACBC particles form throughout the volume of the drop within one minute after initiating $(NH_4)_2CO_3$ flow through the channels. Particles grow and eventually coalesce over the course of ~30 minutes, sinking and becoming an aggregated mass that rests at the aqueous/surfactant+oil interface (Figure 10.7a). Growth of ACBC slows approximately 30 minutes after precipitation. Imaging with crossed polarizers allowed ACBC to be distinguished from crystalline precipitates from the absence of birefringence (Figure 10.7d). Confocal Raman microscopy of the non-birefringent precipitates is consistent with that from bulk ACBC (Figure 16.9). From the linear relationship between the shift in the ν_1 mode peak and x previously established for ACBC (chapter 7) the barium content of the precipitates was found to be similar to that of precipitates formed in bulk solution (Figure 16.10).

Using the first detection of birefringence as an indicator of crystallization, the number of drops containing ACBC which had not crystallized, N_0, was tracked over time. The ratio of N_0 to the total number of drops, N, describes the crystallization rate[42] and is plotted in Figure 16.9g. It is immediately apparent that ACBC crystallized much more rapidly than ACC. While 23% of ACC crystallized on average over the course of 50 hours, 72% of ACBC with $x^{feed} = 0.144$ crystallized over the same timeframe. At higher barium content

($x \geq 0.167$), 99-100% of drops crystallized within just 2.2 hours. Furthermore, no crystals were observed for the first 1.2 hours, confining the time during which crystallization occurred to approximately 1 hour. The time between detection of the first and last crystals were similar at these higher compositions, at 27 ± 3 minutes. However, the time until the first crystal was detected decreased with increasing barium, shifting the sharply sloped portion of the curve to earlier times.

In addition to being considerably more rapid, the crystallization rate of ACBC deviated from the single exponential decay expected from classical nucleation with a single barrier height.[42] This behavior was also reflected in the appearance of the transformation process in bright field optical images. In contrast to the obvious dissolution of ACC at the expense of growing vaterite crystals (chapter 7) birefringence appeared across ACBC at many points nearly simultaneously, and increased in intensity without appreciable change in overall shape. For example, at $x^{\text{feed}} = 0.345$ ACBC particles (Figure 10.7b, e) slowly started to become birefringent (Figure 10.7c, f) after 125 minutes. The number and intensity of birefringent regions in a single drop increased over the course of ~10 minutes, until the entire precipitate appeared bright (Figure 10.7d, g). Raman spectra confirm that the birefringent precipitates in drops are balcite, with compositions similar to those obtained from bulk precipitation (Figure 16.10).

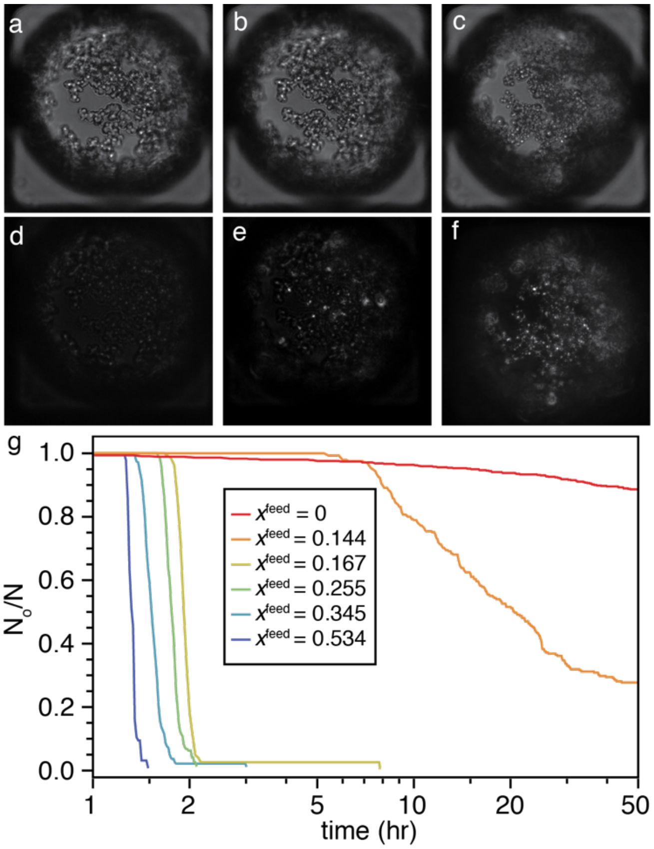

Figure 10.7. Crystallization of ACBC. Imaging under (a-c) bright field and (d-f) polarized light conditions. Initially non-birefringent precipitate (d) becomes birefringent at multiple sites within one minute (e) despite appearing macroscopically unchanged (a, b). After 10 minutes, the entire precipitate becomes birefringent (f) and appears to have increased the precipitate volume, despite maintaining the overall shape observed in the amorphous precipitate (c). (g) Plot of N_o/N versus time, showing the dramatic increase in crystallization rate with increasing barium and a distinct difference in rate behavior.

10.6 **Discussion**

Previously, we have shown that ACBC ($Ca_{1-x}Ba_xCO_3·1.2H_2O$) with $0 < x \leq 0.55$ can by synthesized in aqueous solution and can persist for days after drying (chapter 7). Furthermore, ACBC with $x = 0.50$ can promote the formation of balcite, a hard, high temperature $Ca_{1-x}Ba_xCO_3$ phase with $x = 0.50$.[121] Here, we have extended the ambient temperature synthesis of $Ca_{1-x}Ba_xCO_3$ to compositions $0 < x < 0.50$. We find that at approximately $x \leq 0.25$, the precipitates were enriched with barium compared to the amorphous precursor, displayed anisotropic particle shapes, and were found with vaterite as a co-precipitate. However, for $0.25 < x < 0.5$, the barium content in balcite was nearly identical to that in the ACBC precursor, the particles were spherulitic polycrystals, and no secondary phases were observed. These differences in phase assemblage, composition, and particle shape also corresponded to discontinuous behavior in the carbonate vibrational modes and a dramatic and discontinuous change in the crystallization kinetics. Therefore, we extend the 'balcite' label to $Ca_{1-x}Ba_xCO_3$ with $0.25 < x < 0.50$, and refer to materials with $x < 0.25$ as barium substituted calcite. To understand why balcite forms rapidly and persists at high barium concentrations but not low, the structure of balcite, and its impact on crystallization pathways from ACBC, are discussed.

10.6.1 *Structure of balcite*

Balcite synthesized from ACBC in bulk solution forms as 5-20 μm spherulitic polycrystals with faceted surface features less than 100 nm (Figure 10.1), similar to many other mixed-cation carbonates.[185,186] From X-ray powder diffraction of both as-synthesized and annealed balcite, we confirm the $R\bar{3}m$ symmetry of balcite with $x \cong 0.50$ (Figure 10.2b, c), as determined previously.[121] The initially nanoscale crystallites coarsen when heated (Figure 10.2b, c, Figure 16.2). Coarsening is indicative of high ionic mobility, which is consistent with nanoscale segregation of barium and calcium. Emergence of a superlattice reflection (Figure 10.2c, Figure 16.2) is associated with the separation of calcium and barium to alternating cation planes. This segregation is similar to structural analogs dolomite ($Ca_{0.5}Mg_{0.5}CO_3$)[187] and norsethite ($Mg_{0.5}Ba_{0.5}CO_3$),[186] which also exhibit superlattice reflections due to cation ordering.

It has previously been shown that calcium and barium are distributed homogeneously at the micron scale in balcite.[121] The absence of a superlattice reflection in material synthesized under ambient conditions is a strong indication that calcium and barium are distributed uniformly at the nanoscale prior to heating. At compositions intermediate to calcite and balcite, we observed the gradual disappearance of the (113) diffraction peak with increasing barium concentration (Figure 10.2a). This suggests that compositions with $0 < x < 0.51$ represent a continuum between calcite and balcite structures. Interestingly, this behavior resembles that observed in high temperature calcite and $Ca_{1-x}Ba_xCO_3$ (Figure 16.1).[156] Approaching a critical temperature of $T_c = 970°C$, calcite undergoes a second-order phase transition to 'carbonate disordered' calcite IV.[188,189] This transition is characterized by an inversion about the carbon center of carbonate anions, such that they are effectively rotated 60° about their threefold axes into inequivalent lattice positions. At temperatures above 970°C calcite IV becomes further disordered into a 'carbonate-melted' phase with $R\bar{3}m$ symmetry, labeled calcite V. [188-190] This transition has important implications for the $CaCO_3$-$BaCO_3$ system. Structural similarity between high temperature $Ca_{1-x}Ba_xCO_3$,[156,191,192] and balcite formed from ACBC suggests that the amorphous precursor pathway provides access high-temperature regions of the phase diagram. From the foregoing discussion, it appears that the carbonate ion orientation plays an integral role in the structure of balcite.

10.6.2 *Carbonate orientation*

At high temperatures, witherite (Pmcn) undergoes a first order transition to a calcite-type phase with R3m symmetry at 811°C.[193] This R3m phase has the same cation sublattice as calcite and balcite, and only differs in the anion orientation. In the R3m $BaCO_3$ structure, the apices of triangular carbonates all point the same direction. The addition of barium to calcite at high temperature causes gradual transition from $R\bar{3}c$ to R3m structures, which necessarily proceeds through $R\bar{3}m$ structure, exhibiting mixed carbonate orientations (Figure 11.2).[156,191,192]

Cations are 6-fold coordinated in the $R\bar{3}c$ spacegroup of calcite, while they are 9-fold coordinated in R3m of high temperature $BaCO_3$. There are no reports in the Inorganic Crystal Structure Database of barium with less than 8-fold coordination, and low coordination numbers like the 6-fold coordination barium in the calcite lattice are unfavorable. [194,195] A sufficiently high concentration of barium on 6-fold coordinated site may therefore favor the reconfiguration of neighboring carbonates towards local order that more closely resembles that found in R3m $BaCO_3$. At $x = 0.50$ our XAS results indicate that the coordination number of barium was 8 ± 1.0 (Figure 10.3, Table 10.1). At the same composition, the calcium coordination was 6.8 ± 0.2. This suggests that barium does disrupt the carbonate lattice, favoring higher coordination at the expense of 6-fold coordinated calcium. The large standard deviations, especially for barium, and large Debye-Waller factors for both cations (Table 10.1), suggest that there is a distribution of coordination environments around each cation. This is consistent with a random distribution of calcium and barium, as inferred from the absence of cation ordering reflections in the as-synthesized material (Figure 10.2b, c). To directly probe the effects of barium on carbonates anions, Raman spectroscopy and solid state NMR were employed.

Raman spectroscopy is sensitive to changing symmetry of lattice phonons and carbonate anions. At < 400 cm^{-1}, lattice phonon modes result from collective oscillations of both cations and anions.[169] The persistence of the T and L phonon modes (E_g) of calcite up to $x = 0.51$ confirm that structures maintain calcite-type symmetry at these compositions. Raman spectra of calcite have shown a similar phonon mode peak broadening and shift approaching the aforementioned calcite disordering transition at high temperatures.[196] In balcite, these peaks shift to lower wavenumber and broaden with increasing x, consistent with an increasing amount of barium on calcium lattice sites.

Internal carbonate modes were also affected by the barium content. The ν_1 mode (symmetric stretch, A_{1g}) split into two peaks, with $\nu_{1,2}$ remaining near the ν_1 of calcite at 1086 cm^{-1} and the $\nu_{1,1}$ shifting to lower wavenumbers with increasing barium content

(Figure 10.6a-c). This split is likely an indication of the emergence of a symmetrically inequivalent carbonate position. In the presence of any combination of barium and calcium in the first coordination shell of a carbonate anion, its inversion center is necessarily lost and the A_{1g} symmetry of this mode is reduced. Decreasing intensity, but relative positional invariance of the $\nu_{1,2}$ (Figure 10.6c) suggests that this peak is associated carbonates that retain calcite-like coordination. Decrease of the $\nu_{1,1}$ peak center towards that found in witherite, while increasing in in intensity, suggests that these carbonates are those associated with barium in their first coordination shells. However, this mode shifts less dramatically above $x = 0.21$ than below.

The ν_4 mode also evolves with increasing x. A single peak (asymmetric bending, E_g) in calcite splits into at least two peaks ($\nu_{4,1}$, $\nu_{4,2}$). Similar to the $\nu_{1,1}$ mode, both ν_4 modes appear to exhibit disparate behavior at low and high barium. Nonetheless, an evolution towards a witherite-like distribution of ν_4 modes with increasing is unmistakable. This is similar to the recent observation that strontium incorporated into calcite through an ACSC precursor adopts strontianite-like 9-fold coordination in the calcite lattice at high concentrations.[132] Therefore, it appears that a second population of carbonates, with coordination environments similar to those in witherite, emerges with increasing barium.

10.6.3 *Balcite metastability*

Crystallization of ACC in solution, while often proceeding through metastable vaterite,[100] ultimately yields calcite, the thermodynamically stable phase of $CaCO_3$ at ambient temperature and pressure. Barium is known to slow the growth of calcite[197,198] due to incompatible geometry at surface sites,[199] leading to unfavorable interfacial energetics.[200] In addition, its substitution in the calcite lattice is energetically unfavorable[195] due to the 6-fold coordination imposed by the lattice,[194] indicating that barium can be a potent calcite inhibitor. At moderate supersaturations with respect to both calcite and witherite, an unidentified secondary phase nucleates on the surface of growing calcite crystals,[197] suggesting that barium concentrations in excess of equilibrium solubility in the calcite lattice are difficult to achieve through conventional growth mechanisms. Witherite, the thermodynamically stable phase of $BaCO_3$ at ambient conditions, is less soluble than calcite[201] and has a low tolerance for calcium ions.[156] Therefore, the ground state of the Ca-Ba-CO_3 system is expected to be phase separated calcite and witherite. This is different from analogous mixed cation phases norsethite ($Mg_{0.5}Ba_{0.5}CO_3$) and dolomite ($Mg_{0.5}Ca_{0.5}CO_3$), which are stable relative to phase-separated magnesite and witherite, or magnesite and calcite.[104]

However, barium has been incorporated into calcite in excess of the ~1% thermodynamic limit through rapid precipitation kinetics.[154] At high concentrations (>10 millimolar) 'gels' consistent with the description of ACBC (chapter 9) have been reported, which allow up to 50% of the calcium in $CaCO_3$ to be substituted for barium. Crystalline precipitates reported to form under these conditions have pXRD patterns consistent with balcite but have been indexed as calcite, [202,203] or erroneously described as barytocalcite.[179,204-206]

Because balcite appears to be metastable, and the high degree of barium incorporation is likely a result of rapid formation kinetics, balcite is expected to recrystallize over time. This was observed in bulk samples with $x < 0.34$, where balcite dissolved after stirring for 24 hours in its mother liquor (Figure 16.7). Either vaterite alone or vaterite and balcite with a different composition were obtained. Shifting of the (102) peak in pXRD to lower Bragg angles was consistent with balcite that became enriched with barium as more vaterite formed. Data are not available on the solubility of barium in vaterite, although XRD patterns and Raman spectra of vaterite appeared to be unaffected by the amount of barium in solution (Figure 16.9), suggesting that the solubility of barium in vaterite is very low.

The complete dissolution of balcite with $x = 0.10$ is surprising, as it means that Ba^{2+} dissolved back into solution to a concentration of 50 mM and did not precipitate as witherite, despite being significantly supersaturated (Supplemental Information). This suggests that calcium is an inhibitor of witherite formation. Furthermore, it confirms that balcite with low barium content is less stable than vaterite at this composition. This is consistent with reports that micro- to millimolar concentrations of barium present during aqueous $CaCO_3$ precipitation appear to promote the formation of vaterite.[154,207] With increasing barium content, balcite did not completely dissolve after 24 hours of stirring, but balcite peaks in pXRD shifted to lower Bragg angles, consistent with increasing barium content in the precipitate. Negligible change to the samples with $x = 0.42$ and 0.50 after

24 hours suggests that increasing barium concentrations stabilized balcite against dissolution.

Mutual inhibition of the formation of calcite by barium and witherite by calcium may explain the persistence of balcite in aqueous solution. Only after stirring for months in solution did calcite and witherite peaks emerge from balcite with $x = 0.50$ (Figure 16.6). Disappearance of initial (102) diffraction peak at $2\theta = 28.2°$ and emergence of peaks at both lower and higher Bragg angles indicates that dissolution did not occur in a single step, but appeared to proceed via the formation of balcite with compositions with both more and less barium compared to the starting material. The decomposition of balcite into phase-separated materials from the initially homogeneous distribution of calcium and barium in ACBC precursors is a clear indication that the composition of balcite can evolve through dissolution and re-precipitation. However, evidence from crystallization in confinement, as well as solid state NMR, suggests that the initial crystallization from ACBC may traverse an alternate pathway.

10.6.4 *Transformation mechanism*

Understanding the preferential formation of metastable balcite from ACBC over more stable phases like barytocalcite, other reported $Ca_{0.5}Ba_{0.5}CO_3$ polymorphs alstonite and paralstonite,[156,208,209] or phase separated calcite and witherite, is essential for extending this crystallization pathway to other systems of interest. Different crystallization products for samples enriched with ^{13}C, (vaterite at $x = 0.24$ and witherite at $x = 0.51$), are suggestive of a transformation mechanism that is sensitive to isotope composition. Isotopically enriched ACMC has been shown to crystallize to Mg-calcite via a predominantly dissolution-reprecipitation mechanism.[97] Using drops to study crystallization of ACC in confinement, it was shown that vaterite nucleates via a classical mechanism from ACC, and grows through dissolution of ACC and reprecipitation as vaterite (chapter 7). The behavior observed from ACBC is far different, such that it cannot be described with the same theoretical framework. Future efforts will focus on applying an appropriate kinetic model to the data to extract quantitative information about the transformation process.

10.7 **Conclusions**

These experiments revealed that although balcite is thermodynamically uphill from phase-separated calcite and witherite, it is thermodynamically downhill from ACBC. This emphasizes the importance of the intermediate ACBC phase as an energetic stepping-stone between the supersaturated solution and balcite. This may also explain why balcite was not synthesized at concentrations greater than $x > 0.5$. Beyond this concentration, we observed only phase-separated witherite and balcite with $x = 0.5$. This is consistent with previous reports that suggest ACBC is necessary for the formation of balcite, as ACBC has not been prepared with barium contents in excess of $x = 0.55$ (chapter 11) The transformation mechanism from ACBC to balcite is inconsistent with that previously observed for the crystallization of ACC, and will be investigated further.

10.8 **Materials and Methods**

10.8.1 *Consumables*

Unless otherwise noted, all aqueous solutions were prepared using ultra-pure water (ρ=18.2 MΩ ·cm) prepared with a Barnstead NanoDiamond UF + UV purification unit. Reagent grade (>99%) $BaCl_2{\cdot}2H_2O$, $CaCl_2{\cdot}2H_2O$, $Na_2CO_3{\cdot}2H_2O$, $CaCO_3$, $BaCO_3$, (Sigma-Aldrich), were used without further purification. Iceland spar calcite was obtained from Dave's Down to Earth Rock Shop in Evanston, IL, USA. Geological witherite (cat #M21424) reference material was provided by the Field Museum of Natural History in Chicago, IL USA.

10.8.2 *ACBC/balcite synthesis*

Amorphous calcium barium carbonate (ACBC) was synthesized by rapid mixing of a cold aqueous solution of the alkaline earth chlorides ($[Ca^{2+}]+[Ba^{2+}]$ = 1 M, pH 5.6-5.7, solution A) with a cold aqueous solution of Na_2CO_3 (1 M, pH 11.7, solution B). The mole fraction of Ba x^{feed} was varied between 0 and 1. For instance, to prepare solution A with x^{feed} = 0.50, 3.053 g $BaCl_2{\cdot}2H_2O$ (125 mmol) and 1.838 g $CaCl_2{\cdot}2H_2O$ (125 mmol) were dissolved in water to a final volume of 25 mL. For solution B, 3.100 g Na_2CO_3 (250 mmol) dissolved in water to a final volume of 25 mL. Both solutions were then stored on ice for 2 h. Ice cold solution B was rapidly added to solution A, mixed rapidly and thoroughly by vigorous shaking for 30 s.

To isolate ACBC, the resulting white precipitate was immediately collected by vacuum filtration through a 100 mm diameter Whatman no. 4 cellulose filter paper, washed 3 times with 5 mL cool water (T = 10°C), and dried under vacuum (R.T., p ≈ 10 Pa = 10-1 Torr, 24h). Crystallization of ACBC was initiated by aging at ambient conditions for 24 hours in its mother liquor. It was then collected by vacuum filtration using the same procedure as for ACBC, with an additional drying step at 110°C for 1 hour.

To establish the metastability of balcite, 500 mg of balcite and 10 mL water were combined in a 15 mL polypropylene centrifuge tube and mixed in a Elmi Intelli-Mixer at 30 rpm.

10.8.3 *XRF*

The barium mole fraction, x, of single-phase balcite was determined on a custom built X-ray fluorimeter with an Ag-anode operating at 15 mA and 40 kV. Detector calibration was performed using the Fe and Mo K_α lines of a stainless steel ingot of known composition. Background scattering was subtracted from the raw spectra, and corrections for matrix absorption and Compton scattering were applied using XRF-FP v5.2.7 software from CrossRoads Scientific. Integrated Ba $L_{\alpha,1}$ and Ca K_{α} fluorescence intensity was obtained by fitting Gaussian peak profiles to all Ca and Ba fluorescence peaks. From the Ba $L_{\alpha,1}$ and Ca K_{α} fluorescence intensities, x was determined.

10.8.4 *Scanning electron microscopy (SEM)*

Approximately 5 mg of the dry powder was deposited on carbon tape and coated with ~5 nm osmium with an SPI OPC-60A Osmium Plasma Coater. Imaging was performed in a Hitachi S4800 FE-SEM or Hitachi S8030 operating at 20 keV at a working distance of 10 mm. Energy dispersive spectroscopy (EDS) was collected using AZtec software (Oxford Instruments).

10.8.5 *Powder X-ray diffraction (pXRD)*

Approximately 200 mg of the dry powder was pressed into low background amorphous silica sample holders for diffraction analysis. X-ray diffraction patterns were acquired on a Rigaku Ultima diffractometer using Cu Kα radiation (λ=1.504 Å), 0.05° step size, and sample-to-detector distance of 285 mm.

10.8.6 *Solid-State NMR*

MAS NMR spectra were acquired for the samples using two experimental techniques: Direct Excitation (DE) and ^{1}H-^{13}C Cross-Polarization. The DE technique yields quantitative spectra (using repetition delays that satisfy full relaxation of all species of ^{13}C), however with limited sensitivity (S/N). CP transfers polarization to the ^{13}C nuclei from of the adjacent hydrogen atoms, therefore enhancing the peaks of ^{13}C nuclei that reside in hydrogen rich environments and yielding for those high S/N spectra. By their nature, the peak intensities in such spectra do not reflect the relative abundance of the different chemical species.

^{1}H, ^{13}C NMR measurements were carried out on 500 and 300 MHz AVANCE III (Bruker) spectrometers using a 4 mm triple-resonance MAS NMR probe with 4mm zirconia rotors. Samples were spun at 5000 and 10000 ± 2 Hz. Cross polarization (CP) magic angle spinning (MAS) echo experiments (indirect excitation) were carried out with a 5.0

μs π/2, 10.0 μs π pulse widths, an echo interval τ (200 and 100 μs) identical to the rotor period TR, a ^{1}H decoupling level of 100 kHz, Hartmann- Hahn rf levels were matched at 50 kHz, with contact times (ct) of 0.5, 1, and 2 ms for 13C; relaxation delays of 3 s for 13C. Up to 16k transients were acquired.

Direct ^{13}C excitation echo experiments (DE) were carried out with a 5.0 μs π/2, a 10.0 μs π pulse widths, an echo interval τ equal to the rotor period TR (200 μs), a ^{1}H decoupling level of 100 kHz, and a relaxation delay of 2400 s (2400 s to fully relaxed) for ^{13}C. Direct excitation ^{13}C spectra acquired with recycling delay of 2400 s yield fully relaxed spectra.

^{1}H-^{13}C 2D-HETCOR experiments were run employing the wPMLG5 homonuclear decoupling scheme during t_1 for the ^{1}H chemical shift evolution period. ^{1}H{^{13}C} 2D-HETCOR of glycine was optimized first for ^{1}H resolution and also served to calibrate the ^{1}H chemical shift scale. Time-proportional phase incrimination (TPPI) was used to obtain purely absorptive 2D NMR spectra with frequency sign discrimination along the indirect dimension. The chemical shifts of ^{13}C and ^{1}H are reported relative to TMS and adamantane, respectively, with ±0.1 ppm certainty; linewidths are also determined with ±0.1 ppm certainty. Peak areas were calculated by deconvolution using DMFIT and Topspin.

10.8.7 *Raman microscopy*

Approximately 5 mg of the dry powder was pressed onto a glass slide for Raman analysis. Raman spectra were obtained on a Horiba LabRam confocal Raman microscope with a laser of wavelength λ = 532 nm, operating at a power of 49 mW, and using a diffraction grating with 1800 gr/mm, resulting in a final spectral resolution of 0.39 cm^{-1}. All spectra were recorded from individual precipitate particles using a 100x objective lens in air (0.9 NA, minimum resolution ~361 nm). Mode centers, relative intensities, and full peak width at half maximal intensity (FWHM) were determined by fitting one or more Gaussians to the spectral region of interest. Fitting was performed manually using in-house code written in Mathematica.

10.8.8 *X-ray absorption spectroscopy*

Samples for X-ray absorption spectroscopy were synthesized in the same way as above. Approximately half of the ACBC sample (with x = 0.50) was left in the mother liquor to make the balcite sample. Measurements were performed at the Dow-Northwestern-Dupont collaborative access team (DND-CAT), Sector 5-BM-D of the Advanced Photon Source at Argonne National Laboratory. Samples for Ca K-edge measurements were spread on 8 μm Kapton tape and kept dry under a stream of He gas. For measurements performed at the Ba K-edge, powders were loaded in quartz capillaries Calibration at the Ca K-edge was performed with a geological Iceland spar (calcite) standard, for which the edge energy was set at 4038 eV. ACBC samples were measured relative to this value. Molybdenum foil (Mo K-edge at 20.000 eV) was used to calibrate the Ba K-edge to an absolute scale.

Data was analyzed using the Demeter package.[70] Normalization and background subtraction were carried out in Athena using Autobk. χ-data were weighted by k , k^2, and k^3 between $1.6 < k < 11.5$ Å^{-1} for the Ca K-edge and between $2 < k < 14$ Å^{-1} for the Ba K-edge. Fitting of the data to the crystal structures was performed using Artemis. The theoretical photoelectron scatting amplitudes and phase shifts were calculated using FEFF1. To generate the feff.inp file, which contains a list of the atomic coordinates centered at the absorbing atom, Atoms[71] was used to calculate the atomic coordinates centered at Ca. The total theoretical $\chi(k)$ for each model was then constructed from the most important scattering paths and fit in R-space (Ca K-edge) or k-space (Ba K-edge). Multiple scattering was not considered. While maintaining sufficient number of degrees of freedom, as defined by the Nyquist criterion, the coordination number, bond distance, Debye-Waller factor, amplitude reduction factor, S_o^2, and shift in energy origin, ΔE_o were determined previously. Satisfactory fits were not obtained using S_o^2 from the crystalline reference samples, which for calcite and witherite were >1. Fitting parameters are reported in the Supplemental Information. Coordination numbers and Debye-Waller factors are highly correlated and were fit separately, but in each case with all other parameters floating. The validity of the fits was determined by the R-factor, which was minimized to ≤0.01.

10.8.9 *High resolution synchrotron powder diffraction and Rietveld refinement*

Rietveld refinement was performed with GSAS using the EXPGUI graphical user interface.[210,211]

10.8.10 *In situ synchrotron wide angle X-ray scattering/differential scanning calorimetry*

Low mass aluminum pans (TZero) were filled with approximately 20 mg of powder and hermetically sealed by crimping an aluminum lid to the top of the pan. The pans were heated from 25°C to 600°C and cooled back to 25°C at a rate of 10°C/min in a Linkam DSC600 temperature stage controlled with Linksys32 software. WAXS patterns were collected every minute at intervals of 10°C. Diffuse rings consistent with a polycrystalline material were observed in two-dimensional CCD images. These images were radially integrated using custom beamline software.

10.8.11 *Inductively coupled plasma-optical emission spectroscopy*

The barium mole fraction x^{feed} of solutions of the starting solutions loaded into drops was determined by inductively coupled plasma-optical emission spectrometry (ICP-OES), using a Thermo iCAP 7600 instrument. Solutions were diluted 100x in water and then 200x in 3% by volume aqueous nitric acid. Intensities for the four strongest emission lines of barium (λ = 230.424, 233.527, 455.403, and 493.409 nm) and Ca (λ =315.887, 393.366, 396.847, and 422.673 nm) were recorded in both axial and radial geometries. Intensities were converted to absolute concentrations using a calibration curve recorded for a series of eight standard solutions ranging from 10 μg/mL to 4 ng/mL that were prepared by serial dilution. An average concentration value and standard deviation for barium and calcium was determined from 8 individual values (4 different emission lines in two geometries each). Finally, x^{feed} was calculated according to $x^{\text{feed}} = \frac{[\mathrm{Ca}]}{[\mathrm{Ca}]+[\mathrm{Ba}]}$, using the limits of uncertainty for individual measurements as bounds for the reported error.

11. ACBC to balcite: bioinspired synthesis of a highly substituted high temperature phase from amorphous precursors

11.1 Abstract

Energy efficient synthesis of materials locked in compositional and structural states far from equilibrium remains a challenging goal. Yet, biomineralizing organisms routinely assemble such materials with sophisticated designs and advanced functional properties, often using amorphous precursors. However, incorporation of organics limits the useful temperature range of materials. Herein, we report the bio-inspired synthesis of a highly supersaturated calcite ($Ca_{0.5}Ba_{0.5}CO_3$) that we call balcite, at mild conditions and using an amorphous barium-calcium carbonate (ACBC, $Ca_{1-x}Ba_xCO_3{\cdot}1.2H_2O$) precursor. Balcite not only contains 50 times more barium than the solubility limit in calcite, but also displays the rotational disorder on carbonate sites that is typical for high-temperature calcite. It is significantly harder (30%) and less stiff than calcite, and retains these properties after heating to elevated temperatures. Analysis of balcite local order suggests that it may require the formation of the ACBC precursor and could therefore be an example of non-classical nucleation. These findings demonstrate that amorphous precursor pathways are powerfully enabling and provide unprecedented access to materials far from equilibrium, including high temperature modifications by room-temperature synthesis.

11.2 Results and discussion

A recent paradigm shift in our understanding of $CaCO_3$ precipitation[6,9,80] has revealed a number of metastable intermediates that may precede the final crystalline phase. Amorphous precursors such as amorphous calcium carbonate (ACC) appear to be widespread in nature and can have a strong influence on the composition, structure and properties of the resulting biominerals.[73] ACC and amorphous magnesium carbonate (AMC) form a complete solid solution, which may be used to control the composition of biogenic magnesian calcite.[128] Similarly, it is possible to introduce Sr^{2+} in excess of the equilibrium solubility into the single crystalline calcite spicules deposited by the sea urchin embryo,[76] which are thought to form from an ACC intermediate.[75] 'Non-classical' crystallization of calcium, strontium, and barium carbonates have been described *in vitro*, although amorphous carbonates of the latter are quite labile and have only been observed in confinement.[44,48]

We hypothesize that the amorphous precursor pathway can be generalized to compositions and structures beyond those found in nature. To demonstrate this, we synthesized amorphous calcium barium carbonate (ACBC) using a variant of the ACC synthesis first described by Koga and modified by us for the preparation of amorphous calcium strontium carbonate.[76,153] Briefly, an ice cold aqueous solution of alkaline earth chloride(s) with a total cation concentration of 1M was rapidly mixed with an ice cold aqueous solution of 1M sodium carbonate. The resulting precipitate was filtered after 30s, washed with H_2O at 10°C, and dried under vacuum. The barium cation fraction of the feed solution x^{feed}= $[Ba^{2+}]/([Ba^{2+}]+[Ca^{2+}])$ was systematically varied between 0 and 1 and confirmed with inductively coupled plasma-optical emission spectroscopy (ICP-OES). X-ray fluorescence (XRF) analysis of bulk powders indicated that the cation fraction of barium in the precipitate, x, was proportional to that in solution, x^{feed} through the relationship $x \cong 0.86x^{feed}$ (Figure 11.1a).

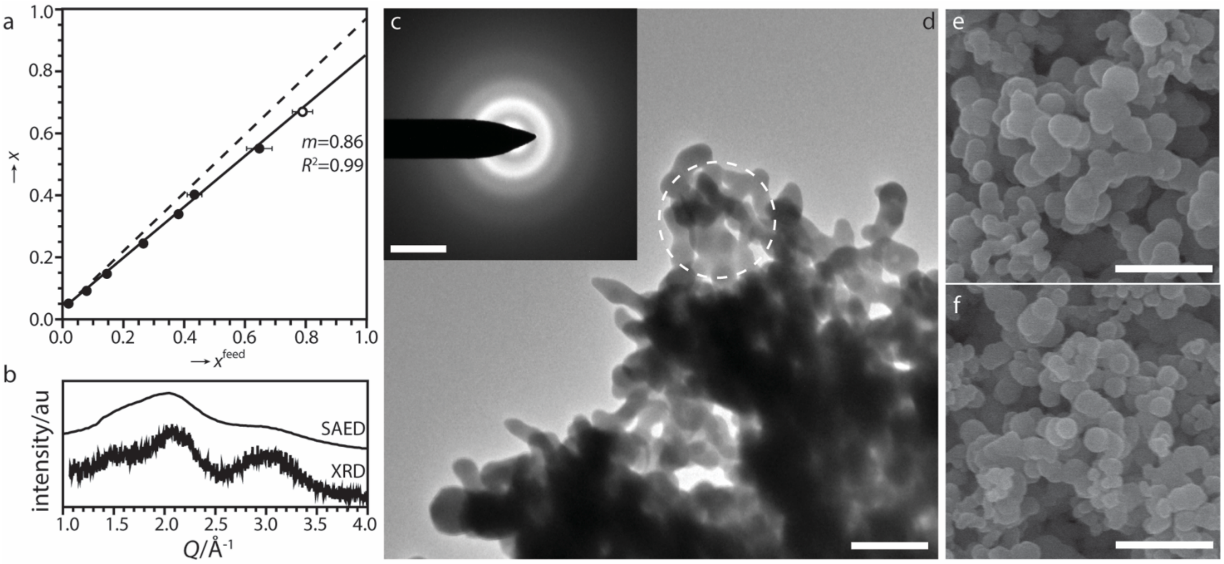

Figure 11.1. (a) Plot of the cation fraction, x, of barium in ACBC powders vs. cation fraction of barium in the feed solution, x^{feed}. Partial, albeit minimal, crystallinity could not be ruled out in the sample with x=0.67 (open circle and Figure 17.1). Error bars represent one standard deviation. (b) Plot of the radially integrated SAED and pXRD intensity vs. scattering vector, Q, of ACBC (x = 0.55, $Q = \frac{4\pi sin\theta}{\lambda}$, where θ is the scattering angle and λ the wavelength of radiation). (c) 2D SAED pattern (scale bar 5 nm^{-1}) and (d) Bright field TEM image of ACBC with x = 0.55. SAED area indicated by dashed circle in (d). (e, f) SEM images of ACC (e) and ACBC (x = 0.55), (f) are indistinguishable. Scale bar represents 500 nm.

Inspection of dry powders by scanning electron microscopy (SEM) and transmission electron microscopy (TEM) revealed that they consisted of roughly spherical, partially coalesced particles approximately 200 nm in diameter (Figure 11.1d-f). Precipitate particles with $x = 0.55$ were indistinguishable from those in ACC formed under similar conditions (Figure 11.1e, f). In a similar concentration regime, spinodal decomposition has been suggested as a mechanism of phase separation in the $CaCO_3$-H_2O system.[6,62] It is unclear whether a spinodal exists also in the (Ba,Ca)CO_3-H_2O system, and our data does not allow us to distinguish the mechanism by which ACBC forms. Witherite and other crystalline phases were apparent in powder X-ray diffraction (pXRD) patterns only for $x \geq 0.67$ (Figure 17.1). Radially integrated selected area electron diffraction (SAED) patterns were qualitatively similar to those recorded by pXRD (Figure 11.1b). Taken together, these results are strong evidence that the low temperature synthesis gave the desired ACBC powders over a range of compositions $x = 0.05 - 0.55$.

Up to $x = 0.55$, ACBC did not crystallize for over seven days when filtered rapidly and kept dry at room temperature. For $x > 0.55$, Bragg peaks in XRD (Figure 17.1), were consistently observed immediately following synthesis. Therefore, we chose ACBC with $x \cong 0.50$ to investigate the precipitates resulting from the crystallization of completely amorphous precursors. ACBC aged in the mother liquor for 24 hours transformed into a white precipitate consisting of spherical particles 10-20 μm in diameter (Figure 11.2a). These particles were birefringent under crossed polarizers (Figure 11.2b) and exhibited a 'Maltese cross' pattern, a hallmark of spherulitic polycrystals.[212] A single phase was observed in pXRD (Figure 11.2c), exhibiting Bragg peaks reminiscent of the most intense reflections in calcite. However, all peaks were shifted to lower Bragg angles (larger *d*-

spacing). In addition, the calcite (113) reflection was notably absent. This indicated that the structure resulting from the crystallization of ACBC with $x = 0.5$ was a derivative of the calcite lattice with similar, but not identical, symmetry.

To obtain a more detailed structural model, Rietveld refinement of synchrotron high-resolution powder X-ray diffraction (hr-pXRD) patterns of single-phase $Ca_{1-x}Ba_xCO_3$ with $x = 0.51$ was performed (Figure 11.2c). Following an earlier proposal for the structure of high-temperature calcite-type $Ca_{1-x}Ba_xCO_3$ phases based on the structural analog $NaNO_3$,[156] we modeled the absence of the calcite (113) reflection by adding an O to the calcite $R\bar{3}c$ unit cell at ($-X$, 0, ¼). This is has been described as a 'disordered carbonate' site,[188] where carbonate anions can occupy an alternate lattice orientation, distinguished

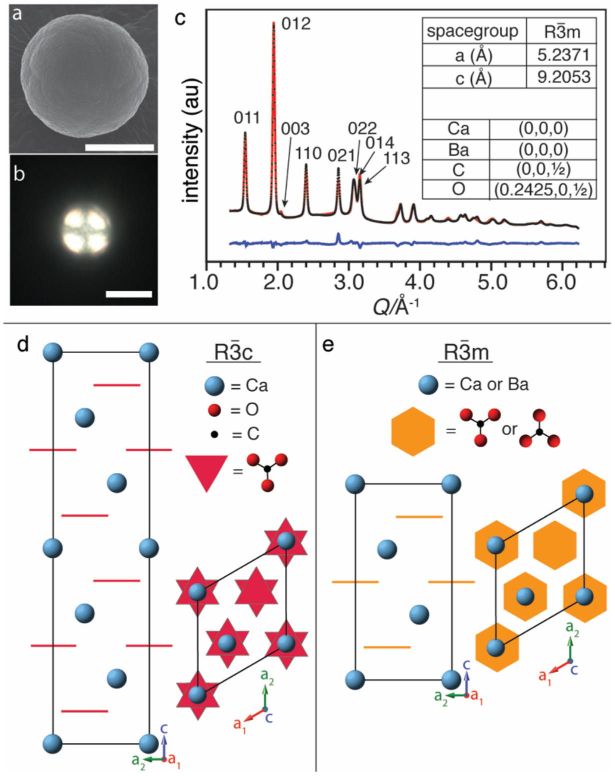

spacegroup	R3̄m
a (Å)	5.2371
c (Å)	9.2053
Ca	(0,0,0)
Ba	(0,0,0)
C	(0,0,½)
O	(0.2425,0,½)

Figure 11.2. (a) SEM image of balcite particle. (b) Polarized light microscopy image, revealing the 'Maltese cross' extinction pattern, a hallmark of spherulitic polycrystals. Scale bars represent 10 μm. (c) Rietveld refinement of hr-pXRD data confirms balcite is in the R3̄m spacegroup. Black markers are measured data, the red line is the fit, and the blue line is the fit residual plotted on the same scale. (d) Rendering of calcite structure in the R3̄c spacegroup, in which carbonate anions (red triangles) are facing opposite directions in alternating planes. (e) Rendering of balcite structure with R3̄m symmetry, where carbonates randomly occupy either of two rotational position at each lattice site, reducing the unit cell c-axis lattice parameter in half.

by a 60° rotation about their 3-fold axis. When this site is occupied, two identical subcells stacked along the [001] direction are produced, which can be described by a new cell with $R\bar{3}m$ symmetry and lattice parameter $c_{R\bar{3}m} = ½c_{R\bar{3}c}$ (Figure 11.2d, e). Rietveld refinement was performed using the $R\bar{3}m$ setting with atom positions Ca (0, 0, 0); Ba (0, 0, 0); C (0,0,½); O (X, 0, ½). Partial occupancy of the O site was set to 0.5, and those of Ca and Ba fixed at 0.49 and 0.51, respectively, based on XRF measurements. A high quality fit (reduced-χ^2 = 0.20) was obtained for the structural parameters given in Figure 11.2c. Taken together, these observations leave little doubt that the structure of balcite prepared at ambient conditions from ACBC is identical to the structure suggested for high-temperature $Ca_{1-x}Ba_xCO_3$.

To confirm this assessment, we heated balcite from 25°C to 600°C and then cooled back to 25°C while collecting synchrotron wide angle X-ray scattering (WAXS) *in situ*. Intense Bragg peaks from balcite were observed across the entire temperature range (Figure 11.3a). Peak centers shifted to lower Q (larger d-spacing) with increasing temperature, and peak width decreased considerably, with a marked sharpening between 525°C and 600°C. Peaks remained narrow, but shifted back to their original positions, in material brought back to room temperature. This confirms that solution-processed balcite is isostructural to high-temperature 'disordered calcite'. Rietveld refinement indicated that peak broadening in the as-synthesized samples was largely due to nanoscale crystallites (average diameter ~25 nm), which coarsened upon heating. Balcite structure does not revert to that of calcite or phase-separate at any temperature investigated.

Attempts to synthesize balcite under conditions where ACBC was not observed, e.g., 1 M $BaCl_2/CaCl_2$ in the presence of calcite and/or witherite, produced only physical mixtures of the two end members. Balcite was only observed under conditions in which ACBC precipitated prior to crystallization, namely high pH (>8) and high concentration (>100 mM). This is consistent with prior observations that describe formation of unspecified 'gels' during synthesis of highly barium-substituted carbonates,[202] which have been indexed as calcite[202] or mistakenly identified as barytocalcite.[206] Recently, it has been suggested that development of local order in ACC can kinetically favor a particular polymorph (e.g., vaterite over calcite) through a reduction in the barrier to nucleation of that particular polymorph.[120] Metastable vaterite ($CaCO_3$) spherulites are well known to crystallize from ACC,[100] and calcite spherulites have been shown to form with ACC as a nucleation center.[213] This is consistent with generalized phase field models of spherulites, which describe glassy, low diffusivity fluids (e.g., amorphous precursors[73]) as critical for initiating this type of growth.[212] Therefore, we hypothesized that ACBC templates the nucleation of balcite, which then grows spherulitically from these nucleation sites. This would be an example of a non-classical nucleation, where a transient phase acts as a heterogeneous nucleator.[214]

We therefore investigated potential indications of structural match between ACBC and balcite that might help explain the formation of a low energy interface between the two phases. Similar short-range order (< 5 Å) in ACBC and balcite was confirmed by Ca-K edge XANES (Figure 11.3b). Spectra of both ACBC and balcite display a single pre-edge feature (1s→3d) at ~4.035 keV that is more intense than in calcite, indicating a reduction in symmetry.[146] A second pre-edge feature (1s→4p) at ~4.040 keV is much broader and split in both ACBC and balcite. The white line at 4.045 keV is broadened in both ACBC and balcite, and the second post-edge peak between 4.055-4.060 keV is nearly absent in ACBC and only slightly more pronounced in balcite. Information about short- and mid-range order was obtained via pair distribution function (PDF) analysis of X-ray total scattering (Figure 11.3c). The lack of long-range order in ACBC is easily observed in the damping of oscillations in the pair distribution function, G(*r*), beyond 15 Å. In contrast, both calcite and balcite have pair correlations extending far beyond 50 Å, as expected for crystalline materials. The first four peaks at 1.3, 2.9, 4.4, and 6.7 Å were found in both balcite and ACBC and were distinct from calcite. Taken together these results suggest that the local coordination environment of calcium ions in ACBC is quite similar to that in balcite, despite the similarity of the long range order of the latter to calcite. This may be the reason why balcite formation is accelerated compared to calcite in the presence of ACBC, and is consistent with a non-classical nucleation mechanism. Whether the subsequent growth of balcite spherulites proceeds by a classical or a non-classical mechanism remains an open question.

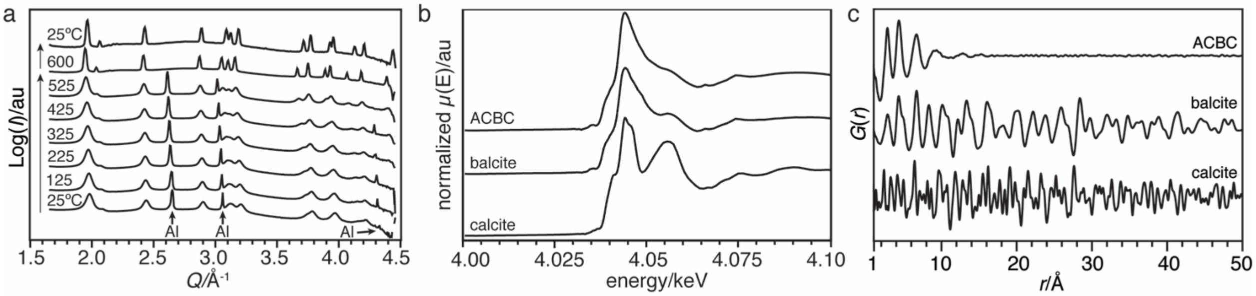

Figure 11.3. (a) In situ WAXS of ACBC ($x = 0.50$) as a function of temperature. (b) Ca K-edge XANES of ACBC (x = 0.55) and balcite (x = 0.51) are qualitatively similar, and distinctly different from calcite, suggesting similar local order in the first coordination shell. (c) Pair distance distribution function (PDF, G(r)) of ACBC (x = 0.55), balcite (x = 0.51), and calcite. ACBC has no pair correlations beyond 15 Å, demonstrating that it is amorphous with short range (< 5 Å) and limited mid range (< 15 Å) order. While balcite does exhibit long-range order, its G(r) has peaks that are broadened by the disorder of the carbonate anions.

The amorphous precursor route allowed us to synthesize balcite with a barium content approximately 50 times higher than the published solubility limit[154] of barium in calcite (Figure 17.2). Given the known impact of substitutional ions, like Mg^{2+} on the hardness of calcite,[215] we used nanoindentation to investigate the mechanical properties of balcite and compare to those of calcite. Nanoindentation hardness measurements performed on balcite spherulite cross sections reported a value of H = 4.1 ± 0.3 GPa (N = 10, Figure 17.3). Calcite spherulites of similar size (Figure 17.4), and containing approximately 6% magnesium substituted for calcium, had a hardness of 3.3 ± 0.3 GPa (N = 10), consistent with previous results.[215] Due to porosity near the center of both balcite and calcite spherulites, measurements were taken in the dense ~3-5 μm wide ring at the periphery of the cross section with an RMS roughness < 1nm (Figure 17.3). Balcite was over 20% harder than these calcite spherulites, and more than 30% harder than single crystalline calcite (2.5 – 3.0 GPa).[216] The hardness of purely inorganic balcite was equivalent to that of synthetic calcite with occluded amino acids, or biogenic calcite, for example the prismatic layer of *Atrina rigida* shells, in which proteins and other organic additives, substitutional magnesium, and hierarchical structuring provide multiple mechanisms of strengthening.[216] Heat-treated balcite had nearly identical hardness to the as-synthesized material (4.1 ± 0.4 GPa, N = 10), indicating that balcite can be processed at temperatures above those at which organics would decompose with no loss of performance. Balcite was not as stiff as calcite, with an average indentation modulus E_I = 52.3 ± 4.2 GPa for as-synthesized and 47.9 ± 3.2 GPa for heat treated balcite. In comparison, the modulus for calcite was 63.6 ± 5.9 GPa, consistent with previous results.[216]

The ambient temperature synthesis of balcite via an amorphous precursor described herein may represent a general, facile route for the production of highly metastable materials with low energy input. One advantage of amorphous precursors is that their relatively high solubility compared to crystalline materials allows *any* lower-energy structure to form via downhill transformations, i.e., Ostwald's rule of stages. Transformation rates to each lower-energy structure are then governed by the relative interfacial energies of each phase, which have a profound impact on nucleation barriers[99] and are often lower for higher energy structures.[17] Our investigation suggests that it may be possible to tune the local order in amorphous materials to reflect that of a particular crystalline polymorph (e.g., balcite), thereby selectively lowering the barrier to its formation. The compositional and structural flexibility in amorphous precursors compared to crystalline ones opens a much wider range of possibilities for this kind of control, here allowing us to kinetically trap a phase that is thermodynamically stable only at elevated temperature but with enhanced hardness compared to equilibrium phases.

11.3 **Experimental section**

11.3.1 *Consumables*

Unless otherwise noted, all aqueous solutions were prepared using ultra-pure water (ρ = 18.2 MΩ ·cm) prepared with a Barnstead NanoDiamond UF + UV purification unit. Reagent grade (>99%) $BaCl_2 \cdot 2H_2O$, $CaCl_2 \cdot 2H_2O$, $Ca(NO_3)_2 \cdot 5H_2O$, $Na_2CO_3 \cdot 2H_2O$, $Mg(NO_3)_2$, $(NH_4)_2SO_4$, $CaCO_3$, and $BaCO_3$ (Sigma-Aldrich) was used without further purification. Iceland spar calcite was obtained from Dave's Down to Earth Rock Shop in Evanston, IL, USA. Geological witherite (cat #M21424) reference material was provided by the Field Museum of Natural History in Chicago, IL USA.

11.3.2 *ACBC and balcite syntheses*

Amorphous calcium barium carbonate (ACBC) was synthesized by rapid mixing of a cold aqueous solution of the alkaline earth chlorides ($[Ca^{2+}]+[Ba^{2+}]$ = 1 M, pH 5.6-5.7, solution A) with a cold aqueous solution of Na_2CO_3 (1 M, pH 11.7, solution B). The mole fraction of barium x^{feed} was varied between 0 and 1. For instance, to prepare solution A with x^{feed}=0.50, $BaCl_2{\cdot}2H_2O$ (3.053 g, 125 mmol) and $CaCl_2{\cdot}2H_2O$ (1.838 g, 125 mmol) were dissolved in water (final volume of 25 mL). For solution B, Na_2CO_3 (3.100 g, 250 mmol) dissolved in water (final volume of 25 mL). Both solutions were then stored on ice for 2 h. Ice cold solution B was rapidly added to solution A, and mixed rapidly and thoroughly by vigorous shaking for 30 s. The resulting white precipitate was immediately collected by vacuum filtration through a 100 mm diameter Whatman no. 4 cellulose filter paper, washed 3 times with cool water (5 mL, $T = 10°C$), and dried under vacuum (R.T., $p \approx 10$ Pa $= 10^{-1}$ Torr, 24h).

Balcite with $x \cong 0.50$ was synthesized by first preparing ACBC in its mother liquor as outlined above. However, the precipitate was only collected by vacuum filtration after standing for 24 h in the mother liquor. Filtration, washing, and drying was carried out as described for ACBC, followed by an additional drying step (110 °C, 1 h). Energy dispersive spectroscopy (EDS) confirmed that the particles had the same composition as the ACBC from which they formed.

Calcite spherulites were prepared using a method modified from a previously reported procedure.[185] A solution of 25 mL of $Ca(NO_3)_2$ (50 mM) and $Mg(NO_3)_2$ (50 mM) was mixed with 25 mL of $(NH_4)_2CO_3$ (50 mM) and $(NH_4)_2SO_4$ (50 mM). The reported method included the $(NH_4)_2SO_4$ with the $Ca(NO_3)_2$ solution, but we found that this led to precipitation of $MgSO_4$. Precipitate began to appear after ~5 minutes, and was left to age for 8 h. The precipitate was filtered, washed with cold water (10 mL, 4 °C) and dried at 110 °C for 1 h. Analysis by EDS showed that the calcite spherulites contained 5.8 ± 0.9 % magnesium substituted for calcium and trace amounts of sulfate as a result of the synthesis procedure.

12. Quasi-2D barium carbonate hydrate via a transient amorphous precursor

12.1 Abstract

Synthesis of persistent metastable materials can provide access to unique properties inaccessible at equilibrium. However, detailed knowledge of reaction pathways is required to avoid the formation of competing or lower-energy phases. Here, we report the synthesis of a metastable hydrated barium carbonate, formed from a very transient amorphous barium carbonate (ABC) precursor. ABC was observed only during the first few hundred milliseconds of precipitation from concentrated aqueous solutions. Rapid crystallization of ABC resulted in the first described $BaCO_3 \cdot H_2O$ phase which we call gortotowskite. Gortotowskite platelets are highly anisotropic, 10-12 nm thick and up to 1 μm in width. It is very metastable and recrystallizes to witherite in less than one minute in solution, but can be preserved for 24 hours after drying under vacuum. Not only is this a promising pathway for the *de novo* synthesis of thin materials, it significantly improves our understanding of phase transformation via metastable intermediates at small time and length scales.

12.2 Results and discussion

Barium carbonate has recently attracted attention for the complex yet controllable nano- and microstructures that can form when precipitated under far-from-equilibrium conditions. For example, in the presence of silica, smoothly curving and branching witherite ($BaCO_3$) structures resemble biologically synthesized minerals.[172,173,217] Growth may occur through the addition of amorphous silica/barium carbonate nanoparticles,[218] analogous to biological crystals.[73] Remarkably similar to the fossilized remains of primitive life forms, these materials provide evidence that a high degree of control over the crystallization process can be exerted without organic molecules.[175] However, despite recent progress establishing a deterministic link between solution conditions and many specific morphologies,[172,173] the exotic crystallization behavior from barium-rich solutions remains incompletely understood.[174,175,217,219]

It appears that the mechanisms that underlie the formation of $BaCO_3$ may exhibit similarities to pathways of CaCO3 crystallization. Amorphous particles, described as liquid-like, can form prior to crystallization of both CaCO3 and BaCO3 in confinement[48,220] or in the presence of charged polymeric additives.[93] Amorphous calcium carbonate (ACC) is a common precursor to crystalline biominerals.[73] Amorphous barium carbonate (ABC) has been synthesized in media containing suspended bacteria,[221] and intracellular barium-containing amorphous carbonate precipitates have recently been found in many species of cyanobacteria.[222] In *vitro*, amorphous barium calcium carbonate (ACBC) solid solutions with over 50% barium cation fraction have been isolated.[121]

However, there are notable differences between precipitation pathways in $CaCO_3$ and $BaCO_3$ systems. Unlike amorphous carbonates of magnesium, calcium, manganese, iron, and radium,[73,130,133] ABC has not been detected in the absence of stabilizing additives and is short-lived even in confinement. ACBC with barium in excess of ~55% cation fraction crystallizes rapidly,[121] and no evidence of ABC was observed in in synthetic liposomes,[44] which can reduce the rate of crystallization of ACC.[99] Calcite and witherite have similar solubilities, and ABC is predicted to have a formation enthalpy similar to that of ACC, suggesting that they experience similar thermodynamic driving forces for crystallization (chapter 9) Therefore precipitation pathways in the $BaCO_3$ system may differ from those commonly observed in the $CaCO_3$ system.

Evidence for amorphous barium carbonate (ABC) was sought using *in situ* time-resolved synchrotron X-ray scattering. High time resolution was achieved by mixing 500 μL each of 1 M $BaCl_2$ and 1 M $NaHCO_3$ in a stopped-flow mixing device and passing the solution through a thin walled (100 μm) 1 mm diameter quartz capillary in the X-ray beam path. A minimum time resolution of 100 ms was achieved, following approximately 10 ms of dead time resulting from the device geometry. Simultaneous measurements in the wide angle (WAXS), medium angle (MAXS) and small angle (SAXS) regions were collected on three separate detectors (Figure 18.1). The continuous range of scattering vectors, q = 0.0020 – 4.50 Å^{-1}, enabled by this detector geometry provided correlated information over real space distances, $d \cong$ 0.1–300 nm. Fitting SAXS curves and indexing Bragg peaks from MAXS and WAXS data yielded simultaneous information about particle crystallinity and shape, and high time resolution allowed growth and transformation kinetics to be quantified.

Signal intensity in SAXS increased with time immediately following mixing (Figure 12.1a). Fitting of the SAXS curves between 0.2 and 1.0 s indicated that roughly isotropic particles grew from 40 nm to 70 nm in radius (Figure 18.2). However, the Porod slope at q

> 0.02 decreased from 4.0 to 3.0, suggesting that the initially dense particles grew with a fractal-like structure (Figure 18.3). WAXS did not change appreciably over this time, indicating that these precipitates were not crystalline (Figure 18.4).

Between 1.0 and 4.0 s, SAXS transitioned into smooth curves with slopes close to -2 at low *q* and -3 at high *q*. This is consistent with scattering from very thin disks or sheets. From the R_g extracted from SAXS fitting, the thickness of these sheets is estimated to be consistent at approximately 13.3 ± 7.5 nm over this time. Simultaneously, Bragg peaks in WAXS emerged (Figure 18.2). Peak intensity was weak compared to the diffuse but strong scattering from water between $q = 0.8 - 4.5$ Å^{-1}. Nonetheless, clear Bragg peaks emerged, confirming that the thin sheets were crystalline. At later times (> 5 seconds), strong Bragg

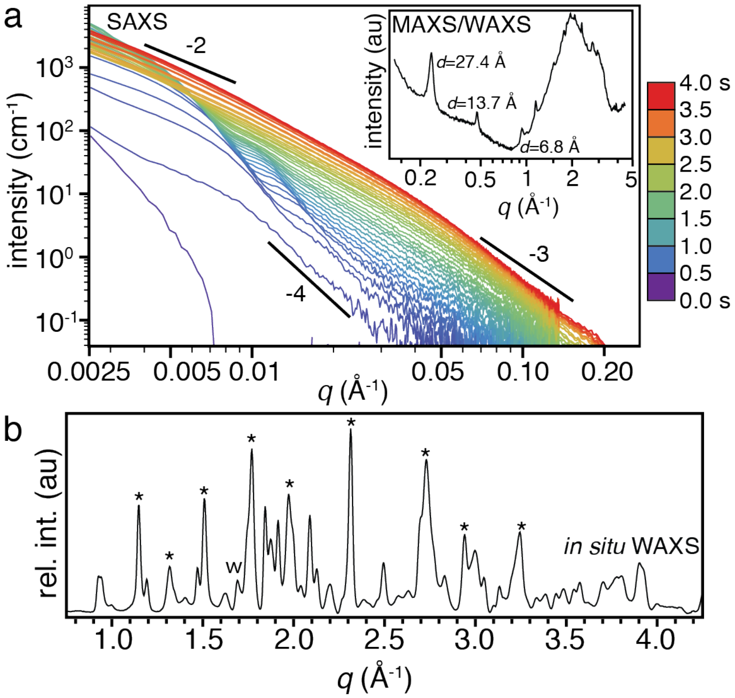

Figure 12.1. Time-resolved X-ray scattering of barium-carbonate rich solutions. (a) SAXS data, acquired at 100 ms intervals. A transition from SAXS curves with periodic oscillations between 0 - 1.0s to a smooth curve with a slope of -2 at low q and -3 at high *q* between 1.0 – 4.0 seconds is observed. (b) At higher *q* reso-

lution after subtraction of water scattering, Bragg peaks are clearly distinguished. An asterisk marks the peaks seen in the inset in (a), and the 'w' indicates the position of the witherite (111) peak.

peaks in MAXS emerged along with those in WAXS (Figure 18.1a, inset). These peaks were located at q = 0.48 $Å^{-1}$ and 0.24 $Å^{-1}$, corresponding to d-spacings of 13.7 Å, and 27.4 Å. Neither witherite, the only stable phase of $BaCO_3$ at ambient conditions,[223] nor any metastable $BaCO_3$ phases observed at ambient temperature,[224-227] account for these diffraction features. In order to better identify this phase, 1 mL each of 1 M $BaCl_2$ and 1 M $NaHCO_3$ were mixed *ex situ*, stirred gently for 30 s, and placed in the quartz capillary in the beam path. This allowed for the removal of CO_2 bubbles that formed after ~5-10 seconds in the stopped-flow mixing device and displaced the solution from the beam path.

Higher q resolution data were acquired with 1 s acquisition times every minute for 25 minutes. Many sharp Bragg peaks were clearly resolved in the first acquisition, after subtraction of the water background (Figure 18.1). Over the course of 30 minutes in solution diffraction from the initially formed phase decreased in intensity relative to that of witherite (Figure 18.5).

This diffraction disappeared immediately after clearing the capillary with air, confirming that crystallization was not occurring on the capillary wall. This confirms that this phase is a metastable precursor to witherite that begins to transform within ~ 1minute in solution.

In situ electron microscopy was performed under cryogenic (Figure 12.2a-c), low magnification (Figure 12.2d) or low dose conditions (Figure 12.2h-i). Cryo-high angle annular dark field (HAADF) STEM imaging on vitrified aqueous samples at the earliest accessible time points (< 5 s) revealed roughly isotropic particles with dense cores and a diffuse, fractal-like outer structure (Figure 12.2a), consistent with SAXS. These particles transformed into aggregates of very thin platelets (Figure 12.2b), that dispersed and grew into faceted particles that extend up to 1 μm in the lateral direction (Figure 12.2c). These platelets eventually crystallize to acicular witherite crystallites (Figure 18.6).

Low magnification TEM images confirm that the bulk powder consisted of very thin flakes after drying. Selected area electron diffraction (SAED) was relatively unchanged after tilting the sample up to 39° in an arbitrary direction, a hallmark of very thin materials (Figure 12.2c-e).[228] This is also reflected in the absence of diffraction spots in the narrow dimension when viewed edge-on (Figure 18.7).

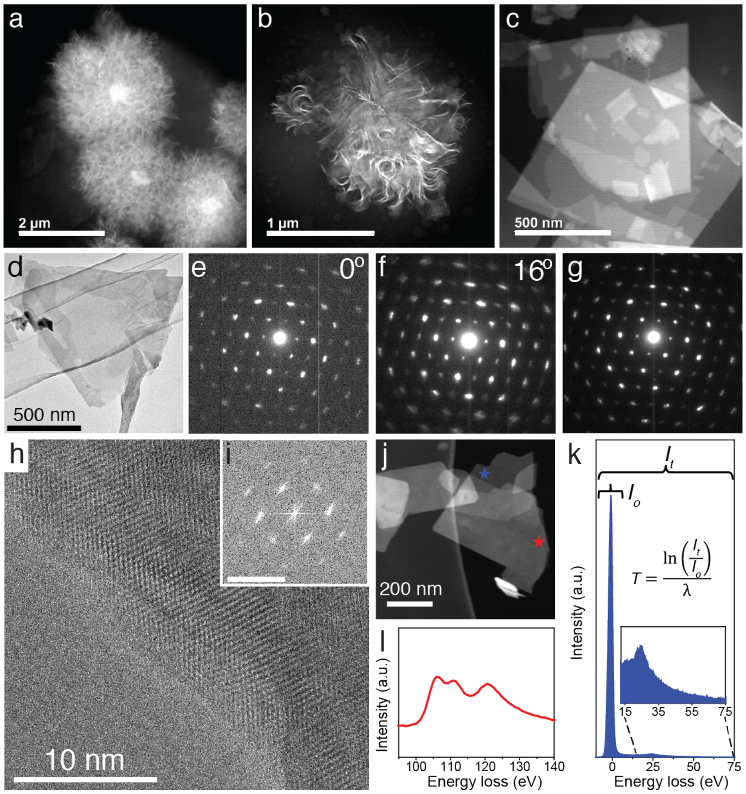

Figure 12.2. Electron microscopy of gortotowskite. (a) Cryo-HAADF STEM images of precipitates vitrified less than 5 seconds after precipitation. (a) initial precipitates (b) platelet formation and (c) dispersion and

growth. (d) TEM of dried flake, which exhibits SAED patterns that change negligibly upon specimen tilting (e-g). (h) Aberration corrected HR-STEM image of a platelet, showing lattice fringes over the entire crystallite. (g) Single-crystallinity was confirmed via the FFT.

Low-dose rate (0.5 $e^-/Å^2/s$) high-resolution aberration corrected STEM with low accelerating voltage (80 kV) revealed lattice fringes that extended across the entire precipitate (Figure 12.2f). Fast Fourier transforms (FFT) confirmed that the particles were single crystals, with lattice spacings of 3.3 Å and 4.1 Å, consistent with pXRD (Figure 12.1) and SAED (Figure 12.2g, i).

Electron energy loss spectroscopy (EELS) in ambient temperature STEM was performed on platelet aggregates. Using the ratio of transmission from the zero-loss peak to energy loss spectra, it was confirmed that individual particles were 10.5 ± 2.5 nm thick (Figure 12.2**k**). EELS also confirmed that the platelets contained barium from the presence of $N_{4,5}$ near-edge near edge spectra (ELNES, Figure 18.9).

Due to the short lifetime of this material in solution, a bulk synthesis procedure was established. Bulk precipitation of $BaCO_3$ was carried out using a method similar to that described previously for the precipitation of amorphous carbonates.[153] Briefly, ice cold aqueous solutions of 1M $BaCl_2$ and 1 M $NaHCO_3$ were rapidly mixed, filtered, washed with cold (~0 °C) water, and dried under vacuum. Power X-ray diffraction (pXRD) of the resulting material was nearly indistinguishable from that obtained from *in situ* WAXS (Figure 18.8), confirming that the transient crystalline phase observed in solution was preserved upon quenching and drying. Preliminary pattern indexing of the bulk pXRD pattern yielded a good fit for the spacegroup P2/m in the monoclinic crystal system, with lattice parameters a = 7.037, b = 19.257, c = 6.884 Å and $\alpha = \gamma$ = 90°, β = 104.2°. Stacks of 2 or 4 platelets along the c-direction are consistent with MAXS peaks at 13.7 and 27.4 Å.

Energy dispersive spectroscopy (EDS) of bulk precipitates in SEM confirm that they contain only carbon, oxygen, and barium (Figure 18.10), but this technique was not sensitive to hydrogen. Structural water content was determined from thermogravimetric analysis (TGA) of bulk powder (Figure 18.11). Weight loss of 1.5 ± 0.4% was observed below 100°C, 6.9 ± 0.4% between 100 – 230°C, and 1.6 ± 0.2% between 235 – 600°C. Excluding the water removed below 100°C, which is likely physisorbed to the high surface area platelets,[130] a weight loss of 8.5 ± 0.4% is consistent with one formula unit of water per $BaCO_3$ unit.

The presence of structural water was confirmed with FTIR and Raman spectroscopy (Figure 12.3a, b). All vibrational modes were similar to those found in calcium carbonate hydrates.[229] A broad peak at 683 cm^{-1} in IR is attributed to lattice water (Figure 12.3). A broad peak at 1653 cm^{-1} is assigned to H_2O bending modes, and the very broad O-H stretching modes are observed at 3409 and 3470 cm^{-1}. Only the O-H stretching mode at 3409 is Raman active. Multiple peaks and shoulders in all water modes suggest that there is more than one inequivalent water environment in the structure. The significantly broadened peaks indicate that some of these environments are somewhat disordered.

All internal carbonate modes including the ν_1 (symmetric stretch), ν_2 (asymmetric bend), ν_3 (asymmetric stretch), ν_4 (asymmetric bend) were active in both Raman and IR. All four were split and exhibited multiple maxima (Figure 18.12), an indication that there are also multiple crystallographically inequivalent carbonate environments in the structure.

The foregoing evidence demonstrates that ABC is a highly transient precursor to a crystalline hydrate of barium carbonate with a formula of $BaCO_3 \cdot H_2O$. We refer to this phase as gortotowskite. Gortotowskite forms from a very short-lived ABC precursor as ~10 nm thin platelets within one second after the start of precipitation in highly concentrated solutions. The presence of multiple carbonate and water lattice sites and large c-axis lattice parameter are indicative of a highly complex structure. Given the significant morphological anisotropy, this may explain the relatively slow growth in the c-axis direction compared to rapid growth in the a-b plane.

ABC thus provides access to a previously uncharacterized phase that may offer important clues about crystallization pathways at short time and length scales. This pathway bears a strong resemblance to that observed in the calcium phosphate system,[3] albeit at much faster timescales. Furthermore, gortotowskite is a precursor to witherite, which may participate in biomorph crystallization pathways in highly supersaturated solutions. The high time-resolution enabled by *in situ* stopped-flow and correlative cryo-STEM techniques provides a new perspective on the formation of $BaCO_3$.

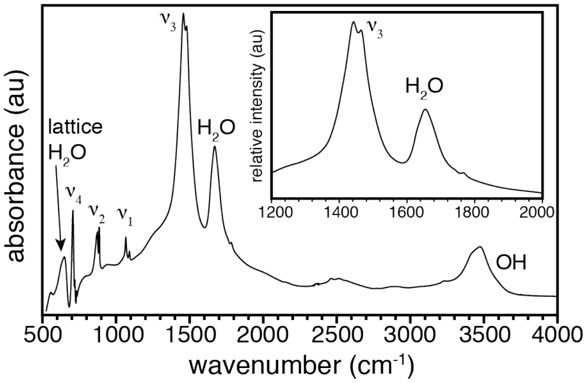

Figure 12.3. Characterization of structural water and carbonates in gortotowskite. (a) Raman and (c) IR spectroscopy confirm the presence of water from H-O-H bending at 1400 cm^{-1} and OH stretching between 3200-3700 cm^{-1}.

13. Summary and Outlook

13.1 Summary

The work presented herein has explored the mechanisms underlying biomineralization, and utilized these concepts to synthesize new carbonate minerals. To start, giant unilamellar vesicles were used as simple mimics of biological confinement (chapters 5 and 6). We demonstrated that the phosphatidylcholine lipid membranes had little interaction with the mineral during precipitation, but that decreasing steric charge shielding by replacing methyl groups on the amines with hydrogen increased the mineral adhesion to the membrane. This did not, however, appear to promote crystallization. We showed that liposomes can dramatically reduce the rate of crystallization of ACC by excluding nucleation accelerants, and by preserving the high kinetic barriers to lower energy structures that result. Rupturing the lipid membrane with detergent, and exposing the mineral to the glass substrate beneath the liposome, resulted in rapid crystallization.

Microfluidically produced water-in-oil emulsions were utilized as liposome analogs to study ACC crystallization kinetics. Using ensembles of hundreds of emulsion drops, we showed that vaterite forms from ACC via a classical, two step nucleation process (chapter 7). Confinement within drops allowed hundreds of individual ACC crystallization events to be quantified for the first time. A single, well-defined rate was confirmed to correspond to the nucleation of vaterite through *in situ* with Raman spectroscopy of the resulting crystals. Transformation occurred via dissolution of ACC and reprecipitation of vaterite. At 1.67 nuclei cm^{-3} s^{-1}, this rate was far too slow to account for the rapid crystallization of

ACC observed in bulk systems, indicating that ACC is a poor nucleator for crystalline calcium carbonate. Most of the transformation in bulk systems occurs through growth of the crystalline phase at the expense of ACC. Comparison with literature values for the crystallization rate of $CaCO_3$ suggests that previous measurements conflate precipitation of ACC with crystallization to vaterite and calcite. Because these measurements are used to calculate a commonly used value for the interfacial energy of calcite, we believe the actual value may be an order of magnitude higher, in line with simulations and measurements not based on precipitation.

Amorphous carbonate precursors are not specific to calcium, and appear to be a more general phenomenon. In chemically similar systems of increasing cation radius, amorphous strontium carbonate (ASC) is also observed in liposomes, but crystallizes rapidly (chapter 5). Amorphous barium carbonate (ABC) does form at the very early stages of precipitation but was not observed in liposomes, which was later discovered to be a result of very rapid crystallization kinetics of ABC (chapter 12).

ACC can be made with over 50% barium substituted for calcium, forming ACBC (chapter 9). ACBC does not exhibit long range order over this entire range of compositions, but does undergo structural evolution with increasing barium. The overall cation coordination number increases due to the higher average coordination number of barium (~9) relative to calcium (~7.5). However, the barium coordination number decreased from 10 to 8 with increasing barium. Simulations suggest that this is due to increasing competition between barium cations for oxygen ligands on carbonate anions, and that this competition changed the local order of the carbonates. This observation was confirmed by vibrational spectra, and helps explain the unique crystallization behavior in the calcium barium carbonate system.

ACBC crystallizes at a dramatically faster rate with increasing barium (chapter 10). I demonstrate that this process appears to be ‘non-classical’. It can be explained by the increasing short- and mid-range order in ACBC with increasing barium, which resembles that of crystalline $Ca_{1-x}Ba_xCO_3$ and selectively lowers the barrier to its formation relative to lower-energy structures.

This $Ca_{1-x}Ba_xCO_3$ phase has been misidentified as calcite in the literature, but we correctly assign the new spacegroup $R\bar{3}m$ and call it balcite (chapter 11). Balcite is only thermodynamically stable above 525°C, and is over 30% harder than calcite.

In the absence of calcium, I show that ABC is a highly transient precursor to a previously uncharacterized $BaCO_3{\cdot}H_2O$ phase. This phase forms as very thin (10 nm) and extremely anisotropic platelets, which themselves recrystallize rapidly into witherite ($BaCO_3$). These examples demonstrate the power of amorphous precursors to enable metastable crystalline materials through thermodynamically downhill transformations, and the ability of confined volumes to reduce the rate of these transformations and enable their quantification.

13.2 **Outlook**

13.2.1 *Amorphous carbonate formation*

The mechanism of ACC formation has been under active investigation for over a decade.[61] Competing theories have suggested aggregation of pre-nucleation clusters,[27,80] the condensation of liquid-like ionic polymers,[7,230,231] or spinodal decomposition into water-rich and calcium carbonate-rich liquids,[6,61,62] which may become ACC through vitrification upon partial dehydration.[162] However, because ACC formation appears to occur within milliseconds after mixing calcium and carbonate containing solutions[232] and is very sensitive to the supersaturation and the presence of additives,[233] there is currently no direct evidence of its formation mechanism.

Imaging with *in situ* electron microscopy is emerging as a viable technique for real-space characterization of aqueous precipitation.[4,5] Its ability to characterize the earliest stages of ACC formation is doubtful, however, despite recent improvements to the method. Because electrons interact strongly with matter, and water constitutes about 98% of the volume of an aqueous solution (chapter 2), the excellent resolution of most electron microscopes is severely reduced by scattering and absorption from water, and the flow-cell windows that contain it. Sample damage and water hydrolysis appear to be concerns under current state-of-the-art imaging conditions,[4] and increasing the beam flux may introduce even more artifacts.[234] Factors aimed at mitigating damage, including low-dose techniques like those employed to image gortotowskite at high resolution in chapter 12, do not offer a clear path towards the high temporal resolution necessary to address the question of ACC formation.

In principle, X-ray scattering should be able to distinguish between each of the proposed ACC formation mechanisms. Compared to electron microscopy, much weaker sample interactions and the availability of high flux synchrotron sources give X-ray methods a clear advantage. Just as SAXS/MAXS/WAXS was used to probe ABC formation in chapter 12, real space features between 1-250 nm can be simultaneously investigated. Condensed prenucleation clusters in the 1-2 nm size regime should be distinguishable from branched ionic polymers. The time evolution of the critical wavelength in spinodal decomposition is well known,[62,235] and expected to be in the 10s of nm for carbonate systems, and should therefore be easy to distinguish from the aggregation of prenucleation clusters or the condensation of ionic polymers.

The challenge for time-resolved X-ray scattering is to collect sufficient signal in a single exposure so that system does not evolve significantly during acquisition. In the case of ABC precipitation, this was achieved by rapid exposures of stationary solutions that were mixed in a stopped-flow mixing device. While acquisition times in the millisecond range are possible, this necessarily comes with a proportional loss in signal.

To overcome this limitation, a continuous-flow mixing device could instead be employed. Calcium and carbonate-containing solutions would be mixed continuously at one end a long capillary positioned in the X-ray beam path. Diffusional mixing would lead to precipitation, progressing along the length of the capillary. At constant flow rates, the solutions would achieve steady-state conditions, such that the distance from the capillary entrance would correspond to increasing reaction times. With sufficiently high flow rates, the earliest times of precipitation would extend over a macroscopic range in the capillary, and the beam could be positioned to record spectra from the initial stages of carbonate formation. At steady state, the scattering signal should not change as a function of time at a given location, allowing long collection times for improved signal. A given sample volume would receive a very small X-ray dose, greatly reducing concerns about beam damage. Similar systems have been used to probe rapid dynamics in protein solutions.[236]

13.2.2 *Amorphous carbonate crystallization and the role of water*

Interesting metastable structures, like balcite and gortotowskite, can result from the crystallization of amorphous precursors. However, as was noted in chapter 9, the role of water in amorphous carbonates is not well understood. Water can become kinetically trapped during crystallization, as it does in balcite in chapter 10. However, it may also be thermodynamically incorporated, as it is in gortotowskite (chapter 12), highlighting its complex role in the crystallization process. In the absence of atomic-scale characterization of the structure and dynamics of water, simulations of these materials are limited in their applicability, and the ability to predict crystallization pathways and energetics will remain elusive. Elucidating the thermodynamics of structural water, and its mechanistic impact on crystallization pathways, will be imperative to establishing a predictive framework of amorphous carbonate crystallization.

Changes in the Raman spectra, including the emergence of subtle peak in OH stretching region that may suggest an increase in water ordering, were observed upon partial dehydration in chapter 9. A careful study of Raman and IR spectra as a function of both time and temperature would provide insight into the dehydration kinetics of ACC and resulting changes to structural water. Isotopic enrichment with ^{13}C for solid state NMR also influenced the crystallization products of ACBC (chapter 10), and it has been shown that ACC crystallization is sensitive to isotopic composition.[97] Vibrational spectra with varying ratios of enrichment of ^{2}H and ^{13}C could reveal the symmetry of both carbonates and water within the amorphous structure. It may also help identify HCO_3^-, OH^-, which are known to exist in ACC precipitated under various conditions but are difficult to resolve by most characterization techniques.

Thermogravimetric analysis is the most common method for determining the water content of ACC. As discussed in chapter 9, water exhibits a range of mobility and dynamics that are reflected in the temperature range and rate at which water is driven out of the structure. Coupling vibrational spectroscopy and/or mass spectroscopic analysis to the gasses evolved from TGA of isotopically enriched samples would enable the known behavior of structural water in the solid to be correlated to its isotopic composition in the gas. Removal of water with an isotope ratio different from that in the solution from which the sample was synthesized may provide important information about the distribution of mobile vs. rigid water.

Small angle neutron scattering with varying levels of isotopic enrichment and dehydration would be a logical compliment to these experiments. The large neutron absorption cross-section of ^1H, four times that of ^{12}C and five times that of ^2H and ^{16}O, would provide excellent contrast for changes in water distribution on the nanoscale. Neutron diffraction for pair distribution function analysis on similarly prepared samples could also provide information about the local structure of water by revealing how strongly the second-shell (Ca-H) pair correlation is dependent on ^2H enrichment.

13.2.3 *Microfluidics for high-throughput studies*

As chapters 7, 8, and 10 and showed, droplet based microfluidics are a powerful platform for quantifying crystallization phenomena. The strengths of these devices are that the droplets can encapsulate almost anything soluble in water, and that good statistics can be obtained through large droplet ensembles. These features should be emphasized in future iterations. A number of drawbacks, including separate devices for droplet creation and storage, lack of temperature control, and limited reactant delivery modes could be improved with specific modifications.

Two devices, one for droplet creation and one for storage, are required because the flow rate of the drop creation device is much higher than what the storage device can tolerate without pushing the drops out of the wells. If the required flow rates could be brought to the same level, devices could very easily be combined on a single chip. Fortunately, alternatives for both droplet creation and storage are widespread in the literature.

For example, high-throughput droplet makers have been described, which take advantage of the minimal dependence on flow rate for drops passing over steps in the dripping regime.[237] This could be coupled with the current storage device, or with an expanded grid of up to 100,000 wells[238] to increase the current capacity by 3 orders of magnitude. This is the most promising strategy for large-scale, high throughput crystallization assays. Devices in which drops are created and stored in the same location are also well known.[239,240] Others create drops serially and pass them through a long outlet channel, where and they remain in place when flow is stopped.[54,241,242] Combinations of long channels and well-trapping approaches also work.[243] Many of these strategies could be easily modified for calcium carbonate precipitation.

The popularity of microfluidics with biologists and protein crystallographers has also motivated solutions for temperature control. The entire device can be immersed in fluid and placed on a temperature controlled stage.[244,245] More precise control could be exerted by micropatterning wires into the substrate prior to bonding the PDMS device, raising the temperature of individual wells by Joule heating. This would be an important modification for studies of biomineralization proteins in drops, like those in chapter 8.

Reactant delivery is perhaps the most significant hurdle to expanding these devices to systems of arbitrary composition. The current design allows for the transport of gasses via diffusion through PDMS from the flanking outer channels. Only systems for which aqueous equilibrium between an ionic species and a gas molecule with appreciable partial pressure under ambient conditions are current possibilities. Carbonates are the obvious top candidates, given their abundance and the well-known aqueous chemistry of CO_2. Similar systems have been proposed for CO_2 capture from flue gas in industrial settings.[246] However, it is not straightforward to determine transport rates, ion concentrations or pH inside the drops. In addition to the finite element transport simulations presented in chapter 7, future investigations will likely require coupled chemical reaction-diffusion simulations and experimental validation with colorimetric and/or fluorescent indicators.

Other systems that may be amenable to gas-diffusion precipitation include sulfates and sulfides, representing biomineral analogs (e.g., $BaSO_4$, $SrSO_4$, and FeS) or semiconductor nanoparticles (e.g., CdS, TeS). However, vapor pressures of SO_2 or H_2S gasses are negligible compared to that of CO_2 over carbonate solutions, which would dramatically reduce transport of these precursors to the drops. Instead of aqueous solutions, elevated pressures of pure gasses could be used, but these are toxic and would have to be handled with care. Precipitation of titanium or iron oxides could be induced by a change in pH, which ammonia could provide. But it appears that changes to the experimental design would help expand the applicability of these devices.

Specifically, changes to the chemistry of the surfactant and oil systems may allow for greater control over the contents of the drops. First, the surfactant can be functionalized to enable the formation of water-in-oil-in-water emulsions using very similar chip designs.[247] The outer oil phase is quickly replaced with aqueous solution after droplet formation. Storage devices could be loaded as before, but reactants could now be delivered in the aqueous phase directly to the droplet interface. As long as one of the reagents could partition across the surfactant bilayer while the other remained trapped on the interior of the drop, precipitation could take place.

Similar emulsion droplets can be made with lipids as the surfactant.[248] Through appropriate choice of the oil phase, the thin oil layer can diffuse away, leaving a giant unilamellar vesicle. Advantages of these GUVs over those in chapters 5 and 6 is that the contents are essentially limited only to constituents with aqueous solubility and vesicle radii and lamellarity are both monodisperse. Transmembrane transporters can self-assemble into single bilayers[248] vastly increasing the diversity and timing of reactants that can be incorporated into the drops. Again, with aqueous solution on the exterior of the drop there is no need for a separate channel flanking the storage wells.

13.2.4 *Beyond minerals*

With the increased flexibility that comes with microfluidically produced vesicles, structures that begin to bear greater resemblance to biological tissues can be fabricated. For example, lipid stabilized emulsions have been printed into a tissue-like material sensitive to osmotic pressure gradients.[249] These materials are made by essentially turning the outlet of the microfluidic device into a 3D printer nozzle. Inclusion of hydrogels in the drops, resembling the cytoskeletal support that most biological membranes rely on, allows viable cells to be encapsulated.[250] These cells may be able to operate autonomously to precipitate mineralized structures. [251,252] Mineral precipitated inside these hydrogels can be used to actuate mechanical responses to electrical stimuli, and have the distinct advantage of being self-healing.[253]

As discussed in chapter 3, my motivation in this dissertation was to divide the complex process of biomineralization into smaller and more manageable pieces to derive a deeper understanding of confinement, metastable precursors, and biomineralization proteins. There is still much to discover about these aspects individually. However, it may now be possible to reintroduce layers of complexity to these systems rivaling those of living things. Advances in bioinspired materials processing in confinement through microfluidics and 3D printing and *in vitro* cell culture are well positioned to integrate mineral precursors for controlled transformations into mineralized composites. Combining mineral and cells within hydrogel scaffolds, responsive to osmotic potentials and electrical stimulus, is a clear step towards lifelike materials.

14. References

(1) Hendley, C. T.; Tao, J.; Kunitake, J. A. M. R.; De Yoreo, J. J.; Estroff, L. A. *MRS Bull.* **2015**, *40* (06), 480–489.

(2) Wang, C.-M.; Liao, H.-G.; Ross, F. M. *MRS Bull.* **2015**, *40* (01), 46–52.

(3) Habraken, W. J. E. M.; Tao, J.; Brylka, L. J.; Friedrich, H.; Bertinetti, L.; Schenk, A. S.; Verch, A.; Dmitrovic, V.; Bomans, P. H. H.; Frederik, P. M.; Laven, J.; van der Schoot, P.; Aichmayer, B.; de With, G.; DeYoreo, J. J.; Sommerdijk, N. A. J. *Nat Comms* **2013**, *4*, 1507–1512.

(4) Nielsen, M. H.; Aloni, S.; De Yoreo, J. J. *Science* **2014**, *345* (6201), 1158–1162.

(5) Ross, F. M. *Science* **2015**, *350* (6267), aaa9886–aaa9886.

(6) Wallace, A. F.; Hedges, L. O.; Fernandez-Martinez, A.; Raiteri, P.; Gale, J. D.; Waychunas, G. A.; Whitelam, S.; Banfield, J. F.; De Yoreo, J. J. *Science* **2013**, *341* (6148), 885–889.

(7) Demichelis, R.; Raiteri, P.; Gale, J. D.; Quigley, D.; Gebauer, D. *Nat Comms* **2011**, *2*, 590–598.

(8) Baumgartner, J. *Nature Materials* **2013**, *12* (4), 310–314.

(9) De Yoreo, J. J.; Gilbert, P. U. P. A.; Sommerdijk, N. A. J. M.; Penn, R. L.; Whitelam, S.; Joester, D.; Zhang, H.; Rimer, J. D.; Navrotsky, A.; Banfield, J. F.; Wallace, A. F.; Michel, F. M.; Meldrum, F. C.; Colfen, H.; Dove, P. M. *Science* **2015**, *349* (6247), 499–507.

(10) Gal, A.; Kahil, K.; Vidavsky, N.; DeVol, R. T.; Gilbert, P. U. P. A.; Fratzl, P.; Weiner, S.; Addadi, L. *Adv. Funct. Mater.* **2014**, *24* (34), 5420–5426.

(11) Marsh, M. E. *Protoplasma* **1999**, *207*, 54–66.

(12) Marsh, M. E.; Ridall, A. L.; Azadi, P.; Duke, P. J. *Journal of Structural Biology* **2002**, *139*, 39–45.

(13) Sone, E. D.; Weiner, S.; Addadi, L. *Journal of Structural Biology* **2007**, *158* (3), 428–444.

(14) Scheffel, A.; Gruska, M.; Faivre, D.; Linaroudis, A.; Plitzko, J. M.; Schüler, D. *Nature* **2005**, *440* (7080), 110–114.

(15) Abreu, F.; Sousa, A. A.; Aronova, M. A.; Kim, Y.; Cox, D.; Leapman, R. D.; Andrade, L. R.; Kachar, B.; Bazylinski, D. A.; Lins, U. *Journal of Structural Biology* **2013**, *181* (2), 162–168.

(16) Mahamid, J.; Sharir, A.; Gur, D.; Zelzer, E.; Addadi, L.; Weiner, S. *Journal of Structural Biology* **2011**, *174* (3), 527–535.

(17) Navrotsky, A. *Proceedings of the National Academy of Sciences* **2004**, *101* (33), 12096–12101.

(18) Debenedetti, P. G. *Metastable Liquids*; Princeton University Press: Princeton, 1996; pp 1–424.

(19) Sear, R. *MRS Bull.* **2016**, *41* (05), 363–368.

(20) De Yoreo, J. J.; Vekilov, P. G. *Reviews in Mineralogy and Geochemistry* **2003**,

57–93.

(21) Sear, R. P. *J. Phys.: Condens. Matter* **2007**, *19* (3), 033101–033128.

(22) Hu, Q.; Nielsen, M. H.; Freeman, C. L.; Hamm, L. M.; Tao, J.; Lee, J. R. I.; Han, T. Y. J.; Becker, U.; Harding, J. H.; Dove, P. M.; De Yoreo, J. J. *Faraday Disc.* **2012**, *159*, 509–543.

(23) Hamm, L. M.; Giuffre, A. J.; Han, N.; Tao, J.; Wang, D.; De Yoreo, J. J.; Dove, P. M. *Proceedings of the National Academy of Sciences* **2014**, *111* (4), 1304–1309.

(24) Forbes, T. Z.; Radha, A. V.; Navrotsky, A. *Geochimica et Cosmochimica Acta* **2011**, *75* (24), 7893–7905.

(25) Bruno, M.; Massaro, F. R.; Pastero, L.; Costa, E.; Rubbo, M.; Prencipe, M.; Aquilano, D. *Crystal Growth & Design* **2013**, *13* (3), 1170–1179.

(26) Sun, W.; Jayaraman, S.; Chen, W.; Persson, K. A.; Ceder, G. *Proceedings of the National Academy of Sciences* **2015**, *112* (20), E2735–E2735.

(27) Gebauer, D.; Cölfen, H. *Nano Today* **2011**, *6* (6), 564–584.

(28) Sommerdijk, N. A. J. M.; With, G. de. *Chem. Rev.* **2008**, *108* (11), 4499–4550.

(29) Meldrum, F. C.; Cölfen, H. *Chem. Rev.* **2008**, *108* (11), 4332–4432.

(30) Nudelman, F.; Lausch, A. J.; Sommerdijk, N. A. J. M.; Sone, E. D. *Journal of Structural Biology* **2013**, *183* (2), 258–269.

(31) Nudelman, F. *Seminars in Cell and Developmental Biology* **2015**, 1–9.

(32) Aizenberg, J. *Bell Labs Tech. J.* **2005**, *10* (3), 129–141.

(33) Love, J. C.; Estroff, L. A.; Kriebel, J. K.; Nuzzo, R. G.; Whitesides, G. M. *Chem. Rev.* **2005**, *105* (4), 1103–1170.

(34) Turnbull, D.; Vonnegut, B. *Industrial and Engineering Chemistry* **1952**, *44*, 1292–1298.

(35) Quigley, D.; Rodger, P. M.; Freeman, C. L.; Harding, J. H.; Duffy, D. M. *The Journal of Chemical Physics* **2009**, *131* (9), 094703–094712.

(36) Giuffre, A. J.; Hamm, L. M.; Han, N.; De Yoreo, J. J.; Dove, P. M. *Proceedings of the National Academy of Sciences* **2013**, 1–9.

(37) Aizenberg, J. *Science* **2003**, *299*, 1–4.

(38) Gong, X.; Wang, Y.-W.; Ihli, J.; Kim, Y.-Y.; Li, S.; Walshaw, R.; Chen, L.; Meldrum, F. C. *Adv. Mater.* **2015**, *27* (45), 7395–7400.

(39) Turnbull, D. *J. Appl. Phys.* **1950**, *21* (10), 1022–1028.

(40) Miyazawa, Y.; Pound, G. M. *Journal of Crystal Growth* **1974**, 45–57.

(41) Sear, R. P. *International Materials Reviews* **2012**, *57* (6), 328–356.

(42) Sear, R. P. *CrystEngComm* **2014**, *16* (29), 6506–6522.

(43) Aizenberg, J.; Whitesides, G. M.; Black, A. J. *Nature* **1999**, 495–498.

(44) Tester, C. C.; Whittaker, M. L.; Joester, D. *Chem. Commun.* **2014**, *50* (42), 5619–4.

(45) Shum, H. C.; Bandyopadhyay, A.; Bose, S.; Weitz, D. A. *Chem. Mater.* **2009**, *21* (22), 5548–5555.

(46) Stephens, C. J.; Ladden, S. F.; Meldrum, F. C.; Christenson, H. K. *Adv. Funct.*

Mater. **2010**, *20* (13), 2108–2115.

(47) Loste, E.; Park, R. J.; Warren, J.; Meldrum, F. C. *Adv. Funct. Mater.* **2004**, *14* (12), 1211–1220.

(48) Wolf, S. E.; Müller, L.; Barrea, R.; Kampf, C. J.; Leiterer, J.; Panne, U.; Hoffmann, T.; Emmerling, F.; Tremel, W. *Nanoscale* **2011**, *3* (3), 1158–1158.

(49) Amstad, E.; Gopinadhan, M.; Holtze, C.; Osuji, C. O.; Brenner, M. P.; Spaepen, F.; Weitz, D. A. *Science* **2015**, 1–6.

(50) Mann, S.; Hannington, J. P.; Williams, R. J. P. *Nature* **1986**, 565–567.

(51) Collier, J.; Messersmith, P. B. *Annu. Rev. Mater. Res.* **2001**, 1–29.

(52) Romanowsky, M. B.; Abate, A. R.; Rotem, A.; Holtze, C.; Weitz, D. A. *Lab Chip* **2012**, *12* (4), 802–806.

(53) Stephens, C. J.; Kim, Y.-Y.; Evans, S. D.; Meldrum, F. C.; Christenson, H. K. *J. Am. Chem. Soc.* **2011**, *133* (14), 5210–5213.

(54) Laval, P.; Crombez, A.; Salmon, J.-B. *Langmuir* **2009**, *25* (3), 1836–1841.

(55) Schenk, A. S.; Albarracin, E. J.; Kim, Y.-Y.; Ihli, J.; Meldrum, F. C. *Chem. Commun.* **2014**, *50* (36), 4729–4.

(56) Cantaert, B.; Beniash, E.; Meldrum, F. C. *Chem. Eur. J.* **2013**, *19* (44), 14918–14924.

(57) Wang, Y.-W.; Christenson, H. K.; Meldrum, F. C. *Adv. Funct. Mater.* **2013**, *23* (45), 5615–5623.

(58) Murray, B. J.; Broadley, S. L.; Wilson, T. W.; Bull, S. J.; Wills, R. H.; Christenson, H. K.; Murray, E. J. *Phys. Chem. Chem. Phys.* **2010**, *12* (35), 10380–10388.

(59) Baumgärtel, H.; Zimmermann, H. W. *Journal of Molecular Liquids* **2011**, *164* (3), 178–186.

(60) Sear, R. P. *International Materials Reviews* **2012**, *57* (6), 328–356.

(61) Faatz, M.; Gröhn, F.; Wegner, G. *Adv. Mater.* **2004**, *16* (12), 996–1000.

(62) Zou, Z.; Habraken, W. J. E. M.; Bertinetti, L.; Politi, Y.; Gal, A.; Weiner, S.; Addadi, L.; Fratzl, P. *Adv. Mater. Interfaces* **2016**, *4*, 1–5.

(63) Sun, W.; Dacek, S. T.; Ong, S. P.; Hautier, G.; Jain, A.; Richards, W. D.; Gamst, A. C.; Persson, K. A.; Ceder, G. *Sci. Rep.* **2016**, 1–9.

(64) Debenedetti, P. G. *Metastable Liquids Concepts and Principles*; Princeton University Press: Princeton, 1996; pp 1–424.

(65) Voorhees, P.; Ratke, L. *Growth and Coarsening*; Springer-Verlag: New York, 2002.

(66) Wang, J.; Toby, B. H.; Lee, P. L.; Ribaud, L.; Antao, S. M.; Kurtz, C.; Ramanathan, M.; Dreele, Von, R. B.; Beno, M. A. *Rev. Sci. Instrum.* **2008**, *79* (8), 085105–085107.

(67) Qiu, X.; Thompson, J. W.; Billinge, S. J. L. *J Appl Crystallogr* **2004**, *37*, 678–680.

(68) Beaucage, G. *J Appl Crystallogr* **1995**, *28*, 717–728.

(69) Ilavsky, J.; Jemian, P. R. *J Appl Crystallogr* **2009**, *42* (2), 347–353.

(70) Ravel, B.; Newville, M. *J Synchrotron Rad* **2005**, *12* (4), 537–541.

(71) Ravel, B. *J Synchrotron Rad* **2001**, 314–316.

(72) Oliver, W. C.; Pharr, G. M. *J. Mater. Res.* **2003**, *19* (1), 3–20.

(73) Addadi, L.; Raz, S.; Weiner, S. *Adv. Mater.* **2003**, *15* (12), 959–970.

(74) Gong, Y. U. T. *PNAS* **2012**, 1–6.

(75) Politi, Y.; Metzler, R. A.; Abrecht, M.; Gilbert, B.; Wilt, F. H.; Sagi, I.; Addadi, L.; Weiner, S.; Gilbert, P. U. P. A. *Proceedings of the National Academy of Sciences* **2008**, *105* (45), 17362–17366.

(76) Tester, C. C.; Wu, C.-H.; Krejci, M. R.; Mueller, L.; Park, A.; Lai, B.; Chen, S.; Sun, C.; Balasubramanian, M.; Joester, D. *Adv. Funct. Mater.* **2013**, *23* (34), 4185–4194.

(77) Mahamid, J.; Aichmayer, B.; Shimoni, E.; Ziblat, R.; Li, C.; Siegel, S.; Paris, O.; Fratzl, P.; Weiner, S.; Addadi, L. *Proceedings of the National Academy of Sciences* **2010**, *107* (14), 6316–6321.

(78) Lowenstam, H. A.; Weiner, S. *On Biomineralization*; Oxford University Press on Demand: New York, 1989.

(79) Galkin, O.; Vekilov, P. G. *Proceedings of the National Academy of Sciences* **2000**, *97* (12), 6277–6281.

(80) Gebauer, D.; Volkel, A.; Cölfen, H. *Science* **2008**, *322* (5909), 1819–1822.

(81) Kellermeier, M.; Melero-García, E.; Glaab, F.; Klein, R.; Drechsler, M.; Rachel, R.; García-Ruiz, J. M.; Kunz, W. *J. Am. Chem. Soc.* **2010**, *132* (50), 17859–17866.

(82) Tester, C. C.; Brock, R. E.; Wu, C.-H.; Krejci, M. R.; Weigand, S.; Joester, D. *CrystEngComm* **2011**, *13* (12), 3975–4.

(83) Tester, C. C.; Wu, C.-H.; Weigand, S.; Joester, D. *Faraday Disc.* **2012**, *159*, 345–12.

(84) Nudelman, F.; Sonmezler, E.; Bomans, P. H. H.; de With, G.; Sommerdijk, N. A. J. M. *Nanoscale* **2010**, *2* (11), 2436–4.

(85) Pouget, E. M.; Bomans, P. H. H.; Goos, J. A. C. M.; Frederik, P. M.; de With, G.; Sommerdijk, N. A. J. M. *Science* **2009**, *323* (5920), 1455–1458.

(86) Quigley, D.; Freeman, C. L.; Harding, J. H.; Rodger, P. M. *The Journal of Chemical Physics* **2011**, *134* (4), 044703–044712.

(87) Gal, A.; Habraken, W.; Gur, D.; Fratzl, P.; Weiner, S.; Addadi, L. *Angew. Chem. Int. Ed.* **2013**, *52* (18), 4867–4870.

(88) Ihli, J.; Wong, W. C.; Noel, E. H.; Kim, Y.-Y.; Kulak, A. N.; Christenson, H. K.; Duer, M. J.; Meldrum, F. C. *Nat Comms* **2014**, *5*, 1–10.

(89) Horger, K. S.; Estes, D. J.; Capone, R.; Mayer, M. *J. Am. Chem. Soc.* **2009**, *131* (5), 1810–1819.

(90) Xu, X.; Han, J. T.; Kim, D. H.; Cho, K. *J. Phys. Chem. B* **2006**, *110* (6), 2764–2770.

(91) Xiao, J.; Wang, Z.; Tang, Y.; Yang, S. *Langmuir* **2010**, *26* (7), 4977–4983.

(92) Walde, P.; Cosentino, K.; Engel, H.; Stano, P. *Chem. Eur. J. of Chem. Bio.*

2010, *11* (7), 848–865.
(93) Homeijer, S. J.; Barrett, R. A.; Gower, L. B. *Crystal Growth & Design* **2010**, *10* (3), 1040–1052.
(94) Brecevic, L.; Nielsen, A. E. *Journal of Crystal Growth* **1989**, *98*, 504–510.
(95) Clarkson, J. R.; Price, T. J.; Adams, C. J. *Faraday Trans.* **1992**, *88* (2), 243–247.
(96) Beniash, E.; Aizenberg, J.; Addadi, L.; Weiner, S. *Proceedings of the Royal Society of London B* **1997**, 461–465.
(97) Giuffre, A. J.; Gagnon, A. C.; De Yoreo, J. J.; Dove, P. M. *Geochimica et Cosmochimica Acta* **2015**, *165*, 407–417.
(98) Bots, P.; Benning, L. G.; Rodriguez-Blanco, J. D.; Roncal-Herrero, T.; Shaw, S. *Crystal Growth & Design* **2012**, *12* (7), 3806–3814.
(99) Whittaker, M. L.; Dove, P. M.; Joester, D. *MRS Bull.* **2016**, *41* (05), 388–392.
(100) Rodriguez-Blanco, J. D.; Shaw, S.; Benning, L. G. *Nanoscale* **2011**, *3* (1), 265–271.
(101) Holtze, C.; Rowat, A. C.; Agresti, J. J.; Hutchison, J. B.; Angilè, F. E.; Schmitz, C. H. J.; Köster, S.; Duan, H.; Humphry, K. J.; Scanga, R. A.; Johnson, J. S.; Pisignano, D.; Weitz, D. A. *Lab Chip* **2008**, *8* (10), 1632–1639.
(102) Wang, X.; Conway, W.; Burns, R.; McCann, N.; Maeder, M. *J. Phys. Chem. A* **2010**, *114* (4), 1734–1740.
(103) Sohnel, O.; Mullin, J. W. *Journal of Crystal Growth* **1982**, *60*, 239–250.
(104) Radha, A. V.; Navrotsky, A. *Reviews in Mineralogy and Geochemistry* **2013**, *77* (1), 73–121.
(105) Fratzl, P.; Weinkamer, R. *Progress in Materials Science* **2007**, *52* (8), 1263–1334.
(106) Koyama, M.; Zhang, Z.; Wang, M.; Ponge, D.; Raabe, D.; Tsuzaki, K.; Noguchi, H.; Tasan, C. C. *Science* **2017**, *355*, 1055–1057.
(107) Mann, K.; Poustka, A. J.; Mann, M. *Proteome Science* **2008**, *6* (1), 22–10.
(108) Mann, K.; Wilt, F. H.; Poustka, A. J. *Proteome Science* **2010**, 1–12.
(109) Livingston, B. T.; Killian, C. E.; Wilt, F.; Cameron, A.; Landrum, M. J.; Ermolaeva, O.; Sapojnikov, V.; Maglott, D. R.; Buchanan, A. M.; Ettensohn, C. A. *Developmental Biology* **2006**, *300* (1), 335–348.
(110) Jain, G.; Pendola, M.; Rao, A.; Cölfen, H.; Evans, J. S. *Biochemistry* **2016**, *55* (31), 4410–4421.
(111) Jain, G.; Pendola, M.; Huang, Y.-C.; Gebauer, D.; Evans, J. S. *Biochemistry* **2017**, acs.biochem.7b00083–13.
(112) Perovic, I.; Chang, E. P.; Lui, M.; Rao, A.; Cölfen, H.; Evans, J. S. *Biochemistry* **2014**, *53* (16), 2739–2748.
(113) Rao, A.; Seto, J.; Berg, J. K.; Kreft, S. G.; Scheffner, M.; Cölfen, H. *Journal of Structural Biology* **2013**, *183* (2), 205–215.
(114) Chang, E. P.; Perovic, I.; Rao, A.; Cölfen, H.; Evans, J. S. *Biochemistry* **2016**, *55* (7), 1024–1035.

(115) Meldrum, F. C. *International Materials Reviews* **2003**, *48* (3), 187–224.

(116) Wilt, F.; Killian, C. E.; Croker, L.; Hamilton, P. *Journal of Structural Biology* **2013**, *183* (2), 199–204.

(117) Gebauer, D.; Gunawidjaja, P. N.; Ko, J. Y. P.; Bacsik, Z.; Aziz, B.; Liu, L.; Hu, Y.; Bergström, L.; Tai, C.-W.; Sham, T.-K.; Edén, M.; Hedin, N. *Angew. Chem. Int. Ed.* **2010**, *49* (47), 8889–8891.

(118) Politi, Y.; Levi-Kalisman, Y.; Raz, S.; Wilt, F.; Addadi, L.; Weiner, S.; Sagi, I. *Adv. Funct. Mater.* **2006**, *16* (10), 1289–1298.

(119) Rodriguez-Navarro, C.; Kudłacz, K.; Cizer, Ö.; Ruiz-Agudo, E. *CrystEngComm* **2016**, *17*, 58–72.

(120) Cartwright, J. H. E.; Checa, A. G.; Gale, J. D.; Gebauer, D.; Sainz-Díaz, C. I. *Angew. Chem. Int. Ed.* **2012**, *51* (48), 11960–11970.

(121) Whittaker, M. L.; Joester, D. *Adv. Mater.* **2017**, *6*, 1606730–1606735.

(122) Kondrat, S. A.; Smith, P. J.; Wells, P. P.; Chater, P. A.; Carter, J. H.; Morgan, D. J.; Fiordaliso, E. M.; Wagner, J. B.; Davies, T. E.; Lu, L.; Bartley, J. K.; Taylor, S. H.; Spencer, M. S.; Kiely, C. J.; Kelly, G. J.; Park, C. W.; Rosseinsky, M. J.; Hutchings, G. J. *Nature* **2016**, *531* (7592), 83–87.

(123) Bloch, L.; Kauffmann, Y.; Pokroy, B. *Crystal Growth & Design* **2014**, *14* (8), 3983–3989.

(124) Saika-Voivod, I.; Poole, P. H.; Sciortino, F. *Nature* **2001**, *412*, 1–4.

(125) Mishima, O.; Suzuki, Y. *Nature* **2002**, *419* (6907), 597–599.

(126) Sheng, H. W.; Liu, H. Z.; Cheng, Y. Q.; Wen, J.; Lee, P. L.; Luo, W. K.; Shastri, S. D.; Ma, E. *Nature Materials* **2007**, *6* (3), 192–197.

(127) Sel, O.; Radha, A. V.; Dideriksen, K.; Navrotsky, A. *Geochimica et Cosmochimica Acta* **2012**, *87* (C), 61–68.

(128) Radha, A. V.; Fernandez-Martinez, A.; Hu, Y.; Jun, Y.-S.; Waychunas, G. A.; Navrotsky, A. *Geochimica et Cosmochimica Acta* **2012**, *90* (C), 83–95.

(129) Radha, A. V.; Navrotsky, A. *American Mineralogist* **2014**, *99* (5-6), 1063–1070.

(130) Radha, A. V.; Navrotsky, A. *Crystal Growth & Design* **2015**, *15* (1), 70–78.

(131) Matsunuma, S.; Kagi, H.; Komatsu, K.; Maruyama, K.; Yoshino, T. *Crystal Growth & Design* **2014**, *14* (11), 5344–5348.

(132) Littlewood, J. L.; Shaw, S.; Peacock, C. L.; Bots, P.; Trivedi, D.; Burke, I. T. *Crystal Growth & Design* **2017**, *17* (3), 1214–1223.

(133) Matyskin, A. V.; Ebin, B.; Tyumentsev, M.; Allard, S.; Skarnemark, G.; Ramebäck, H.; Ekberg, C. *J Radioanal Nucl Chem* **2016**, 1–7.

(134) Radha, A. V.; Forbes, T. Z.; Killian, C. E.; Gilbert, P. U. P. A.; Navrotsky, A. *Proceedings of the National Academy of Sciences* **2010**, 16438–16443.

(135) Schmidt, M. P.; Ilott, A. J.; Phillips, B. L.; Reeder, R. J. *Crystal Growth & Design* **2014**, *14* (3), 938–951.

(136) Plimpton, S. *Journal of Computational Physics* **2016**, 1–19.

(137) Raiteri, P.; Gale, J. D.; Quigley, D.; Rodger, P. M. *J. Phys. Chem. C* **2010**, *114* (13), 5997–6010.

(138) Kresse, G.; Furthmüller, J. *Physical Review B* **1996**, *64* (16), 11169–11186.

(139) Kresse, G.; Joubert, D. *Physical Review B* **1995**, *59* (3), 1758–1775.

(140) Perdew, J. P.; Burke, K.; Ernzerhof, M. *Phys. Rev. Lett.* **1996**, *77* (18), 3865–3868.

(141) Ong, S. P.; Richards, W. D.; Jain, A.; Hautier, G.; Kocher, M.; Cholia, S.; Gunter, D.; Chevrier, V. L.; Persson, K. A.; Ceder, G. *Computational Materials Science* **2013**, *68*, 314–319.

(142) Denton, A. R.; Ashcroft, N. W. *Physical Review A* **1991**, 1–4.

(143) OKeeffe, M. *Acta Crystallographica* **1979**, *A35*, 772–775.

(144) Gueta, R.; Natan, A.; Addadi, L.; Weiner, S.; Refson, K.; Kronik, L. *Angew. Chem. Int. Ed.* **2007**, *46* (1-2), 291–294.

(145) Goodwin, A. L.; Michel, F. M.; Phillips, B. L.; Keen, D. A.; Dove, M. T.; Reeder, R. J. *Chem. Mater.* **2010**, *22* (10), 3197–3205.

(146) Sowrey, F. E.; Skipper, L. J.; Pickup, D. M.; Drake, K. O.; Lin, Z.; Smith, M. E.; Newport, R. J. *Phys. Chem. Chem. Phys.* **2004**, *6* (1), 188–192.

(147) Michel, F. M.; MacDonald, J.; Feng, J.; Phillips, B. L.; Ehm, L.; Tarabrella, C.; Parise, J. B.; Reeder, R. J. *Chem. Mater.* **2008**, *20* (14), 4720–4728.

(148) Fulton, J. L.; Heald, S. M.; Badyal, Y. S.; Simonson, J. M. *J. Phys. Chem. A* **2003**, *107* (23), 4688–4696.

(149) Levi-Kalisman, Y.; Raz, S.; Weiner, S.; Addadi, L.; Sagi, I. *Adv. Funct. Mater.* **2002**, *12* (1), 43–47.

(150) Swainson, I. P. *American Mineralogist* **2008**, *93* (7), 1014–1018.

(151) Finch, A. A.; Allison, N.; Steaggles, H.; Wood, C. V.; Mosselmans, J. F. W. *Chemical Geology* **2010**, *270* (1-4), 179–185.

(152) Reeder, R. J.; Tang, Y.; Schmidt, M. P.; Kubista, L. M.; Cowan, D. F.; Phillips, B. L. *Crystal Growth & Design* **2013**, *13* (5), 1905–1914.

(153) Koga, N.; Nakagoe, Y.; Tanaka, H. *Thermochimica Acta* **1998**, *318*, 239–244.

(154) Tesoriero, A.; Pankow, J. *Geochimica et Cosmochimica Acta* **1996**, *60* (6), 1053–1063.

(155) Dietzel, M.; Gussone, N.; Eisenhauer, A. *Chemical Geology* **2004**, *203* (1-2), 139–151.

(156) Chang, L. L. *Journal of Geology* **1965**, *73* (2), 346–368.

(157) Rez, P.; Sinha, S.; Gal, A. *J Appl Crystallogr* **2014**, *47* (5), 1651–1657.

(158) Ihli, J.; Kim, Y.-Y.; Noel, E. H.; Meldrum, F. C. *Adv. Funct. Mater.* **2012**, *23* (12), 1575–1585.

(159) Kababya, S.; Gal, A.; Kahil, K.; Weiner, S.; Addadi, L.; Schmidt, A. *J. Am. Chem. Soc.* **2015**, *137* (2), 990–998.

(160) Blue, C. R.; Dove, P. M. *Geochimica et Cosmochimica Acta* **2015**, *148* (C), 23–33.

(161) Plummer, L. N.; Bunsenberg, E. *Geochi* **1982**, *46*, 1011–1040.

(162) Dorvee, J. R.; Veis, A. *Journal of Structural Biology* **2013**, *183* (2), 278–303.

(163) Chaudhari, M. I.; Soniat, M.; Rempe, S. B. *J. Phys. Chem. B* **2015**, *119* (28),

8746–8753.
(164) Raiteri, P.; Demichelis, R.; Gale, J. D. *J. Phys. Chem. C* **2015**, *119* (43), 24447–24458.
(165) Sen, S.; Kaseman, D. C.; Colas, B.; Jacob, D. E.; Clark, S. M. *Phys. Chem. Chem. Phys.* **2016**, *18* (30), 20330–20337.
(166) Saharay, M.; James Kirkpatrick, R. *Chemical Physics Letters* **2014**, *591*, 287–291.
(167) Sinha, S.; Rez, P. *Materials Chemistry and Physics* **2015**, *157*, 56–62.
(168) Carteret, C.; Dandeu, A.; Moussaoui, S.; Muhr, H.; Humbert, B.; Plasari, E. *Crystal Growth & Design* **2009**, *9* (2), 807–812.
(169) Valenzano, L.; Noël, Y.; Orlando, R.; Zicovich-Wilson, C. M.; Ferrero, M.; Dovesi, R. *Theor Chem Account* **2007**, *117* (5-6), 991–1000.
(170) Prencipe, M.; Pascale, F.; Zicovich-Wilson, C. M.; Saunders, V. R.; Orlando, R.; Dovesi, R. *Phys Chem Minerals* **2004**, *31* (8), 559–564.
(171) Cobourne, G.; Mountjoy, G.; Rodriguez-Blanco, J. D.; Benning, L. G.; Hannon, A. C.; Plaisier, J. R. *Journal of Non-Crystalline Solids* **2014**, *401*, 154–158.
(172) García-Ruiz, J. M.; Melero-García, E.; Hyde, S. T. *Science* **2009**, *323*.
(173) Noorduin, W. L.; Grinthal, A.; Mahadevan, L.; Aizenberg, J. *Science* **2013**, *340*.
(174) Eiblmeier, J.; Schürmann, U.; Kienle, L.; Gebauer, D.; Kunz, W.; Kellermeier, M. *Nanoscale* **2014**, *6* (24), 14939–14949.
(175) Nakouzi, E.; Steinbock, O. *Science Advances* **2016**, 1–14.
(176) Sondi, I.; Matijević, E. *Chem. Mater.* **2003**, *15* (6), 1322–1326.
(177) Škapin, S. D.; Sondi, I. *Crystal Growth & Design* **2005**, *5* (5), 1933–1938.
(178) Shatskiy, A. F.; Litasov, K. D.; Palyanov, Y. N. *Russian Geology and Geophysics* **2015**, *56* (1-2), 113–142.
(179) Grandjean, A.; Leturcq, G. *Journal of Nuclear Materials* **2005**, *345* (1), 11–18.
(180) Puli, V. S.; Pradhan, D. K.; Riggs, B. C.; Chrisey, D. B.; Katiyar, R. S. *Journal of Alloys and Compounds* **2014**, *584*, 369–373.
(181) Kaabar, W.; Bott, S.; Devonshire, R. *Spectrochimica Acta Part A: Molecular and Biomolecular Spectroscopy* **2011**, *78* (1), 136–141.
(182) Sevelsted, T. F.; Herfort, D.; Skibsted, J. *Cement and Concrete Research* **2013**, *52*, 100–111.
(183) Papenguth, H. W.; Kirkpatrick, R. J.; Montez, B.; Sandberg, P. A. *American Mineralogist* **1989**, *74*, 1152–1158.
(184) Nebel, H.; Neumann, M.; Mayer, C.; Epple, M. *Inorg. Chem.* **2008**, *47* (17), 7874–7879.
(185) Tracy, S. L.; François, C. J. P.; Jennings, H. M. *Journal of Crystal Growth* **1998**, *193*, 374–381.
(186) Pimentel, C.; Pina, C. M. *Geochimica et Cosmochimica Acta* **2014**, *142* (C), 217–223.
(187) Reeder, R. J. *Aquatic Geochemistry* **2000**, *6*, 213–226.
(188) Ishizawa, N.; Setoguchi, H.; Yanagisawa, K. *Sci. Rep.* **2013**, *3*, 1–5.

(189) Ishizawa, N. *Powder Diffr.* **2014**, *29* (S1), S19–S23.
(190) Dove, M. T.; Powell, B. M. *Phys Chem Minerals* **1989**, *16*, 503–507.
(191) Lander, J. J. *The Journal of Chemical Physics* **1949**, *17* (10), 892–11.
(192) Redfern, S. A. T.; Salje, E.; Navrotsky, A. *Contributions to Mineralogy and Petrology* **1989**, *101*, 479–484.
(193) Antao, S. M.; Hassan, I. *Phys Chem Minerals* **2007**, *34* (8), 573–580.
(194) Reeder, R. J.; Labmle, G. M.; Northrup, P. A. *American Mineralogist* **1999**, *84*, 1049–1060.
(195) Menadakis, M.; Maroulis, G.; Koutsoukos, P. G. *Computational Materials Science* **2007**, *38* (3), 522–525.
(196) Gillet, P.; Biellmann, C.; Reynard, B.; McMillan, P. *Phys Chem Minerals* **1993**, *20* (1), 1–19.
(197) Astilleros, J. M.; Pina, C. M.; Fernández-Díaz, L.; Putnis, A. *Geochimica et Cosmochimica Acta* **2000**, *64* (17), 2965–2972.
(198) Fernández-Díaz, L.; Astilleros, J. M.; Pina, C. M. *Chemical Geology* **2006**, *225* (3-4), 314–321.
(199) Reeder, R. J. *Geochimica et Cosmochimica Acta* **1996**, *60* (9), 1543–1552.
(200) Menadakis, M.; Maroulis, G.; Koutsoukos, P. G. *J Math Chem* **2008**, *46* (2), 484–491.
(201) Bunsenberg, E.; Plummer, L. N. *Geochimica et Cosmochimica Acta* **1986**, *50*, 2225–2233.
(202) Terada, J. *Journal of the Physical Society of Japan* **1953**, *8* (2), 1–9.
(203) Cam, N.; Georgelin, T.; Jaber, M.; Lambert, J. F.; Benzerara, K. *Geochimica et Cosmochimica Acta* **2015**, *161*, 36–49.
(204) Massoni, N.; Rosen, J.; Chartier, M.; Cozzika, T. *Journal of Nuclear Materials* **2013**, *441* (1-3), 152–158.
(205) Massoni, N.; Le Gallet, S.; Hoffmann, S.; Launeau, P.; Grin, Y.; Bernard, F. *Journal of the European Ceramic Society* **2015**, *35* (1), 297–308.
(206) Massoni, N.; Le Gallet, S. *Journal of Nuclear Materials* **2016**, *467*, 13–19.
(207) Kitano, Y.; Kanamori, N.; Oomori, T. *Geochemical Journal* **1971**, *4*, 183–206.
(208) Sartori, F. *Lithos* **1975**, *8*, 199–207.
(209) Railsback, L. B. *Carbonates and Evaporites* **1999**, *14* (1), 1–20.
(210) Larson, A. C.; Van Dreele, R. B. *LANSCE, MS-H* **1994**, 86–748.
(211) Toby, B. H. **2001**, *34*, 210–213.
(212) Gránásy, L.; Pusztai, T.; Tegze, G.; Warren, J. A.; Douglas, J. F. *Phys. Rev. E* **2005**, *72* (1), 011605–011615.
(213) Zhong, C.; Chu, C. C. *Crystal Growth & Design* **2010**, *10* (12), 5043–5049.
(214) Sear, R. P. *International Materials Reviews* **2012**, *57* (6), 328–356.
(215) Kunitake, M. E.; Mangano, L. M.; Peloquin, J. M.; Baker, S. P.; Estroff, L. A. *Acta Biomaterialia* **2013**, *9* (2), 5353–5359.
(216) Kim, Y.-Y.; Carloni, J. D.; Demarchi, B.; Sparks, D.; Reid, D. G.; Kunitake, M. E.; Tang, C. C.; Duer, M. J.; Freeman, C. L.; Pokroy, B.; Penkman, K.; Har-

ding, J. H.; Estroff, L. A.; Baker, S. P.; Meldrum, F. C. *Nature Materials* **2016**, *15* (8), 903–910.
(217) Eiblmeier, J.; Kellermeier, M.; Deng, M.; Kienle, L.; García-Ruiz, J. M.; Kunz, W. *Chem. Mater.* **2013**, *25* (9), 1842–1851.
(218) Eiblmeier, J.; Dankesreiter, S.; Pfitzner, A.; Schmalz, G.; Kunz, W.; Kellermeier, M. *Crystal Growth & Design* **2014**, *14* (12), 6177–6188.
(219) Opel, J.; Hecht, M.; Rurack, K.; Eiblmeier, J.; Kunz, W.; Cölfen, H.; Kellermeier, M. *Nanoscale* **2015**, *7* (41), 17434–17440.
(220) Wolf, S. E.; Leiterer, J.; Kappl, M.; Emmerling, F.; Tremel, W. *J. Am. Chem. Soc.* **2008**, *130* (37), 12342–12347.
(221) Chen, L.; Shen, Y.; Xie, A.; Huang, B.; Jia, R.; Guo, R.; Tang, W. *Crystal Growth & Design* **2009**, *9* (2), 743–754.
(222) Couradeau, E.; Benzerara, K.; Gerard, E.; Moreira, D.; Bernard, S.; Brown, G. E., Jr; Lopez-Garcia, P. *Science* **2012**, *336*, 459–462.
(223) Holl, C. M.; Smyth, J. R.; Laustsen, H. M. S.; Jacobsen, S. D.; Downs, R. T. *Phys Chem Minerals* **2000**, *27*, 467–473.
(224) Nishino, T.; Sakurai, T.; Ishizawa, N.; Mizutani, N.; Kato, M. *Journal of Solid State Chemistry* **1987**, *69*, 24–29.
(225) Strobel, R.; Maciejewski, M.; Pratsinis, S. E.; Baiker, A. *Thermochimica Acta* **2006**, *445* (1), 23–26.
(226) Ischenko, V.; Woltersdorf, J.; Pippel, E.; Köferstein, R.; Abicht, H.-P. *Solid State Sciences* **2007**, *9* (3-4), 303–309.
(227) Ono, S. *Phys Chem Minerals* **2007**, *34* (4), 215–221.
(228) Meyer, J. C.; Geim, A. K.; Katsnelson, M. I.; Novoselov, K. S.; Booth, T. J.; Roth, S. *Nature* **2007**, *446* (7131), 60–63.
(229) Tlili, M. M.; Amor, M. B.; Gabrielli, C.; Joiret, S.; Maurin, G.; Rousseau, P. *J. Raman Spectrosc.* **2002**, *33* (1), 10–16.
(230) Raiteri, P.; Gale, J. D. *J. Am. Chem. Soc.* **2010**, *132* (49), 17623–17634.
(231) Kellermeier, M.; Raiteri, P.; Berg, J. K.; Kempter, A.; Gale, J. D.; Gebauer, D. *ChemPhysChem* **2016**, *17* (21), 3535–3541.
(232) Bolze, J.; Peng, B.; Dingenouts, N.; Panine, P.; Narayanan, T.; Ballauff, M. *Langmuir* **2002**, *18* (22), 8364–8369.
(233) Bolze, J.; Pontoni, D.; Ballauff, M.; Narayanan, T.; Cölfen, H. *Journal of Colloid and Interface Science* **2004**, *277* (1), 84–94.
(234) Woehl, T. J.; Jungjohann, K. L.; Evans, J. E.; Arslan, I.; Ristenpart, W. D.; Browning, N. D. *Ultramicroscopy* **2013**, *127*, 53–63.
(235) Zou, Z.; Bertinetti, L.; Politi, Y.; Jensen, A. C. S.; Weiner, S.; Addadi, L.; Fratzl, P.; Habraken, W. J. E. M. *Chem. Mater.* **2015**, *27* (12), 4237–4246.
(236) Burke, K. S.; Parul, D.; Reddish, M. J.; Dyer, R. B. *Lab Chip* **2013**, *13* (15), 2912–10.
(237) Ofner, A.; Moore, D. G.; Rühs, P. A.; Schwendimann, P.; Eggersdorfer, M.; Amstad, E.; Weitz, D. A.; Studart, A. R. *Macromol. Chem. Phys.* **2016**,

1600472–10.
(238) Labanieh, L.; Nguyen, T.; Zhao, W.; Kang, D.-K. *Micromachines* **2015**, *6* (10), 1469–1482.
(239) Shim, J.-U.; Cristobal, G.; Link, D. R.; Thorsen, T.; Jia, Y.; Piattelli, K.; Fraden, S. *J. Am. Chem. Soc.* **2007**, *129* (28), 8825–8835.
(240) Boukellal, H.; Selimović, S.; Jia, Y.; Cristobal, G.; Fraden, S. *Lab Chip* **2009**, *9* (2), 331–338.
(241) Laval, P.; Giroux, C.; Leng, J.; Salmon, J.-B. *Journal of Crystal Growth* **2008**, *310* (12), 3121–3124.
(242) Ildefonso, M.; Revalor, E.; Punniam, P.; Salmon, J. B.; Candoni, N.; Veesler, S. *Journal of Crystal Growth* **2012**, *342* (1), 9–12.
(243) Schmitz, C. H. J.; Rowat, A. C.; Köster, S.; Weitz, D. A. *Lab Chip* **2009**, *9* (1), 44–49.
(244) Selimović, S.; Jia, Y.; Fraden, S. *Crystal Growth & Design* **2009**, *9* (4), 1806–1810.
(245) Akella, S. V.; Mowitz, A.; Heymann, M.; Fraden, S. *Crystal Growth & Design* **2014**, *14* (9), 4487–4509.
(246) Vericella, J. J.; Baker, S. E.; Stolaroff, J. K.; Duoss, E. B.; Hardin, J. O.; Lewicki, J.; Glogowski, E.; Floyd, W. C.; Valdez, C. A.; Smith, W. L.; Satcher, J. H.; Bourcier, W. L.; Spadaccini, C. M.; Lewis, J. A.; Aines, R. D. *Nat Comms* **2015**, *6*, 6124–6127.
(247) Chiu, Y.-L.; Chan, H. F.; Phua, K. K. L.; Zhang, Y.; Juul, S.; Knudsen, B. R.; Ho, Y.-P.; Leong, K. W. *ACS Nano* **2014**, *8* (4), 3913–3920.
(248) Arriaga, L. R.; Datta, S. S.; Kim, S.-H.; Amstad, E.; Kodger, T. E.; Monroy, F.; Weitz, D. A. *Small* **2013**, *10* (5), 950–956.
(249) Villar, G.; Graham, A. D.; Bayley, H. *Science* **2013**, *340* (6128), 48–52.
(250) Håti, A. G.; Bassett, D. C.; Ribe, J. M.; Sikorski, P.; Weitz, D. A.; Stokke, B. T. *Lab Chip* **2016**, 1–10.
(251) Wu, C.-H.; Park, A.; Joester, D. *J. Am. Chem. Soc.* **2011**, *133* (6), 1658–1661.
(252) Knapp, R. T.; Wu, C.-H.; Mobilia, K. C.; Joester, D. *J. Am. Chem. Soc.* **2012**, *134* (43), 17908–17911.
(253) Lei, Z.; Wang, Q.; Sun, S.; Zhu, W.; Wu, P. *Adv. Mater.* **2017**, *25*, 1700321–1700326.
(254) Carteret, C.; La Pierre, De, M.; Dossot, M.; Pascale, F.; Erba, A.; Dovesi, R. *The Journal of Chemical Physics* **2013**, *138* (1), 014201–014213.
(255) Gunasekaran, S.; Anbalagan, G.; Pandi, S. *J. Raman Spectrosc.* **2006**, *37* (9), 892–899.
(256) Anderson, F. A.; Brecevic, L. *Acta Chemica Scandinavica* **1991**, *45*, 1018–1024.
(257) Coleyshaw, E. E.; Crump, G.; Griffith, W. P. *Spectrochimica Acta Part A: Molecular and Biomolecular Spectroscopy* **2003**, *59* (10), 2231–2239.
(258) Yue, L.; Shui, M.; Xu, Z. *Spectroscopy Letters* **2001**, *34* (6), 793–802.

(259) Lin-Hai, Y.; Miao, S.; Zhu-de, X. *Journal of Zhejiang University* **2000**, *1* (2), 178–183.

(260) Garrels, R. M.; Thompson, M. E.; Siever, R. *American Journal of Science* **1960**, *258*, 402–418.

(261) Jain, A.; Ong, S. P.; Hautier, G.; Chen, W.; Richards, W. D.; Dacek, S.; Cholia, S.; Gunter, D.; Skinner, D.; Ceder, G.; Persson, K. A. *APL Materials* **2013**, *1* (1), 011002–011012.

(262) Malis, T.; Cheng, S. C.; Egerton, R. F. *Journal of Electron Microscopy Technique* **1988**, *8*, 193–200.

15. Appendix A: Supplemental information for chapter 9

15.1 Thermogravimetric analysis

Water content for materials synthesized with 1 M Na_2CO_3 (pH 11.2) ranged from 0.90 to 1.40 formula units. The average was 1.2 ± 0.2, as described in the materials and methods (Figure 15.1). When 1 M $(NH_4)_2CO_3$ (pH 9.2) was used in place of 1 M Na_2CO_3, the water content ranged from 1.44-1.28 formula units, decreasing with increasing x. When 0.1 M solutions of $(NH_4)_2CO_3$ and $BaCl_2$ were used, water content ranged from 1.11-1.29, increasing with x. Across all experimental conditions, water content was within the range 0.9-1.44. Given the range of water content observed over all conditions, there seems to be no correlation between total water content and the counterion in solution, or the total concentration.

ACBC made from 0.1 M solutions had three distinct regions of weight loss below 400°C, previously linked to the sequential loss of fluid-like, mobile, rigid and trapped H_2O and hydroxyl ions.[135] These three regions were nearly indistinguishable in ACBC made from 1 M solutions of either carbonate source. The total fractional weight loss, Δa_T, weight lost upon crystallization, Δa_c, water content, n (from the formula $Ca_{1-x}Ba_xCO_3.nH_2O$) and crystallization onset temperature, T_c, are given in Table 15.1. Water lost during crystallization, defined as the weight loss occurring within the temperature range bounded by a crystallization exotherm peak also did not correlate with x. Rapid mass loss above ~550°C is consistent with decomposition into CaO, BaO, and CO_2.

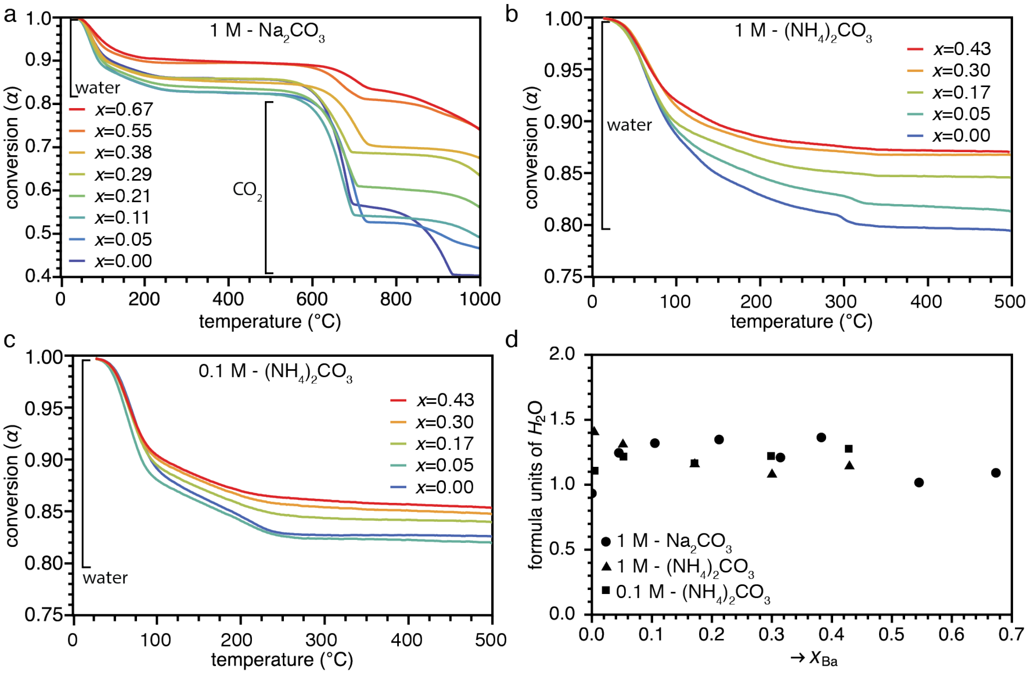

Figure 15.1. Thermogravimetric analysis of ACBC. (a) Plot of conversion α vs. temperature T for 1 M solutions and Na_2CO_3 carbonate source. Loss of water occurs in the range from 30-500°C, loss of CO_2 at T >500°C. (b-c) Plot conversion α vs. temperature T for ACBC precipitated from 1 M (c) and 0.1 M (d) $(NH_4)_2CO_3$ solutions. (d) Plot of stoichiometric coefficient for water, n, vs. x for all three conditions investigated in (a-c).

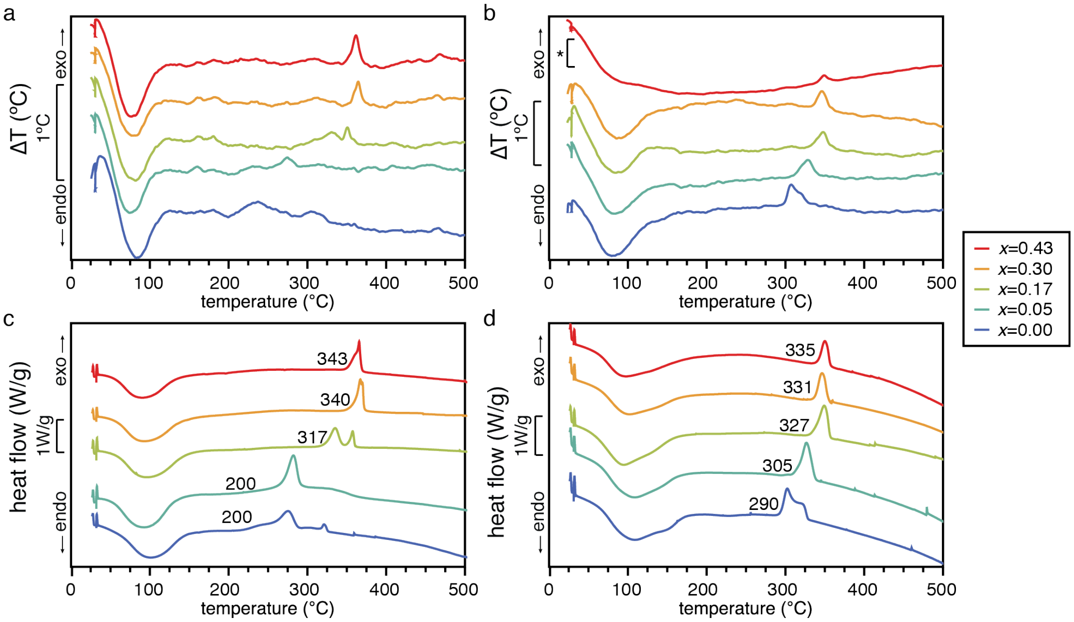

Figure 15.2. DTA (a-b) and DSC (c-d) of ACBC from Figure 15.1b-c. In DTA, the y-axis scale is the difference between the set temperature and actual measured temperature. In DSC, the scale is the power delivered to

the sample normalized by the mass, in W/g. Endotherms at ~100 °C correspond to the loss of water, and exotherms above ~200 °C, annotated in (c) and (d) correspond to the crystallization of ACBC.

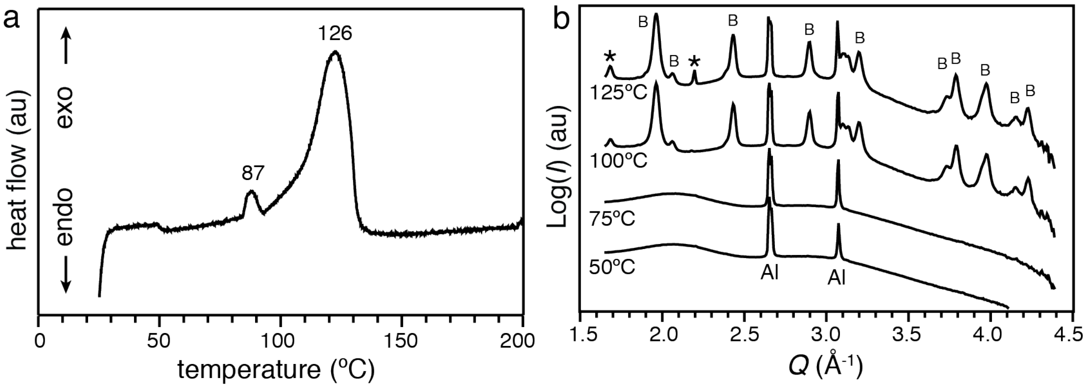

Figure 15.3. Simultaneous in situ DSC/WAXS of ACBC with x = 0.50. (a) Qualitative DSC curve showing exothermic crystallization peaks. Heat flow could not be quantified in this system due to the absence of a reference thermocouple. (b) Crystallization to balcite (B) observed after the first crystallization exotherm. Further crystallization resulted in separate, unidentified peaks (*). Samples were contained within sealed aluminum pans, producing different conditions from Figure 15.2 that may explain the lower crystallization temperature in this experiment.

Table 15.1. Thermal analysis of ACBC

x	Δa_T (wt%)	Δa_c (wt%)	n	T_c (°C)
0.1 M solutions				
0.00	16.65	1.90	1.11	200
0.05	17.26	0.04	1.23	200
0.17	15.31	0.03	1.26	317
0.30	14.54	0.12	1.24	340
0.43	13.98	0.11	1.29	343
1 M solutions				
0.00	20.62	1.12	1.44	290
0.05	18.72	1.62	1.34	305
0.17	15.45	0.28	1.22	327
0.30	13.24	0.05	1.24	331
0.43	12.96	0.11	1.29	335

15.2 Vibrational spectroscopy

Raman spectra of ACBC contained many low-intensity features in addition to the most intense ν_1 mode. Many of these features have previously been observed in ACC or other carbonates. In Raman spectra, the ν_3 mode (asymmetric stretch) appeared as at least two weak, broad modes in the range between 1300 and 1600 cm^{-1} (Figure 15.4). This was in contrast to calcite, where the ν_3 mode was a single sharp peak at 1435 cm^{-1}, and witherite, where there was one sharp peak at 1409 cm^{-1} and a broader peak at 1508 cm^{-1}. The ν_2 mode (out-of-plane bending) that is not active in calcite or witherite is just barely recognizable in ACBC spectra (not shown).

The ν_1 mode of ACBC shifted to lower wavenumber with increasing barium content, approaching the single ν_1 mode peak of witherite at 1059 cm^{-1}. In calcite there are two degenerate ν_4 modes,[169] but witherite exhibits four predicted Raman-active modes.[254] For the split ν_4 mode, the mode at higher wavenumber, $\nu_{4,1}$, also shifted to lower wavenumber over the same range of compositions. The $\nu_{4,2}$ mode on the other hand, mirrored this trend only up to x = 0.21. Above this value, the Raman shift remained nearly constant at 7 cm^{-1}. As a consequence, the distance between the two ν_4 mode centers decreased. Peak centers and the $\nu_{4,1}/\nu_{4,2}$ ratio bore an increasing resemblance to the ν_4 of witherite (Figure 15.3-15.10).

In addition to the normal modes, combination bands and higher harmonics were also observed. These include a weak peak at 1740 cm^{-1} that has been attributed to ν_1+ν_4 in ACC and appears at 1800 cm^{-1} and 1750 cm^{-1} in calcite and witherite,[255] respectively. Higher combination bands, like those at 2146 cm^{-1} and 2172 cm^{-1} in calcite, were not observed in ACBC.[256] Other combination bands (e.g., $2\nu_2+\nu_4$) in calcite and witherite between 2400-2600 cm^{-1} and 2800-3000 cm^{-1}, were observed as faint features in some ACBC samples, but overlapping OH-stretching modes[257] made quantification difficult.

The ν_1 and ν_4 modes showed similar behavior in IR spectra. However, the magnitude of the mode center shift was larger in IR (Figure 15.6, Table 15.2). The maxima of the $\nu_{3,1}$ mode of ACC at ~1415 cm^{-1} shifted to 1395 cm^{-1} at x = 0.55, while the $\nu_{3,2}$ shifted from ~1482 cm^{-1} to 1440 cm^{-1}. Fitting of the most intense ν_3 of ACBC could not be performed due to the numerous broad, overlapping bands. Combination bands of lattice and internal modes have been suggested to contribute to the broad signal in this region,[256,258] resulting in counterintuitive broadening for crystalline materials and reduction in peak width for poorly-crystalline samples.[259] With no evidence of crystallinity in XRD, SAED, and polarized light, the distinctly different peak profiles ACBC compared to calcite and witherite favors the interpretation that ACBC contains multiple distributions of ν_3 mode frequencies over the possibility of contributions from lattice coupling. A notable exception to the general shift towards lower wavenumbers, the ν_2 mode was largely unaffected by increasing barium content. However, a clear increase in intensity of the ν_4 mode relative to the ν_2 was observed with increasing barium content.

In IR spectra (Figure 15.5), the ν_1 mode was observed in ACBC and witherite, but not in calcite, where it is forbidden (Figure 15.5d). The broad ν_4 mode was split in ACBC, in contrast to sharp, single features in calcite and witherite (Figure 15.5b). The Ramaninactive ν_2 had at least two broad IR modes in ACBC, fewer than in calcite and witherite (Figure 15.5c). The characteristic sharp ν_3 peak superimposed upon very broad tails was observed in calcite at 1421 cm^{-1} and in witherite at 1429 cm^{-1}. In ACBC, at least two broad but intense bands were attributed to ν_3 modes, between 1300-1600 cm^{-1} (Figure 15.5d). Combination modes, like the ν_1+ν_3 (Figure 15.5e) are observed between 2400-2700 cm^{-1}. Evidence of water and hydroxyl groups was present in IR spectra of ACBC as an H-O-H stretch at 1650 and very broad OH-stretching modes extending from 2500-3800 cm^{-1}(Figure 15.5d,f).[257]

Table 15.2. Vibrational spectra of ACBC

x	Raman modes			IR modes				
	$\nu_{4,1}$[a]	$\nu_{4,2}$[a]	ν_1[a]	$\nu_{4,1}$[b]	$\nu_{4,2}$[b]	ν_2[b]	ν_1[a]	ν_3[c]
0	726.8	699.6	1079.7	745	713	866	1077	~1300-1600
0.05	725.0	698.6	1078.7	722	695	866	1073	~1300-1600
0.11	723.4	697.3	1077.0	719	692	866	1071	~1300-1600
0.21	720.3	694.3	1074.8	718	690	866	1069	~1300-1600
0.29	717.6	692.8	1072.2	712	689	866	1068	~1300-1600
0.38	717.0	693.6	1070.9	709	688	866	1067	~1300-1600
0.55	713.1	692.9	1067.7	708	687	866	1063	~1300-1600
0.67	711.1	692.3	1066.0	705	687	866	1062	~1300-1600

[a] *Mode centers of Gaussians fit to experimental spectra;* [b] *selected by eye because fitting found to be unreliable due to low intensity;* [c] *approximate range*

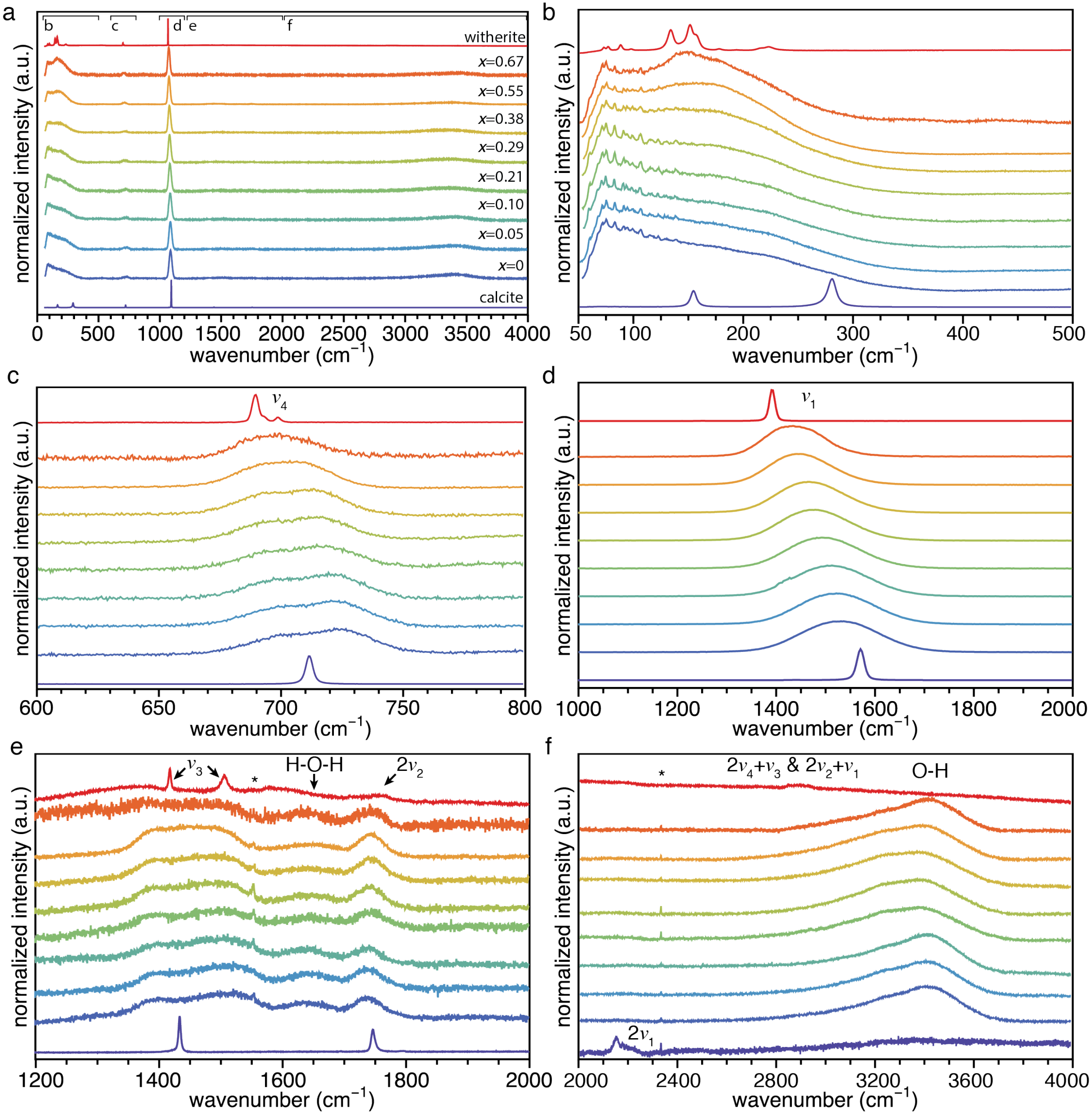

Figure 15.4. Raman spectra of ACBC with different compositions. (a) Full spectra. Increased resolution of individual regions given in b-f. (b) Phonon mode region, showing the increase in intensity below 300 cm^{-1} in ACBC with increasing *x*. (c) Carbonate ν_4 mode. (d) Carbonate ν_1 mode. (e) Carbonate ν_3 mode and $2\nu_2$ harmonic, and subtle H-O-H stretching mode. (f) High wavenumber modes, including the O-H stretching mode of water and/or hydroxyl ions. Note that the very small peaks marked with an asterisk in (d) and (e) are an artefact that results from joining spectra recorded over an extended range.

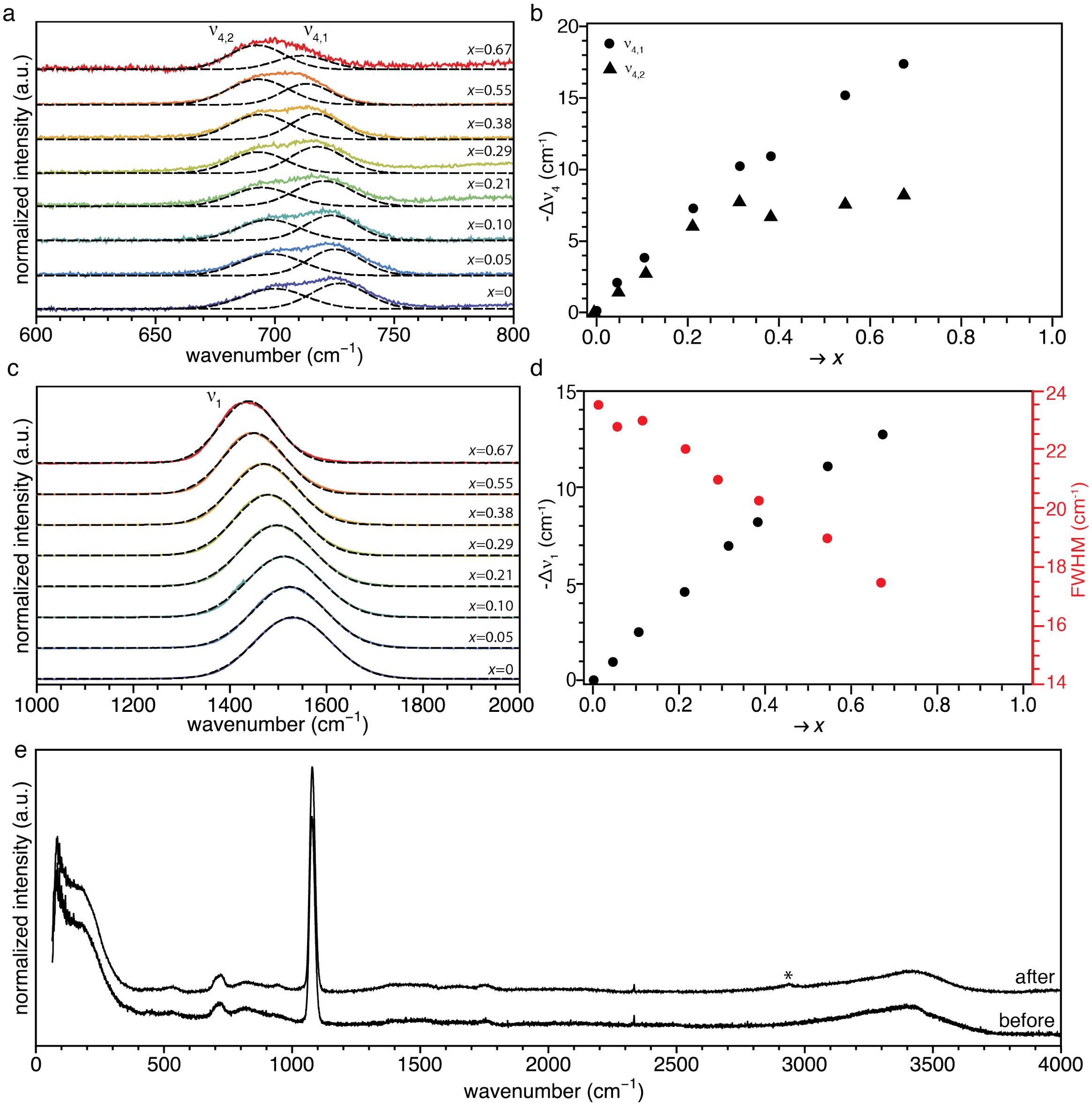

Figure 15.5: Raman spectra of ACBC. (a) The ν_4 mode in ACC and ACBC was split into $\nu_{4,1}$ and $\nu_{4,2}$ modes. Position and intensity were identified by fitting the experimental data as the sum of two Gaussians (b) Peak centers of the $\nu_{4,1}$ and $\nu_{4,2}$ shifted to lower wavenumbers with increasing barium content. Note that while the $\nu_{4,1}$mode shift showed nearly linearly over the whole range, the $\nu_{4,2}$ reached a plateau at x~0.3. In addition the shift in mode wavenumber, the relative intensity of the two modes inverted over the range in composition. (c) The ν_1 mode center shifted nearly linearly to lower wavenumbers (d). Shift of the ν_1 center relative to that of ACC (black) and the corresponding reduction in the FWHM (red). Calcite and witherite have FWHM of 2 cm^{-1}. (e) Full Raman spectra of ACBC with x = 0.41 before and after dehydration under vacuum at 50°C for 8 hours, normalized to the ν_1 mode. Water loss is confirmed by the reduction in intensity of the OH stretch between ~2800-3700 cm^{-1}. The (*) indicates the location of a peak that arises in this range after partial dehydration, but no appreciable change in the acoustic phonon mode region (<300 cm^{-1}) is observed.

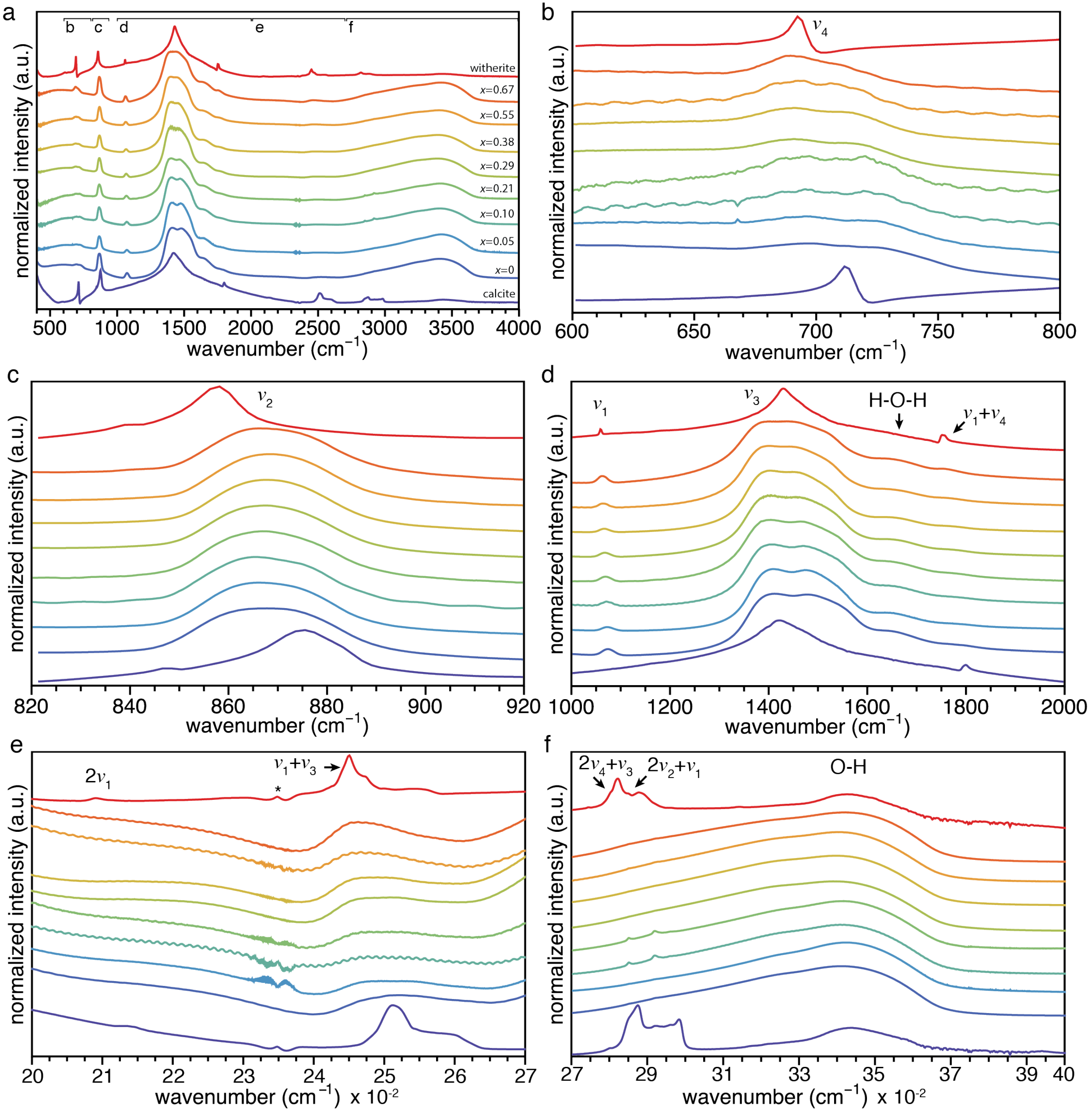

Figure 15.6. (a) FTIR spectra of ACBC. (a) Full spectra, normalized to the intensity of the ν_3 mode. (b-f) Detail spectra of regions indicated in (a), normalized to the data point with the highest intensity. (b) Carbonate ν_4 mode. (c) Carbonate ν_2 mode. (d) Weak carbonate ν_1 and intense carbonate ν_3 modes, as well as H-O-H stretch above 1600 cm^{-1} and the $\nu_1 + \nu_4$ combination band. (e) Carbonate $2\nu_1$ harmonic and $\nu_1 + \nu_3$ combination band. (*) indicates artifact from subtraction of background containing atmospheric CO_2. (f) Carbonate $2\nu_4 + \nu_3$ and $2\nu_2 + \nu_1$ combination bands, and a broad O-H stretching mode.

15.3 Estimation of the solubility product for simulated ACBC structures

Solubilities of ACBC were obtained from

$$-RTlnK_{sp}^{Ca_{1-x}Ba_xCO_3} = (1-x)\mu_{Ca^{2+}}^{o} + x\mu_{Ba^{2+}}^{o} + \mu_{CO_3^{2-}}^{o} - \mu_{Ca_{1-x}Ba_xCO_3}^{o} \qquad (15.1)$$

where $\mu_{Ca_{1-x}Ba_xCO_3}^{o}$ is calculated from the DFT formation energies, and the standard state chemical potentials of Ca^{2+}, Ba^{2+}, and CO_3^{2-} ions in solution are referenced to reproduce the experimental $K_{sp}^{\mathrm{calcite}}$ and $K_{sp}^{\mathrm{witherite}}$.[26] This referencing scheme captures all entropic contributions to the chemical potentials of solvated ions, under the approximation that vibrational contributions to the entropy difference between competing solids at 298K are negligible. We approximate calcite ($pK_{sp} = 8.48$)[161] and witherite ($pK_{sp} = 8.56$)[201] to have the same solubility of $pK_{sp} = 8.5$ so that the free-energy of the solvated ions referenced to the phase separated calcite and witherite can be expressed as

$$\mu_{Ca^{2+}}^{o} + \mu_{CO_3^{2-}}^{o} = \mu_{Ba^{2+}}^{o} + \mu_{CO_3^{2-}}^{o} = -RTln(10^{-8.5}) \approx 50\ kJ/mol \qquad (15.2)$$

In this case, the solubility of ACBC structures can be expressed as a function of their ΔH_c,

$$log_{10}K_{sp}^{Ca_{1-x}Ba_xCO_3} = -8.5 + log_{10}\left[exp\left(\frac{\Delta H_c}{RT}\right)\right] \approx -8.5 + 0.43 \cdot \Delta H_c \qquad (15.3)$$

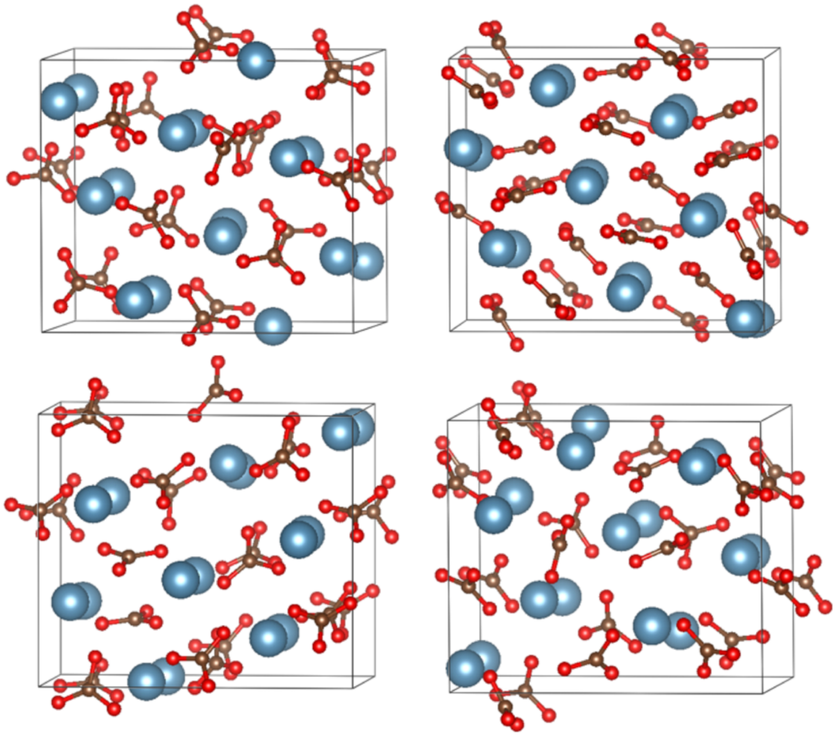

Figure 15.7. Representative ACC structures after relaxation in DFT. Calcium ions were replaced with barium prior to DFT relaxation to form ACBC.

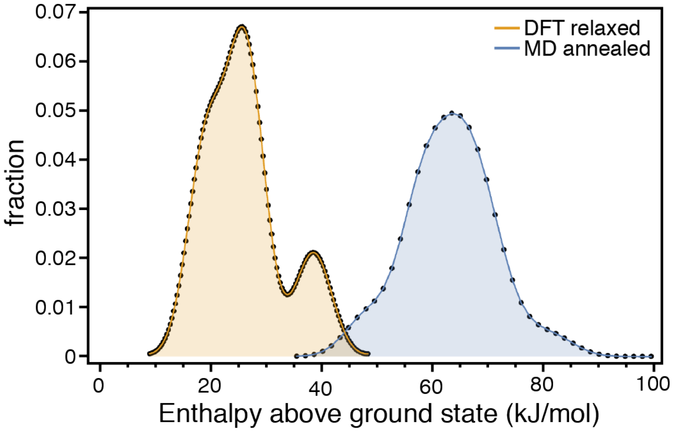

Figure 15.8. Comparison of the enthalpy above the ground state for MD-relaxed (blue) and DFT-relaxed (orange) ACBC. DFT relaxation produces considerably lower energy structures, which are more dense and accurately reproduce experimental enthalpies of crystallization.

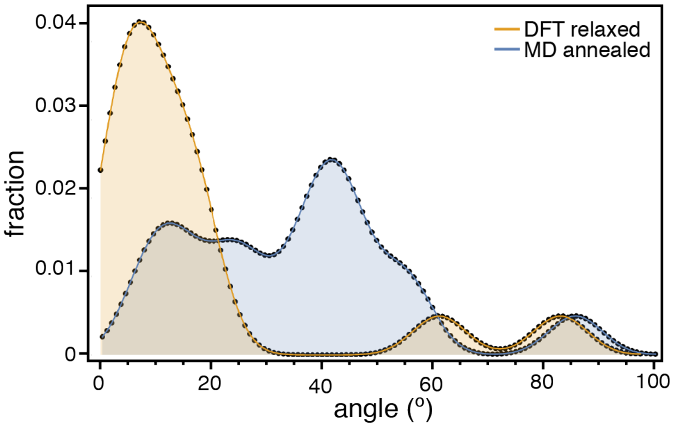

Figure 15.9. Alignment of carbonate orientations for all simulated structures, quantified by the average angle between the vector normal to the plane of oxygens.

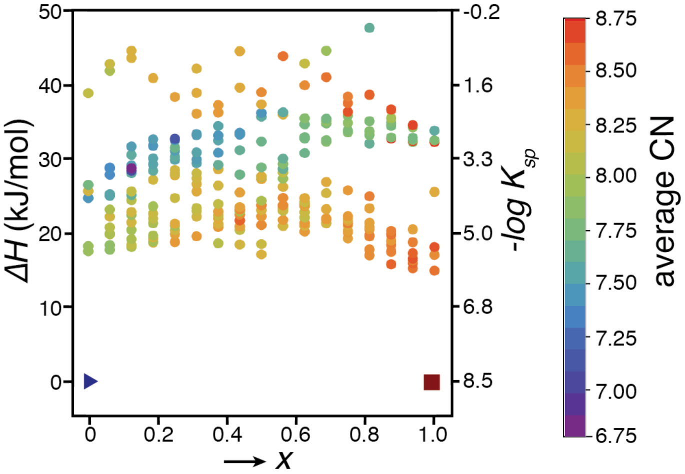

Figure 15.10. Plot of ΔH, i.e. the difference in enthalpy between ACBC (solid circles) and a phase-separated mixture of calcite ($CaCO_3$, solid triangle) and witherite ($BaCO_3$, solid square), as a function of barium content x. Markers are colored by the average cation coordination number.

15.4 **EXAFS Fitting**

Close inspection of the EXAFS of both cations reveals trends that are consistent with changing carbonate alignment (Table 15.3-Table 15.8). As mentioned in 9.5.6, disorder in the first coordination shell around both cations required two separate nearest neighbor oxygen distances. These distances, and the average number of oxygen at each distance, changed with composition. For example, the number of oxygen closest to calcium increased from an average of 2.4 ± 0.17 at x = 0 to 4.5 ± 0.08 at x = 0.05, then decreased back to 2.3 ± 0.24 between x = 0.05 – 0.55 (Table 15.3-Table 15.8). This trend correlated with the overall barium coordination number, and is also consistent with bond distances for both $Ca-O_1$ and $Ba-O_1$ (Table 9.1).

Table 15.3. Ca K-edge EXAFS parameters (1st shell)

$Ca-O_1$

x	CN	CN Distribution			R $Ca-O_1$ (Å)			σ^2 (Å^2)		
		CN $Ca-O_{1,1}$	CN $Ca-O_{1,2}$	St. dev.	R $Ca-O_{1,1}$	R $Ca-O_{1,2}$	St. dev.	σ^2 $Ca-O_{1,1}$	σ^2 $Ca-O_{1,2}$	St. dev.
0	6.8	2.44	4.36	0.17	2.21	2.40	0.01	0.002	0.002	0.001
0.01	6.8	3.60	2.90	0.08	2.32	2.48	0.01	0.022	0.005	0.002
0.05	6.8	4.14	2.36	0.08	2.31	2.50	0.01	0.007	0.005	0.001
0.10	6.8	3.51	2.99	0.09	2.29	2.47	0.01	0.002	0.002	0.001
0.21	6.8	3.31	3.19	0.06	2.30	2.47	0.01	0.003	0.003	0.001
0.38	6.8	3.12	3.38	0.05	2.28	2.45	0.01	0.002	0.002	0.001
0.55	6.4	2.28	4.22	0.24	2.19	2.39	0.01	0.001	0.004	0.001

Table 15.4. Ca K-edge EXAFS parameters (2nd shell)

Ca-C

x	CN	CN Distribution			R Ca-C_1 (Å)			σ^2 (Å^2)		
		CN Ca-$O_{1,1}$	CN Ca-$O_{1,2}$	St. dev.	R Ca-$C_{1,1}$	R Ca-$C_{1,2}$	St. dev.	σ^2 Ca-$C_{1,1}$	σ^2 Ca-$C_{1,2}$	St. dev.
0	6.8	1.77	4.73	0.17	3.06	3.54	0.12	0.005	0.022	0.022
0.01	6.8	2.57	3.93	0.08	2.94	3.11	0.01	0.002	0.004	0.001
0.05	6.8	3.91	2.59	0.16	2.94	3.13	0.01	0.004	0.002	0.001
0.10	6.8	4.09	2.41	0.35	2.88	3.49	0.05	0.007	0.016	0.010
0.21	6.8	3.66	2.84	0.13	2.88	3.04	0.01	0.005	0.002	0.001
0.38	6.8	2.74	3.76	0.13	2.82	3.08	0.01	0.010	0.007	0.002
0.55	6.4	2.60	3.90	0.17	2.95	3.21	0.01	0.004	0.004	0.001

Table 15.5. Ca K-edge EXAFS parameters (3rd shell)

Ca-O_2

x	CN	CN Distribution			R Ca-O_2 (Å)			σ^2 (Å^2)		
		CN Ca-$O_{2,1}$	CN Ca-$O_{2,2}$	St. dev.	R Ca-$O_{2,1}$	R Ca-$O_{2,2}$	St. dev.	σ^2 Ca-$O_{2,1}$	σ^2 Ca-$O_{2,2}$	St. dev.
0	5.75	5.8	--	0.24	3.75	--	0.19	0.028	--	0.028
0.01	8.00	3.99	4.01	0.60	3.35	4.11	0.03	0.024	0.023	0.005
0.05	8.00	2.31	5.69	0.28	3.90	4.14	0.02	0.004	0.009	0.002
0.10	8.00	4.20	3.80	0.42	3.04	4.10	0.05	0.011	0.020	0.010
0.21	8.00	4.09	3.91	0.13	3.14	3.40	0.01	0.007	0.011	0.001
0.38	8.00	1.67	6.33	0.27	3.50	4.01	0.03	0.013	0.025	0.005
0.55	8.00	3.75	2.25	0.16	3.41	3.66	0.01	0.003	0.001	0.001

Table 15.6. Ca K-edge EXAFS parameters (4th shell)

Ca-(Ca/Ba)

x	CN	CN Distribution			R Ca-(Ca/Ba) (Å)			σ^2 (Å^2)		
		CN Ca-$(Ca/Ba)_1$	CN Ca-$(Ca/Ba)_2$	St. dev.	R Ca-$(Ca/Ba)_1$	R Ca-$(Ca/Ba)_2$	St. dev.	σ^2 Ca-$(Ca/Ba)_1$	σ^2 Ca-$(Ca/Ba)_2$	St. dev.
0	--	--	--	--	--	--	--	--	--	--
0.01	--	--	--	--	--	--	--	--	--	--
0.05	4.91	4.91	--	0.69	4.54	--	0.01	0.016	--	0.002
0.10	--	--	--	--	--	--	--	--	--	--
0.21	3.82	3.82	--	0.61	4.39	--	0.02	0.020	--	0.004
0.38	--	--	--	--	--	--	--	--	--	--
0.55	8.00	2.07	6.93	0.63	3.72	4.33	0.02	0.019	0.027	0.004

Table 15.7. Ba K-edge EXAFS parameters (1st shell)

Ba-O$_1$

x_{Ba}	CN	CN Distribution			R Ba-O$_1$ (Å)			σ^2 (Å^2)		
		CN Ba-O$_{1,1}$	CN Ba-O$_{1,2}$	St. dev.	R Ba-O$_{1,1}$	R Ba-O$_{1,2}$	St. dev.	σ^2 Ba-O$_{1,1}$	σ^2 Ba-O$_{1,2}$	St. dev.
0	--	--	--	--	--			--		
0.01	11	3.64	7.36	0.97	2.58	2.78	0.06	0.013	0.008	0.005
0.05	12	6.67	5.53	0.68	2.62	2.76	0.05	0.031	0.009	0.015
0.10	9.5	3.95	5.55	1.10	2.74	2.87	0.07	0.008	0.008	0.018
0.21	9	2.40	6.60	1.61	2.76	2.93	0.10	0.014	0.014	0.012
0.38	8	2.44	5.56	1.17	2.75	2.86	0.09	0.008	0.008	0.013
0.55	8	2.86	5.14	0.98	2.69	2.84	0.06	0.007	0.007	0.010

Table 15.8. Ba K-edge EXAFS parameters (2nd shell)

Ba-C$_1$

x_{Ba}	CN	CN Distribution			R Ba-C$_1$ (Å)			σ^2 (Å^2)		
		CN Ba-C$_{1,1}$	CN Ba-C$_{1,2}$	St. dev.	R Ba-C$_{1,1}$	R Ba-C$_{1,2}$	St. dev.	σ^2 Ba-C$_{1,1}$	σ^2 Ba-C$_{1,2}$	St. dev.
0	--	--	--	--	--			--		
0.01	12	4.18	7.82	2.84	3.05	3.69	0.14	0.008	0.024	0.015
0.05	12	7.24	4.76	1.66	2.97	3.65	0.06	0.016	0.017	0.005
0.10	8.5	2.56	5.94	3.43	2.73	3.68	0.24	0.033	0.021	0.016
0.21	10	2.55	7.45	2.62	2.80	3.66	0.24	0.036	0.023	0.014
0.38	9	4.70	4.30	0.94	2.76	3.66	0.04	0.012	0.013	0.003
0.55	11	2.95	8.05	1.80	2.83	3.64	0.17	0.030	0.022	0.009

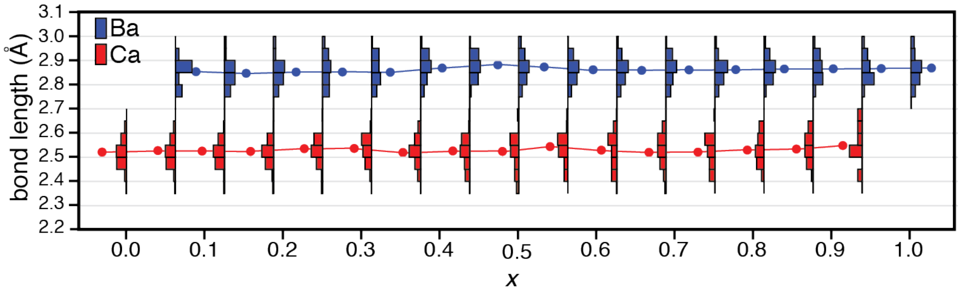

Figure 15.11. Frequency of the cation-oxygen bond lengths for calcium (red) and barium (blue) in ACBC as a function of composition. Bin widths are 0.75 Å. No appreciable change in bond length is observed as a function of x.

16. Appendix B: Supplemental information for chapter 10

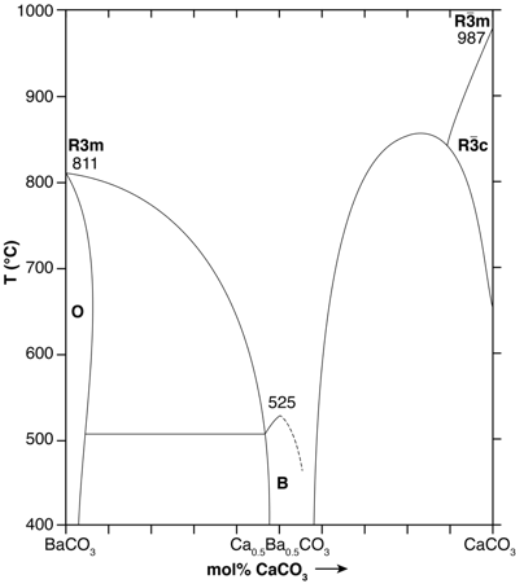

Figure 16.1. Pseudobinary phase diagram of the $BaCO_3$-$CaCO_3$ system.[156] Witherite (O) undergoes a first order transformation to a calcite-type R3m phase above 811°C. Barytocalcite (B) recrystallizes into a 'disordered calcite' phase above 525°C. Approaching 970°C calcite ($R\bar{3}c$) gradually transforms into a high temperature phase with $R\bar{3}m$ symmetry through the progressive rotation of carbonates in the calcite lattice about their 3-fold axes.[188,192]

16.1 $BaCO_3$-$CaCO_3$ phase behavior

Barytocalcite undergoes a reversible first-order transition into the 'carbonate-disordered-calcite'-type phase above 525°C,[156,191]. Less frequently, it has been referred to as 'disordered barytocalcite', in reference to the low temperature structure at the composition $Ca_{0.5}Ba_{0.5}CO_3$.[178] It is likely that the stability field of barytocalcite, as reported phase diagram (Figure 16.1), does not extend to room temperature.[156,260] It is also possible that barytocalcite has a high kinetic barrier to formation, analogous to other binary carbonates norsethite ($Mg_{0.5}Ba_{0.5}CO_3$) and dolomite ($Ca_{0.5}Mg_{0.5}CO_3$), and is only observed at higher temperatures,[104,186] but it has also been suggested that barytocalcite may be stabilized by minor impurities (i.e., strontium).[202]

At higher pressures, aragonite is the equilibrium phase of $CaCO_3$. A well-known but 'anomalous' increase in the stability of calcite relative to aragonite at higher temperatures arises from a structural rearrangement of calcite.[192]

Phase separation of balcite into calcite and witherite was expected based on the reported phase diagram of the $CaCO_3$-$BaCO_3$ system[156] and DFT calculated formation energies from the Materials Project Database.[261] Balcite is metastable relative to barytocalcite ($Ca_{0.5}Ba_{0.5}CO_3$) below 525°C.[156] Barytocalcite itself appears to be metastable,[261] having a higher formation energy than orthorhombic solid-solutions of the same composition (aragonite + witherite) or the ground state, phase separated phases (calcite + witherite). This may an indication of a crossover in stability below ~ 400°C, where experimental data are not available.

Table 16.1. EDS composition of balcite precipitates.

Feed solution: ICP-OES		ACBC: XRF		Balcite: EDS	
x_{feed}	std. dev.	x	std. dev.	x	std. dev.
0		0		-	-
0.060	0.0035	0.045	0.001	0.10	0.01
0.127	0.0073	0.105	0.001	0.21	0.02
0.251	0.0116	0.212	0.002	0.34	0.01
0.369	0.0127	0.314	0.003	0.39	0.01
0.422	0.0248	0.382	0.002	0.42	0.01
0.640	0.0370	0.545	0.003	0.51	0.02
0.785	0.0254	0.673	0.004	0.51	0.01

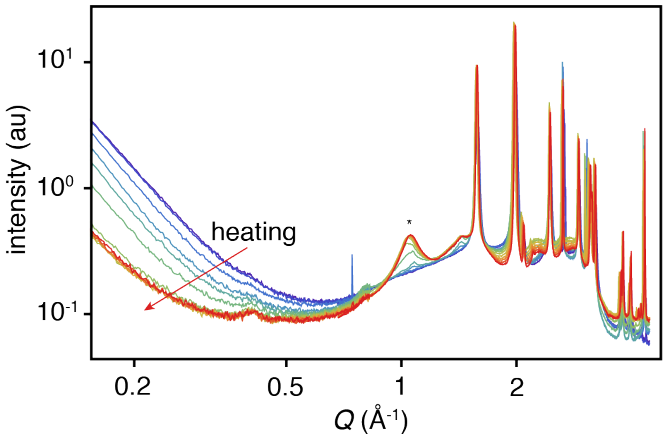

Figure 16.2. In situ WAXS of balcite upon heating from 25-600°C. Diffraction peaks are relatively unaffected by increasing temperature, but diffuse scattering changes appreciably upon heating. Most prominently, scattering below Q = 0.5 shifts to lower Q, and a broad peak emerges at Q~1.05 (Å^{-1}), consistent with a superlattice reflection of the (003) at Q ~ 2.1 (Å^{-1}).

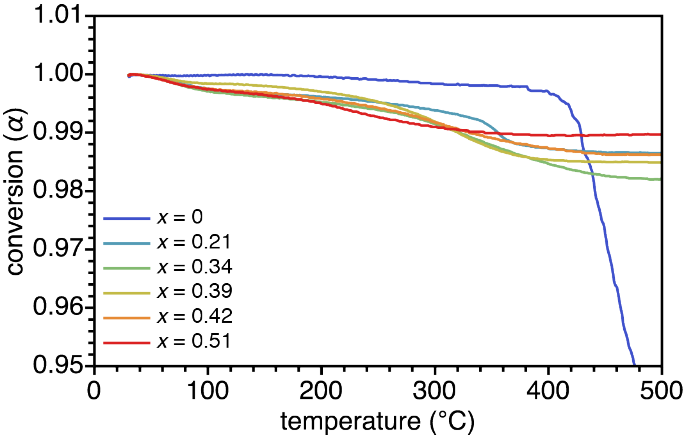

Figure 16.3. TGA of samples crystallized from ACBC. All samples show gradual but minimal weight loss up to 500°C, except for x = 0, which contained some vaterite and began to decompose around 400°C.

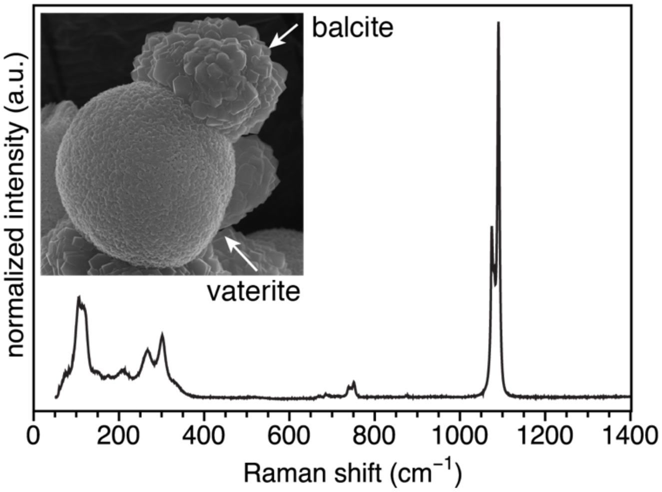

Figure 16.4. SEM image of balcite and vaterite present in sample crystallized from ACBC with x = 0.21 (Figure 10.2a). Vaterite (center) was easily identified by the absence of faceted crystallites and rough, nano-featured texture. Balcite (top right) was distinguished by its polycrystalline faceting and Ba signal by EDS in SEM, and by its unique split Raman υ_1 mode in the Raman microscope.

16.2 Samples for NMR

^{13}C-enriched balcite was characterized with X-ray fluorescence to determine the composition, and powder X-ray diffraction (XRD) to determine the phase assemblage. XRF analysis of bulk powders indicated that the cation fraction of barium in the precipitate, x, was 0.51, 0.41, 0.31, and 0.24. This is 81% ± 3% of the ratio in solution, slightly lower than previously observed for balcite made with natural isotope abundance (86%). XRD (Figure 10.2) showed that all powders contained balcite, which is easily distinguished by the most intense (102) peak between 28-30 °2θ. Surprisingly, powders A and B contained witherite ($BaCO_3$) as an impurity co-precipitate. This was unexpected, as previous syntheses had traces of witherite only above $x = 0.55$. Therefore, it appears that increasing the amount of ^{13}C in the sodium carbonate starting solution affects the composition, and phase distribution, of the product. This is an interesting observation worth further investigation, but was not conducted in this study.

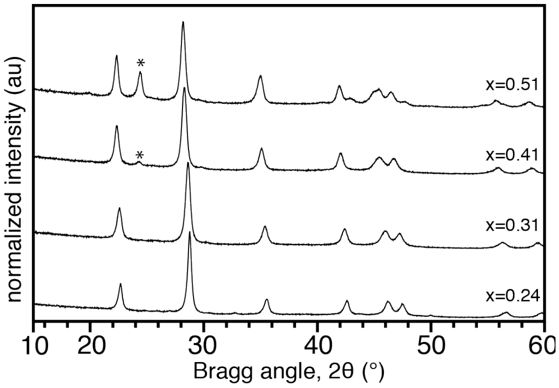

Figure 16.5. XRD of ^{13}C-enriched balcite powders. (*) denotes highest intensity witherite peak. Intense peak between 28-30° is the (102), analogous to the (104) of calcite.

16.3 **Balcite metastability**

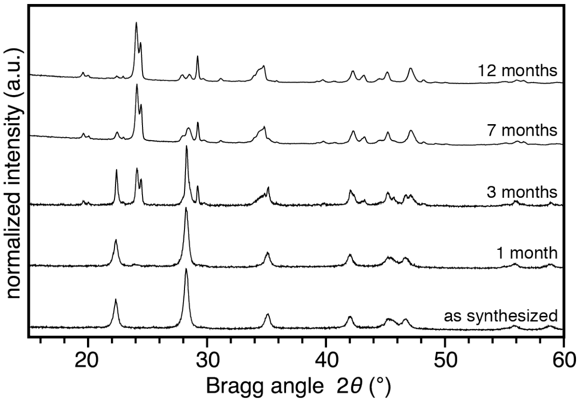

Figure 16.6. Dissolution of balcite with x = 0.48 over time.

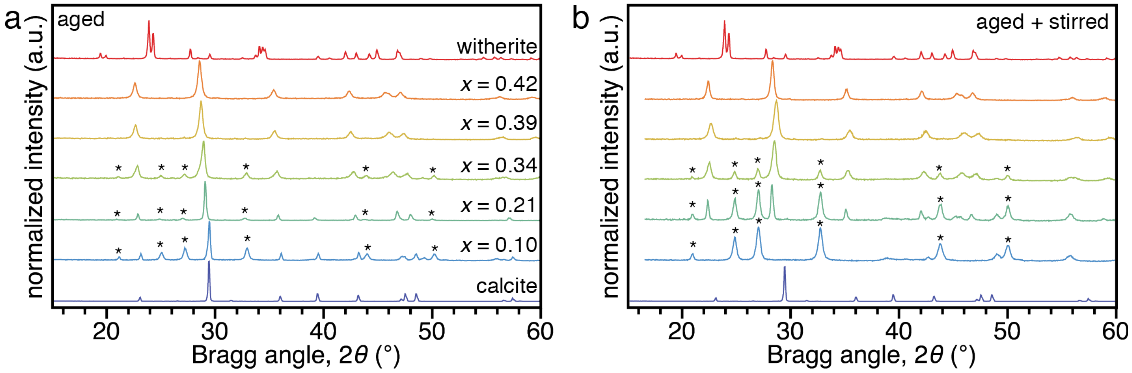

Figure 16.7. The same compositions as those in Figure 10.2 (up to $x = 0.51$), but stirred constantly during the 24 hours in solution. At $x \leq 0.21$ much more vaterite formed when stirred, with the $x = 0.05$ sample completely converted to vaterite at the expense of balcite.

Witherite and calcite powders were suspended in water with calcite/witherite molar ratios from 0.1 to 0.9 in increments of 0.1. After 30 days the powders were filtered, washed with water, and dried overnight at 110°C. Only calcite and witherite were observed at all compositions, with no evidence of balcite (Figure 16.8). Mixing either witherite with 100 mM $CaCl_2$, or calcite with 100 mM $BaCl_2$ for the same duration yielded only witherite calcite physical mixtures (Figure 16.8).

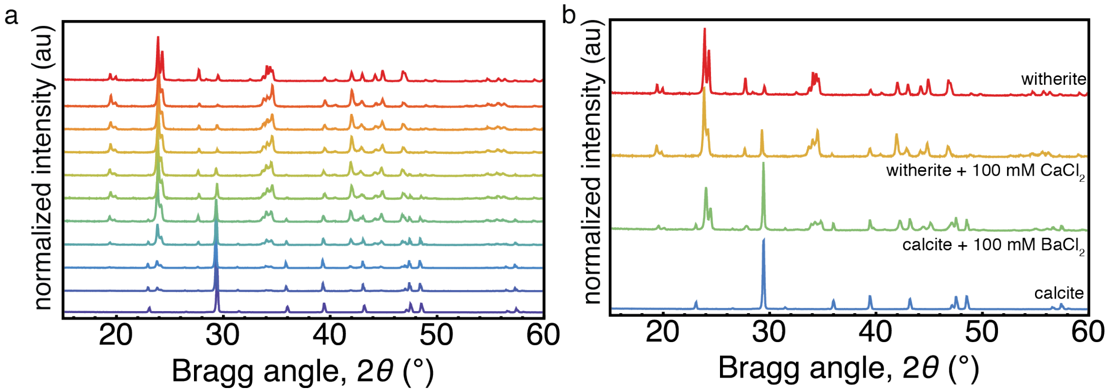

Figure 16.8. (a) Physical mixtures of calcite and witherite ranging from pure calcite (blue, bottom) to pure witherite (red, top). No indications of balcite formation are observed at any mixing fraction after 30 days in

constantly stirred aqueous solution. (b) Balcite does not form through the addition of witherite to 100 mM $CaCl_2$ or calcite to 100 mM $BaCl_2$.

16.4 Supersaturation with respect to witherite

$$\sigma = ln\frac{AP}{K_{sp}}$$

$$K_{sp,vaterite} = 10^{-7.9} = a^{e}_{Ca^{2+}} \cdot a^{e}_{{CO_3}^{2-}}$$

$$a_{{CO_3}^{2-}} = (10^{-7.9})^{1/2} = 112\ \mu M$$

$$K_{sp,witherite} = 10^{-8.562} = a^{e}_{Ba^{2+}} \cdot a^{e}_{{CO_3}^{2-}}$$

$$\sigma_{witherite} = ln\frac{(112\ \mu M) \cdot (50\ mM)}{10^{-8.562}\ M^2} = 7.6$$

16.5 Raman spectroscopy of precipitates in confinement

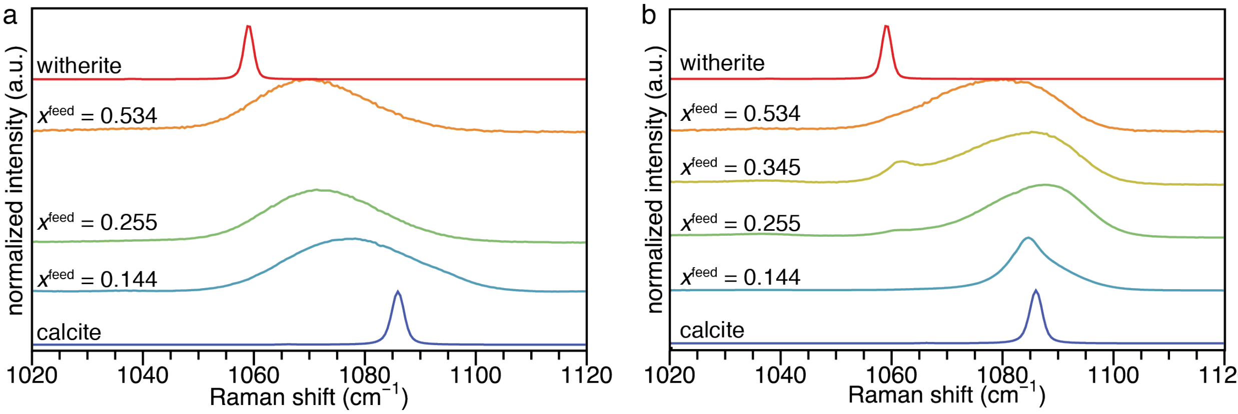

Figure 16.9. Raman spectroscopy of drop-encapsulated precipitates. (a) ACBC and (b) balcite from starting solutions with nominal barium cation fraction given by x.

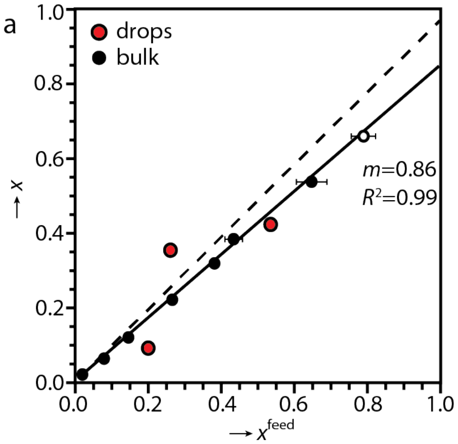

Figure 16.10. Composition of ACBC in drops, calculated from the shift in the ν_1 Raman mode shift, compared with bulk ACBC.[121]

17. Appendix C: Supplemental information for chapter 11

17.1 Inductively coupled plasma-optical emission spectroscopy

The barium mole fraction x^{feed} of solutions of the starting materials was determined by inductively coupled plasma-optical emission spectrometry (ICP-OES), using a Thermo iCAP 7600 instrument. Solutions were diluted 100x in water and then 200x in 3% by volume aqueous nitric acid. Intensities for the four strongest emission lines of barium (λ = 230.424, 233.527, 455.403, and 493.409 nm) and Ca (λ =315.887, 393.366, 396.847, and 422.673 nm) were recorded in both axial and radial geometries. Intensities were converted to absolute concentrations using a calibration curve recorded for a series of eight standard solutions ranging from 1 µg/mL to 4 ng/mL that were prepared by serial dilution. An average concentration value and standard deviation for barium and calcium was determined from 8 individual values (4 different emission lines in two geometries each, Table Table 17.1). Finally, x^{feed} was calculated according to $x^{\text{feed}}= \frac{[\text{Ca}]}{[\text{Ca}]+[\text{Ba}]}$, using the limits of uncertainty for individual measurements as bounds for the reported error. ICP-OES was also used confirm the composition of some ACBC samples. An aliquot of the dry powder (~1 mg) was dissolved in 3% nitric acid (10 mL), and then diluted by 100x in 3% aqueous nitric acid. Both values agree within the experimental error for each measurement (Supplemental Table Table 17.2), justifying the use of both techniques for stoichiometry determination.

17.2 XRF

The barium mole fraction, x, of single-phase balcite was determined on a custom built X-ray fluorimeter with an Ag-anode operating at 15 mA and 40 kV. Detector calibration was performed using the Fe and Mo K_α lines of a stainless steel ingot of known composition. Background scattering was subtracted from the raw spectra, and corrections for matrix absorption and Compton scattering were applied using XRF-FP v5.2.7 software from CrossRoads Scientific. Integrated barium $L_{\alpha,1}$ and Ca K_α fluorescence intensity was obtained by fitting Gaussian peak profiles to all calcium and barium fluorescence peaks. From the barium $L_{\alpha,1}$ and calcium K_α fluorescence intensities, x was determined. Three technical replicates were performed at each composition.

17.3 Scanning electron microscopy (SEM)

Approximately 5 mg of the dry powder was deposited on carbon tape and coated with ~8 nm osmium with an SPI OPC-60A Osmium Plasma Coater. Imaging was performed in a Hitachi S4800 FE-SEM or Hitachi S8030 operating at 20 keV at a working distance of 10 mm. Energy dispersive spectroscopy (EDS) was collected using AZtec software (Oxford Instruments) using an Oxford AZtec X-max 80 SDD EDS detector. Spectra for balcite and calcite spherulites were collected from rectangular areas approximately 5 μm x 5 μm within five separate particles and averaged. Data were fit with a Gaussian peak profiles and converted to atomic percent using calibrated standards MgO (Mg K-edge 1.0 – 1.4 keV), $CaCO_3$ (Ca K-edge 3.5 – 3.9 keV), and $BaTiO_3$ (Ba L-edges 4.3 – 5.7 keV). The cation mole fraction for barium (or magnesium) was normalized by the total cation mole fraction to give $x = \frac{[\mathrm{Ba}]}{[\mathrm{Ca}]+[\mathrm{Ba}]}$, or $x = \frac{[\mathrm{Mg}]}{[\mathrm{Ca}]+[\mathrm{Mg}]}$ to give the overall composition $Ca_{1-x}Ba_xCO_3$ or $Ca_{1-x}Mg_xCO_3$. Line scans across balcite and calcite particle cross sections were collected at 30 keV for a minimum of 600 seconds total collection time, with 100 μs dwell time at 50 nm intervals. Data was smoothed with a mean filter distance of five, and normalized to the overall composition measured on a 5 μm x 5 μm rectangular area.

Table 17.1. ACBC/Balcite composition summary

Feed solution: ICP-OES		**ACBC: XRF**		**Balcite: EDS**	
x_{feed}	std. dev.	x	std. dev.	x	std. dev.
0		0		-	-
0.060	0.0035	0.045	0.001	-	-
0.127	0.0073	0.105	0.001	-	-
0.251	0.0116	0.212	0.002	-	-
0.369	0.0127	0.314	0.003	-	-
0.422	0.0248	0.382	0.002	-	-
0.640	0.0370	0.545	0.003	0.52	0.02
0.785	0.0254	0.673	0.004	-	-

Table 17.2. ICP-OES/XRF comparison

ACBC: ICP-OES		**ACBC: XRF**	
x	std. dev.	x	std. dev.
0.009	0.0003	0.01	0.001
0.042	0.0026	0.04	0.001
0.088	0.0066	0.09	0.001
0.171	0.0097	0.19	0.002
0.304	0.0094	0.33	0.002
0.438	0.0019	0.45	0.002

17.4 Powder X-ray diffraction (pXRD)

Approximately 200 mg of the dry powder was pressed into low background amorphous silica sample holders for diffraction analysis. X-ray diffraction patterns were acquired on a Rigaku Ultima diffractometer using copper Kα radiation (λ = 1.504 Å), 0.05° step size, and sample-to-detector distance of 285 mm.

17.5 High resolution synchrotron powder diffraction (hr-pXRD) and Rietveld refinement

Synchrotron powder XRD pattern of balcite ($Ca_{1-x}Ba_xCO_3$, where x = 0.50) was performed at Sector 5-BM-D of the Advanced Photon Source at Argonne National Laboratory. The wavelength, λ, was set to 0.2748 Å (50 keV) and collected on a MAR345 two-dimensional plate detector. Data were calibrated with polycrystalline silicon and integrated with Datasqueeze. The pattern was indexed with JADE2010 software. Pattern indexing yielded $R\bar{3}m$, $R3m$, or $R32$, as the most likely space groups for balcite. $R3m$ and $R32$ did not produce adequate fits in Rietveld refinement. Rietveld refinement was performed with GSAS using the EXPGUI graphical user interface[210,211] using the $R\bar{3}m$ setting with atom positions Ca (0, 0, 0); Ba (0, 0, 0); C (0,0,½); O (X, 0, ½). Partial occupancy of the O site was set to 0.5, and those of Ca and Ba fixed at 0.49 and 0.51, respectively, based on XRF measurements.

17.6 In situ synchrotron wide angle X-ray scattering

Low mass aluminum pans (TZero) were filled with approximately 20 mg of powder and hermetically sealed by crimping an aluminum lid to the top of the pan. The pans were heated from 25°C to 600°C and cooled back to 25°C at a rate of 10 °C min^{-1} using a Linkam (Linkam Scientific Instruments, Tadworth, UK) controlled temperature stage. WAXS patterns were collected every minute at intervals of 10 °C. Diffuse rings consistent with a polycrystalline material were observed in two-dimensional CCD images. These images were radially integrated using custom beamline software.

17.7 X-ray total scattering

X-ray total scattering was performed at the Dow-Northwestern-Dupont collaborative access team (DND-CAT), Sector 5-BM-D of the Advanced Photon Source at Argonne National Laboratory. The X-ray energy (20.000 keV, λ = 0.6195 Å) was selected with a Si(111) monochromator, and calibrated with a Mo foil at the Mo K-edge. Data was collected in Bragg-Brentano geometry with a Huber D8219 diffractometer (2θ = 4-169°). The step size was 0.5° and the dwell time was 10 s. Four Si-drift solid state detectors with multichannel analyzers (MCA, ~250 eV resolution at 20 keV) were used to simultaneously measure elastic scattering, Ca K-edge, and Ba L-edge fluorescence. Total fluorescence signal was used for normalization of the elastic scattering. Spectra were also normalized for incident beam intensity measured with an ion chamber (pN_2 = 550 Torr and pAr = 16 Torr). Scattering from the sample holder and Compton scattering were subtracted, and an absorption correction applied based on sample composition using GetPDFx2 package.[67]

The reduced structure factor f(Q) was determined from the total scattering intensity I(Q) by subtraction of atomic scattering and background. Real space information was then obtained by Fourier transformation of f(Q). The resulting pair distribution function, G(r), the probability of finding an arbitrary pair of atoms separated by the distance, r, provides real space information about the interatomic distances on the ~1-50 Å length scale.

17.8 **X-ray absorption spectroscopy**

Samples for X-ray absorption spectroscopy were synthesized in the same way as above, with drying times of at least 4 hours under vacuum. Measurements were performed at the Dow-Northwestern-Dupont collaborative access team (DND-CAT), Sector 5-BM-D of the Advanced Photon Source at Argonne National Laboratory. Samples were spread on 8 μm Kapton tape and kept dry under a stream of He gas. Calibration at the Ca K-edge was performed with a geological Iceland spar (calcite) standard, for which the edge energy was set at 4038 eV. ACBC samples were measured relative to this value. Data was analyzed using the Demeter package.[70] Normalization and background subtraction were carried out in Athena using Autobk. χ-data were weighted by k , k^2, and k^3 between $1.6 < k < 11.5$ Å^{-1} for the Ca K-edge and between $2 < k < 14$ Å^{-1} for the Ba K-edge.

17.9 **Nanoindentation**

Powders were mounted in EpoTek epoxy resin, with a 4:1 ratio of base to curing agent, cured for at least 24 hours at room temperature. Flat surfaces were obtained via argon ion milling in a Leica TIC3X equipped with a cryo-stage, operating at 8 kV and 3 mA, $5 \cdot 10^{-6}$ mbar, and a stage temperature set point of -25°C. Milling was followed by air plasma treatment at $6 \cdot 10^{-1}$ Torr for 2 min for a final surface cleaning. Nanoindentation was performed in a Hysitron TI 950 TriboIndenter using a Berkovich diamond indenter geometry to a peak load of 1000 μN. Tip shape and piezo control were calibrated with a fused quartz standard prior to testing each sample. Particle surfaces were imaged with the same in diamond tip before and after indentation. Porosity in the center of the spherulite particles, measured from the root-mean-squared height profile from images obtained with the indenter tip, required indents to be taken from ~5-10 μm thick shells on the outside of the particles that were fully dense and had roughness less than 1 nm rms. After elastic relaxation, indents were approximately 50 nm deep and 1.5 μm across. At least 10 measurements across at least 3 particles each were collected for as-synthesized balcite, balcite heated to 600°C, spherulitic magnesian calcite, and single crystalline calcite.

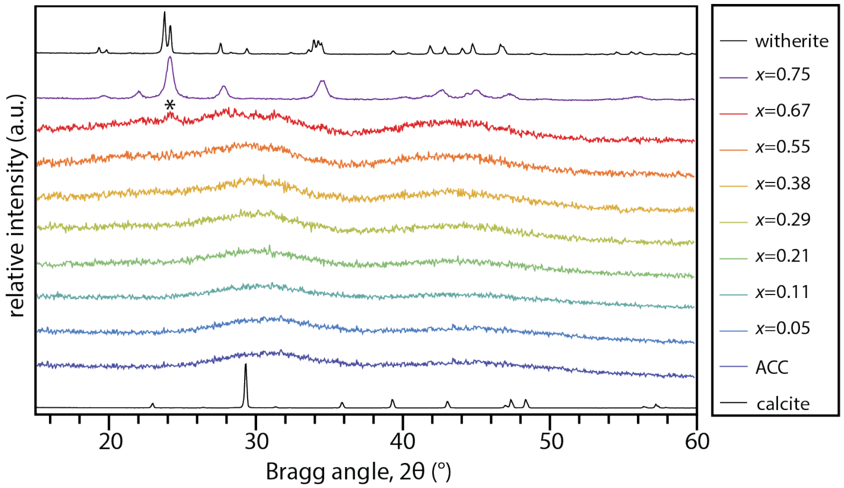

Figure 17.1. pXRD patterns of ACBC and reference compounds. Note that the ACBC sample with x = 0.67 may contain a small amount of witherite (asterisk).

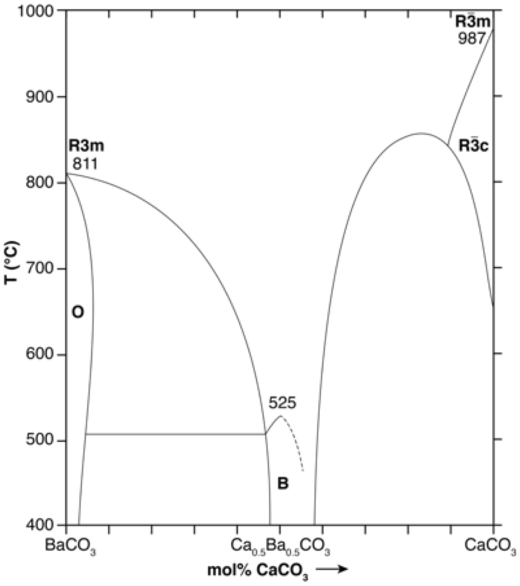

Figure 17.2. Pseudobinary phase diagram of the $BaCO_3$-$CaCO_3$ system, modified from ref[156]. Witherite (O) undergoes a first order transformation to a calcite-type R3m phase above 811°C. Barytocalcite (B) recrystallizes into a ‘disordered calcite’ phase above 525°C. Approaching 970°C calcite ($R\bar{3}c$) gradually transforms into a high temperature phase with $R\bar{3}m$ symmetry through the randomization of carbonate orientation about their 3-fold axes. There appears to be a gradual (second order) transition from $R\bar{3}c$ to $R\bar{3}m$ structures with increasing barium at higher temperatures.

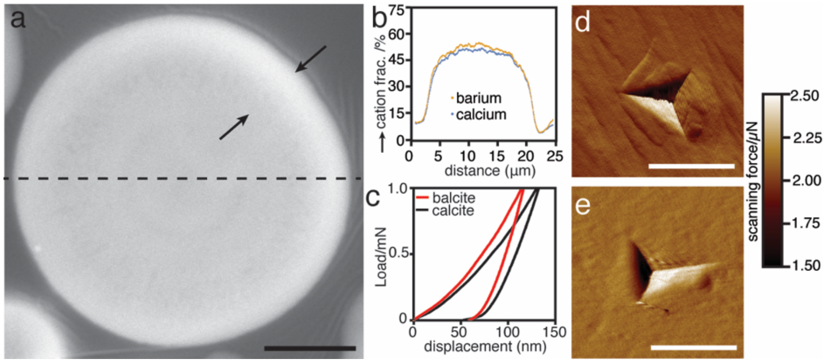

Figure 17.3. Balcite particle cross section and hardness measurements. (a) SEM image of a cross section of a balcite spherulite prepared by broad beam ion milling. Arrows indicate the dense rim on the exterior of a spherulite. (b) Plot of barium and calcium cation fractions against distance along the dashed line in (a), determined by SEM-EDS. Note that while the shape of the profile is affected by the hemispherical shape of the particle, the relative amounts of Ba and Ca are within expectations and do not change significantly across the spherulite. (c) Representative nanoindentation load-displacement curves for a balcite spherulite and a calcite spherulite, from which the hardness, H, and indentation modulus, EI was calculated using established methods.[4] (d, e) Probe force images of calcite (d) and balcite (e) generated by scanning the indenter tip across the surface after nano-indentation. Scale bar represents 2 µm.

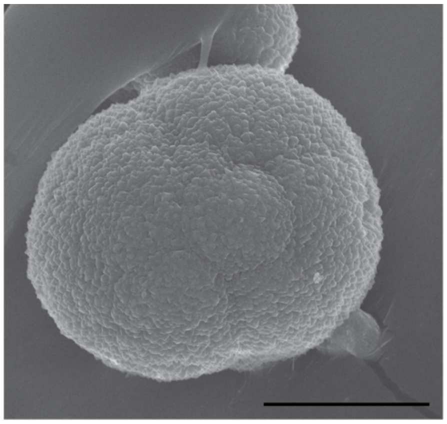

Figure 17.4. SEM images of spherulites of magnesian calcite. Scale bar represents 10 µm.

18. Appendix C: Supplemental information for chapter 12

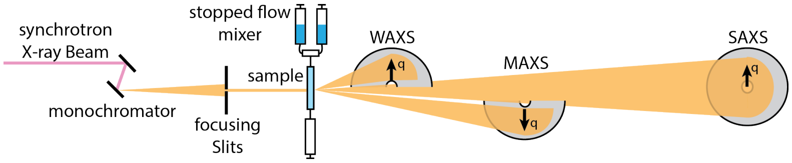

Figure 18.1. Schematic of time-resolved X-ray scattering configuration. A stopped-flow mixer allowed for rapid and repeatable precipitation in solution. The aqueous precipitate was passed through a thin walled (100 μm) glass capillary, where scattering was acquired over a continuous range of scattering vectors q = 0.002 – 5 $Å^1$ with three separate detectors.

18.1 X-ray scattering

SAXS was acquired with a 75 ms acquisition time and 25 ms readout time. Patterns were azimuthally averaged and plotted as the scattering intensity versus the scattering vector, $q = \frac{4\pi sin\theta}{\lambda}$, where θ is the scattering angle and λ the wavelength of radiation. WAXS is generally considered the region $q > 1$ $Å^{-1}$, where real-space scattering distances $d = \frac{2\pi}{q}$ are on the order of interatomic or interplanar spacings. For q<<1, the scattered intensity $I(q)$ can be written as

$$I(q) = |A(q)|^2 = \left|\int_v \rho_o(r)e^{iqr}dr\right|^2 \qquad (18.1)$$

where v is the particle volume, $A(q)$ is the normalized amplitude of scattering, and $\rho_o(r)$ the electron density of the scattering particle relative to its surroundings. From this expression, the increase in scattered intensity with time can be attributed to the increase in volume of growing particles. In the limit of small q, the scattering function simplifies to the Guinier approximation:

$$□(□) = □□^{-\frac{(□□_□)^2}{3}} \qquad (18.2)$$

where R_g is the radius of gyration and G is equal to $(\rho_o v)^2$. In the limit of larger q, a power law dependence takes the form

$$I(q) = \frac{B}{q^4} \tag{18.3}$$

where B is Porod's constant, equal to $2\pi\rho_o^2 S_v$ where S_v is the particle surface to volume ratio. Using the unified model of Beaucage,[68] the scattering intensity from low and high q can be considered independent and additive, giving a total scattering intensity

$$I_i(q) = \sum_i G_i e^{-\frac{(qR_g)^2}{3}} + e^{-\frac{\left(qR_{g,CO}\right)^2}{3}} B_i \left[\frac{erf\,\left(\frac{qR_g}{\sqrt{6}}\right)^3}{q}\right]^{P_i} \tag{18.4}$$

where i is the number of scattering levels (e.g. 2 for discs, one each for the thickness and diameter). $R_{g,CO}$ is the cutoff radius from a smaller level, effectively limiting the contribution of smaller particles on the scattering from larger ones.

The total volume of precipitates can be calculated from the Porod invariant, Q_v, by

$$Q_v = \int_{q=0}^{\infty} q^2 I(q)\,dq \tag{18.5}$$

This parameter is independent of the particle shape, and can therefore be used to quantify the total volume of precipitate, even for polydisperse distributions or particle type mixtures.

18.2 **SAXS data fitting**

Data fitting was performed in the Irena package[69] for Igor Pro. The 'Unified Fit' model[1] was applied to all data. Only four fit parameters, R_g, G, P, and B were required for convergent fits with standard residuals of < 10 over the entire q range. At t < 0.7 s, a single R_g was sufficient for convergent fits (Figure 18.2). This suggests that the particles were relatively isotropic. Through the first 0.7 seconds, R_g increased from 31 to 54 nm. Assuming spherical particles, the particle radius, R, was calculated from $R^2 = \frac{5}{3}R_g^2$, giving radii from 40 to 70 nm. The Porod invariant, Q_v, increased linearly during this time, an indication of continual growth. However, P decreased from 4.0 to 3.0, which is indicative of a rough surface. This suggests that the initially smooth particles underwent a roughening transition during growth.

Beginning at t > 0.7 s, the single unified fit failed to produce physically realistic results (e.g., unphysical S_v values). P decreased below 3.0 and the Q_v diverged. Two unified levels were required, with two of each parameter R_g, G, P, and B. The size cutoff for the larger R_g, (R_{g2}) was fixed at the value of the smaller R_g, (R_{g1}). The smaller dimension remained relatively invariant at R_{g1} = ~9 nm, while the larger dimension grew slightly between 0.7 < t < 0.1.3 s but also stabilized around R_{g2} = 50 nm (Figure 18.2). Under the assumption that these two radii originate from disk-like particles, the thickness, T, using the formula $T^2 = 2R_g^2$ for thin platelets, a thickness of nm was obtained, in excellent agreement with EELs measurements.

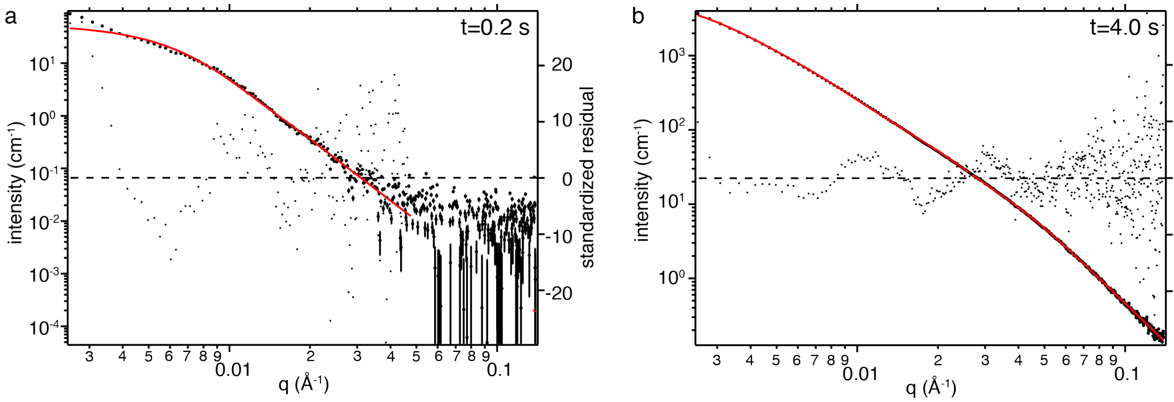

Figure 18.2. SAXS fitting in Irena. (a) First time point after the initiation of mixing (0.1 s) exhibiting a single Guinier shoulder above q = 0.01 $Å^{-1}$ and a Porod slope of ~4 below 0.01 $Å^{-1}$. (b) After 4.0 seconds, there were two distinct Guinier/Porod regions above and below q = 0.02 $Å^{-1}$. Note the lower intensity, greater noise in the high q region, and larger standardized residual in (a). A slight deviation from the fit towards higher intensities at low q suggests that the particles may aggregate to some degree.

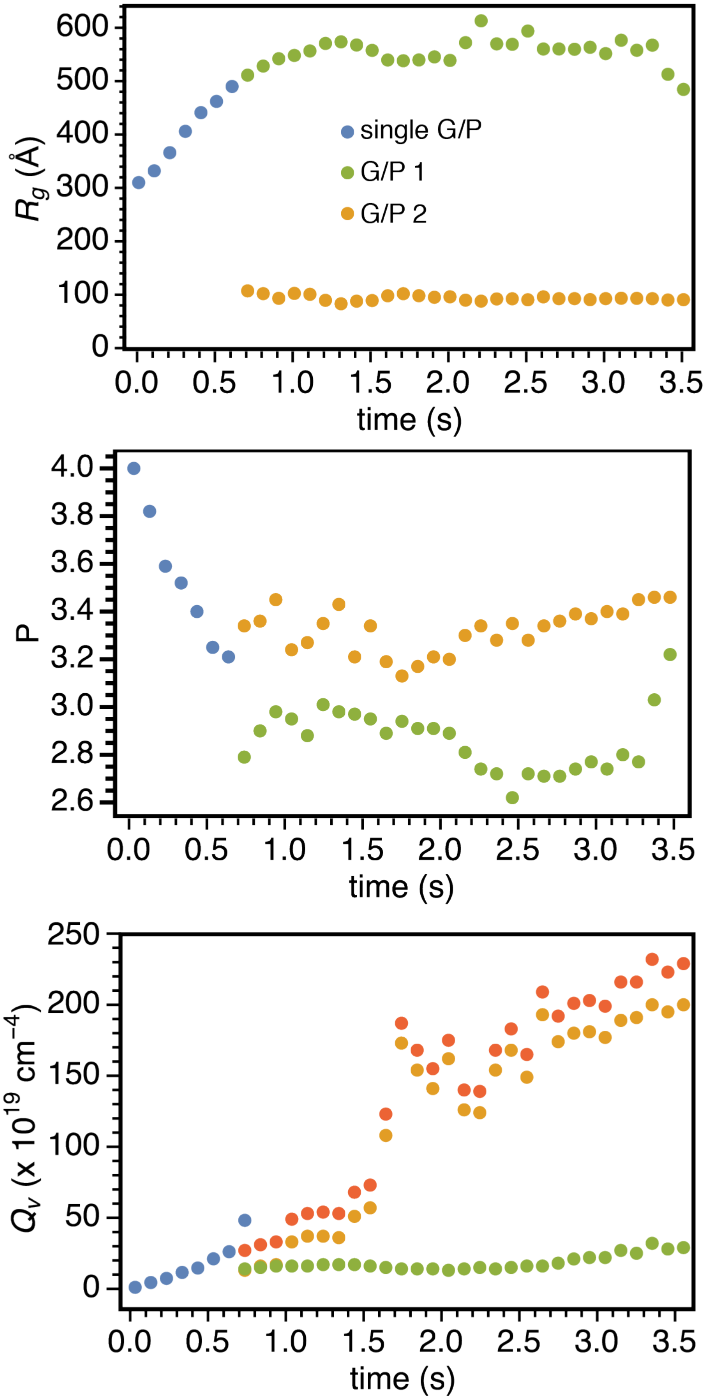

Figure 18.3. SAXS fitting parameters extracted from Guinier/Porod unified fits, like those shown in Figure 18.2. (a) R_g of initial isotropic particles (blue) and anisotropic particles with two separate R_g (green and yellow). (b) Porod slopes, showing a decrease in time for the first-formed particles, with relatively stable values for the anisotropic particles. (c) Porod invariant, showing continually increasing precipitate volume with time.

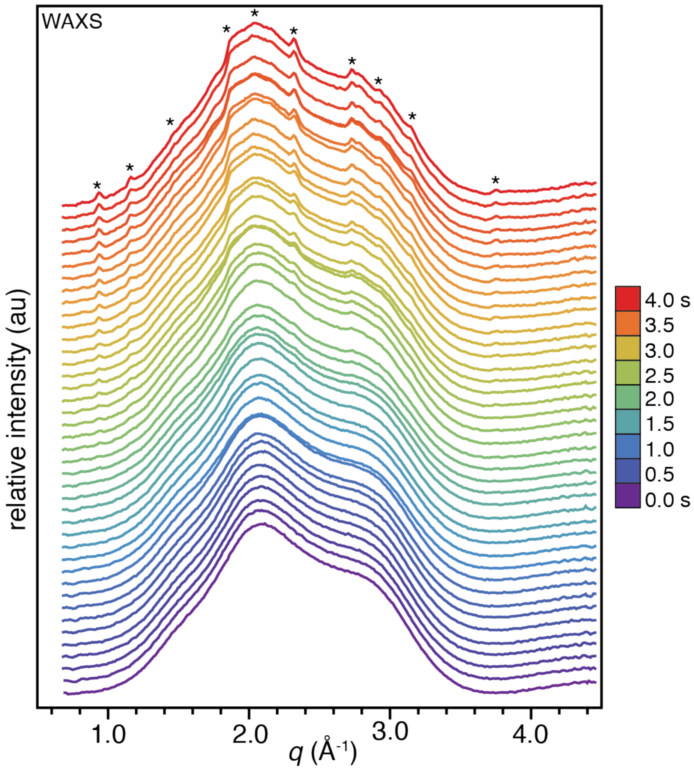

Figure 18.4. WAXS corresponding SAXS data shown in Figure 12.1. Bragg peaks begin to appear between 1-2 seconds, concurrent with a change in SAXS behavior.

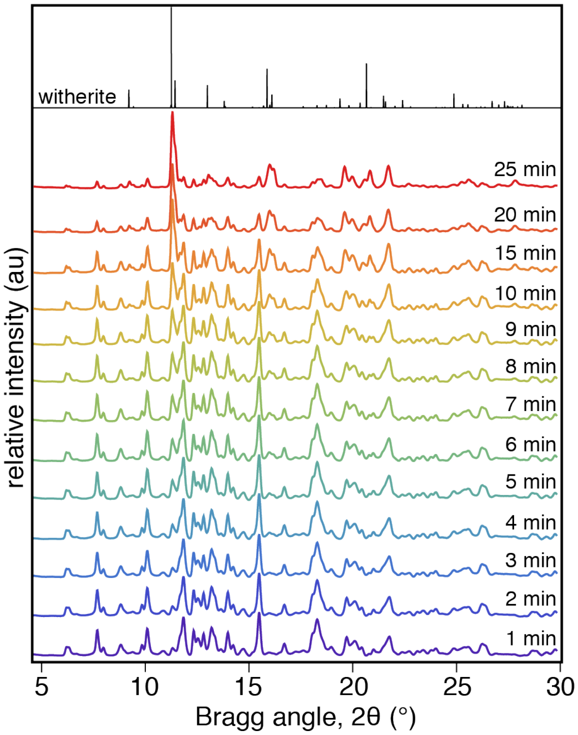

Figure 18.5. Synchrotron X-ray diffraction of $BaCO_3$ precipitation in solution. Gortotowskite transforms into witherite over the course of 30 minutes.

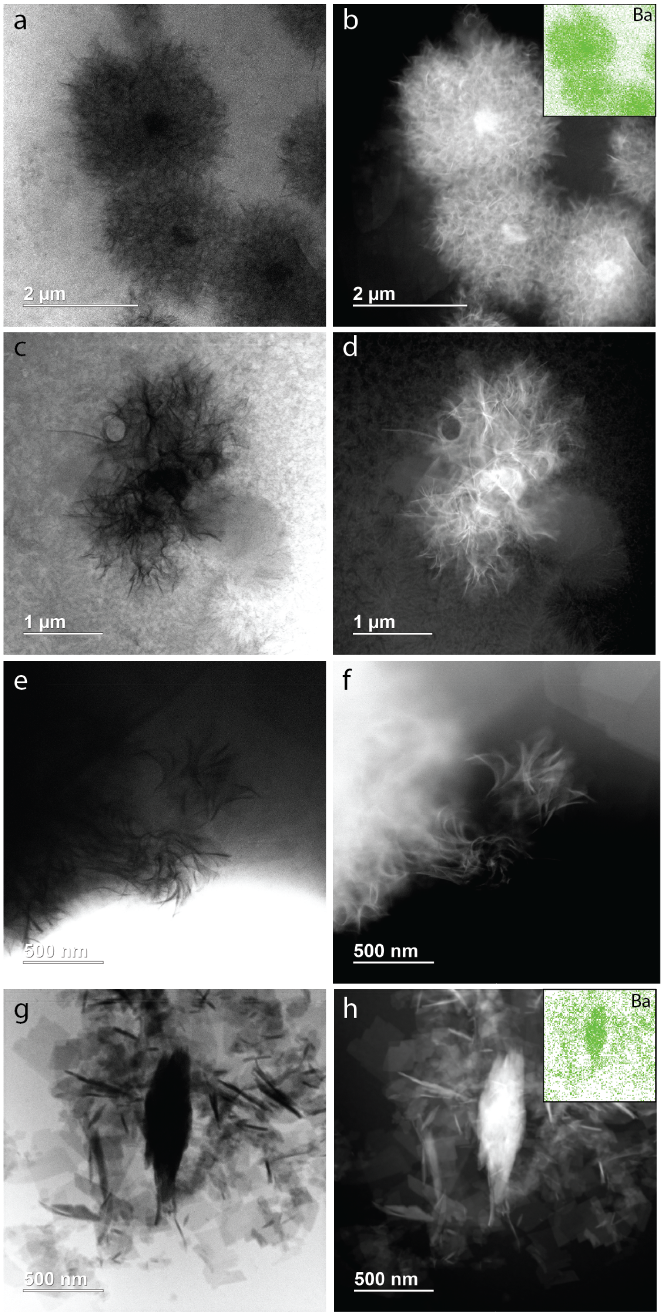

Figure 18.6. Cryo-TEM (a, c, e, g) and cryo-STEM (b, d, f, h) of gortotowskite precipitation. Initially, precipitates were condensed, isotropic particles with dense cores (a, b) approximately 40 nm in diameter. EDS (inset, b) confirmed that the particles were barium rich and that the dense cores were enriched in barium. The diffuse network around the dense cores is consistent with the fractal-type structure predicted from the decreasing Porod slope during growth in SAXS. These particles transitioned into aggregates of this platelets (c, d), as expected from SAXS. These aggregates dispersed in solution (e, f), growing to > 500 nm in edge length before recrystallizing into acicular spherulites that resemble witherite (g, h).

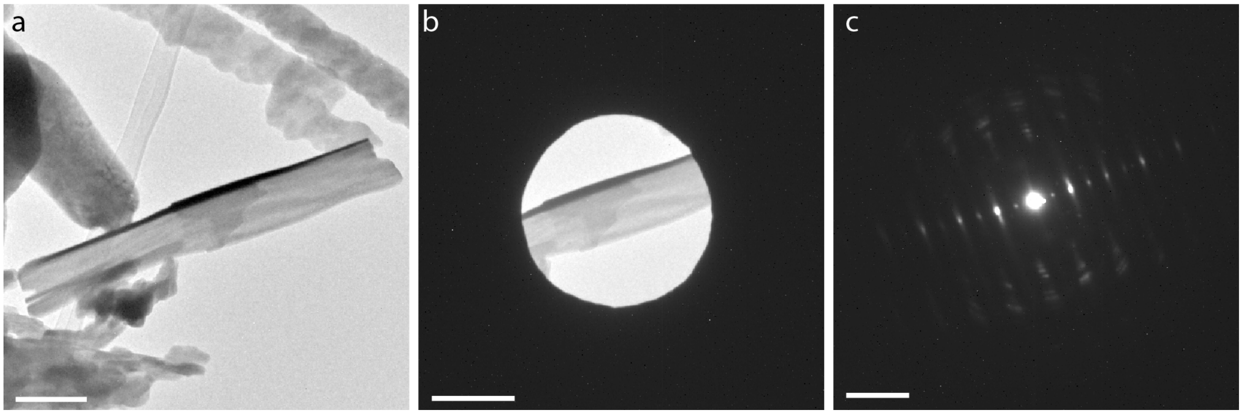

Figure 18.7. Edge-on view of gortotowskite. (a) Bright field TEM. Scale bars represent 200 nm. (b) SAED aperture centered on stack of platelets. (c) SAED pattern, exhibiting strong diffraction only in the plane of the particle but not in the narrow dimension. Diffraction spots exhibit 6.8 Å spacing, consistent with the in-plane diffraction shown in Figure 12.2. Streaks running perpendicular to these most pronounced diffraction spots confirm that individual platelets are quite thin.

18.3 **Electron energy-loss spectrometry (EELS) and high annular dark field (HAADF) imaging**

Parallel EEL spectra were recorded on a Hitachi HD2300 dedicated STEM, fitted with a Gatan Enfina Spectrometer. The electron microscope is equipped with a field emission gun (FEG) operated at 200 keV.

18.3.1 *Thickness determination*

In order to assess a local absolute specimen thickness t of the thin platelets, the log-ratio EELS procedure described by Malis *et al.* was followed.[262] This method requires a known characteristic mean free path for inelastic scattering, λ, with a relation to the specimen thickness t as

$$\frac{t}{\lambda} = \ln\left(\frac{I_t}{I_0}\right) \tag{18.6}$$

with I_t is the total electrons in the electron energy loss spectrum and I_0 the amount of electrons that did not lose energy (*i.e.* the zero-loss peak). The mean free path (units in nm) can be given as

$$\lambda = \frac{106\, F\, E_0}{E_m \ln(2\beta E_0/E_m)} \tag{18.7}$$

with E_0 the incident beam energy in keV, β the spectrum collection angle in mrad, and F is a relativistic factor given by

$$F = \frac{1 + (E_0/1022)}{(1 + (E_0/511))^2} \tag{18.8}$$

The E_m term is some average energy loss (in eV), depending on an “effective” atomic number Z_{eff} according to

$$E_m \approx 7.6 {Z_{eff}}^{0.36} \tag{18.9}$$

with

$$Z_{eff} = \frac{\sum_i f_i {Z_i}^{1.3}}{\sum_i f_i {Z_i}^{0.3}} \tag{18.10}$$

Mean free paths can be fitted within ~ 20% by the above equations (18.7) and (18.9), an acceptable degree of accuracy for many applications.

We acquired zero-loss spectra at low convergence angle α and collection angle β (7 mrad and 8 mrad, respectively). These values were chosen since they reflected adequate count rates in the EELS spectrum. Since the magnification was relatively high (> 100,000 X), an entrance aperture of 3 mm was selected. Total collection times equaled 0.01 second, summed over 10 individually acquired spectra. The dispersion was set to 0.3 eV/channel.

18.3.2 *Ba N-edge acquisition*

Ba $N_{4,5}$ edges were obtained at α = 21 mrad and β = 8 mrad, with a total acquisition time of 5 seconds (summed over 20 individually acquired spectra), at a dispersion of 0.1 eV/channel.

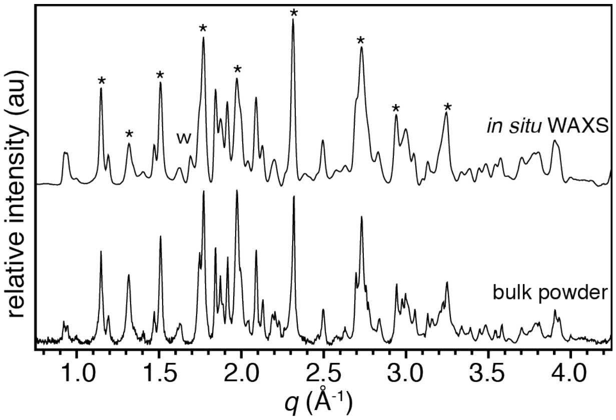

Figure 18.8. Comparison of in situ WAXS and pXRD of the bulk powder, confirming that they are the same phase.

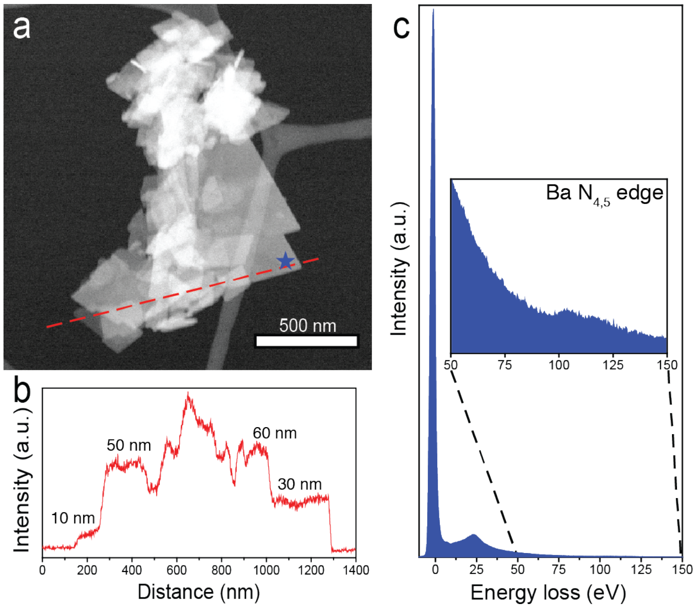

Figure 18.9. (a) EELS linescan across an aggregate of gortotowskite platelets, showing discrete changes in thickness in approximately 10 nm intervals. (b) EELS spectrum from location marked with blue star in (a), showing large zero-loss peak Ba $N_{4,5}$-edge ELNES

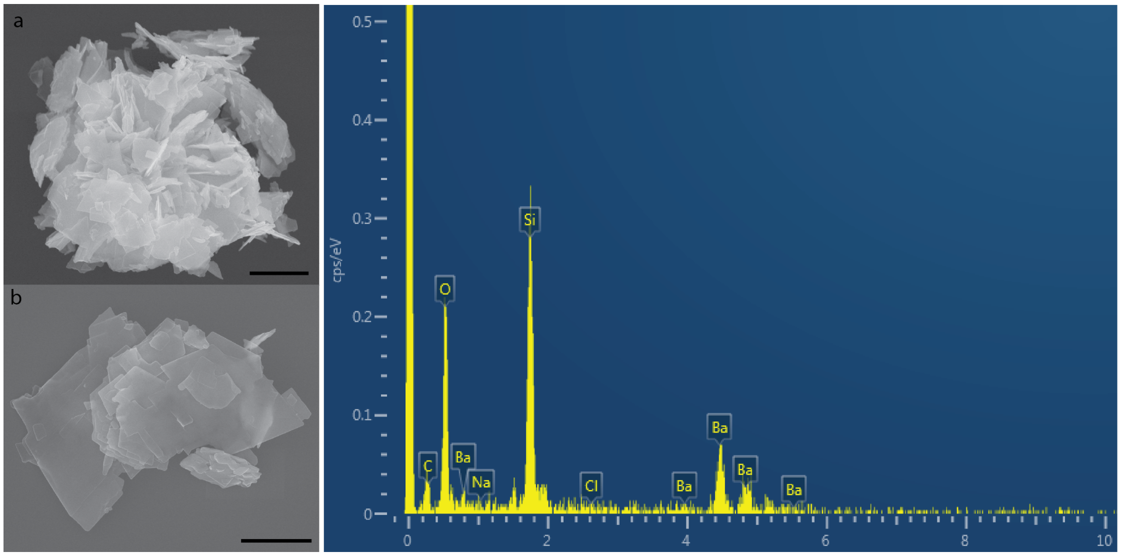

Figure 18.10. (a-b) SEM images of gortotowskite, and (c) EDS, confirming the presence of C, O, and Ba. Background signal from the Si substrate (1.7 eV) and a small (unlabeled) peak near 1.5 eV from the Al sample holder were also present.

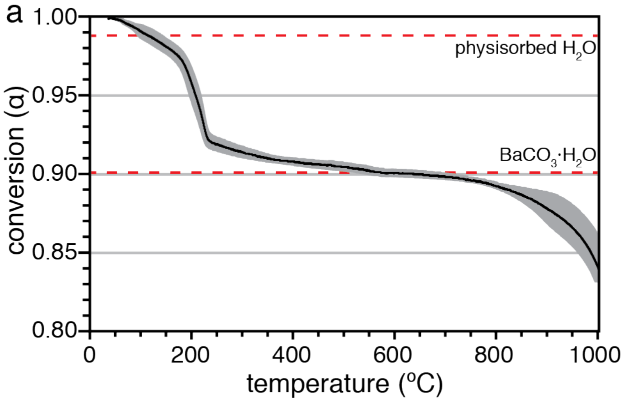

Figure 18.11. TGA of gortotowskite. Mass loss due to the removal of physisorbed water is expected to occur below 100°C, which accounts for 1.5% of the initial mass. Approximately 8.4% of the initial mass is lost between 100 – 600°C, which is consistent with one formula unit of water per $BaCO_3$. Above 600°C mass loss increases with temperature, and is ascribed to decomposition of $BaCO_3$ into CO_2 and BaO. Error (gray) represents one standard deviation from four separate measurements.

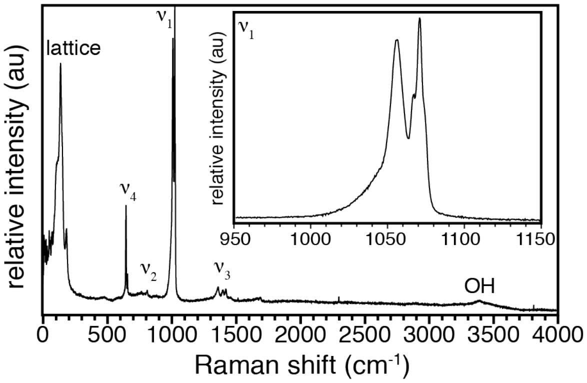

Figure 18.12. Raman spectrum of gortotowskite.